TUNING THE FUNCTIONALITY OF GRAPHENE OXIDE FOR ADSORPTION AND SENSING APPLICATIONS

Thesis submitted to the
University of Calicut for the partial fulfilment of
the requirements for the award of the degree of

DOCTOR OF PHILOSOPHY IN PHYSICS
Under the Faculty of Science

By

ARUNA UNNIKRISHNAN

DEPARTMENT OF PHYSICS
UNIVERSITY OF CALICUT
KERALA, INDIA 673 635

JANUARY 2025

Tuning the functionality of Graphene Oxide for Adsorption and Sensing Applications

Ph.D. Thesis in Physics

Author:

Aruna Unnikrishnan
Research Scholar
Laboratory for Mesoscopic Sciences and Devices
Department of Physics
University of Calicut
Calicut University (PO) – 673635, Kerala, India.
Email: arunaun70@gmail.com

Under the guidance of

Dr. Libu K. Alexander
Associate Professor
Department of Physics
University of Calicut
Calicut University (PO) – 673635, Kerala, India.
Email: lka@uoc.ac.in

UNIVERSITY OF CALICUT
DEPARTMENT OF PHYSICS

Dr. LIBU K. ALEXANDER
PhD (IIT Bombay), PDF (Paris, Canberra)
Associate professor
Room F12, Department of Physics

Calicut University P.O
Kerala, India. 673 635
Tel : +919446376861(M)
email: lka@uoc.ac.in

CERTIFICATE

Certified that the work presented in the thesis, entitled **''Tuning the functionality of Graphene Oxide for Adsorption and Sensing Applications''** is based on the authentic record of research carried out by **Mrs. ARUNA UNNIKRISHNAN** under my guidance in the Department of Physics, University of Calicut, Calicut University P.O, Kerala-673635 and this work has not been included in any other thesis submitted previously for the award of any degree.

Calicut University
25 January 2025

Dr. Libu K. Alexander

UNIVERSITY OF CALICUT
DEPARTMENT OF PHYSICS

Dr. LIBU K. ALEXANDER
PhD (IIT Bombay), PDF (Paris, Canberra)
Associate professor
Room F12, Department of Physics

Calicut University P.O
Kerala, India. 673 635
Tel : +919446376861(M)
email: lka@uoc.ac.in

CERTIFICATE

Certified that the work presented in the thesis, entitled "**Tuning the functionality of Graphene Oxide for Adsorption and Sensing Applications**" is based on the authentic record of research carried out by **Mrs. ARUNA UNNIKRISHNAN** under my guidance in the Department of Physics, University of Calicut, Calicut University P.O. Kerala-673635 and this work has not been included in any other thesis submitted previously for the award of any degree. Also certified that the corrections suggested by the adjudicators have been incorporated in this revised thesis.

Calicut University
14 July 2025

Dr. Libu K. Alexander

DECLARATION

Certified that the work presented in this thesis, entitled **''Tuning the functionality of Graphene Oxide for Adsorption and Sensing Applications''** is based on the original research work done by me under the supervision and guidance of **Dr. Libu K. Alexander**, Associate Professor, Department of physics, University of Calicut, University P.O, Kerala-673635 and has not been included in any other thesis submitted previously for the award of any degree. The contents of the tesis are undergone plagiarism check using iThenticate software at C.H.M.K Library, University of Calicut, and the similarity index found within the permissible limit. I also declare that the thesis is free of AI generated contents

Calicut University
25 January 2025 **Aruna Unnikrishnan**

Dr. Libu K. Alexander
Associate Professor
Department of physics
University of Calicut

ABSTRACT

Graphene oxide (GO), a versatile two-dimensional material, exhibits unique properties due to its oxygen-containing functional groups, making it an ideal candidate for adsorption and sensing applications. This thesis focuses on systematically tuning the functionality of GO through various modifications to enhance its performance in these domains. The research is divided into five working chapters, each exploring a distinct modification strategy.

The first chapter investigates the chemical modification of GO using sodium hydroxide (NaOH). By varying the NaOH concentration, significant alterations in the oxygen functional groups and their distribution within GO were observed. Our study identified a threshold NaOH concentration of 5.45:1 (NaOH:GO by weight) as critical for reducing graphene oxide (GO), as evidenced by enhanced π-π* transitions in UV-visible spectra and an increased ID/IG ratio in Raman analysis. We established that UV-visible absorbance maxima, rather than peak shifts, serve as a more reliable indicator of GO reduction. Unlike with $NaBH_4$, where pH and absorbance maxima followed similar trends, NaOH reduction showed distinct behaviour, with absorbance maxima proving more indicative of the reduction pathway. This conclusion was further validated by Raman analysis, confirming that pH does not play a decisive role in GO reduction. This study provides a foundation for optimizing GO's structure to meet specific application needs.

In the second chapter, GO was combined with activated carbon to form a composite material in simple step aimed at enhancing its adsorption capabilities. GOAC demonstrated exceptional efficiency in removing different dyes like methylene blue, rhodamine b, congo red, their mixtures and antibiotics - ciprofloxacin. We evaluated GOACs adsorption kinetics and found that these reactions followed pseudo second order kinetics and also proposed corresponding mechanisms for integration. Such performance addresses critical challenges in industrial wastewater treatment showcasing the synergistic interaction between GO and activated carbon.

The third chapter examines the formation of a reduced graphene oxide-gold nanoparticle (rGO-Au) composite for sensing applications. This composite was

evaluated for uric acid detection using UV-visible spectroscopy, where a fivefold enhancement in sensitivity was observed compared to GO or gold nanoparticles alone. The rGO-Au composite showed excellent performance within physiologically relevant detection ranges, emphasizing its potential for biosensing applications in medical diagnostics and environmental monitoring.

In the fourth chapter, the effect of synthesis time on GO's properties was systematically studied. GO samples prepared with synthesis durations of 2, 4, 8, and 18 hours, designated as GO2Hr, GO4Hr, GO8Hr, and GO18Hr, were evaluated for adsorption and sensing applications. Adsorption studies revealed that GO2Hr exhibited superior performance for methylene blue and naphthalene in a short duration. For MB adsorption, we achieved the highest adsorption capacity of 1285mg/g at the best time of 4 minutes. These samples were also tested for ascorbic acid sensing, underscoring the importance of synthesis time as a key parameter in tailoring GO's functionality.

The final chapter explores the integration of GO into a 3D melamine sponge (MSGO) to create a composite structure for simultaneous dye removal and oil-water separation. MSGO samples derived from time-varied GO synthesis demonstrated excellent performance, particularly in saline conditions. MSGO2 showed exceptional adsorption kinetics and efficient oil-water separation for different set of oils in tap water and sea water, making it a promising material for real-world environmental remediation.

In conclusion, this thesis presents a systematic approach to modifying GO and its composites to optimize their functionality for adsorption and sensing applications. The findings contribute significantly to the understanding of GO's potential as a multifunctional material and offer practical solutions for challenges in environmental and biosensing technologies.

Keywords Graphene oxide, adsorption, sensing, oil water separation, methylene blue, rhodamine b, congo red, ciprofloxacin, naphthalene, ascorbic acid, uric acid, adsorption kinetics,

ACKNOWLEDGMENT

I would like to extend my heartfelt gratitude to everyone who has supported and contributed to the successful completion of this thesis. This research would not have been possible without the guidance, encouragement, and collaboration of many individuals, to whom I am deeply indebted.

First and foremost, I would like to express my deepest gratitude to my esteemed guide, Dr. Libu K. Alexander, for his unwavering support, guidance, and insight throughout this research journey. His scientific rigor and constant pursuit of perfection have profoundly shaped the direction and quality of my work. Whenever I felt low in motivation or lagged in progress, a meeting with him was all it took to reignite my enthusiasm and push me to work even harder than before. His innovative ideas and encouragement to refine and better my research were invaluable at every stage. I am especially thankful for his approachable and friendly nature, which made complex discussions easier, and for the generous time and effort he invested to ensure the success of this study. His mentorship has been a pivotal force, not just in this thesis, but in my growth as a researcher.

I would also like to extend my sincere thanks to Dr. Mohammed Shahin Thayyil, the present Head of the Department of Physics, University of Calicut, for his support and encouragement. I am equally grateful to all the former Heads of the Department, as well as the teaching and non-teaching staff, for their assistance and cooperation throughout my research work. Their contributions, both direct and indirect, have played a vital role in the successful completion of this thesis.

I would like to express my heartfelt gratitude to Dr. Kishore Sridharan, Faculty, Department of Nanoscience and Nanotechnology, for his invaluable assistance with the SEM analysis. I was at an impasse with this aspect of my research, and his insightful guidance proved transformative, significantly shaping the course of my thesis work.

I would like to express my heartfelt gratitude to both my former and present lab mates for their invaluable support and for fostering a collaborative and positive work environment. Special thanks to Dr. Raseen Nannakkal, Dr. Vidya Rajan, and Dr. Bintu Thomas for their guidance and camaraderie during the early stages of my research. I am equally grateful to my current lab mates, Dr. Anju K, Dr. Sravan Das P, Reeja G Nair, and Reshmi, who have always been readily available to provide assistance, clarification, and encouragement in both academic matters and beyond. Their constant help and shared insights have been instrumental in the smooth progress of my research. I would also like to extend my sincere thanks to all the MPhil and MSc students who have been a part of this journey.

I would also like to extend my heartfelt gratitude to my dear friends in the Department of Physics for their companionship, support, and encouragement throughout this journey. A special mention goes to Parvathy T., who has been my pillar of strength during this entire period, from our MPhil days to the completion of this research. Words cannot fully express my appreciation for her unwavering support and constant presence by my side, through every small and significant event. Her encouragement, friendship, and understanding have been invaluable, and I truly owe her more than just a 'thank you.'

I extend my heartfelt gratitude to all my teachers from my school days through my degree, postgraduate, and MPhil studies, who have shaped my academic journey and inspired my passion for learning. A special mention goes to Anny Minni Jose, Dr. Sabu PG, Shafi KM, Dr. Daughty John and Dr. Subasa Chandra Sahoo whose guidance, encouragement, and wisdom have left a lasting impact on me. Each of my teachers has played a vital role in moulding me into the person and researcher I am today, and I am forever thankful for their contributions to my growth.

I would also like to acknowledge the Principal of EMEA College for his willingness to give NOC and for allowing me to complete my PhD work in part-time mode during the final phase of my research. This flexibility was crucial in helping me balance my academic commitments and progress toward the completion of my thesis. I am deeply grateful to the Head of the Department, Dept of Mathematics and

Physics, EMEA college, Dr. Ramsiya M, and my colleagues Dr. Abdul Rasheed Paloly, Ms. Suneena PD, Ms. Nashath A, Ms, Mubeena, Mr. Muhammed Ajmal, and Ms. Shahana Sherin, for their immense support and encouragement during this journey. Their willingness to adjust hours, share responsibilities, and accommodate my needs allowed me to focus on the critical writing and submission phases of my PhD. Their generosity and cooperation have been instrumental in helping me complete my research, and I am truly thankful for their understanding and assistance.

I would like to express my deepest gratitude to my parents, NP Unnikrishnan and Meera Bai K, for their unconditional love, support, and encouragement throughout my life. They have been my constant source of strength, and their belief in me has carried me through every challenge. They eagerly awaited the day of my thesis submission, constantly encouraging me to pursue my dreams. Their belief in my potential and desire to see me soar to new heights has been a driving force throughout my journey, and I dedicate this achievement to them. I am equally grateful to my sibling, Dr. Aswathi Unnikrishnan, for her unwavering support and for always being there when I needed guidance or encouragement.

A special mention goes to my uncle, Nandakumar K, who is the very reason I chose to pursue physics and continued in this field. His influence and passion for the subject have inspired me from the very beginning, and I am forever thankful for his role in shaping my academic journey.

I would also like to extend my heartfelt thanks to my mother-in-law, Rohini Devi, for her constant encouragement and support, and to all my near and dear family members, whose love and care have been invaluable throughout this journey. Their presence has been a source of comfort and motivation, and I am truly grateful for each one of them.

I owe an immeasurable debt of gratitude to my dear husband, Mr. Sujith E, for his inexpressible support throughout this journey. His constant encouragement, understanding, and willingness to share household duties allowed me the time and focus to complete my research. He has always taken great care to ensure I present myself well, beautifying me in my dressing and style, and I know that he will be even

happier than I am, at the submission of this thesis. During my pregnancy, despite the university being far from his workplace, he selflessly drove me to and from the campus, ensuring my comfort and well-being. His love, patience, and sacrifices have been beyond words, and I could not have come this far without him by my side.

I also want to express my deep gratitude to my daughter, Kalhara A S, for her patience and understanding, even at such a young age. She often stayed calm, allowing me to work on my PhD, and I know she endured a lot when I left her at just six months old to continue my research. The thought of her missing her mama during that time still weighs on my heart. Now, she asks me with excitement, "When will I come to your school to have biriyani, Mama?" Her love and innocence have been a constant source of motivation for me to push through and complete this journey.

There are many people whose names may not have been explicitly mentioned in this acknowledgement, but I am truly grateful to each and every one of you. Your support, encouragement, and contributions, whether big or small, have played a vital role in the successful completion of my research, and I deeply appreciate your presence throughout this journey.

Above all, I thank God for His countless blessings, guidance, and grace throughout this journey. It is through His strength and wisdom that I have been able to persevere and complete this work, and I am forever grateful for His presence in every step of my life.

Aruna Unnikrishnan

PUBLICATIONS

1. Unnikrishnan, A., & Alexander, L. K. (2024). **The concentration-dependent effect of NaOH on graphene oxide: Revisited as a reducing agent**. *Journal of Physics and Chemistry of Solids*, *190*, 111978. https://doi.org/10.1016/j.jpcs.2024.111978

2. Unnikrishnan, A., & Alexander, L. K. (2024). **Organic dye sequestration using Graphene Oxide–Activated Carbon (GOAC) composite unaided by linker molecule**. *Journal of Materials Science: Materials in Electronics*, *35*(6), 417. https://doi.org/10.1007/s10854-024-12230-2

3. Unnikrishnan, A., Megha, V., & Alexander, L. K. (2024). **Ascorbic acid sensing utilizing graphene oxide based on UV–Visible bathochromic shift.** *Journal of Materials Science: Materials in Electronics*, *35*(13), 904. https://doi.org/10.1007/s10854-024-12672-8

4. Unnikrishnan, A., Alexander, L.K. (2025) **Serum Level Biosensing of Uric Acid Using RGO-Au Nanocomposite Based On UV–Vis Spectroscopy**. *Plasmonics*, 1-8. https://doi.org/10.1007/s11468-025-03141-x

PAPERS PRESENTED IN INTERNATIONAL/NATIONAL CONFERENCES

1. ***"Role of H_2O_2 in Graphene Oxide Synthesis"*** AMALIT International Conference 2022 organised by Amal College of Advanced studies, Nilambur on 15 - 17 February 2022.

2. ***"A Novel Approach to Ascorbic Acid Sensing Utilizing Graphene Oxide"*** International conference on advances in material science and chemistry ICAMSC 2023, organised by Amrita Vishwa Vidyapeedam during 02 - 04 November 2023 and received **BEST ORAL PRESENTATION** for the same.

3. ***"Enhanced Adsorption of Ciprofloxacin Antibiotic using Graphene Oxide Activated Carbon Composite"*** International conference on advanced materials for sustainability ICAMS 2023 organised by Calicut University during 21 - 23 December 2023.

4. ***"Efficient Removal of Rhodamine B Using Graphene Oxide-Activated Carbon Composite"*** International conference on advanced functional materials and devices AFMD 2024 organised by SRM University during 26-29 February 2024.

CONTENTS

	Page No.
Preface	
List of Figures	
List of Tables	
Abbreviations used in the thesis	
1. Introduction	**1-28**
1.1 Background and Significance	1
1.2 Graphene Oxide: An Overview	2
1.2.1 Structure and Properties of Graphene Oxide	2
1.2.1.1 Structural Characteristics	2
1.2.1.2 Physical Properties	3
1.2.1.3 Chemical Properties	4
1.2.1.4 Optical Properties	4
1.2.2 Functionality of Graphene Oxide	5
1.2.3 Synthesis Methods of Graphene Oxide	6
1.2.3.1 Hummers Method	6
1.2.3.2 Brodie Method	7
1.2.3.3 Staudenmaier Method	8
1.2.3.4 Modified Hummers Method	8
1.2.3.5 Other Synthesis Methods	9
1.3 Tuning the Functionality of Graphene Oxide	10
1.3.1 Chemical Modifications	10
1.3.2 Composite formation	11
1.3.3 Synthesis Conditions	12
1.3.4 Loading in 3D matrix	12
1.4 Adsorption and Sensing Applications of Graphene Oxide	13
1.4.1 Adsorption Applications of Graphene Oxide	13
1.4.2 Sensing Applications of Graphene Oxide	15
1.5 Motivation	16

1.6 Objectives of the Thesis	17
1.7 Organization of the Thesis	18
1.8 References	21
2. Methods and Experimental techniques	**25-75**
2.1. Synthesis of Graphene Oxide	25
2.2. Materials and methods used	26
2.2.1. Materials used	26
2.3. Experimental techniques	26
2.3.1. X-Ray Diffraction Analysis	27
2.3.2. Raman spectroscopy	32
2.3.3. UV-Visible spectrometer	36
2.3.4. Thermogravimetric analysis	42
2.3.5. BET surface analysis	46
2.3.6. Scanning electron microscope	50
2.3.7. Dynamic Light Scattering technique	57
2.3.8. Fourier transform infrared spectroscopy	60
2.3.9. Laboratory equipment	64
2.4 Adsorption	64
2.5 References	68
3. Graphene Oxide modification using NaOH treatment	**77-99**
3.1 Introduction	79
3.2 Experimental details	80
3.3 Results and discussions	80
3.3.1 Raman spectra	85
3.3.2 Absorbance maxima in UV-visible spectra	87
3.3.3 Concentration dependent effect of NaOH	88
3.3.4 Effect of pH on the reduction of GO	90
3.3.5 Comparing peak shift and absorbance maxima: their relative significance	92
3.3.6 The threshold amount of NaOH for reduction of GO	92
3.4 Comparative analysis with literature	93
3.5 Conclusion	93

3.6 References	95
4. Graphene oxide modification using activated carbon – composite formation	**101-141**
4.1. Introduction	103
4.2. Experimental details	104
4.2.1. Synthesis of GO and GOAC composite	104
4.3. Results and discussions	104
4.3.1. Characterisations	104
4.3.2. Methylene blue adsorption experiment	110
4.3.2.1 MB calibration	112
4.3.2.2 Adsorption kinetics	113
4.3.2.3 Regeneration	114
4.3.2.4 Mechanism	115
4.3.2.5 Comparison with other adsorbents	117
4.3.3. Rhodamine B adsorption experiment	117
4.3.3.1 RhB calibration	119
4.3.3.2 Adsorption kinetics	120
4.3.3.3 Mechanism	123
4.3.3.4 Comparison with other adsorbents	124
4.3.4. Congo red adsorption	125
4.3.5. The mixture of dyes	126
4.3.5.1 Regeneration	128
4.3.6. Ciprofloxacin antibiotic adsorption	129
4.3.6.1 Ciprofloxacin calibration	131
4.3.6.2 Adsorption kinetics	131
4.3.6.3 Mechanism	133
4.3.6.4 Comparison with other adsorbents	134
4.4. Conclusion	135
4.5. References	136
5. Graphene oxide modification using gold nanoparticles – composite formation	**143-157**
5.1. Introduction	145

5.2. Experimental details	146
5.2.1. Gold nanoparticle synthesis	146
5.2.2. Graphene oxide synthesis	147
5.2.3. rGO-Au nanocomposite synthesis	147
5.3. Results and discussion	147
5.3.1. Characterization	147
5.3.2. Uric acid sensing	149
5.4. Comparison of uric acid sensing with reports from literature.	152
5.5. Conclusion	154
5.6. References	155
6. Graphene oxide modification by time varying reaction	**159-187**
6.1. Introduction	161
6.2. Experimental details	162
6.2.1. Synthesis of GO	162
6.3. Results and discussions	162
6.3.1. Characterisation techniques	162
6.3.2. Methylene blue Adsorption experiment	167
6.3.2.1 Adsorption kinetics	169
6.3.2.2 Comparison table	171
6.3.2.3 Regeneration	171
6.3.2.4 Mechanism	172
6.3.3. Naphthalene adsorption experiment	173
6.3.3.1 Adsorption Kinetics	175
6.3.3.2 Mechanism	178
6.3.3.3 Comparison table	179
6.3.4. Biosensing with ascorbic acid Vitamin C	180
6.4. Conclusion	183
6.5. References	185
7. Graphene oxide modification using melamine sponge	**189-204**
7.1. Introduction	191

7.2. Experimental details	192
7.2.1. Loading graphene oxide to melamine sponge	192
7.2.2. Adsorption experiment	193
7.2.3. Adsorption Kinetics	195
7.2.4. Oil water separation experiment	196
7.2.4.1 Methodology	196
7.3. Results and discussions	197
7.4. Conclusion	201
7.5. References	203
8. Summary and Conclusion	**205**
9. Recommendations	**211**

LIST OF FIGURES

Figure No.	*Title*	*Page No.*
1.1	**Outline of the importance of modifying GO**	16
1.2	Outline of the Thesis	20
2.1	Diagram of X-ray diffraction at the lattices.	27
2.2	Image showing different components of the XRD machine	29
2.3	Image of X-ray diffractometer at Department of Physics, University of Calicut.	31
2.4	Image of X-ray diffractometer at CSIF, University of Calicut.	31
2.5	Schematic representation of the origin of Raman lines	33
2.6	Schematic of a micro-Raman spectrometer	34
2.7	Image of Raman Spectrometer used. (photo of the micro-Raman set up at the Department of Physics, University of Calicut).	36
2.8	Schematic diagram of instrumentation of double beam UV-visible spectrometer.	40
2.9	Image of UV-visible Spectrometer used. (at Laboratory for mesoscopic sciences and devices, Department of Physics, University of Calicut).	42
2.10	Image of TGA instrument at *CSIF*, University of Calicut.	46
2.11	Image of BET instrument at *CSIF*, University of Calicut.	50
2.12	Schematic of a scanning electron microscope	51
2.13	Image of FESEM at CSIF, University of Calicut	57
2.14	Schematic diagram of instrumentation of DLS instrument	58
2.15	Image of DLS instrument at Department of Nanoscience and nanotechnology, University of Calicut	60
2.16	*FTIR Spectrometer*	63
3.1	XRD pattern of GO obtained via Hummer's method	81
3.2	UV plot of NaOH-treated samples.	81
3.3	Fitted curves for UV-visible spectra for NaOH-treated GO samples.	83
3.4	The bathochromic shift in peak position corresponding to maximum absorbance for Peak 1.	84
3.5	Variation of absorbance maxima of P_{230} with NaOH dose	84
3.6	Raman spectra of GN1 to GN8	85

3.7	ID/IG ratio with the amount of NaOH	86
3.8	The UV-visible absorbance and π - π* transitions mechanisms	88
3.9	Variation in pH and Normalised absorbance maxima with the addition of NaOH to GO solution	91
3.10 A 3.10 B	The study involved assessing pH fluctuations resulting from the introduction of various reducing agents to GO. The alterations in peak positions observed in UV-visible spectra upon the introduction of different reducing agents served as a valuable indicator of the extent of reduction achieved	91
4.1	Synthesis of GOAC composite	104
4.2	The Raman spectra of graphene oxide (GO), activated carbon (AC), and the GOAC Composite	105
4.3	The x-ray diffraction (XRD) spectra of graphene oxide (GO), activated carbon (AC), and the GOAC composite	106
4.4	Adsorption - desorption isotherm of the samples	106
4.5	FTIR Spectra of GO, AC and GOAC.	107
4.6	TGA analysis of GO, AC and GOAC	109
4.7	FE-SEM images of (a)GO, (b)AC, (c)GOAC and (d)porous nature of AC in lower magnification	109
4.8	UV-visible spectrum plots of MB dye adsorption by 0.01 g of a) GO, b) AC, and c) GOAC	110
4.9	UV-visible spectrum plots of MB dye adsorption by 0.005 g of a) GO, b) AC, and c) GOAC	111
4.10	Variation of removal efficiency with contact time for MB using (a) 0.01g of adsorbent, and (b) 0.005g of adsorbent	111
4.11	Calibration curve for MB	112
4.12	Pseudo first order kinetic model for the adsorption of MB onto (a) 0.01g of adsorbents, (b) 0.005g of adsorbents.	113
4.13	Pseudo second order kinetic model for the adsorption of MB onto (a) 0.01g of adsorbent, (b) 0.005g of adsorbent.	113
4.14	Percentage removal efficiency of the regenerated GOAC composite in consecutive cycles	115
4.15	Interaction of the GOAC composite with methylene blue.	116
4.16	UV-visible plots of RhB dye adsorption by 0.01 g of a) GO, b) AC, and c) GOAC	118
4.17	Removal percentage of RhB dye adsorption by 0.01 g of a) GO, AC, and GOAC	119
4.18	Calibration curve for RhB	119

4.19	Pseudo-first-order kinetic fit	120
4.20	Pseudo second-order kinetic fit	121
4.21	Elovich kinetic model fit	122
4.22	UV-visible plots of CR dye adsorption by 0.01 g of a) GO, b) AC, and c) GOAC	125
4.23	Removal percentage of CR dye adsorption by 0.01 g of GO, AC, and GOAC	126
4.24	Removal percentage of methylene blue, rhodamine B and congo red dye and the mixture of these three dyes with 0.01g of GOAC composite.	127
4.25	Consecutive cycles of dye mixture removal	128
4.26	UV-visible absorbance spectra of CF adsorption onto a) GO, b) AC and c) GOAC composite	130
4.27	Percentage of removal of CF with time for GO, AC and GOAC composite	130
4.28	Calibration curve for CF	131
4.29	[A] Pseudo First order kinetic model for adsorption of 10ppm CF onto GO, AC and GOAC composite. [B] Pseudo Second-order kinetic model for adsorption of 10ppm CF onto GO, AC and GOAC composite.	132
5.1	X-ray diffraction pattern of GO with a single intense peak	147
5.2	UV-visible absorbance spectra of gold nanoparticles (Au-nanoparticle), graphene	148
5.3	DLS spectra for Au nanoparticles and rGO-Au nanocomposite. DLS spectra give the average particle size of the materials.	149
5.4	UV-visible absorbance spectra when varied concentrations of uric acid (1 mg/dL to 20 mg/dL) interact with a solution of (a) GO - the inset of the figure shows the UV vis spectra of uric acid solution at 5 mg/dL concentration resulting in absorption maxima at 0.33 A.U, (b) Au nanoparticles (c) rGO-Au nanocomposite and (d) magnified image of the peak ~ 285 nm with rGO-Au nanocomposite (e) absorbance maxima of UV vis spectra peak at ~285 nm for the sensing elements in contact with 5mg/dL solution of uric acid.	150
5.5	Variation of absorbance maxima with analyte concentration, corresponding to the 285 nm peak of uric acid, with graphene oxide, gold nanoparticles, and rGO-Au nanocomposite as the biosensing element.	151

6.1	XRD patterns of graphene oxide samples synthesised under different modification times [GO2Hr, GO4Hr, GO8Hr, and GO18Hr].	163
6.2	Effect of modification time on the variation of 2θ and d-spacing.	163
6.3	Raman spectra of graphene oxide samples [GO2Hr, GO4Hr, GO8Hr, and GO18Hr].	164
6.4	Variation of ID/IG ratio of Raman spectra for each set of GO samples	165
6.5	FTIR spectra of different GO samples [GO2Hr, GO4Hr, GO8Hr, and GO18Hr].	165
6.6	FESEM images of sample GO2Hr	167
6.7	UV-visible absorbance plots of MB dye adsorption by 0.01 g of GO2Hr, GO4Hr, GO8Hr and GO18Hr. The absorbance of 10ppm MB is 1.8914, and after adsorption, the absorbance became 0.0038, 0.0075, 0.3506 and 1.3108 for GO2Hr, GO4Hr, GO8Hr and GO18Hr samples respectively.	168
6.8	Pseudo-second-order kinetic model fit	169
6.9	The GO2Hr sample was regenerated after each adsorption cycle, and the adsorption experiment was repeated for four additional consecutive cycles. 100% dye removal was obtained even after five cycles.	172
6.10	Depiction of the four different interaction mechanisms of MB adsorption by GO sample.	173
6.11	UV-visible absorbance for naphthalene adsorption on GO samples.	174
6.12	Naphthalene removal percentage for GO samples	175
6.13	Pseudo-first-order kinetic fit for naphthalene adsorption for GO samples	175
6.14	Pseudo-second-order kinetic fit for naphthalene adsorption for GO samples	176
6.15	[A] $FeCl_3$ and $K_3[Fe(CN)_6]$ are mixed in desired concentrations and we have a light green hue coloured solution. [B] When Ascorbic acid is added to the mixture of $FeCl_3$ and $K_3[Fe(CN)_6]$ Prussian blue colour is formed. [C] The figure illustrates the colour variation depending on the concentration of ascorbic acid.	181
6.16	UV visible spectra of solution with ascorbic acid, GO, $FeCl_3$ and $K_3[Fe(CN)_6]$, to compare the effect of GO2Hr, GO4Hr, GO8Hr, GO18Hr.	182
7.1	Synthesis of MSGO samples	193

7.2	UV-visible absorbance plots of MB dye adsorption using MSGO2, MSGO4, MSGO8 and MSGO18.	194
7.3	Dye removal percentage for each MSGO sample	194
7.4	**(a)** Pseudo first-order kinetic model and **(b)** pseudo-second-order kinetic model fit for dye adsorption using MSGO samples.	195
7.5	**(a)** Schematic of the experimental setup for oil-water separation. A funnel loaded with MSGO is connected to a measuring cylinder, allowing a mixture of oil and water to pass through the material. **(b)** Oil water mixture top view **(c)** oil remaining in the funnel, after the water has been filtered out.	197
7.6	UV-visible absorbance spectra of various oil-water mixtures prepared in tap water. Initially, a 5 ppm Methylene Blue (MB) solution is prepared in tap water, and its spectrum is recorded. The oil-water mixtures prepared, are passed through MSGO2, and the UV-visible spectra of the filtrates are also recorded	198
7.7	UV-visible absorbance spectra of various oil-water mixtures prepared in sea water. Initially, a 5 ppm Methylene Blue (MB) solution is prepared in sea	199
7.8	Dye removal percentage of methylene blue (MB) for different sets of oil-water mixture in tap water and sea water.	200

LIST OF TABLES

Table No.	*Title*	*Page No.*
3.1	Peak shift in UV-visible spectra with respect to NaOH addition	82
3.2	Table showing ID/IG ratio of Raman spectra.	86
3.3	pH variation with respect to addition of reagent to GO	90
4.1	ID/IG ratios of samples	105
4.2	BET analysis parameters	107
4.3	FTIR Spectra analysis	108
4.4	Calibration for MB	112
4.5	Adsorption kinetic parameters	114
4.6	Comparison of methylene blue dye adsorption by various adsorbents in literature	117
4.7	Calibration for RhB	119
4.8	Pseudo-first-order kinetic variables of RhB adsorption onto GOAC composite	121
4.9	Pseudo-second-order kinetic variables of RhB adsorption onto GOAC composite	122
4.10	Elovich kinetic variables of RhB adsorption onto GOAC composite	123
4.11	Comparison of rhodamine B dye adsorption by various adsorbents in the literature.	124
4.12	Removal percentage and adsorption capacity of Methylene blue, Rhodamine B and Congo red dye and the mixture of these three dyes with 0.01g of GOAC composite	127
4.13	Calibration for CF	131
4.14	Adsorption kinetic parameters for pseudo-first and pseudo-second order kinetics for the adsorption of CF onto GO, AC and GOAC composite	132
4.15	Comparison table showing the adsorption parameters of various adsorbents towards ciprofloxacin antibiotic.	134
6.1	Summary of the kinetics variables for MB adsorption onto GO samples	170
6.2	Comparison of adsorption capacities of GO for different dyes in the literature	171

6.3	Adsorption kinetic parameters for naphthalene adsorption for GO samples	176
6.4	Comparison table showing the adsorption parameters of various adsorbents towards naphthalene	179
7.1	Adsorption kinetic parameters	195
7.2	Absorbance values after adsorption and removal percentage of methylene blue (MB) for different sets of oil-water mixture in tap water and sea water	200

ABBREVIATIONS USED IN THE THESIS

GO	:	Graphene oxide
RGO	:	Reduced graphene oxide
MS	:	Melamine sponge
AC	:	Activated Carbon
MB	:	Methylene Blue
RhB	:	Rhodamine B
CR	:	Congo Red
CF	:	Ciprofloxacin
AA	:	Ascorbic acid
UA	:	Uric acid
XRD	:	X-ray Diffraction
UV	:	Ultraviolet
vis	:	Visible
FTIR	:	Fourier transform infrared spectroscopy
BET	:	Brunauer–Emmett–Teller
DLS	:	Dynamic light scattering

PREFACE

Graphene oxide (GO) is a revolutionary material that has garnered immense attention due to its remarkable properties, including a large surface area, abundant oxygen functional groups, mechanical strength, and high chemical reactivity. These features make GO an excellent candidate for various applications, such as sensing, adsorption, and thermal management. However, pristine GO faces inherent limitations, such as agglomeration, uneven distribution of functional groups, and limited stability under certain conditions. These challenges restrict the GO's full potential in advanced applications, highlighting the need for strategic modifications to tune and enhance its functionality.

The motivation for the works mentioned in this thesis stems from the necessity to overcome these limitations and fully harness the capabilities of GO for diverse and impactful applications. By systematically modifying GO, it is possible to improve its chemical and thermal stability, increase hydrophilicity, and prevent agglomeration. These enhancements pave the way for GO-based composites with tailored properties to meet specific functional requirements. For example, tuning the distribution of oxygen functional groups can significantly enhance GO's adsorption capacity and sensing efficiency. Similarly, embedding GO into three-dimensional structures like melamine sponges can improve its performance, particularly in environmental remediation and pollutant management.

This thesis, titled "**Tuning the Functionality of Graphene Oxide for Adsorption and Sensing Applications**," focuses on addressing these challenges by systematically exploring methods to enhance GO's properties. The research is structured around three primary objectives. The first objective is to enhance the adsorptive and sensing applications of GO by leveraging its oxygen functional groups. Through controlled synthesis and modification techniques, this work examines how the distribution and density of these functional groups can be optimized to improve performance. The second objective seeks to expand the role of GO-based nanocomposites in environmental remediation and chemical sensing.

By synthesizing and characterizing composites such as graphene oxide activated carbon composite (GOAC) and reduced graphene oxide-gold nanoparticles (rGO-Au), the study demonstrates their superior adsorption capabilities and sensitivity in detecting analytes like uric acid. Finally, the third objective investigates the impact of integrating GO into three-dimensional matrices, such as melamine sponges, to enhance its adsorption properties for applications like oil-water separation and dye removal.

The chapters of this thesis systematically address these objectives. The initial chapters delve into the synthesis and chemical modification of GO, emphasizing the influence of NaOH on the material's functional group distribution and overall properties. These insights serve as the foundation for subsequent studies on GO-based composites. The middle chapters explore the synthesis of GO-based nanocomposites and their applications in chemical sensing and adsorption, demonstrating significant advancements in performance. The final chapters examine the integration of GO into three-dimensional structures, highlighting the enhanced efficiency of these materials in real-world applications, such as environmental remediation.

The functional versatility of graphene oxide (GO) largely stems from its oxygen-containing functional groups, which significantly influence its adsorptive and sensing capabilities. A major objective of this thesis was to enhance these functionalities by systematically modifying the oxygen groups through various chemical and physical treatments. In Chapter 3, the chemical reduction of GO using NaOH was explored to tune the distribution and density of these functional groups. By identifying a threshold NaOH concentration of 5.45:1 (NaOH:GO by weight), we demonstrated that NaOH acts as a reducing agent, effectively altering the π-π^* transitions and enhancing adsorption properties. UV-visible spectroscopy and Raman analysis revealed that absorbance maxima, rather than pH or peak shifts, serve as reliable indicators of reduction. These findings provided a framework for precisely controlling GO's functional groups to optimize its performance in adsorption and sensing applications. Furthermore, in Chapter 6, the influence of synthesis time on GO's oxygen functional groups was studied, revealing that GO

prepared with shorter synthesis times (e.g., GO2Hr) exhibited superior adsorption efficiency for dyes like methylene blue. These studies highlight the critical role of oxygen functional groups in enhancing GO's versatility and provide actionable insights into their optimization.

Graphene oxide-based nanocomposites exhibit synergistic properties, making them highly effective for environmental remediation and chemical sensing. To expand their applications, this thesis explored the formation of GO composites with activated carbon and gold nanoparticles. Chapter 4 focused on synthesizing a GO-activated carbon composite, demonstrating remarkable efficiency in removing dyes and pollutants, even under challenging saline conditions. The enhanced adsorption capacity resulted from the combined surface area and functional group interactions of GO and activated carbon, making this composite a highly effective agent for industrial wastewater treatment and oil spill cleanup. In Chapter 5, we evaluated the reduced graphene oxide-gold nanoparticle (rGO-Au) for uric acid detection, where UV-visible spectroscopy revealed a fivefold increase in sensitivity compared to GO or Au alone. This exceptional performance within physiologically relevant ranges underscores the potential of GO-based nanocomposites for biosensing applications. These composites' systematic synthesis and evaluation highlight their dual role as effective tools for environmental remediation and precise chemical sensing.

The integration of graphene oxide into a three-dimensional (3D) matrix represents a novel approach to enhancing its adsorptive properties. In Chapter 7, we explored the incorporation of GO into a melamine sponge template, creating a 3D structure (MSGO) with superior adsorptive and oil-water separation capabilities for different sets of oils in tap water and saline water. MSGO samples, synthesized using GO prepared with varying synthesis times, were evaluated for their performance in removing dyes and separating oil from water. Among the samples, MSGO2 exhibited exceptional adsorption kinetics and efficiency in saline conditions, making it a promising material for real-world environmental applications. The 3D structure not only provided a larger surface area but also facilitated the accessibility of functional groups, enhancing the material's adsorptive capacity. This study

demonstrates 3D matrix-aided GO structures' transformative potential in addressing critical environmental remediation challenges.

The findings presented in this thesis underscore the transformative potential of tuning GO's functionality through systematic modifications. By addressing the challenges of pristine GO and leveraging its unique properties, this research contributes to advancing nanomaterials for critical applications. Furthermore, it opens up new avenues for future exploration, such as scaling up the synthesis of modified GO composites, investigating their use in energy storage, and expanding their applications in biomedical sensing. This thesis systematically addressed the discussed objectives by modifying GO through targeted chemical treatments, composite formation, and structural integration. Each strategy was carefully designed and experimentally validated to enhance GO's adsorption and sensing functionalities, contributing significantly to its application in environmental and chemical sensing technologies.

As Richard Feynman famously remarked, "There's plenty of room at the bottom," signifying the endless opportunities in nanoscience. This research exemplifies that vision, pushing the boundaries of what GO can achieve and laying a foundation for innovative solutions to global challenges. It is hoped that the insights gained from this work will inspire further advancements in the field of graphene-based materials and their applications.

CHAPTER 1
INTRODUCTION

1.1 Background and Significance

Graphene oxide (GO), the oxidised form of graphene, has garnered considerable attention in recent years due to its distinctive combination of properties. Unlike pristine graphene, GO is rich in oxygen-containing functional groups, such as hydroxyl, epoxy, and carboxyl, which confer hydrophilicity and facilitate chemical modifications. These functional groups make GO an attractive material for various applications, particularly in the fields of adsorption and sensing.

The extraordinary surface area and tuneable surface chemistry of GO enable it to interact effectively with a wide range of substances. In adsorption applications, GO's large surface area and functional groups allow for the efficient capture and removal of contaminants from air, water, and industrial effluents. This has significant implications for environmental remediation, as the ability to remove pollutants such as heavy metals, dyes, and organic compounds is crucial for maintaining ecological balance and human health.

In the realm of sensing, GO's functional groups can be exploited to detect a variety of chemical and biological species with high sensitivity and specificity. Specifically, the property of GO reduction by sensing materials, such as ascorbic acid and uric acid, can be utilised to detect these analytes using UV-visible absorbance spectra. This method offers an effective alternative to more complex electrochemical or voltammetric methods. This makes GO-based sensors highly valuable in biomedical diagnostics, environmental monitoring, and industrial process control.

Despite its promising potential, the performance of GO in adsorption and sensing applications can be significantly influenced by its structural and chemical properties. Therefore, tuning the functionality of GO to optimise these properties is of paramount importance. This involves modifying the type and density of functional

groups, adjusting the degree of oxidation, and manipulating the structural features of GO, such as its defect density and flake size.

The functionality of GO can be enhanced through various methods, including chemical treatments, thermal reduction, plasma modification, and hybridisation with other materials. By understanding and controlling these modifications, it is possible to tailor GO to meet the specific requirements of different applications, thereby maximising its effectiveness and efficiency.

The significance of this research lies in its potential to advance the development of high-performance GO-based materials for critical applications in adsorption and sensing. The insights gained from this study will contribute to the fundamental understanding of GO's properties and pave the way for innovative solutions to environmental, biomedical, and industrial challenges. As such, this thesis aims to provide a comprehensive exploration of the strategies for tuning the functionality of graphene oxide, ultimately enhancing its performance and broadening its application scope.

1.2. Graphene Oxide: An overview

1.2.1 Structure and Properties of Graphene Oxide

Graphene oxide (GO) is a single-atomic-layered material derived from graphite, characterised by the presence of various oxygen-containing functional groups. These functional groups, including hydroxyl, epoxy, carbonyl, and carboxyl groups, are distributed across the basal plane and edges of the graphene sheet, imparting GO with distinct chemical and physical properties that differ significantly from those of pristine graphene [1].

1.2.1.1 Structural Characteristics

The structure of GO is inherently amorphous due to the random distribution of functional groups, which disrupts the sp^2-hybridized carbon network of graphene. This disruption converts some of the sp^2 carbon atoms to sp^3 hybridisation, introducing defects and distortions in the hexagonal lattice. The degree of oxidation

and the type of functional groups present can vary depending on the synthesis method and conditions, leading to variations in GO's structural and chemical properties.

- **Layered Structure**: GO retains the layered structure of its parent graphite, but the interlayer spacing is significantly increased due to the presence of oxygen functionalities and water molecules intercalated between the layers [2]. The expanded spacing enhances GO's dispersibility in water and other polar solvents, facilitating its manipulation and processing.

- **Functional Groups**: The oxygen-containing functional groups are key to GO's reactivity and ability to undergo further chemical modifications. Hydroxyl and epoxy groups are typically found on the basal plane, while carbonyl and carboxyl groups are located at the edges. The distribution and density of these groups can be controlled through various chemical treatments [3].

1.2.1.2 Physical Properties

The introduction of oxygen functionalities alters the physical properties of GO compared to pristine graphene, particularly in terms of electronic, mechanical, and thermal characteristics.

- **Electronic Properties**: GO is an electrical insulator or a semiconductor, depending on the degree of oxidation [4]. The disruption of the π-conjugated network reduces its electrical conductivity compared to graphene. However, partial reduction of GO can restore some conductivity, making it suitable for applications requiring tunable electronic properties.

- **Mechanical Properties**: Despite the presence of defects and functional groups, GO retains excellent mechanical strength and flexibility [5]. The tensile strength and Young's modulus of GO are lower than those of pristine graphene but still sufficient for many applications, especially when incorporated into composite materials.

- **Thermal Properties**: The thermal conductivity of GO is significantly lower than that of graphene due to phonon scattering caused by defects and functional groups [6]. However, GO exhibits good thermal stability, which can be enhanced through thermal reduction processes.

1.2.1.3 Chemical Properties

The presence of various functional groups on the GO surface makes it highly reactive and chemically versatile. This reactivity allows GO to interact with a wide range of materials and enables various functionalisation strategies.

- **Hydrophilicity**: GO is highly hydrophilic due to its oxygen functional groups, making it easily dispersible in water and other polar solvents [7]. This property is advantageous for applications in aqueous environments and facilitates further chemical modifications.

- **Functionalisation**: The functional groups on GO provide sites for further chemical modifications, such as grafting of polymers, metal nanoparticles, and other molecules. This functionalisation can enhance GO's properties and tailor it for specific applications, such as adsorption, sensing, and catalysis [8].

1.2.1.4 Optical Properties

GO exhibits unique optical properties that are distinct from those of graphene, primarily due to the presence of functional groups and defects.

- **Absorption and Fluorescence**: GO shows strong absorption in the ultraviolet and visible regions due to electronic transitions associated with its functional groups. Additionally, GO can exhibit photoluminescence, with emission wavelengths that can be tuned by varying the degree of oxidation and the type of functional groups [9].

- **Optoelectronic Applications**: The tuneable optical properties of GO make it suitable for applications in optoelectronic devices, such as photodetectors, solar cells, and light-emitting devices [10].

1.2.2 Functionality of Graphene Oxide

Graphene oxide (GO) is a unique material with a two-dimensional structure that exhibits various oxygen-containing functional groups, including hydroxyl, epoxy, and carboxyl groups. These functional groups are typically located at the edges and basal planes of the GO sheets, significantly altering their properties compared to pristine graphene. The presence of these oxygen functionalities enables GO to interact with a wide range of molecules and ions, making it highly versatile for applications in different fields.

One of the key properties of graphene oxide is its hydrophilicity, which stems from the polar nature of the oxygen-containing groups. This makes GO highly dispersible in water and other polar solvents, facilitating its use in aqueous environments. The carboxyl groups, in particular, allow GO to interact with various organic and inorganic molecules, leading to the formation of stable colloidal suspensions. This property is advantageous for applications such as water purification, where GO acts as an adsorbent for pollutants like heavy metals, dyes, and organic contaminants [11]. Its high surface area and chemical reactivity further enhance its adsorption capacity [12].

The functional groups in GO also play a crucial role in its chemical reactivity and tunability. By modifying the oxygen content, GO's electronic, optical, and mechanical properties can be tailored for specific applications. For instance, the reduction of GO, which removes oxygen functionalities, results in reduced graphene oxide (rGO) with restored electrical conductivity [13]. This tunable conductivity makes GO and its derivatives valuable in applications such as sensors, where the presence of functional groups allows for the detection of specific molecules, while the reduced form can enable efficient electron transport. The combination of high sensitivity and selective chemical interactions makes GO-based materials promising for sensing applications, including gas sensors and biosensors.

In addition, the functional groups in GO provide anchoring sites for further chemical modifications, enabling the formation of composites with other materials. This opens up a wide range of possibilities in areas like catalysis, energy storage, and

biomedical applications – other than the molecular detection mentioned above. For example, GO composites have been explored as electrode materials in batteries and supercapacitors, where their conductivity and large surface area enhance charge storage capacity. Similarly, in drug delivery systems, the biocompatibility and functional versatility of GO allow for the controlled release of therapeutic agents.

Overall, the functionality of graphene oxide, largely determined by its oxygen-containing groups, is central to its wide-ranging applications. By leveraging the tunable chemical, mechanical, and electrical properties of GO, researchers continue to explore new ways to utilise this material in fields as diverse as environmental remediation, energy storage, and healthcare.

1.2.3 Synthesis Methods

The synthesis of graphene oxide (GO) is a critical step that significantly influences its structural, chemical, and physical properties. Various synthesis methods have been developed to produce GO, each with its own set of advantages and challenges. The most commonly used methods for synthesising GO involve the oxidation of graphite, a process that introduces oxygen-containing functional groups into the graphene layers. Among these methods, the Hummers, the Brodie, and the Staudenmaier methods are the most notable. Each method differs in the type and concentration of oxidising agents, reaction conditions, and the extent of oxidation achieved.

1.2.3.1 Hummers Method [14]

The Hummers method is the most widely adopted technique for synthesising GO due to its relative simplicity, efficiency, and ability to produce large quantities of GO. This method involves the oxidation of graphite using a mixture of concentrated sulfuric acid (H_2SO_4), potassium permanganate ($KMnO_4$), and sodium nitrate ($NaNO_3$). Hummers method in brief:

Graphite powder is mixed with concentrated sulfuric acid, and sodium nitrate is added to intercalate the graphite layers. Potassium permanganate is then gradually introduced, initiating the oxidation process. This exothermic reaction requires careful

temperature control to prevent over-oxidation and degradation of the material. Once the oxidation is complete, the mixture is diluted with water, and hydrogen peroxide is added to reduce residual permanganate and manganese dioxide by-products. The resulting product is then thoroughly washed with water and acids to remove impurities and unreacted chemicals, followed by filtration and drying to yield the final graphene oxide (GO) product.

Advantages: The Hummers method is efficient and scalable, making it suitable for large-scale production. It produces GO with a high degree of oxidation and good dispersibility in water and other polar solvents.

Challenges: One of the main drawbacks of the Hummers method is the generation of hazardous by-products, such as toxic gases (e.g., NO_2 and N_2O_4) and acidic waste, which require careful handling and disposal.

1.2.3.2 Brodie Method [15]

The Brodie method is one of the earliest techniques developed for synthesising GO, dating back to 1859. This method involves the oxidation of graphite using fuming nitric acid (HNO_3) and potassium chlorate ($KClO_3$) as the oxidising agents. The process is typically carried out as:

Graphite is mixed with fuming nitric acid, and potassium chlorate is gradually added while maintaining a controlled temperature, typically below room temperature, to prevent excessive heat buildup. This oxidation process introduces oxygen-containing functionalities, disrupting the graphite layers. After oxidation, the material is repeatedly washed with water and acids to remove unreacted chemicals and by-products. Finally, the oxidised graphite is filtered and dried to produce graphene oxide (GO).

Advantages: The Brodie method produces GO with a relatively high degree of oxidation and good thermal stability. It also allows for better control over the oxidation process compared to some other methods.

Challenges: The use of potassium chlorate as an oxidising agent poses significant safety risks due to its potential to form explosive mixtures. Additionally, the process is slower and less efficient than the Hummers method, making it less suitable for large-scale production.

1.2.3.3 Staudenmaier Method [16]

The Staudenmaier method is a modification of the Brodie method, developed in 1898, and involves the use of a mixture of concentrated sulfuric acid and fuming nitric acid as the oxidising agents, along with potassium chlorate. The steps in this method include:

Graphite is initially mixed with concentrated sulfuric acid and fuming nitric acid, and potassium chlorate is gradually added in small portions to initiate the oxidation process. This exothermic reaction is carefully controlled to prevent runaway reactions. After oxidation, the oxidised graphite is washed thoroughly with water and acids to remove impurities, and then it is filtered and dried to obtain graphene oxide (GO).

Advantages: The Staudenmaier method allows for a higher degree of oxidation and better control over the functional group distribution on GO compared to the Brodie method. It also produces GO with a more homogeneous structure.

Challenges: Similar to the Brodie method, the Staudenmaier method involves the use of hazardous chemicals, particularly potassium chlorate, which poses safety risks. The method is also more time-consuming and labour-intensive compared to the Hummers method.

1.2.3.4 Modified Hummers Method [17]

Given the challenges associated with the original Hummers method, several modified versions have been developed to improve safety, reduce environmental impact, and enhance the quality of GO produced. These modifications include:

1. **Use of Safer Oxidising Agents**: Some modified methods replace sodium nitrate with other agents, such as potassium persulfate ($K_2S_2O_8$) or phosphoric acid (H_3PO_4), to reduce the generation of toxic gases.

2. **Improved Purification**: Enhanced washing and purification steps are employed to remove residual metal ions and by-products, resulting in higher-purity GO.

3. **Green Chemistry Approaches**: Some recent modifications focus on using environmentally friendly solvents and oxidising agents to minimise the environmental impact of GO synthesis.

Advantages: These modifications improve the safety and environmental sustainability of the GO synthesis process while maintaining or enhancing the final product's quality.

Challenges: Some modified methods may involve more complex procedures or higher costs, which could limit their scalability.

1.2.3.5 Other Synthesis Methods

In addition to the classical methods mentioned above, other approaches for synthesising GO have been explored, including electrochemical oxidation, plasma-assisted methods, and microwave-assisted synthesis. These methods offer alternative routes for GO production with specific advantages, such as reduced reaction times, lower environmental impact, or improved control over the GO structure.

- **Electrochemical Oxidation** [18]: In this method, the graphite electrodes are electrochemically oxidised in an acidic electrolyte solution. This approach allows for better control over the oxidation process and can produce high-quality GO with fewer defects. It is also considered a greener method due to the absence of hazardous chemicals.

- **Plasma-Assisted Methods** [19]: Plasma treatments can be used to oxidise graphite or graphene in a controlled manner, introducing oxygen functionalities to the

surface. This method is advantageous for producing GO with specific surface properties and functional group distributions.

- **Microwave-Assisted Synthesis** [20]: Microwave irradiation rapidly oxidises graphite in the presence of oxidising agents. This method offers a faster and more energy-efficient alternative to conventional thermal processes.

Advantages: These alternative methods provide additional flexibility in GO synthesis, enabling the production of GO with tailored properties for specific applications.

Challenges: Many of these methods are still in the experimental stage or are less established than traditional chemical oxidation methods, which may limit their adoption for large-scale production.

1.3 Tuning the functionality of Graphene Oxide

1.3.1 Chemical Modifications

Tuning the functionality of graphene oxide (GO) through chemical modifications is a key approach in tailoring its properties for specific applications. Chemical treatments can be employed to selectively modify the oxygen-containing functional groups, which are crucial to GO's reactivity and behaviour. By altering the type, concentration, or distribution of these functional groups, the physical, chemical, and electronic properties of GO can be precisely controlled.

One common method for tuning GO's functionality is treating it with reducing agents. This process, known as reduction, removes oxygen functionalities, converting GO into reduced graphene oxide (rGO). The extent of reduction can be controlled, allowing the material's electrical conductivity, hydrophilicity, and chemical reactivity to be adjusted. Strong reducing agents like hydrazine or sodium borohydride can significantly decrease the oxygen content, enhancing conductivity. In contrast, mild reducing agents can partially restore the electronic properties of graphene without completely eliminating the functional groups.

Alternatively, the introduction of certain chemicals during the synthesis of GO can influence the distribution of functional groups. For instance, adding excess potassium permanganate during the oxidation process can result in over-oxidation, increasing the number of oxygen functionalities and altering their distribution across the GO sheets [21]. This can enhance GO's affinity for water and improve its dispersibility but may reduce its conductivity and mechanical strength. Conversely, using lower concentrations of oxidising agents can produce GO with fewer oxygen groups, yielding a material with better conductivity and more graphene-like properties.

Post-synthesis modifications, such as the addition of acids or alkalis, can also affect the functional group profile of GO. Acid treatments can enhance the carboxyl group concentration [22], making GO more suitable for applications like ion exchange or adsorption. In contrast, alkali treatments, such as adding sodium hydroxide, can induce deoxygenation or convert functional groups into more reactive forms. These chemical modifications provide a versatile means of tuning GO for diverse applications, ranging from energy storage and sensors to environmental remediation and biomedical uses.

1.3.2 Composite formation

Tuning the functionality of graphene oxide (GO) through composite formation involves combining GO with other materials, such as metals, polymers, or nanoparticles, to enhance its properties and tailor it for specific applications. In composites, the functional groups on GO serve as reactive sites that facilitate bonding or interaction with the added material. This can lead to improved mechanical strength, thermal stability, or conductivity, depending on the nature of the composite.

Composite formation can also alter the distribution and concentration of functional groups in GO, allowing for more controlled reactivity. For instance, adding metal nanoparticles can enhance GO's catalytic or sensing properties by creating active sites for chemical interactions, while incorporating polymers can improve GO's flexibility and processing ability for applications in coatings or membranes. By adjusting the composite components, GO can be customised for specific uses, such as

in sensors, energy storage devices, or environmental remediation technologies, where precise functionalisation is key to optimising performance.

1.3.3 Synthesis Conditions

Tuning the functionality of graphene oxide (GO) by varying its synthesis conditions—such as dosages, reaction time, temperature, and pH—can significantly affect the nature and distribution of its oxygen-containing functional groups. For instance, increasing the oxidant dosage during synthesis can lead to higher oxidation levels, introducing more hydroxyl, epoxy, and carboxyl groups, which enhance GO's hydrophilicity and reactivity. However, excessive oxidation can result in the over-oxidation of the graphene structure, potentially degrading its mechanical strength and conductivity.

The synthesis time and temperature also play a crucial role in determining the functional group profile. Longer reaction times and higher temperatures typically lead to more thorough oxidation, altering the density and location of functional groups. On the other hand, adjusting the pH during synthesis can influence the balance between different oxygen functionalities. A basic environment, for example, can partially reduce GO, reduce the number of oxygen groups and improve conductivity, while acidic conditions promote higher oxidation. By fine-tuning these parameters, researchers can control the properties of GO for targeted applications such as adsorption, sensing, and catalysis.

1.3.4 Loading in 3D matrix

Tuning the functionality of graphene oxide (GO) by loading it in different matrices, such as incorporating it into sponges, polymers, or creating 3D structures, enhances its properties and broadens its applications. By embedding GO into 3D frameworks, like melamine sponges or polymer matrices, its large surface area is preserved, while the structure gains added benefits such as improved mechanical strength, flexibility, and reusability. These modifications allow GO to retain its essential properties, such as adsorption capacity and chemical reactivity, while

improving its practical usability in fields like oil-water separation, filtration, and catalysis.

Incorporating GO into these structures also influences the distribution of functional groups. In a 3D matrix, the functional groups on GO are more accessible, increasing interaction sites for target molecules, which can improve performance in applications like sensing or environmental remediation. Additionally, the structural modification can help distribute oxygen-containing groups more uniformly, enhancing the overall efficiency of the material without compromising the original functions of GO. Thus, such loading expands the potential of GO, making it suitable for advanced applications in various industries.

1.4 Adsorption and Sensing Applications of Graphene Oxide

1.4.1 Adsorption Applications of Graphene Oxide

Graphene oxide (GO) is highly effective in adsorption applications due to its large surface area and the presence of oxygen-containing functional groups, which facilitate strong interactions with a variety of adsorbates. This makes GO an excellent material for removing pollutants like dyes, antibiotics, and polycyclic aromatic hydrocarbons (PAHs) from contaminated water and other environments [23,24].

In dye adsorption, GO is commonly used to remove harmful organic dyes such as methylene blue, congo red, and rhodamine B, which are often found in industrial wastewater. The hydrophilic nature and functional groups on GO allow it to interact strongly with these dye molecules, enhancing their adsorption. Similarly, GO is effective in adsorbing antibiotics like tetracycline and ciprofloxacin, emerging water pollutants due to pharmaceutical industry waste. The interaction between GO's surface and antibiotic molecules is driven by hydrogen bonding, π-π interactions, and electrostatic forces, depending on the functional groups present on the GO and the structure of the antibiotic.

GO is also well-suited for the adsorption of polycyclic aromatic hydrocarbons (PAHs), a class of organic compounds known for their environmental persistence and potential carcinogenicity. The large surface area and π-π interactions between the

aromatic rings of PAHs and the graphene oxide layers enhance the adsorption efficiency of GO for these pollutants.

Key factors such as surface area, the availability of functional groups, and the interaction mechanisms between GO and the adsorbates are crucial for effective adsorption. The pH of the solution, temperature, and initial concentration of the pollutant also influence the adsorption process. GO's versatility and tunability make it a highly promising material for removing a wide range of environmental contaminants, particularly dyes, antibiotics, and PAHs, in water treatment applications.

Adsorption experiments with graphene oxide (GO) are typically conducted by preparing an aqueous adsorbate solution and adding a known quantity of GO. The mixture is stirred or shaken to ensure thorough interaction between the GO and the adsorbate. Samples are taken at specific time intervals to monitor the adsorption process. The concentration of the adsorbate before and after exposure to GO is measured using UV-visible spectroscopy, a widely used analytical technique.

In UV-visible spectroscopy, the solution is exposed to light over a specific wavelength range, and the absorbance of the adsorbate is measured. Each adsorbate typically has a characteristic absorption peak at a specific wavelength, and the decrease in the intensity of this peak corresponds to the amount of adsorbate removed from the solution. The amount of adsorbate adsorbed onto GO can be quantified by comparing the initial and final absorbance values. This data is then used to calculate adsorption capacity, and kinetic models like pseudo-first-order or pseudo-second-order are often applied to analyse the adsorption behaviour and mechanisms.

1.4.2 Sensing Applications of Graphene Oxide

Graphene oxide (GO) has emerged as a versatile material for sensing applications due to its high surface area, functional groups, and ability to interact with various organic molecules. GO can be used to detect a wide range of chemical and biological substances, making it valuable for environmental monitoring, medical diagnostics, and industrial applications. Various methods have been employed for sensing using GO, including electrochemical sensing, fluorescence-based detection, and surface-enhanced Raman spectroscopy (SERS).

Electrochemical sensing with GO involves measuring changes in electrical signals when target molecules interact with the GO surface. While this method is highly sensitive and allows real-time detection, it requires complex instrumentation and is susceptible to interference from other ions in the environment [25]. Fluorescence-based sensing utilises GO's ability to quench fluorescence when target molecules bind to its surface. Although effective, this method can suffer from photobleaching, which reduces the signal over time [26]. Surface-enhanced Raman spectroscopy (SERS) provides molecular-level information and is highly sensitive, but it can be expensive and requires sophisticated equipment [27].

Sensing using UV-visible spectroscopy offers a simpler, cost-effective approach by monitoring changes in light absorbance of GO-based materials upon interaction with specific analytes [28]. UV-visible spectroscopy has been employed to detect various ions such as Fe^{3+} [29], Cu^{2+}, Pb^{2+}, and Cd^{2+}[30], as well as biomolecules including hemoglobin, beta-nicotinamide adenine dinucleotide (NAD), flavin adenine dinucleotide (FAD), elastin, collagen, cytochrome c, tryptophan, DNA [31], and numerous other chemical species [32,33]. When GO-based composites, particularly those with metal nanoparticles like gold (rGO-Au), are employed for UV-visible based detection, surface plasmon resonance (SPR) can be exploited for enhanced sensitivity [34].

1.5 Motivation

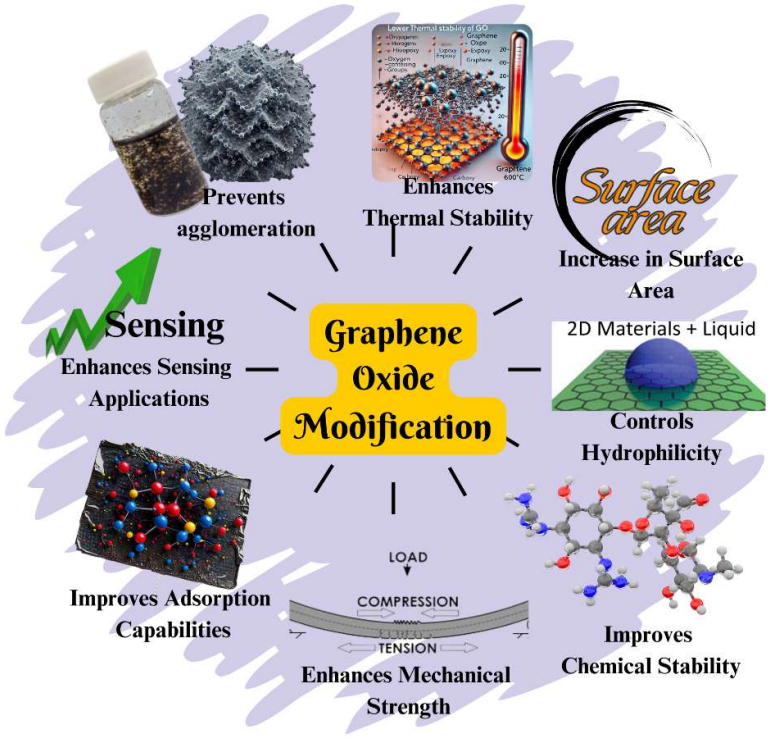

Figure1.1: **Outline of the importance of modifying GO**

Graphene oxide (GO) is a revolutionary material that has garnered immense interest due to its remarkable properties, such as a large surface area, rich functional groups, mechanical strength, and high chemical reactivity. These features make GO an excellent candidate for various applications, including sensing, adsorption, and thermal management. However, despite these advantages, pristine GO suffers from several limitations. For instance, GO can be prone to agglomeration, has limited stability under certain conditions, and its functionality is constrained by the uneven distribution of oxygen-containing groups. These limitations create a barrier to fully utilising GO's potential in advanced applications.

One promising solution to overcome these drawbacks is through the modification of GO, a process that can tune and enhance its functionality. As depicted in the Figure1.1, modifying GO prevents agglomeration, enhances thermal and chemical stability, increases surface area, and improves hydrophilicity. This leads to

the creation of GO composites with tailored properties for specific applications. For example, modified GO improves sensing capabilities, adsorption capacity, and mechanical strength, allowing for more versatile and high-performance materials. By controlling the distribution of functional groups or integrating GO into 3D structures like sponges, the material's functionality can be precisely adjusted to meet the demands of real-world applications.

The motivation for this research lies in addressing the gap in current GO applications, particularly the need to fine-tune GO's properties to meet specific functional requirements. Current studies have not fully explored the potential of modified GO for advanced applications like environmental remediation, energy storage, and biomedical sensing. By systematically modifying GO, we can unlock its full potential and contribute significantly to these fields.

As famed material scientist Richard Feynman once said, "There's plenty of room at the bottom," highlighting the endless possibilities at the nanoscale. Modifying GO opens up new horizons for material scientists, offering a pathway to innovate and address critical global challenges. This research seeks to push the boundaries of what GO can achieve, making it an ideal focus for anyone passionate about advancing nanomaterials and their applications.

1.6 Objectives of the thesis

The primary objectives of this thesis are as follows:

- ***Explore enhancement of adsorptive and sensing applications of graphene oxide utilising oxygen functional groups.***
- ***Expand the role of graphene oxide-based nanocomposites as an environmental remediation agent and chemical sensing element***
- ***Explore the impact of a special layout of graphene oxide aided by 3D matrix on its adsorptive properties.***

This thesis aims to systematically enhance the functionality of graphene oxide (GO) by optimising its oxygen functional groups to improve its adsorption-driven applications. By precisely controlling the type, amount, and distribution of these groups, the study seeks to augment GO's efficiency for specific purposes, such as dye removal and oil-water separation. Additionally, the work emphasises the development of GO-based nanocomposites, showcasing their potential in environmental remediation, including pollutant adsorption in saline and aqueous systems, and their application in chemical sensing due to their improved physicochemical properties. Furthermore, the research explores the incorporation of GO into a three-dimensional matrix, such as a melamine sponge, to investigate how the spatial arrangement of GO enhances its adsorption capabilities, accessibility to active sites, and overall performance in multifunctional applications.

1.7 Organisation of the Thesis

The thesis is structured into nine chapters. The first chapter serves as an introduction to the thesis, while the second chapter details the methods and experimental techniques, including the characterization methods and synthesis procedures utilized in this work. The core of the thesis comprises five dedicated chapters, each focusing on a unique approach to modifying graphene oxide (GO) to enhance its functionality for adsorption and sensing applications.

Chapter 3: Graphene Oxide Modification Using NaOH Treatment

The first chapter focuses on modifying graphene oxide using NaOH treatment. This method alters the oxygen-containing functional groups in GO, which plays a critical role in its reduction process and properties. The study examines how varying pH levels influence these modifications, setting the foundation for further applications in adsorption. This chapter also explains the threshold value of NaOH for it to act as a reducing agent for GO.

Chapter 4: Graphene Oxide Modification using Activated Carbon - Composite Formation

Graphene oxide-activated carbon composite is synthesised in simple means without any linker molecules and is studied for its adsorption capability, particularly for the removal of dyes such as methylene blue, rhodamine B, a mixture of dyes, and antibiotics from aqueous solutions.

Chapter 5: Graphene Oxide Modification using Gold Nanoparticles – Composite Formation

The rGO-Au composite is evaluated for its potential in uric acid sensing. The chapter highlights the enhanced sensing properties of the composite compared to GO or gold nanoparticles alone.

Chapter 6: Graphene Oxide Modification Through Time-Varying Reactions

The third chapter focuses on the effect of synthesis time variations on graphene oxide. GO is synthesised with different reaction durations, and the resulting materials are studied for adsorption and sensing applications:

- **Adsorption**: Methylene Blue and naphthalene are used as model pollutants to study adsorption efficiency.
- **Ascorbic Acid Sensing**: The GO synthesised under varying reaction times is further evaluated for its potential in ascorbic acid detection, providing insights into the impact of synthesis conditions on the material's performance.

Chapter 7: Graphene Oxide Modification Using Melamine Sponge

The final chapter presents the integration of graphene oxide with a melamine sponge to form a 3D composite structure. This composite is investigated for its dual functionality:

- **Adsorption**: Methylene Blue dye is used to test the adsorption capacity of the composite.

- **Oil-Water Separation**: The sponge-based GO structure is evaluated for its efficiency in separating oil from water in fresh water and saline water, addressing an important environmental application.

This systematic organisation reflects the progression of modifying graphene oxide through various techniques and composites to optimise its use in environmental and sensing applications.

Chapter 8: Conclusion

This chapter encapsulate the concluding remarks and provide a comprehensive summary of the key findings from the thesis work.

Chapter 9: Recommendations

The final chapter propose future directions for further exploration in this field and offer recommendations for advancing the practical applications of graphene oxide-based materials. These insights aim to bridge existing research gaps and inspire innovative approaches for enhancing the functionality of graphene oxide in diverse domains.

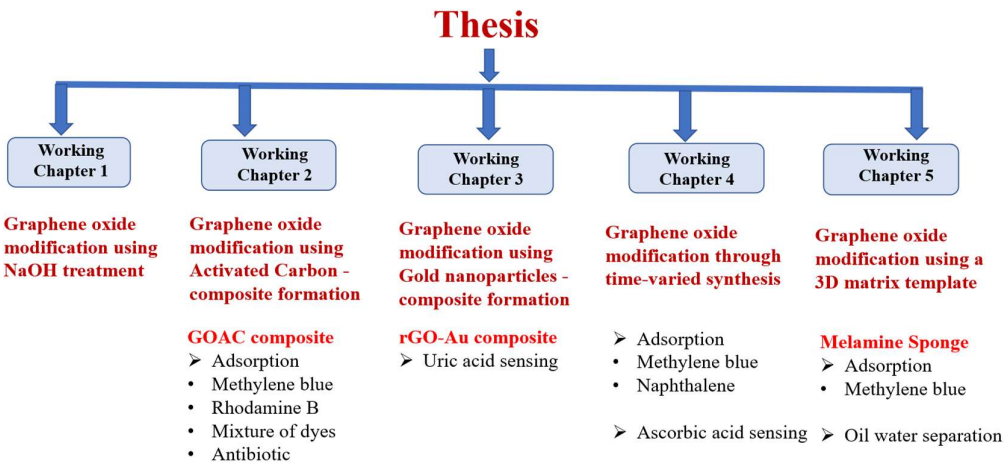

Figure 1.2: Outline of the Thesis

References

1. Liu, C., Shen, J., Liao, C. Z., Yeung, K. W. K., & Tjong, S. C. (2018). Novel electrospun polyvinylidene fluoride-graphene oxide-silver nanocomposite membranes with protein and bacterial antifouling characteristics. *eXPRESS Polymer Letters*, *12*(4), 365–382. https://doi.org/10.3144/expresspolymlett.2018.31

2. Díez-Pascual, A. M., Sainz-Urruela, C., Vallés, C., Vera-López, S., & Andrés, M. P. S. (2020). Tailorable Synthesis of Highly Oxidised Graphene Oxides via an Environmentally-Friendly Electrochemical Process. *Nanomaterials*, *10*(2), 239. https://doi.org/10.3390/nano10020239

3. Botas, C., Álvarez, P., Blanco, P., Granda, M., Blanco, C., Santamaría, R., Romasanta, L. J., Verdejo, R., López-Manchado, M. A., & Menéndez, R. (2013). Graphene materials with different structures prepared from the same graphite by the Hummers and Brodie methods. *Carbon*, *65*, 156–164. https://doi.org/10.1016/j.carbon.2013.08.009

4. Neto, A. H. C., Guinea, F., Peres, N. M. R., Novoselov, K. S., & Geim, A. K. (2009). The electronic properties of graphene. *Reviews of Modern Physics*, *81*(1), 109–162. https://doi.org/10.1103/revmodphys.81.109

5. Zhang, L. L., Zhou, R., & Zhao, X. S. (2010). Graphene-based materials as supercapacitor electrodes. *Journal of Materials Chemistry*, *20*(29), 5983. https://doi.org/10.1039/c000417k

6. Burger, N., Laachachi, A., Ferriol, M., Lutz, M., Toniazzo, V., & Ruch, D. (2016). Review of thermal conductivity in composites: Mechanisms, parameters and theory. *Progress in Polymer Science*, *61*, 1–28. https://doi.org/10.1016/j.progpolymsci.2016.05.001

7. Alam, S. N., Sharma, N., & Kumar, L. (2017). Synthesis of Graphene Oxide (GO) by Modified Hummers Method and Its Thermal Reduction to Obtain Reduced Graphene Oxide (rGO)*. *Graphene*, *06*(01), 1–18. https://doi.org/10.4236/graphene.2017.61001

8. Khan, M., Tahir, M. N., Adil, S. F., Khan, H. U., Siddiqui, M. R. H., Al-Warthan, A. A., & Tremel, W. (2015). Graphene based metal and metal oxide nanocomposites: synthesis, properties and their applications. *Journal of Materials Chemistry A*, *3*(37), 18753–18808. https://doi.org/10.1039/c5ta02240a

9. Grigorenko, A. N., Polini, M., & Novoselov, K. S. (2012). Graphene plasmonics. *Nature Photonics*, *6*(11), 749–758. https://doi.org/10.1038/nphoton.2012.262

10. Martinez-Martinez, R., Islam, M. M., Krishnaprasad, A., & Roy, T. (2022). Graphene–oxide interface for optoelectronic synapse application. *Scientific Reports*, *12*(1), 5880.

11. Li, M., Zhang, X., Zhang, Y., Xu, X., Liu, Y., Zhang, Y., ... & Liang, Y. (2024). Effect of interaction between dissolved organic matter and iron/manganese (hydrogen) oxides on the degradation of organic pollutants by in-situ advanced oxidation techniques. *Science of The Total Environment*, 170351.

12. Wang, X., Huang, S., Zhu, L., Tian, X., Li, S., & Tang, H. (2014). Correlation between the adsorption ability and reduction degree of graphene oxide and tuning of adsorption of phenolic compounds. *Carbon*, *69*, 101-112.

13. Guex, L. G., Sacchi, B., Peuvot, K. F., Andersson, R. L., Pourrahimi, A. M., Ström, V., ... & Olsson, R. T. (2017). Experimental review: chemical reduction of graphene oxide (GO) to reduced graphene oxide (rGO) by aqueous chemistry. *Nanoscale*, *9*(27), 9562-9571.

14. Hummers, W. S., & Offeman, R. E. (1958). Preparation of Graphitic Oxide. *Journal of the American Chemical Society*, *80*(6), 1339. https://doi.org/10.1021/ja01539a017

15. Brodie, B. C. (1859). XIII. On the atomic weight of graphite. *Philosophical transactions of the Royal Society of London*, (149), 249-259.

16. Staudenmaier, L. (1898) Verfahren zur Darstellung der Graphitsäure. Berichte der deutschen chemischen Gesellschaft, 31, 1481-1499. http://dx.doi.org/10.1002/cber.18980310237

17. Zaaba, N., Foo, K., Hashim, U., Tan, S., Liu, W., & Voon, C. (2017). Synthesis of Graphene Oxide using Modified Hummers Method: Solvent Influence. *Procedia Engineering*, *184*, 469–477. https://doi.org/10.1016/j.proeng.2017.04.118

18. Kumar, N., & Srivastava, V. C. (2018). Simple Synthesis of Large Graphene Oxide Sheets via Electrochemical Method Coupled with Oxidation Process. *ACS Omega*, *3*(8), 10233–10242. https://doi.org/10.1021/acsomega.8b01283

19. Alam, K., Jo, Y. Y., Park, C., & Cho, H. (2020). Synthesis of Graphene Oxide Using Atmospheric Plasma for Prospective Biological Applications *International Journal of Nanomedicine*, *Volume 15*, 5813–5824. https://doi.org/10.2147/ijn.s254860

20. Wang, X., Tang, H., Huang, S., & Zhu, L. (2014). Fast and facile microwave-assisted synthesis of graphene oxide nanosheets. *RSC Advances*, *4*(104), 60102–60105. https://doi.org/10.1039/c4ra12022a

21. Lyn, F. H., Peng, T. C., Ruzniza, M. Z., & Hanani, Z. N. (2019). Effect of oxidation degrees of graphene oxide (GO) on the structure and physical properties of chitosan/GO composite films. *Food Packaging and Shelf Life*, *21*, 100373.

22. Guo, S., Raya, J., Ji, D., Nishina, Y., Ménard-Moyon, C., & Bianco, A. (2020). Is carboxylation an efficient method for graphene oxide functionalisation?. *Nanoscale Advances*, *2*(9), 4085-4092.

23. Thakur, K., & Kandasubramanian, B. (2019). Graphene and graphene oxide-based composites for removal of organic pollutants: a review. *Journal of Chemical & Engineering Data*, *64*(3), 833-867.

24. Khan, A., Wang, J., Li, J., Wang, X., Chen, Z., Alsaedi, A., ... & Wang, X. (2017). The role of graphene oxide and graphene oxide-based nanomaterials in the removal of pharmaceuticals from aqueous media: a review. *Environmental Science and Pollution Research*, *24*, 7938-7958.

25. Shah, N. S., Thotathil, V., Zaidi, S. A., Sheikh, H., Mohamed, M., Qureshi, A., & Sadasivuni, K. K. (2022). Picomolar or beyond limit of detection using molecularly imprinted polymer-based electrochemical sensors: A review. *Biosensors*, *12*(12), 1107.

26. Ludvikova, L., Simon, E., Deygas, M., Panier, T., Plamont, M. A., Ollion, J., ... & Espagne, A. (2024). Near-infrared co-illumination of fluorescent proteins reduces photobleaching and phototoxicity. *Nature Biotechnology*, *42*(6), 872-876.

27. Schlücker, S. (2014). Surface-Enhanced raman spectroscopy: Concepts and chemical applications. *Angewandte Chemie International Edition*, *53*(19), 4756-4795.

28. Darabdhara, G., Das, M. R., Singh, S. P., Rengan, A. K., Szunerits, S., & Boukherroub, R. (2019). Ag and Au nanoparticles/reduced graphene oxide composite materials: synthesis and application in diagnostics and therapeutics. *Advances in colloid and interface science*, *271*, 101991.

29. Karami, C., Alizadeh, A., Taher, M. A., Hamidi, Z., & Bahrami, B. (2016). UV-visible spectroscopy detection of iron (III) ion on modified gold nanoparticles with a hydroxamic acid. *Journal of Applied Spectroscopy*, *83*, 687-693.

30. Qader, S., Mohammed, A., Muhammed, A. M., Omer, R., & Qader, A. (2024). Determination of Three Metal Ions (Cu2+, Pb2+, Cd2+) by Ultraviolet-visible Spectroscopy. *Journal of Physical Chemistry and Functional Materials*, *7*(2), 88-100.

31. Soltani, S., Ojaghi, A., & Robles, F. E. (2019). Deep UV dispersion and absorption spectroscopy of biomolecules. *Biomedical Optics Express*, *10*(2), 487-499.

32. Rocha, F. S., Gomes, A. J., Lunardi, C. N., Kaliaguine, S., & Patience, G. S. (2018). Experimental methods in chemical engineering: Ultraviolet visible spectroscopy—UV-Vis. *The Canadian Journal of Chemical Engineering*, *96*(12), 2512-2517.

33. Ikeda, A., Hennig, C., Rossberg, A., Tsushima, S., Scheinost, A. C., & Bernhard, G. (2008). Structural determination of individual chemical species in a mixed system by iterative transformation factor analysis-based X-ray absorption spectroscopy combined with UV− Visible absorption and quantum chemical calculation. *Analytical chemistry*, *80*(4), 1102-1110.

34. Patil, P. O., Pandey, G. R., Patil, A. G., Borse, V. B., Deshmukh, P. K., Patil, D. R., ... & Bari, S. B. (2019). Graphene-based nanocomposites for sensitivity enhancement of surface plasmon resonance sensor for biological and chemical sensing: A review. *Biosensors and Bioelectronics*, *139*, 111324.

CHAPTER 2

METHODS AND EXPERIMENTAL TECHNIQUES

This chapter provides an in-depth discussion of the synthesis of graphene oxide. The chapter also encompasses a concise overview of various experimental techniques employed for the structural, morphological and optical characterisation of the materials.

2.1 Synthesis of Graphene Oxide

In this thesis, we employed one of the most reputed chemical methods, the Hummers' method [1], to synthesise graphene oxide. This method involves the oxidation of graphite using strong chemical oxidants, including $NaNO_3$, $KMnO_4$, and H_2SO_4, to produce graphite oxide. The Hummers' method is widely recognised as an efficient and dependable approach for producing large quantities of graphite oxide, making it a preferred choice in laboratory research.

2 g of graphite powder and 1 g of sodium nitrate were mixed with 96 ml of concentrated sulphuric acid. The mixture was kept in an ice bath under vigorous stirring. 6 g of potassium permanganate was gradually added to this mixture. After removing the ice bath, the mixture was stirred at room temperature for 18 hours. As the reaction extended, the mixture turned out to be pasty and had a brownish colour. Thereafter, 150 ml of distilled water was slowly added to the paste. After further dilution with 240 ml of water, 5ml of 30% hydrogen peroxide was added to the mixture. Then, the colour of the diluted solution changes to brilliant yellow along with bubbling. After continuous stirring for 2 hours, the mixture was filtered and washed with 10% aqueous HCl solution, water and ethanol. The resulting thick liquid is well-sonicated and dried to obtain graphene oxide (GO).

2.2. Materials and Methods Used

2.2.1. Materials Used

Table 2.1. *The materials used in the thesis.*

Sl. No.	Name of Chemicals	Purity and manufacturer
1.	Graphite flake	99.8%, Alfa Aesar
2.	Potassium permanganate	98.5%, Emplura, Merck
3.	Sodium nitrate	99%, Avra
4.	Hydrogen peroxide	35 % w/w aq. solution, Alfa Aesar
5.	Conc. sulphuric acid	98%, Merck
6.	Con. hydrochloric acid	35% Qualigen
7.	Sodium hydroxide	98% Qualigen
8.	Activated Carbon	Avra
9.	Methylene blue dye	Spectrochem
10.	Rhodamine B dye	Alfa Aesar
11.	Congo Red dye	Spectrochem
12.	L-Ascorbic acid	99% Emplura, Merck
13.	Tetrachloro auric acid	49%, Spectrochem
14.	Trisodium citrate dihydrate	99%, Spectrochem
15.	Ferric chloride	96% Emplura, Merck
16.	Potassium ferricyanide	98% SRL
17.	Uric acid	99% Nice chemicals

2.3 Experimental techniques

In material science, the characterisation of materials is crucial to understanding their structural, morphological, thermal, optical, and chemical properties. Graphene oxide (GO) and its derivatives have garnered significant attention due to their exceptional properties, which are dependent on their synthesis methods. This chapter provides an overview of the characterisation techniques employed to analyse graphene oxide and its composites, focusing on their application to study the modifications introduced during the research. The chosen methods are instrumental in establishing a correlation between structural attributes and functional performance in adsorption and sensing applications.

2.3.1 X-Ray Diffraction Analysis

The atomic molecular structure of crystalline materials can be determined by an effective technique called X-ray diffraction (XRD) experiments. This involves exposing a crystalline sample to X-rays to study the atomic structure of crystal lattice interiors and how X-rays diffract. Chemistry, materials science, geology, and solid-state physics are just a few of the disciplines that extensively use XRD [2][3].

Theory of X-ray diffraction

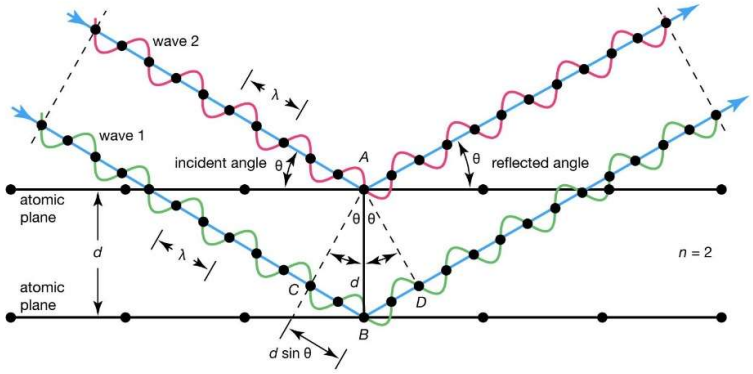

Figure 2.1 *Diagram of X-ray diffraction at the lattices. The diagram adapted from [4*]

XRD is based on the principle of Bragg's law, which states that when X-rays strike a crystal lattice, due to X-ray waves constructively scattered by atomic planes in the lattice, they will reflect at specific angles somehow. Braggs law can be expressed mathematically as follows [5]:

$$\mathbf{n\lambda = 2d\sin(\theta)} \qquad \textbf{(2.1)}$$

Where:

- n is the order of the diffraction peak
- λ is the wavelength of the incident X-ray
- d is the spacing between crystal lattice planes
- θ is the angle of incidence between the incident X-ray and the lattice plane

X-rays interact with the electron clouds of the atoms in the crystal lattice when they impinge on a crystalline substance. The crystal lattice planes scatter the X-rays, and constructive interference takes place when the requirements of Bragg's Law are satisfied for a specific set of crystal planes [5]. The material's crystal structure, including the locations of the atoms within the unit cell, can be ascertained by measuring the angles and intensities of the diffracted X-rays [6][7].

Instrumentation:

The following elements are frequently found in XRD instrumentation [3][8][9]:

- **X-ray sources:** High-energy X-ray sources, such as sealed tubes or spinning anode generators, are used by XRD instruments. These sources emit X-rays with a specific wavelength, typically 0.1 to 2.5 angstroms.
- **Monochromator:** Wind-blown X-rays have different wavelengths. A monochromator is used to select a specific wavelength, increasing the size of the diffraction patterns. Single crystals enriched with graphite and other materials are used to diffract, and specific X-ray wavelengths are selected.
- **Sample holder:** A sample holder is attached to a mirror-shaped sample, allowing for precise rotation and orientation adjustment. The sample holder can be rotated to different angles to collect diffraction data.
- **Goniometer:** The goniometer is a mechanical device that holds the sample holder and allows for precise rotation and rotation. This allows for accurate control of incidence and lateral distortion.
- **Detection:** Scattered X-rays are captured by X-ray detectors such as scintillation counters or solid-state detectors. These detectors record the intensity of diffracted X-rays as a function of diffraction angle.
- **Data Collection Systems:** Modern XRD machines often use state-of-the-art data collection systems that digitally interpret information from

diffraction patterns. These systems allow for rapid data collection and analysis.

- **Computer software:** Computer software is used to verify the crystal structure, and a variety of software programs are employed to analyse the data gathered. These methods take the diffraction pattern and apply statistics and Fourier transformation to create a three-dimensional electron density map. From there, atomic locations inside the crystal lattice can be ascertained.

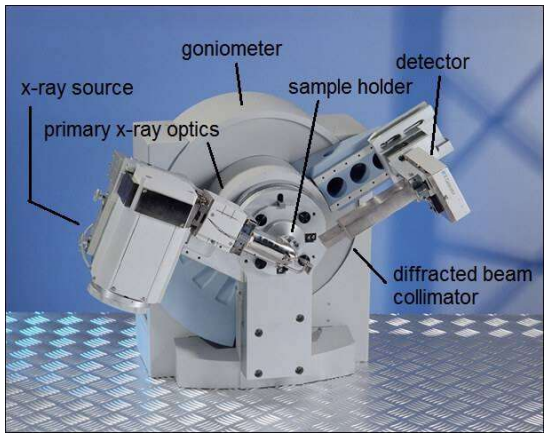

Figure 2.2 *Image showing different components of the XRD machine. The image is adapted from [13].*

Applications of XRD

X-ray diffraction (XRD) has a huge range of applications throughout numerous medical and industrial fields. Here are some splendid utilities of XRD

- **Material Characterisation [10] :** The crystal structure and segment composition of materials are frequently studied using XRD. It aids in finding various crystalline stages, comparing their purity, and revealing lattice characteristics. Chemistry, geology, and substances technology all depend on this.

- **Pharmaceuticals [11] :** X-ray diffraction (XRD) is used to analyse the crystal structures of therapeutic compounds. This leads to a better understanding of

medication polymorphism, which affects medication stability, solubility, and bioavailability.

- **Mineralogy and Geology [12] :** XRD is crucial for identifying and determining minerals' crystal structures. It encourages geological research, resource exploration, and the study of Earth's dynamics.
- **Crystallography [13] :** X-ray diffraction (XRD) is the fundamental technique in crystallography that identifies atomic and molecule structures. It is essential to understanding the arrangement of atoms in complex molecules.
- **Thin Films and Coatings [14] :** The semiconductor and optical sectors use thin films and coatings, which XRD aids in characterising. It gives details about the texture, orientation of crystals, and thickness of the coating.
- **Catalyst Research [15] :** By examining changes in the crystal structures of catalysts during chemical reactions, XRD is used to investigate catalysts and their activity. It facilitates comprehension of catalytic processes.
- **Archaeology and Art Conservation [16] :** In the fields of archaeology and art conservation, XRD is used to examine historical objects and artworks to ascertain their age, composition, and preservation requirements.
- **Nanomaterials [17] :** The size, crystallinity, and structure of nanoparticles and nanomaterials can be determined with the aid of X-ray diffraction (XRD), which is essential for modifying their characteristics.

Figure 2.3 *Image of X-ray diffractometer at Department of Physics, University of Calicut.*

Figure 2.4 *Image of X-ray diffractometer at CSIF, University of Calicut.*

We used a Rigaku Miniflex600 X-ray diffractometer with Cu-Kα radiation (1.5406 Å) in θ/2θ mode with a step size of 0.005° and scan speed of 4 degrees/minute from department of physics, University of Calicut and **X'pert^3 Powder**, Floor Standing Multi-Purpose X-ray Diffractometer from CSIF, Calicut University for investigations in this thesis.

Information from XRD

An abundance of information regarding the **crystallographic structure** of materials can be found in X-ray Diffraction (XRD) patterns. By comparing the positions and intensities of the diffraction peaks to established crystal structures, an analysis of these patterns can identify the phases that are present in a sample [3][8]. Furthermore, information on the crystal structure, including **symmetry and lattice characteristics**, can be ascertained. Peak broadening in XRD allows one to assess the **size of the crystallites** and whether **microstrain** exists in the crystal lattice. It is also possible to infer information about the preferred orientation or texture in polycrystalline samples. The method makes quantitative phase analysis easier and sheds light on the relative abundances of various phases. Broad humps, which are indicative of **amorphous or weakly crystalline phases**, can be found in XRD patterns. Additional topics that can be investigated by careful examination of XRD data include stress analysis inside the crystal lattice, **temperature-dependent investigations**, assessment of particle size in nanomaterials, measurement of **thin film thickness**, and **identification of defects and dislocations** [9][18][19]. Complementary techniques may be employed to thoroughly understand material properties and crystallographic expertise is frequently required for interpretation.

2.3.2 Raman Spectroscopy

Raman spectroscopy is a non-destructive analytical technique for studying vibrational, rotational, and other low-frequency molecule modes. It provides illuminating data on molecular structure, relationships, and composition of chemicals.

The foundation of Raman spectroscopy is the Raman scattering phenomenon, which occurs when monochromatic light—typically from a laser—interacts with a sample and causes frequency shifts in the scattered light due to molecular vibrations.[20][21] The majority of light falling on a transparent sample in a Raman experiment will transmit; the remaining portion of light will scatter in two ways: either as Raman scattering (inelastic scattering) or as Rayleigh (elastic scattering)[22]. Generally speaking, Stokes lines—comparatively more intense than Anti-Stocks lines—form the Raman spectrum [23]. Light that has been inelastically dispersed is

gathered and plotted as a Raman spectrum. The intensity of inelastically scattered light as a function of wave number makes up the spectrum. One of the crucial variables in the Raman spectrum is the wave number shift or δv. The difference in wave number between the radiations measured and the radiation from the source is known as the Raman shift [21].

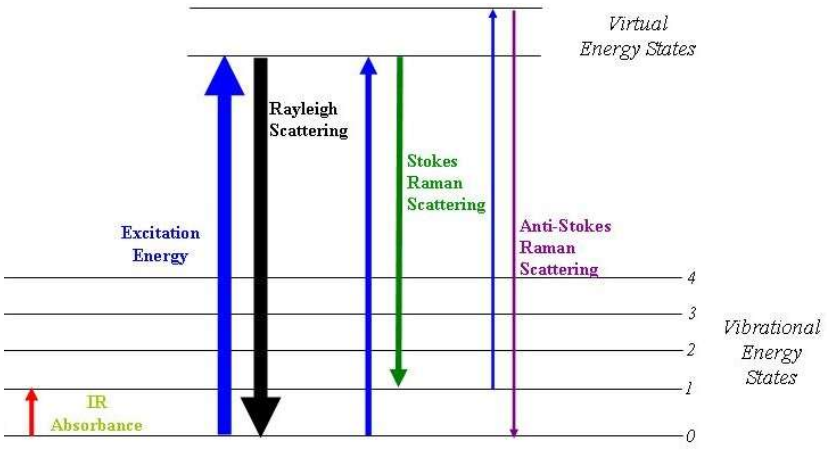

Figure 2.5 *Schematic representation of the origin of Raman lines - adapted from [23]*

In order to identify chemical compounds and investigate molecular interactions, information on the vibrational modes of the sample's molecules can be obtained from the energy shifts in the scattered light–Raman shift [24].

Instrumentation

The following elements are commonly found in the Raman spectrometer [21,25-28]:

1. **Laser Source**: The sample is illuminated using a monochromatic, coherent light source, usually a laser. Gas, diode, and solid-state lasers (such as Nd:YAG) are frequently utilised types of lasers.

2. **Sample Interaction Region**: The laser light interacts with the sample in a predetermined area. The molecular vibrations of the sample control the intensity of the dispersed light.

3. **Monochromator or Filters**: A monochromator or filters are utilised to separate the excitation laser line from the Raman scattered light. This keeps the laser light from interfering, and only the Raman-shifted frequencies can reach the detector.

4. **Detector**: The scattered light spectrum is recorded by a sensitive detector, such as a charge-coupled device (CCD) or photomultiplier tube (PMT). The energy shifts (also known as Raman shifts) in this spectrum indicate the sample's vibrational modes.

5. **Spectrometer**: A Raman spectrum can be produced by dividing the Raman-scattered light into various wavelengths using a spectrometer.

6. **Sample Stage**: A sample stage or holder enables exact sample positioning and manipulation during analysis.

7. **Optical Components**: The laser light is focused and directed onto the sample using mirrors, lenses, and beam splitters. The scattered light is then collected for examination.

8. **Data Analysis Software**: Sample identification and structural analysis are made possible by employing specialised software to analyse the Raman spectrum and detect distinctive peaks that correspond to molecule vibrations.

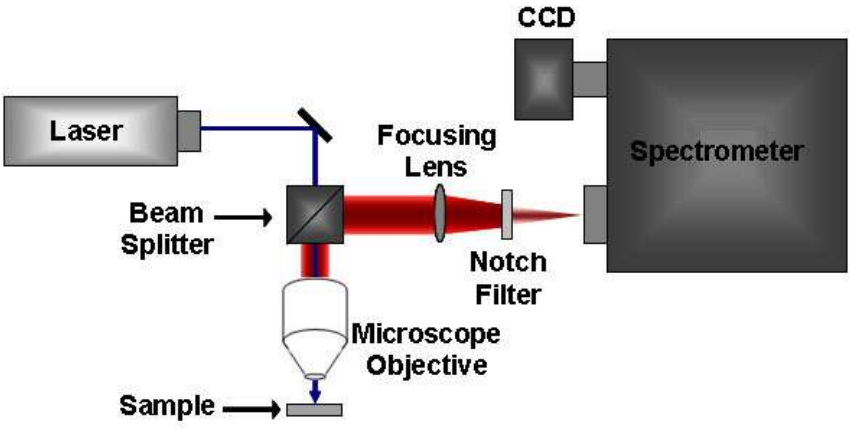

Figure 2.6 *Schematic of a micro-Raman spectrometer [29]*

Raman spectroscopy's capacity to offer insightful details on molecular vibrations and the structural properties of materials makes it useful in a wide range of scientific domains. Raman spectra are often used for the following purposes:

1. **Chemical Identification** [30]: Raman spectroscopy is a non-destructive technique to identify and characterise chemical substances. It is conducive to differentiating between various organic and inorganic chemical kinds.

2. **Pharmaceutical Analysis** [31]: Raman spectroscopy is used in the pharmaceutical industry to analyse drug formulations, spot fake medications, and monitor the crystalline structure of pharmaceutical components.

3. **Materials Science** [32]: Polymers, nanomaterials, and ceramics are among the materials whose characteristics are studied by researchers using Raman spectroscopy. It is helpful for researching flaws, phase transitions, and characterising structural changes in materials.

4. **Geological Analysis** [33]: Geologists use Raman spectroscopy to identify and categorise minerals and geological samples. It can shed light on rocks and minerals' structural characteristics and composition.

5. **Biomedical Research** [34]: Raman spectroscopy can be used to examine biological materials, such as tissues and cells. It can support biomolecular interaction analysis, cancer diagnosis, and cellular change monitoring.

6. **Environmental Analysis** [35]: Raman spectroscopy is utilised in ecological monitoring, including soil composition analysis, atmospheric gas research, and pollution detection in air and water.

7. **Forensic Science** [36]: To help solve crimes, forensic scientists use Raman spectroscopy to analyse traces of evidence, such as narcotics, explosives, and fibres.

8. **Conservation of Art and Cultural Heritage** [37]: Raman spectroscopy helps art historians and conservators analyse the materials, pigments, and dyes used

in artworks and cultural artefacts. It supports efforts at restoration and preservation.

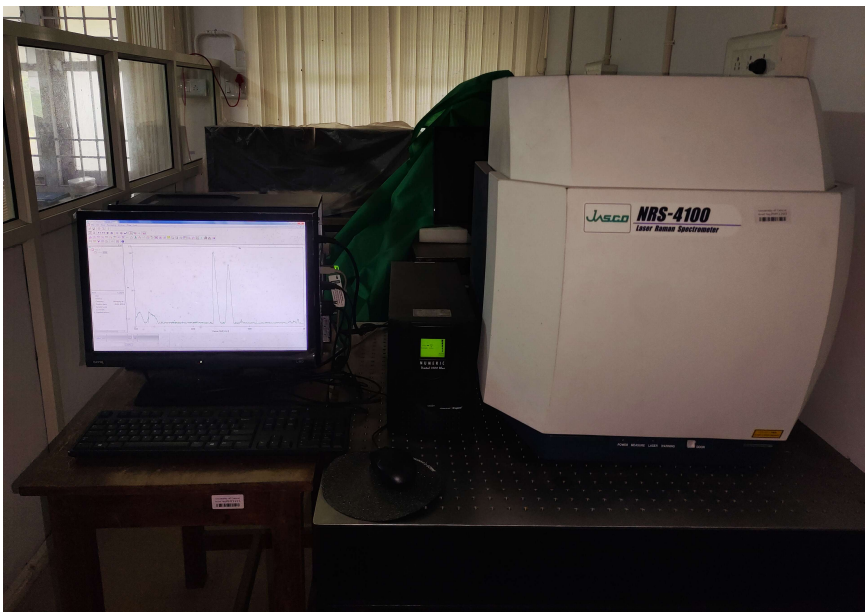

Figure 2.7 *Image of Raman Spectrometer used. (photo of the micro-Raman set up at the Department of Physics, University of Calicut).*

JASCO nrs 4500 Spectrometer was used for performing Raman measurements with 2sec exposure and accumulation 40 under a 532 nm laser source throughout the thesis work.

2.3.3 UV-visible Spectrophotometer

UV-visible spectroscopy is a basic analytical method that measures the amount of ultraviolet (UV) and visible light molecules absorbed by the sample. This technique offers insightful information on the concentration, electrical structure, and chemical characteristics of the materials being studied.

UV-visible spectroscopy measures the amount of light absorbed at particular wavelengths by passing a UV or visible light beam through a material. The resulting spectrum, sometimes referred to as an absorption spectrum, illustrates the connection between the light's wavelength and level of absorption. Usually, it comprises peaks and troughs representing the electrical changes happening within the molecules.

Electrons are promoted from lower-energy (valence) orbitals to higher-energy (conduction) orbitals during these transitions [38-39].

In several scientific domains, such as chemistry, biochemistry, pharmaceuticals, and materials science, UV-visible spectroscopy is extensively employed for chemical analysis, concentration measurement, and molecular property research [40-41].

The basis of UV-visible spectroscopy is the observation that various molecules absorb light at different wavelengths, namely in the visible and UV portions of the electromagnetic spectrum, that fall between 190 and 900 nm. The resulting absorption spectrum offers essential details regarding the molecules' electrical structures, such as :

1. **Concentration Determination** [42]: The concentration of a particular analyte in a sample is frequently ascertained using UV-visible spectroscopy. This is accomplished by measuring the sample's absorbance at a certain wavelength and comparing the results with the calibration curve.

2. **Chemical Identification** [43]: Chemical analysis and compound identification can be aided by the distinctive absorption patterns in UV-visible spectra, which can be used to determine the existence of particular functional groups or chromophores in molecules.

3. **Quantitative Analysis** [44]: UV-visible spectroscopy is used to quantitatively study the concentration of analytes in various samples, such as liquids, gases, and solids.

4. **Kinetic Studies** [45]: By tracking variations in absorbance over time, it is possible to get insights into reaction rates and mechanisms through the study of reaction kinetics.

5. **Quality Control** [46]: UV-visible spectroscopy is used in the pharmaceutical industry, among other industries, to assess product quality and batch-to-batch uniformity.

6. **Research on Biological and Biochemical Processes** [47]: Understanding biomolecules such as proteins, nucleic acids, and enzymes requires the use of UV-visible spectroscopy. It is useful for researching enzyme kinetics, estimating protein concentrations, and evaluating the purity of nucleic acids.

7. **Environmental Analysis** [48]: To help with environmental monitoring and regulatory compliance, environmental scientists employ UV-visible spectroscopy to identify and measure contaminants in samples of water, air, and soil.

8. **Material Characterisation** [49]: UV-visible spectroscopy is used in materials research to look at the electrical characteristics of materials, such as polymers, semiconductors, and nanoparticles.

Generally speaking, UV-visible spectroscopy is a broad and flexible method that offers crucial details regarding the electrical characteristics and concentrations of molecules, making it a vital resource in both academic and commercial contexts.

Beer-Lambert Law

A foundational idea in the spectroscopy study is the Beer-Lambert Law, sometimes referred to as Beer's Law or the Lambert-Beer Law. It explains the connection between a solution's solute concentration and the amount of light it can absorb. August Beer and Johann Lambert, two scientists who made separate contributions to establishing the law, are honoured in the law's name.

Beer-Lambert Law can be expressed mathematically as follows:

$$\boldsymbol{A = \varepsilon c l} \qquad \textbf{(2.2)}$$

Where:

- A is the absorbance of the solution.
- ε (epsilon) is the molar absorptivity or molar extinction coefficient, a constant characteristic of the substance being analysed.

- c is the concentration of the solute in the solution, usually expressed in moles per liter (Molarity).
- l is the path length of the sample through which the light passes, typically measured in centimeters.

According to the rule, a solution's absorbance is directly proportional to the concentration of the absorbing species and the sample's path length. By measuring a solute's absorbance at a certain wavelength, scientists can utilise this connection to calculate the concentration of the solute in a solution, which is helpful in quantitative analysis.

Instrumentation

The following elements are commonly found in UV-visible spectroscopy instrumentation [50-58]:

- **Light Source**: Deuterium Lamp (UV): Produces light with an ultraviolet wavelength of 190-380 nm. Visible Tungsten lamp: This type of lamp emits light between 380 and 750 nm.
- **Monochromator**: A monochromator divides light into its distinct wavelengths after it has passed through the sample. This separation can be accomplished with a prism or diffraction grating.
- **Sample Holder**: Since quartz is transparent in the ultraviolet spectrum, a quartz cuvette is typically used for UV-visible spectroscopy. The cuvette is filled with the sample solution and then put into the spectrophotometer.
- **Detectors:** For measuring light intensity at various wavelengths, photomultiplier tubes (PMTs) or photodiode array detectors are frequently employed. The light signal is transformed by the detector into an electrical signal, which is then processed by the device.

- **Amplifiers**: The spectrophotometer's electronics amplify and process the electrical signal from the detector. For additional investigation, the signal is frequently digitalised.

- **Data Output**: Usually, a computer or built-in screen shows the results. The absorption spectrum, which illustrates how the absorbance changes with wavelength, could be included in the output.

- **Wavelength Selector**: This gives the user the option to select the precise light wavelength that will pass through the sample. This is crucial for choosing the right wavelength to analyse a certain molecule.

- **Control Unit**: The user can adjust parameters including wavelength, scan speed, and other experimental settings using a unit that controls the apparatus.

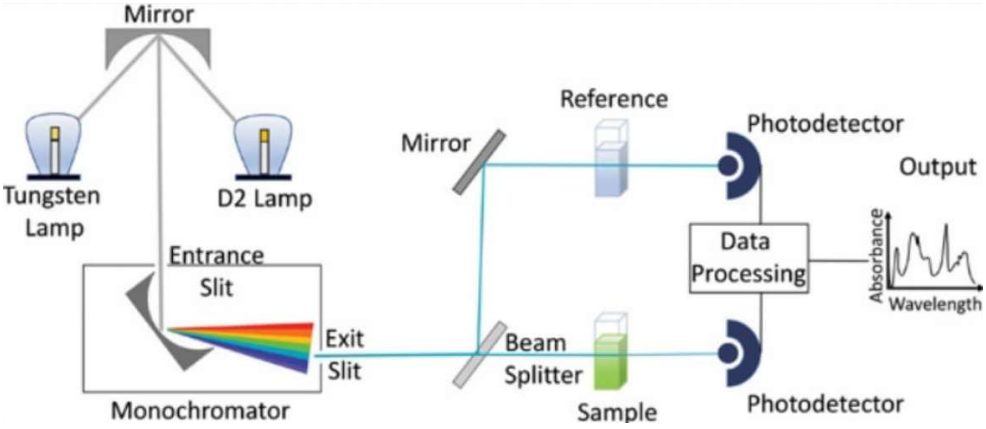

Figure2.8 *Schematic diagram of instrumentation of double beam UV-visible spectrometer. Adapted from [59].*

Calibration Standard: The equipment is calibrated using calibration standards, guaranteeing precise and trustworthy measurements. Solutions with established concentrations of a reference substance are frequently employed as standards.

UV and Visible Region: The electromagnetic spectrum is divided into two separate parts by UV-visible spectroscopy. The visible spectrum (400–800 nm) includes lower-energy transitions that give rise to the colours we see, whereas the UV region (usually 190–400 nm) deals with higher-energy transitions involving electronic excitations.

Baseline Correction: A baseline correction is frequently carried out to acquire accurate spectra. To remove solvent interference, this entails measuring the absorbance of a blank (solvent or reference solution) and subtracting it from the absorbance of the sample.

Limitations of UV-Visible Spectra

Despite being a useful analytical instrument, UV-visible spectroscopy has many intrinsic limitations. Its primary focus is on electronic transitions, which restricts its capacity to give in-depth analysis of particular functional groups or molecular structures. To absorb UV or visible light, compounds need to have chromophores, which limits the use of the approach to molecules with certain characteristics. The method may suffer with overlapping absorption bands, be sensitive only to solvent absorption, and lack sensitivity for trace analysis. Furthermore, UV-visible spectroscopy is not sensitive enough to distinguish minute variations in molecule configurations or to provide detailed structural information. Its limitations are further compounded by its sensitivity to temperature fluctuations and the difficulties associated with analysing samples containing water. Notwithstanding these limitations, UV-visible spectroscopy is still widely used in many different domains, and for a more thorough investigation, researchers frequently combine it with complementing techniques [60-63].

Mechanism of UV visible spectra

The mechanism behind UV-visible spectra revolves around the absorption of electromagnetic radiation by molecules, specifically in the ultraviolet (UV) and visible regions. Molecules capable of absorbing UV or visible light possess chromophores, such as conjugated double bonds or aromatic rings, with π electrons that can undergo electronic transitions. The selection rules govern the allowed transitions, requiring a change in the molecule's dipole moment. When a molecule absorbs light, its electrons are promoted from a lower energy level (ground state) to a higher energy level (excited state). The energy difference between these states corresponds to specific wavelengths of light. The resulting absorption spectrum provides insights into the electronic structure and composition of the molecules, with

peaks indicating different electronic transitions. Factors like molar absorptivity, concentration, and path length influence the intensity of absorption, as described by the Beer-Lambert Law. Overall, UV-visible spectroscopy offers a valuable tool for studying molecular electronic transitions and understanding the characteristics of absorbing species.

Figure 2.9 *Image of UV-visible Spectrometer used. (at Laboratory for mesoscopic sciences and devices, Department of Physics, University of Calicut).*

We used JASCO V-550 spectrometer with wavelength ranging from 200 to 900 nm in our analyses.

2.3.4 Thermogravimetric Analysis (TGA)

Thermogravimetric Analysis (TGA) is a commonly used method for analysing the thermal stability and decomposition behaviour of materials in chemistry, materials science, and other scientific fields. It measures the weight change of a sample as a function of temperature or time [64].

The basic design of a TGA device consists of a sample pan that is balanced and heated at predetermined rates. There is a steady change in the sample's weight with respect to time or temperature. The resulting thermogram provides information about the thermal reactions occurring in the sample [65].

Thermal degradation, phase transitions, and reactions can be detected through TGA. The fundamental principle is based on the fact that as the temperature increases, the sample undergoes physical and chemical changes, leading to weight loss or gain [66].

Instrumentation

The instrumentation of a thermogravimetric analysis (TGA) apparatus consists of several essential parts and features intended to provide accurate control and measurements during thermal analysis. Typically, the following elements are included in the extensive instrumentation [65-67]:

- **Balance**

  The highly sensitive balance, or microbalance, is the central component of the TGA apparatus. Throughout the experiment, this part measures the sample's mass continually.

- **Furnace**

  The sample must get controlled heating from the furnace. It is intended to precisely reach and maintain a given temperature. Adjustable heating rates are a common feature of modern TGA devices, enabling more flexible investigations.

- Sample Holder

  A key component of the TGA setup is the sample pan, which holds the material being investigated. It needs to be composed of a substance that, at varying temperatures, doesn't react with the sample.

- **Gas Flow System**

  A gas flow system is built into TGA instruments to regulate the environment surrounding the sample. Depending on the needs of the analysis, common gases utilised include nitrogen, air, or other inert gases. This mechanism aids in stopping unintended interactions with oxygen in the atmosphere.

- **Temperature Control System**

Accurate temperature regulation is essential for TGA investigations. Modern instruments make use of sophisticated temperature control systems, which frequently include feedback mechanisms to precisely maintain the required temperature.

- **Data Acquisition System**

  Real-time measurement recording and analysis are made possible by the data acquisition mechanism built into TGA devices. By gathering information on the sample's weight variations in relation to temperature or time, this device creates a thermogram.

- **Software**

  Researchers may set up and manage the experiment's parameters, including temperature ramp rates, gas flow rates, and other conditions, with the help of user-friendly control software. It also makes data visualisation and analysis easier.

Applications of TGA

There are numerous uses for thermogravimetric analysis (TGA) in both scientific and industrial domains. The capacity of TGA to offer insightful details on the composition, stability, and thermal characteristics of materials accounts for its adaptability. Here are a few sophisticated uses for TGA:

- **Determination of Decomposition Temperature [68]**

TGA is frequently used to determine the temperature at which a material experiences thermal decomposition. Understanding the temperature stability of substances like polymers, medications, and chemical molecules depends on this.

- **Evaluation of Thermal Stability [69]**

The thermal stability of materials under various circumstances can be assessed with the use of TGA. Researchers can identify the onset of thermal degradation by examining the behavior of materials at high temperatures.

- **Inorganic Materials and Ceramics [70]**

The thermal behavior of ceramics and inorganic materials is examined using TGA. It facilitates comprehension of reactions, sintering, and phase changes that these materials undergo.

- **Characterisation of Polymers [71]**

TGA is widely used in polymer characterisation. It offers details on the decomposition behavior, composition, and thermal transitions of polymers, which is crucial for product development and quality assurance.

- **Pharmaceutical Applications [72]**

In the pharmaceutical sector, TGA investigates the thermal characteristics of drugs and pharmaceutical formulations. It assists in determining the temperature at which medications deteriorate, providing vital details for formulation and storage settings.

- **Environmental Evaluation [73]**

Environmental scientists use TGA to investigate the breakdown of organic and inorganic substances in environmental samples. This knowledge is crucial for understanding the fate of waste materials and pollutants.

- **Quality Control in Materials Production [74]**

During material production, TGA is integral to quality control procedures, helping manufacturers ensure materials meet specific thermal stability requirements and identifying potential issues in production.

- **Biofuels and Biomass Characterisation [75]**

TGA analyses biomass and biofuels to determine their thermal degradation profiles, which are essential for understanding combustion processes and optimising energy output.

- **Study of Reactive and Explosive Materials [76]**

The thermal behavior of reactive and explosive materials is investigated using TGA. Understanding decomposition and ignition temperatures is vital for safety evaluations and developing materials with controlled reactivity.

- **Evaluation of Agricultural and Food Products** [77]

In the food industry, TGA examines the characteristics of agricultural goods, providing insights into processes like lipid oxidation, dehydration, and breakdown, which affect food safety and quality.

Figure 2.10 *Image of TGA instrument at CSIF, University of Calicut.*

We used the Perkin Elmer STA 8000 simultaneous thermal analyser to check the thermal stability of the samples from the Central Sophisticated Instrumentation Facility (*CSIF*) of the *University* of *Calicut.*

2.3.5 Brunauer-Emmett-Teller (BET) surface analysis

The Brunauer-Emmett-Teller (BET) analysis is a commonly used method for finding the surface area of porous materials. The BET method, created in 1938 by Stephen Brunauer, Paul Hugh Emmett, and Edward Teller, has grown to be a widely used technique for figuring out a solid's specific surface area, especially in chemistry, materials science, and catalysis[78].

The adsorption of gas molecules onto the surface of a solid material is the foundation of the BET theory. The study is predicated on monolayer adsorption, in which the energies of the following layers are higher, and the initial layer is energetically favoured. The BET equation calculates the surface area by comparing the amount of gas adsorbed at a specific pressure to the amount adsorbed at saturation pressure [79-82].

The BET equation is given by:

$$\frac{P}{(V_m - V)} = \frac{1}{C} + \frac{C-1}{C}\frac{1}{P_0 V_m} \qquad \textbf{(2.3)}$$

where:

- P is the equilibrium pressure.
- V is the quantity adsorbed at pressure P.
- V_m is the monolayer capacity.
- C is a constant related to the energy of multilayer adsorption.
- P_0 is the saturation pressure.

Instrumentation

For performing Brunauer-Emmett-Teller (BET) analysis, specific equipment meant to gauge gas adsorption onto a solid surface is required. The main elements and capabilities of a typical BET instrument are described below [78-82]:

- **Gas Adsorption Analyzer**

The gas adsorption analyser is the central component of BET instrumentation. Because of its vast range of applications and inert nature, nitrogen is a frequently used gas. During the adsorption process, the instrument must give accurate control over the temperature and pressure parameters.

- **Sample Chamber**

The solid under inquiry is placed in the sample chamber. Proper dispersion of the material—which is often in powder form—is necessary to guarantee precise measurements. The analysis will take place in a stable atmosphere according to the chamber's design.

- **System of Degassing**

The sample is frequently put through a degassing procedure to remove any impurities or adsorbed gases before BET analysis. The degassing technique usually entails heating the sample under a vacuum to guarantee that the sample is clean and stable before the adsorption measurements begin.

- **System for Controlling Pressure**

To expose the sample to different pressures of the adsorbing gas, the instrument needs a precise pressure control mechanism. In order to produce precise adsorption isotherms, the pressure control system makes sure that the adsorption process takes place under regulated circumstances.

- **Detectors**

To calculate the amount of gas adsorbed at equilibrium for various pressures, detectors are necessary. Thermal conductivity detectors and electromechanical devices are examples of frequently used detectors. Accurately detecting minute variations in the amount of petrol is essential to getting trustworthy data.

- **Temperature Control System**

Since BET analysis is often carried out at various temperatures, a temperature control system is required for the device. This permits temperature fluctuations during the adsorption process, making it possible to identify the adsorption isotherms at various temperatures.

- **Data Acquisition System**

The data produced during the BET analysis must be recorded and analysed using a sophisticated data gathering system. This technology makes it easier to calculate specific surface area using the BET equation by gathering data on gas adsorption as a function of temperature and pressure.

- **Software for Data analysis**

Typically, BET devices come with specialised software and a computer interface. Using the BET equation to determine precise surface area values, researchers may also do data analysis and alter the experimental parameters while keeping an eye on the adsorption process in real-time – using a software interface.

- **Vacuum system**

A vacuum system is incorporated to guarantee appropriate sample degassing. Before the actual adsorption measurements, it helps clear the sample surface of impurities and adsorbed gases.

- **Gas Handling System**

The instrument has a gas handling system to introduce the adsorbing gas into the sample chamber at specified pressures. Throughout the adsorption process, this system ensures the atmosphere is constant and controlled.

- **Sample Holder**

The solid sample is intended to be accommodated by the sample holder, also known as the cell. It must be able to preserve the homogeneity and integrity of the sample during the adsorption procedure.

Figure 2.11 *Image of BET instrument at CSIF, University of Calicut.*

Throughout this research, we used BELSORP-max, an automatic gas adsorption measuring unit for all adsorption-desorption, surface area and porosity measurements from the Central Sophisticated Instrumentation Facility (CSIF) of the University of Calicut.

2.3.6 Scanning electron microscope (SEM)

High-resolution images and comprehensive surface data about samples can be obtained using the incredibly flexible scanning electron microscopy technique. It is a kind of electron microscopy that, in contrast to optical microscopy, creates images with far higher resolution by scanning a specimen's surface with a concentrated electron beam. A SEM instrument's resolution might be as little as one nanometer or as high as several [83-84].

A focussed stream of electrons is projected and scanned across a sample's surface using a scanning electron microscope (SEM), which uses specialised detectors to gather the various signals that are produced. The interaction between the electrons in the beam and the atoms in the sample results in a variety of signals that can be utilised to determine the composition and topography of the surface. Real-time images can be shown on an external monitor with software that links the position of the beam

with the intensity of electrons detected by the detector(s). The two most popular types of detectors utilised for high-resolution imaging in a scanning electron microscope (SEM) are the secondary electron detector (SED) and the backscattered electron detector (BSD). Energy dispersive X-ray spectroscopy (EDS) detectors provide access to microanalysis of the surface composition [84].

SEM can be used for direct analysis of a broad variety of solid materials. Specialised imaging techniques like low-vacuum or low-kV imaging are frequently needed for biological materials and insulating samples to lessen surface charge and beam damage. To reduce charge, insulating samples can have a small layer of gold or platinum sputter coated on them.

Instrumentation

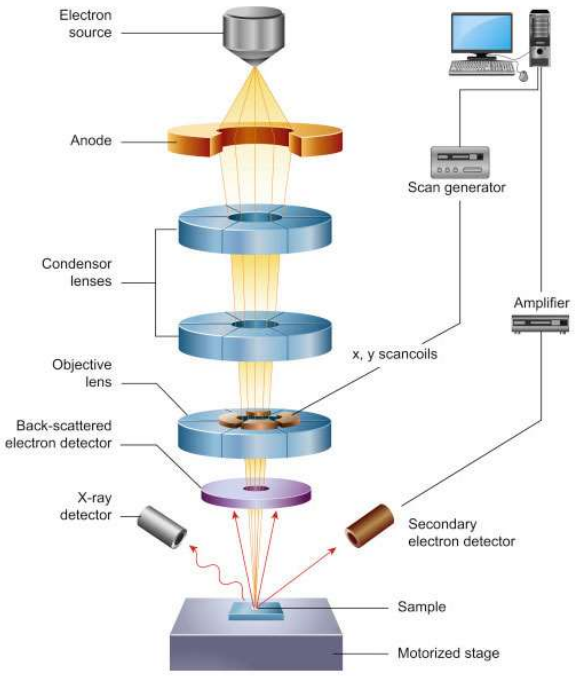

Figure 2.12: *Schematic of a scanning electron microscope adapted from [85]*

The main components of SEM include [86]:

1. Electron source (gun)
2. Condenser lenses
3. Objective lens
4. X-Y scan coils & scan generator
5. Detectors
6. Sample stage
7. Computer and display to view the images
8. External vacuum pump(s)

Electron source (gun)

A scanning electron microscope's (SEM) electron source is an essential component since it has a big impact on the instrument's analytical capabilities. This component, often known as the "electron gun," must produce a steady, brilliant stream of electrons that the column's lenses may defocus onto the sample. Tungsten filaments, solid-state hexaboride crystals, and field emission guns are the three most common types of electron emitters used in SEMs.

- **Tungsten (W) Filament**

Tungsten Filament is made of a 100 μm-long tungsten wire with an inverted V form that is heated resistively to release electrons. This is the most basic sort of electron source, designed for the first generation of electron microscopes. Due to its low cost, it continues to be the most widely used form of electron source today. Because of its comparatively broad emission area, tungsten hairpins have the lowest resolution available. The tungsten eventually evaporates over time due to the extraordinarily high temperatures (~2800 K) at which they work, resulting in column pollution. This also means that tungsten filaments are vulnerable to sudden burnout after around 100 hours of beam-on operation. Due to their sensitivity to temperature

changes, SEM systems with tungsten sources also need regular beam stigmation and alignment adjustments.

- **Lanthanum Hexaboride (LaB6) or Cerium Hexaboride (CeB6)**

The sources employ a precisely polished LaB6 or CeB6 crystal with a sharp tip for thermionic emission. Because hexaboride crystals have a smaller work function than tungsten, they can emit 10 times as many electrons at any accelerating voltage, resulting in a brighter emission. These sources are well-liked for high-performance SEM instruments because of their high brightness characteristic. Improved signal-to-noise and improved resolution are two of their main benefits. They have a working lifetime that is ten to fifteen times longer and requires less regular stigmation adjustment due to their substantially higher level of stability as compared to tungsten. Furthermore, these sources do not burn out but gradually deteriorate over time, enabling planned source modifications. CeB6 sources have a longer lifespan because they are more evaporation-resistant than LaB6 sources.

- **Field emission gun**

The FEG source is a tungsten wire with an extremely sharp tip (less than 100 nm) that generates the electron beam using field electron emission. By applying an electric field to the tip to extract the electrons and using a second field to accelerate them down the column, the process is known as electron tunnelling. In SEM, Schottky FEGs are commonly employed. These sources are thermionic emitters helped by the field. The highest resolutions can be achieved because FEG sources generate electron beams with maximum brightness and coherence.

Lenses

In a SEM, the electron beam is manipulated by electromagnetic lenses. The lens is made from a copper wire solenoid. The applied magnetic field strength depends on the current flowing through the solenoid. A beam crossover forms at a certain distance from the lens as a result of off-axis electrons being bent towards the optic axis when they travel through this magnetic field.

Reducing the diameter of the principal beam that the electron source emits is the fundamental function of a condenser lens. The electron beam is focused as it travels down the column from the source by a sequence of condenser lenses. A condenser aperture can be employed to further lower the beam diameter and keep off-axis electrons out of the system. The phrase "spot size" refers to the smaller the spot the beam will have when it contacts the surface, the narrower it is.

The working distance and probe size are determined by focusing the beam onto the sample surface using the objective lens, which is always the last lens in the column. Optimising the spatial resolution requires careful adjustment of the objective lens and objective aperture. Longer working distances (small α) correlate to a bigger depth of field and lower spatial resolution than shorter working distances (large α) because of variations in beam convergence angle (α).

Scanning coils

Scanning coils deflect the beam in the X and Y axes once it has been focused, allowing it to scan sterically across the sample's surface. Real-time image viewing is possible by synchronising the scanning coils with the software that operates the detectors and displays the image on an external monitor.

Sample chamber

Samples are mounted and put into an evacuated chamber. A translation stage, tilt and rotation mechanisms, electrical feed-throughs to external devices, temperature-control stages for cryogenic heating or cooling, optical cameras, and a host of additional tools to aid in sample analysis can all be found in the sample chamber.

Detectors [87]

When an electron beam interacts with a sample, several things happen in a scanning electron microscope (SEM). Typically, distinct detectors are required to differentiate between typical X-rays, backscattered electrons, and secondary

electrons. The signals have varying penetration depths depending on the accelerating voltage and sample density.

- **Backscattered electron detector (BSD)**

Electrons that are elastically scattered are picked up by a backscattered electron detector (BSD). These electrons come from below the sample's surface and have a higher energy. As a result, when compared to a picture obtained using a SED, the resolution of a BSD image will be lower. Lower vacuum levels enable less sample preparation work and lessen the chance of beam damage when using a BSD. A solid-state sensor is the component of the most prevalent kind of BSD. In the semiconductor sensor material, incident electrons pair to produce electron-hole pairs, producing a current proportional to the backscatter electron yield. Above the sample, a four-quadrant BSD is arranged in an annulus around the optic axis. Topographic and elemental contrast (composition) imaging modes are made possible by this architecture, which also provides unique signals in each quadrant and enables the acquisition of many backscatter electrons.

- **Secondary electron detector (SED)**

For scanning electron microscopy, a secondary electron detector (SED) provides images with a resolution that is not reliant on the material. SED images offer the highest resolution topographical information and enable visualisation of the inelastically scattered electrons generated near the sample surface. SED image data does not provide information on the composition of the substance.

An Everhart-Thornley (E-T) detector finds secondary electrons. The ET detector is positioned above the sample to one side and consists of a scintillator inside a Faraday cage. The Faraday cage receives a positive bias to draw low-energy electrons, which a scintillator converts into light (photons). The final signal is then obtained by amplifying the photon signals with a photomultiplier tube.

Working of SEM [88-91]

The electron gun produces electrons at the top of the column, which are then accelerated through it at a predetermined accelerating voltage (1 keV – 30 keV). Apertures and condenser lenses work together to decrease the beam diameter. The objective lens, which focuses the beam on the sample surface, is the last lens in the column. Depending on the kind of electron cannon, accelerating voltage, and lens arrangement, the beam diameter in a scanning electron microscope (SEM) can vary from less than one nanometer to twenty nanometers.

The sample is set up on a stage within the chamber, and a number of pumps are used to keep the chamber and column vacuum. The microscope's design will determine the vacuum level. Variable pumping is a feature of certain microscopes that enables low-vacuum imaging by maintaining the sample chamber at a lower vacuum level than the remainder of the column.

Scan coils above the objective lens regulate where the electron beam lands on the sample. These coils make X-Y plane beam scanning of the sample's surface possible. When the scanned beam hits the sample, it produces a range of signals, including backscattered electrons, secondary electrons, and distinctive X-rays. Then, the proper detectors pick up on these signals.

Pixel by pixel, a grayscale image can be viewed in real-time by using the scan generator and an external computer with specialised software to synchronise the information obtained by the detector (beam's X, Y position at each time interval) with the scan generator's intensity readings. The signal-to-noise ratio can be adjusted based on how long the electron beam dwells at each X,Y point. The magnification depends on the scanned region's size; smaller scanned areas equate to greater magnifications. Changing the pixels in a particular scan area is also possible, which may affect the perceived resolution.

The morphology of the samples was investigated using Scanning Electron Microscopy (ZEISS GEMINI SEM 300) from the Central Sophisticated Instrumentation Facility (CSIF), University of Calicut, throughout the thesis.

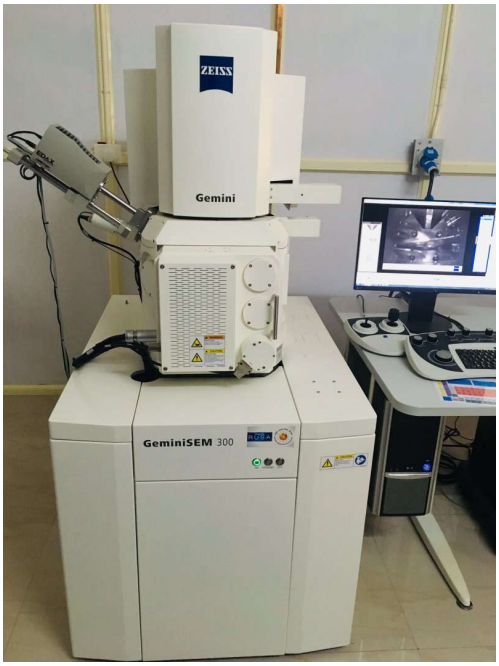

Figure 2.13: *Image of FESEM at CSIF, University of Calicut*

2.4.7 Dynamic Light Scattering Technique (DLS)

Dynamic Light Scattering (DLS) spectroscopy is a scientific method used to measure the size of particles or molecules that are suspended in a liquid or solution. It's like using a special light to see how big and tiny things are in a liquid [92].

DLS works by shining a laser beam into the liquid sample containing particles. These particles scatter the laser light in different directions. By analysing how the intensity of this scattered light changes over very short periods of time (milliseconds), one can calculate the size of the particles. The bigger the particles, the slower the intensity changes, and vice versa. This technique takes advantage of the Brownian motion, which is the random movement of particles in a fluid, to determine particle size [93].

Instrumentation:

To perform DLS spectroscopy, scientists use a special instrument called a DLS spectrometer or particle size analyser. This device includes [94,95]:

- **Laser**: A highly focused laser beam directed at the sample.
- **Detector**: Sensors that capture the scattered light at different angles.
- **Computer**: Software that analyses the data to calculate particle sizes based on the intensity fluctuations of the scattered light.

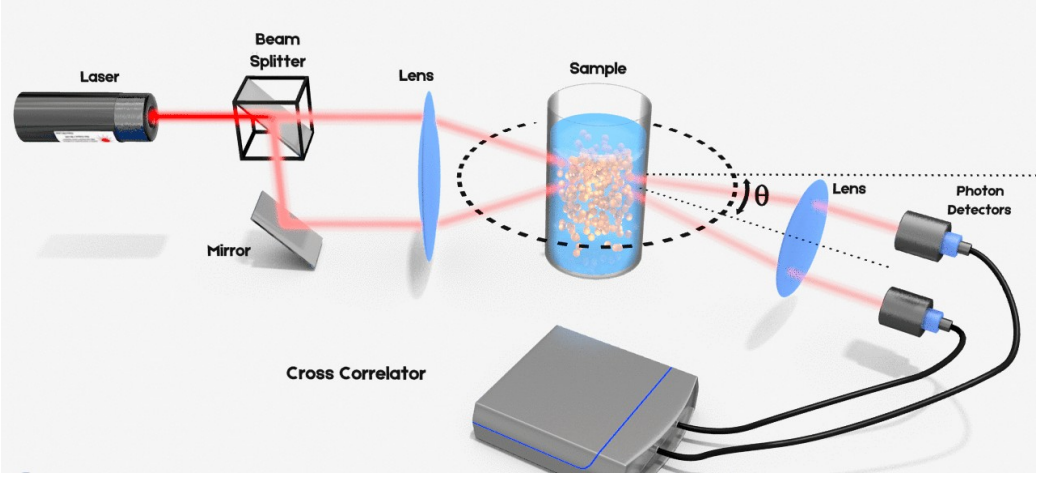

Figure2.14 *Schematic diagram of instrumentation of DLS instrument. Adapted from [96]*

This method is incredibly useful because it provides precise information about the size distribution of these particles without disturbing the sample too much.

One of the major benefits of DLS spectroscopy is its non-destructive nature. This means that scientists can study the particles without altering them or needing to prepare the sample extensively. They simply shine a laser into the liquid and observe how the light scatters off the particles. This makes it ideal for studying delicate substances like proteins or nanoparticles, where maintaining their integrity is crucial for accurate analysis.

Moreover, DLS spectroscopy is highly sensitive and versatile. It can detect particles ranging from just a few nanometers to micrometres. This sensitivity allows researchers to analyse very small particles that might be difficult to study using other methods. The technique also provides rapid measurements with high precision, making it invaluable in both research settings and industrial applications where quick and accurate data is essential.

DLS spectroscopy plays a key role in research and development in various fields such as biotechnology, nanotechnology, materials science, and environmental monitoring. For example, in biotechnology and pharmaceutical industries, scientists use DLS to understand the size and behavior of proteins and viruses in solutions, which is critical for developing new drugs and vaccines. In nanotechnology, DLS helps characterise nanoparticles for drug delivery, electronics, and catalysis applications. Additionally, environmental science aids in studying pollutants and particles in natural waters, providing insights into environmental health.

Applications:

DLS spectroscopy has diverse applications across various scientific fields:

- **Biotechnology and Pharmaceuticals** [97]: Measuring the size of proteins, viruses, and other biomolecules in solution.
- **Nanotechnology** [98]: Characterising nanoparticles and their aggregates.
- **Materials Science** [99]: Analysing colloidal suspensions, polymers, and surfactant systems.
- **Environmental Science** [100]: Studying pollutants and particles in natural waters.
- **Food and Beverage Industry** [101]: Monitoring emulsions and colloidal stability.

Figure 2.15 *Image of DLS instrument at Department of Nanoscience and nanotechnology, University of Calicut*

2.3.8 Fourier transform Infrared spectroscopy (FTIR)

Fourier transform Infrared spectroscopy is a powerful analytical technique widely used to identify and study chemical compounds and molecular structures based on their vibrational modes. This technique exploits the interaction of infrared (IR) radiation with matter, providing valuable insights into the molecular composition and bonding environment of a sample. [102]

FTIR spectroscopy is based on the absorption of infrared radiation by molecules, which excites their vibrational and rotational modes. The energy of IR radiation corresponds to the vibrational energies of chemical bonds, making this technique highly sensitive to functional groups and molecular environments. The key regions of the IR spectrum are:

- **Mid-IR region (4000–400 cm^{-1}):** Most commonly used, as it contains characteristic absorption bands for functional groups.
- **Near-IR and Far-IR regions:** Less frequently used but provide additional information about overtone transitions and lattice vibrations, respectively.

The absorption of IR radiation causes changes in the dipole moment of a molecule, making polar bonds especially responsive to IR spectroscopy. Nonpolar bonds, while less responsive, can also exhibit IR absorption if asymmetric vibrations occur.

Instrumentation

The primary components of an FTIR spectrometer include [103-104]:

1. **IR Radiation Source:** Typically a Globar (silicon carbide) or a Nernst filament, which emits a broad spectrum of IR radiation.
2. **Interferometer:** The heart of the FTIR instrument, where a Michelson interferometer modulates the IR radiation by splitting it into two beams using a beam splitter. The recombined beams create an interference pattern.
3. **Sample Holder:** Samples can be analysed in various states—solid (e.g., using KBr pellets), liquid (e.g., in liquid cells), or gaseous (e.g., in gas cells).
4. **Detector:** Commonly a deuterated triglycine sulfate (DTGS) detector or mercury cadmium telluride (MCT) detector records the intensity of transmitted or reflected IR radiation.
5. **Computer System:** Processes the raw interferogram using Fourier Transform to convert it into a readable IR spectrum.

Working

The working of an FTIR spectrometer involves the following steps [102-104]:

1. **Emission of IR Radiation:** The source emits IR radiation covering a wide range of wavelengths.
2. **Interferogram Generation:** The IR beam is split into two paths in the interferometer. One path reflects off a stationary mirror, the other off a moving mirror. When these beams recombine, they create an interferogram, a composite signal containing all IR frequencies.

3. **Sample Interaction:** The IR radiation passes through or reflects off the sample, where specific wavelengths are absorbed based on molecular vibrations.

4. **Detection and Transformation:** The detector captures the resulting signal, and the computer applies Fourier Transform to generate an absorbance or transmittance spectrum.

The FTIR spectrum is a plot of absorbance (or transmittance) versus wavenumber (cm^{-1}). Key information includes:

- **Functional Group Identification:** Peaks in characteristic regions reveal specific functional groups, such as O-H, C-H, C=O, and N-H.
- **Chemical Bonding and Environment:** Shifts in peak positions and intensities indicate variations in molecular interactions, such as hydrogen bonding or conjugation.
- **Quantitative Analysis:** Peak areas or heights can correlate with specific components' concentration.
- **Structural Insights:** Patterns of peaks in the fingerprint region (1500–400 cm^{-1}) are unique to individual compounds, aiding in precise identification.

Applications

1. **Material Characterisation [105]:**
    - Identifying polymers, composites, and advanced materials.
    - Studying functional group modifications in graphene oxide (GO) and reduced GO composites.
2. **Chemical Analysis [106]:**
    - Monitoring reaction progress and studying chemical mechanisms.
    - Assessing purity and composition of pharmaceuticals and chemicals.

3. **Environmental Science [107]:**
    - Detecting pollutants and studying adsorption mechanisms in water treatment.
    - Identifying contaminants in air, soil, and water samples.
4. **Biological Studies [108]:**
    - Analysing biomolecules, such as proteins, lipids, and carbohydrates.
    - Investigating cellular structures and metabolic processes.
5. **Forensic and Security Applications [109]:**
    - Detecting explosives and illicit substances.
    - Analysing paint, fibers, and other forensic evidence.

Figure 2.16 *FTIR Spectrometer. Image adapted from* ***[110]***

We used the Agilent Cary 660 FTIR Spectrometer Central Sophisticated Instrumentation Facility (*CSIF*) of the *University* of *Calicut throughout this research work.*

2.3.9 Laboratory equipment

For the synthesis process, various laboratory instruments and equipment were utilised to ensure precise preparation and characterisation of the materials. The following equipments at the Laboratory for Mesoscopic Sciences and Devices, Dept of Physics, University of Calicut, were employed:

- **Magnetic Stirrer:** IKA C-MAG HS4 Digital, manufactured by IKA, for controlled and consistent stirring.
- **Ultrasonic Cleaner:** Frontline Ultrasonic Cleaner and GT Sonicator are used for effective dispersion and mixing of materials.
- **Ovens:** Hot air oven and vacuum oven from Rotek are employed for drying and thermal treatments.
- **Centrifuge:** REMI R8C, manufactured by REMI, for efficient separation of materials during the synthesis process.

The use of these materials, methods, characterization techniques, and laboratory instruments significantly contributed to achieving the improved results presented in this thesis.

2.4 Adsorption [111-115]

Adsorption refers to the adhesion of particles onto a surface. To illustrate, consider a sponge absorbing water. In this scenario, water molecules enter the sponge and can be found both within its structure and adhering to its surface. If adsorption were the dominant process, water molecules would solely accumulate on the surface of the sponge without penetrating its interior. Here, the water molecules act as the adsorbate, while the sponge serves as the adsorbent.

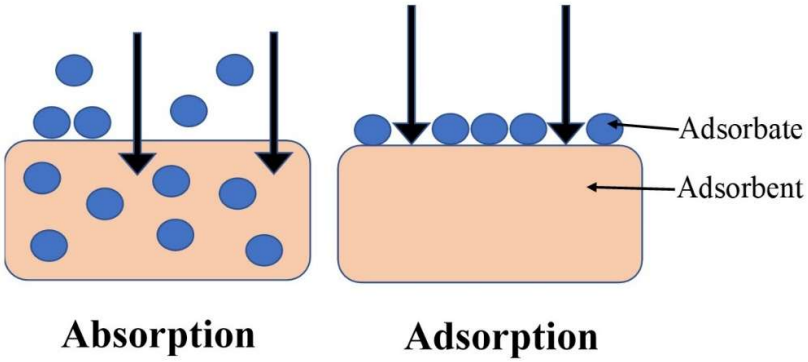

The removal percentage in adsorption indicates how effectively an adsorbent removes an adsorbate from a solution. It is calculated using the formula:

$$\boldsymbol{R\% = \frac{(C_0 - C_t)}{C_0} \times 100} \qquad \textbf{(2.4)}$$

The adsorption capacity in adsorption refers to the amount of adsorbate that an adsorbent can hold or adsorb per unit weight of the adsorbent. It is a key parameter for evaluating the efficiency of an adsorbent and is typically expressed in units such as mg/g (milligrams of adsorbate per gram of adsorbent).

The equilibrium adsorption capacity (q_e) is calculated using the formula:

$$\boldsymbol{q_e = \frac{(C_0 - C_t)}{w} \times V} \qquad \textbf{(2.5)}$$

where C_0 and C_t signify the initial concentration of adsorbate and at a definite time t, respectively. w and V are the weight of the adsorbent and the volume of adsorbate solution, respectively.

Adsorption kinetics

The study of adsorption rate, including the mechanisms and variables influencing the adsorption process over time, is known as adsorption kinetics. Optimising adsorption processes for a variety of applications, such as environmental remediation, gas separation, and catalysis, requires a thorough understanding of adsorption kinetics. Based on experimental evidence, several kinetic models have

been created to explain and forecast adsorption behaviour. Let's examine a few of the popular kinetic models:

Pseudo-First-Order Kinetic model [113,114]:

This model assumes that the adsorption process follows a first-order kinetic mechanism, but the actual rate may deviate from first-order kinetics due to external factors. Here the rate of change of the adsorption capacity is proportional to the concentration of active sites per unit mass of adsorbent material. The pseudo-first-order rate equation can be written as:

$$\frac{dq_t}{dt} = k_1(q_e - q_t) \quad \textbf{(2.6)}$$

$$\log (q_e - q_t) = \log q_e - \frac{k_1}{2.303} t \quad \textbf{(2.7)}$$

where q_t is the adsorption capacity at a specific time (t), q_e represents the equilibrium adsorption capacity and k_1 is the pseudo-first-order rate constant.

Pseudo-Second-Order Kinetics [113,114]:

Similar to the pseudo-first-order model, the pseudo-second-order model assumes that the adsorption process follows a second-order kinetic mechanism but accounts for deviations from ideal behaviour. The rate of change of the concentration of occupied active sites per unit mass of the adsorbent material is proportional to the square of the concentration of free active sites per unit mass of sorbent. The rate equation can be expressed as:

$$\frac{dq_t}{dt} = k_2(q_e - q_t)^2 \quad \textbf{(2.8)}$$

$$\frac{t}{q_t} = \frac{1}{k_2 q_e^2} + \frac{1}{q_t} t \quad \textbf{(2.9)}$$

where k_2 is the pseudo-second-order rate constant.

Elovich Kinetic model [115]:

The Elovich model describes adsorption kinetics by considering the surface heterogeneity and the presence of active sites on the adsorbent surface. It can be expressed as:

$$\frac{dq_t}{dt} = \alpha e^{-\beta q t} \qquad \textbf{(2.10)}$$

$$q_t = \frac{1}{\beta} ln(\alpha\beta) + \frac{1}{\beta} ln(t) \qquad \textbf{(2.11)}$$

where α and β are the Elovich constants.

2.5 References

1. Hummers, W. S., & Offeman, R. E. (1958). Preparation of Graphitic Oxide. Journal of the American Chemical Society, 80(6), 1339. https://doi.org/10.1021/ja01539a017

2. Cullity, B. D., & Stock, S. R. (2001). Elements of X-ray diffraction. Prentice Hall.

3. Jenkins, R., & Snyder, R. L. (1996). Introduction to X-ray powder diffractometry. John Wiley & Sons.

4. https://www.britannica.com/science/X-ray-diffraction

5. Klug, H. P., & Alexander, L. E. (1974). X-ray diffraction procedures: For polycrystalline and amorphous materials. John Wiley & Sons.

6. Bragg, W. H., & Bragg, W. L. (1913). **X-rays and crystal structure**. Proceedings of the Royal Society of London. Series A, Containing Papers of a Mathematical and Physical Character, 88(605), 428-438.

7. Jenkins, R., & Snyder, R. L. (1996). **Introduction to X-ray powder diffractometry**. John Wiley & Sons. (Chapter 8)

8. Rhodes, G. (2017). **Crystallography made crystal clear**. Academic Press.

9. Mittemeijer, E. J., & Welzel, U. (2012). **Depth-resolved residual stress analysis with high spatial resolution by X-ray and neutron diffraction: A review**. Materials Science and Engineering: R: Reports, 72(4-6), 97-159.

10. Jeoung-Ah, K. (2004). The characterisation of paper composite porcelain in a fired state by XRD and SEM. *Journal of the European Ceramic Society*, *24*(15-16), 3823-3831.

11. Thakral, S., Terban, M. W., Thakral, N. K., & Suryanarayanan, R. (2016). Recent advances in the characterization of amorphous pharmaceuticals by X-ray diffractometry. *Advanced Drug Delivery Reviews*, *100*, 183-193.

12. Lavina, B., Dera, P., & Downs, R. T. (2014). Modern X-ray diffraction methods in mineralogy and geosciences. *Reviews in Mineralogy and Geochemistry*, *78*(1), 1-31.

13. Ameh, E. S. (2019). A review of basic crystallography and x-ray diffraction applications. *The international journal of advanced manufacturing technology*, *105*(7), 3289-3302.

14. Lee, S. L., Windover, D., Doxbeck, M., Nielsen, M., Kumar, A., & Lu, T. M. (2000). Image plate X-ray diffraction and X-ray reflectivity characterization of protective coatings and thin films. *Thin Solid Films*, *377*, 447-454.

15. Grunwaldt, J. D., & Clausen, B. S. (2002). Combining XRD and EXAFS with on-line catalytic studies for in situ characterization of catalysts. *Topics in Catalysis*, *18*, 37-43.

16. Giumlia-Mair, A., Albertson, C., Boschian, G., Giachi, G., Iacomussi, P., Pallecchi, P., ... & Stock, S. (2010). Surface characterisation techniques in the study and

conservation of art and archaeological artefacts: a review. *Materials Technology*, *25*(5), 245-261.

17. Sharma, R., Bisen, D. P., Shukla, U., & Sharma, B. G. (2012). X-ray diffraction: a powerful method of characterizing nanomaterials. *Recent Res Sci Technol*, *4*(8), 77-79.

18. Louis, B., & Kumar, S. (2007). X-ray diffraction studies on catalysts: Recent developments in characterisation of catalysts. Advances in X-ray Analysis, 50, 1-10.

19. Dejoie, C., & Pagès-Camagna, S. (2013). X-ray diffraction and X-ray fluorescence methods in art and archaeology. X-ray Spectrometry, 42(4), 250-256.

20. Smith, E., & Dent, G. (2005). **Modern Raman Spectroscopy: A Practical Approach**. John Wiley & Sons.

21. Ferraro, J. R., & Basile, L. J. (1989). **Introduction to Raman Spectroscopy**. CRC Press.

22. Hollas, J. M. (2004). **Modern Spectroscopy**. John Wiley & Sons. (Chapter 9)

23. https://chemistry.stackexchange.com/questions/35747/why-does-stokes-raman-not-relax-to-the-ground-state-while-anti-stokes-does

24. Chalmers, J.M. and Griffiths, P.R. (2011). Handbook of Vibrational Spectroscopy. Wiley

25. Ferraro, J.R., Nakamoto, K., and Brown, C.W. (2003). Introductory Raman Spectroscopy. Academic Press

26. Edwards, H.G.M. and Chalmers, J.M. (2005). Raman Spectroscopy in Archaeology and Art History. Royal Society of Chemistry

27. Matousek, P. and Stone, N. (2009). Development of Deep Raman Spectroscopy for Noninvasive, In Vivo Diagnostic Applications. Chemical Society Reviews

28. Overmann, J. and Garcia-Pichel, F. (2012). The Phototrophic Way of Life. Springer

29. https://chem.libretexts.org/Bookshelves/Analytical_Chemistry/Physical_Methods_in_Chemistry_and_Nano_Science_%28Barron%29/04%3A_Chemical_Speciation/4.03%3A_Raman_Spectroscopy

30. Vašková, H. (2011). A powerful tool for material identification: Raman spectroscopy. *Int. J. Math. Model. Methods Appl. Sci*, *5*(7), 1205-1212.

31. Chowdhry, B. Z., Jabeen, S., & Alexander, B. (2009). Raman spectroscopy in pharmaceutical analysis. *European Pharmaceutical Review*, *5*, 34-39.

32. Neuville, D. R., De Ligny, D., & Henderson, G. S. (2014). Advances in Raman spectroscopy applied to earth and material sciences. *Reviews in mineralogy and geochemistry*, *78*(1), 509-541.

33. Edwards, H. G., Hutchinson, I. B., Ingley, R., Parnell, J., Vítek, P., & Jehlička, J. (2013). Raman spectroscopic analysis of geological and biogeological specimens of relevance to the ExoMars mission. *Astrobiology*, *13*(6), 543-549.

34. Otto, C., De Grauw, C. J., Duindam, J. J., Sijtsema, N. M., & Greve, J. (1997). Applications of micro-Raman imaging in biomedical research. *Journal of Raman spectroscopy*, *28*(2-3), 143-150.

35. Ong, T. T., Blanch, E. W., & Jones, O. A. (2020). Surface Enhanced Raman Spectroscopy in environmental analysis, monitoring and assessment. *Science of The Total Environment*, *720*, 137601.

36. Kuptsov, A. H. (1994). Applications of Fourier transform Raman spectroscopy in forensic science. *Journal of Forensic Sciences*, *39*(2), 305-318.

37. Bitossi, G., Giorgi, R., Mauro, M., Salvadori, B., & Dei, L. (2005). Spectroscopic techniques in cultural heritage conservation: a survey. *Applied Spectroscopy Reviews*, *40*(3), 187-228.

38. Hollas, J.M. (2004). *Modern Spectroscopy*. John Wiley & Sons.

39. Smith, B.C. (1996). *Infrared Spectral Interpretation: A Systematic Approach*. CRC Press.

40. Pavia, D.L., et al. (2014). *Introduction to Spectroscopy*. Cengage Learning.

41. Christian, G.D. (2003). *Analytical Chemistry*. John Wiley & Sons.

42. Haiss, W., Thanh, N. T., Aveyard, J., & Fernig, D. G. (2007). Determination of size and concentration of gold nanoparticles from UV− Vis spectra. *Analytical chemistry*, *79*(11), 4215-4221.

43. Alam, T. (2015). Estimation of chemical oxygen demand in wastewater using UV-VIS spectroscopy.

44. Antonov, L. (2013). Absorption UV–Vis spectroscopy and chemometrics: from qualitative conclusions to quantitative analysis. *Tautomerism: methods and theories*, 25-47.

45. Pyun, E., Mathisen, R. J., & Sung, C. S. P. (1989). Kinetics and mechanisms of thermal imidization of a polyamic acid studied by ultraviolet-visible spectroscopy. *Macromolecules*, *22*(3), 1174-1183.

46. Giridhar, V., & Mahavidyalaya, A. (2015). Quality control of herbal drugs through UV-Vis spectrophotometric analysis. *International Journal of Ayurvedic Medicine*, *6*(1), 102-109.

47. Mesquita, D. P., Quintelas, C., Amaral, A. L., & Ferreira, E. C. (2017). Monitoring biological wastewater treatment processes: recent advances in spectroscopy applications. *Reviews in Environmental Science and Bio/Technology*, *16*, 395-424.

48. Kaur, G., Singh, H., & Singh, J. (2021). UV-vis spectrophotometry for environmental and industrial analysis. In *Green Sustainable Process for Chemical and Environmental Engineering and Science* (pp. 49-68). Elsevier.

49. Aceto, M., Agostino, A., Fenoglio, G., Idone, A., Gulmini, M., Picollo, M., ... & Delaney, J. K. (2014). Characterisation of colourants on illuminated manuscripts by

portable fibre optic UV-visible-NIR reflectance spectrophotometry. *Analytical methods*, *6*(5), 1488-1500.

50. Nakamoto, K. (2008). *Infrared and Raman Spectra of Inorganic and Coordination Compounds*. Wiley.

51. Banwell, C.N. and McCash, E.M. (1994). *Fundamentals of Molecular Spectroscopy*. McGraw-Hill.

52. Liptak, M.D., et al. (2009). "UV-Vis Spectroscopy Basics." *Chemistry LibreTexts*. Retrieved from https://chem.libretexts.org

53. Moore, D.S. (2005). "Instrumentation in UV-Vis Spectroscopy." *Review of Scientific Instruments*. DOI: 10.1063/1.1890851.

54. Baker, M.J., et al. (2016). "Advances in Spectroscopy for Biomedical Applications." *Analytical Chemistry*. DOI: 10.1021/acs.analchem.5b04661.

55. Bell, S.E.J. and Burns, D.T. (2013). *Introduction to Spectroscopy*. Springer.

56. Mohr, P.J., et al. (2014). "Data Analysis in Spectroscopy." *Journal of Analytical Chemistry*. DOI: 10.1021/j100512a019.

57. Nielsen, C.J., et al. (2003). *Spectral Data for Quantitative Analysis*. Springer.

58. Price, W. (2012). "The Role of Baseline Correction in Spectroscopy." *Spectroscopy Reviews*. DOI: 10.1080/05704928.2011.620247.

59. https://onlinelibrary.wiley.com/doi/10.1002/cjce.23344

60. March, J. (1985). *Advanced Organic Chemistry: Reactions, Mechanisms, and Structure*. Wiley.

61. Engel, T. and Reid, P. (2012). *Physical Chemistry*. Pearson.

62. Connors, K.A. (1990). *Chemical Kinetics: The Study of Reaction Rates in Solution*. Wiley.

63. Cammann, K. (1998). *Instrumental Analytical Chemistry*. Springer

64. Haines, P. J., & Chemistry, R. S. O. (2002, January 1). Principles of Thermal Analysis and Calorimetry. Royal Society of Chemistry

65. Gabbott, P. (2008, April 30). Principles and Applications of Thermal Analysis. John Wiley & Sons.

66. Jeske, H., Schirp, A., & Cornelius, F. (2012, September). Development of a thermogravimetric analysis (TGA) method for quantitative analysis of wood flour and polypropylene in wood plastic composites (WPC). Thermochimica Acta, 543, 165–171. https://doi.org/10.1016/j.tca.2012.05.016

67. Slezak, R., Krzystek, L., & Ledakowicz, S. (2018, August). Thermogravimetric analysis coupled with mass spectrometry of spent mushroom substrate and its fractions. Journal of Analytical and Applied Pyrolysis, 133, 1–8. https://doi.org/10.1016/j.jaap.2018.05.010

68. Yao, F., Wu, Q., Lei, Y., Guo, W., & Xu, Y. (2008). Thermal decomposition kinetics of natural fibers: activation energy with dynamic thermogravimetric analysis. *Polymer Degradation and Stability*, *93*(1), 90-98.

69. Doyle, C. D. (1961). Estimating thermal stability of experimental polymers by empirical thermogravimetric analysis. *Analytical Chemistry*, *33*(1), 77-79.

70. Buenhombre, J. L. M. (2005). Thermal analysis of inorganic materials. *Repositorio da Universidade da Coruña*, *1*.

71. Groenewoud, W. M. (Ed.). (2001). *Characterisation of polymers by thermal analysis*. Elsevier.

72. Giron, D. (2002). Applications of thermal analysis and coupled techniques in pharmaceutical industry. *Journal of thermal analysis and Calorimetry*, *68*(2), 335-357.

73. Šimkovic, I., & Csomorová, K. (2006). Thermogravimetric analysis of agricultural residues: oxygen effect and environmental impact. *Journal of applied polymer science*, *100*(2), 1318-1322.

74. Mansfield, E., Kar, A., & Hooker, S. A. (2010). Applications of TGA in quality control of SWCNTs. *Analytical and bioanalytical chemistry*, *396*, 1071-1077.

75. Saldarriaga, J. F., Aguado, R., Pablos, A., Amutio, M., Olazar, M., & Bilbao, J. (2015). Fast characterization of biomass fuels by thermogravimetric analysis (TGA). *Fuel*, *140*, 744-751.

76. Hussein, A. K., Elbeih, A., & Zeman, S. (2017). Thermal decomposition kinetics and explosive properties of a mixture based on cis-1, 3, 4, 6-tetranitrooctahydroimidazo-[4, 5-d] imidazole and 3-nitro-1, 2, 4-triazol-5-one (BCHMX/NTO). *Thermochimica Acta*, *655*, 292-301.

77. Kristl, M., Muršec, M., Šuštar, V., & Kristl, J. (2016). Application of thermogravimetric analysis for the evaluation of organic and inorganic carbon contents in agricultural soils. *Journal of Thermal Analysis and Calorimetry*, *123*, 2139-2147.

78. Sinha, P., Datar, A., Jeong, C., Deng, X., Chung, Y. G., & Lin, L. C. (2019). Surface area determination of porous materials using the Brunauer–Emmett–Teller (BET) method: limitations and improvements. The Journal of Physical Chemistry C, 123(33), 20195-20209.

79. Sing, K. S. (1998). Adsorption methods for the characterisation of porous materials. Advances in colloid and interface science, 76, 3-11.

80. Jayakantha, D. R., Gunawardhana, N., Bandara, H. M. N., Comini, E., Gunawardana, N. M., & Karunarathne, S. M. M. L. (2021). Low cost automated instrumentation for the measurement of the specific surface area of powders by the Brunauer–Emmett–Teller (BET) method. Instrumentation Science & Technology, 50(1), 47-56.

81. Naderi, M. (2015). Surface area: brunauer–emmett–teller (BET). In Progress in filtration and separation (pp. 585-608). Academic Press.

82. Mohan, V. B., Jayaraman, K., & Bhattacharyya, D. (2020). Brunauer–Emmett–Teller (BET) specific surface area analysis of different graphene materials: a comparison to their structural regularity and electrical properties. Solid State Communications, 320, 114004.

83. Zhou, W., Apkarian, R., Wang, Z. L., & Joy, D. (2007). Fundamentals of scanning electron microscopy (SEM). Scanning microscopy for nanotechnology: techniques and applications, 1-40.

84. Vernon-Parry, K. D. (2000). Scanning electron microscopy: an introduction. III-Vs review, 13(4), 40-44.

85. https://www.nanoscience.com/techniques/scanning-electron-microscopy/

86. Kannan, M. (2018). Scanning electron microscopy: Principle, components and applications. A textbook on fundamentals and applications of nanotechnology, 81-92.

87. Oatley, C. W. (1981). Detectors for the scanning electron microscope. Journal of Physics E: Scientific Instruments, 14(8), 971.

88. Mohammed, A., & Abdullah, A. (2018, November). Scanning electron microscopy (SEM): A review. In Proceedings of the 2018 International Conference on Hydraulics and Pneumatics—HERVEX, Băile Govora, Romania (Vol. 2018, pp. 7-9).

89. Ul-Hamid, A. (2018). A beginners' guide to scanning electron microscopy (Vol. 1, p. 402). Cham: Springer International Publishing.

90. Cazaux, J. (2005). Recent developments and new strategies in scanning electron microscopy. Journal of microscopy, 217(1), 16-35.

91. Smith, K. C. A., & Oatley, C. W. (1955). The scanning electron microscope and its fields of application. British Journal of Applied Physics, 6(11), 391.

92. Babick, F. (2020). Dynamic light scattering (DLS). In Characterisation of nanoparticles (pp. 137-172). Elsevier.

93. Sandhu, R., Singh, N., Dhankhar, J., Kama, G., & Sharma, R. (2018). Dynamic light scattering (DLS) technique, principle, theoretical considerations and applications. Nanotechnol. Biochem. Tech. Assess. Qual. Saf. Milk Milk Prod, 135-137.

94. Misono, T. (2019). Dynamic light scattering (DLS). Measurement techniques and practices of colloid and interface phenomena, 65-69.

95. Lorber, B., Fischer, F., Bailly, M., Roy, H., & Kern, D. (2012). Protein analysis by dynamic light scattering: Methods and techniques for students. Biochemistry and molecular biology education, 40(6), 372-382.

96. https://lsinstruments.ch/en/theory/dynamic-light-scattering-dls/3d-cross-correlation

97. Den Engelsman, J., Garidel, P., Smulders, R., Koll, H., Smith, B., Bassarab, S., ... & Jiskoot, W. (2011). Strategies for the assessment of protein aggregates in pharmaceutical biotech product development. *Pharmaceutical research*, *28*, 920-933.

98. Shukla, V., Niveria, K., Shashidhar, P., & Verma, A. K. (2023). Dynamic light scattering (DLS) particle size analysis for biomedical nanotechnology. In *Analytical Techniques for Biomedical Nanotechnology* (pp. 16-1). Bristol, UK: IOP Publishing.

99. Baalousha, M., & Lead, J. R. (2012). Rationalizing nanomaterial sizes measured by atomic force microscopy, flow field-flow fractionation, and dynamic light scattering: sample preparation, polydispersity, and particle structure. *Environmental science & technology*, *46*(11), 6134-6142.

100. Domingos, R. F., Baalousha, M. A., Ju-Nam, Y., Reid, M. M., Tufenkji, N., Lead, J. R., ... & Wilkinson, K. J. (2009). Characterizing manufactured nanoparticles in the environment: multimethod determination of particle sizes. *Environmental science & technology*, *43*(19), 7277-7284.

101. Mattarozzi, M., Suman, M., Cascio, C., Calestani, D., Weigel, S., Undas, A., & Peters, R. (2017). Analytical approaches for the characterization and quantification of nanoparticles in food and beverages. *Analytical and bioanalytical chemistry*, *409*, 63-80.

102. Dutta, A. (2017). Fourier transform infrared spectroscopy. Spectroscopic methods for nanomaterials characterisation, 73-93.

103. Smith, B. C. (2011). Fundamentals of Fourier transform infrared spectroscopy. CRC press.

104. Schardt, M., Murr, P. J., Rauscher, M. S., Tremmel, A. J., Wiesent, B. R., & Koch, A. W. (2016). Static Fourier transform infrared spectrometer. Optics Express, 24(7), 7767-7776.

105. Notingher, I., Jones, J. R., Verrier, S., Bisson, I., Embanga, P., Edwards, P., ... & Hench, L. L. (2003). Application of FTIR and Raman spectroscopy to characterisation of bioactive materials and living cells. *Journal of Spectroscopy*, *17*(2-3), 275-288.

106. He, X., Liu, X., Nie, B., & Song, D. (2017). FTIR and Raman spectroscopy characterization of functional groups in various rank coals. *Fuel*, *206*, 555-563.

107. Simonescu, C. M. (2012). Application of FTIR spectroscopy in environmental studies. *Advanced aspects of spectroscopy*, *29*(1), 77-86.

108. Movasaghi, Z., Rehman, S., & ur Rehman, D. I. (2008). Fourier transform infrared (FTIR) spectroscopy of biological tissues. *Applied Spectroscopy Reviews*, *43*(2), 134-179.

109. Weber, A., Hoplight, B., Ogilvie, R., Muro, C., Khandasammy, S. R., Pérez-Almodóvar, L., ... & Lednev, I. K. (2023). Innovative vibrational spectroscopy research for forensic application. *Analytical Chemistry*, *95*(1), 167-205.

110. https://www.torontomu.ca/analytical-centre/instrumentation/spectroscopy/

111. Qiu, H., Lv, L., Pan, B. C., Zhang, Q. J., Zhang, W. M., & Zhang, Q. X. (2009). Critical review in adsorption kinetic models. *Journal of Zhejiang University-Science A*, *10*(5), 716-724.

112. Musah, M., Azeh, Y., Mathew, J. T., Umar, M. T., Abdulhamid, Z., & Muhammad, A. I. (2022). Adsorption kinetics and isotherm models: a review. *CaJoST*, *4*(1), 20-26.

113. Revellame, E. D., Fortela, D. L., Sharp, W., Hernandez, R., & Zappi, M. E. (2020). Adsorption kinetic modeling using pseudo-first order and pseudo-second order rate laws: A review. *Cleaner Engineering and Technology*, *1*, 100032.

114. Moussout, H., Ahlafi, H., Aazza, M., & Maghat, H. (2018). Critical of linear and nonlinear equations of pseudo-first order and pseudo-second order kinetic models. *Karbala International Journal of Modern Science*, *4*(2), 244-254.

115. Aharoni, C., & Tompkins, F. C. (1970). Kinetics of adsorption and desorption and the Elovich equation. In *Advances in catalysis* (Vol. 21, pp. 1-49). Academic Press.

CHAPTER 3

GRAPHENE OXIDE MODIFICATION USING NaOH TREATMENT

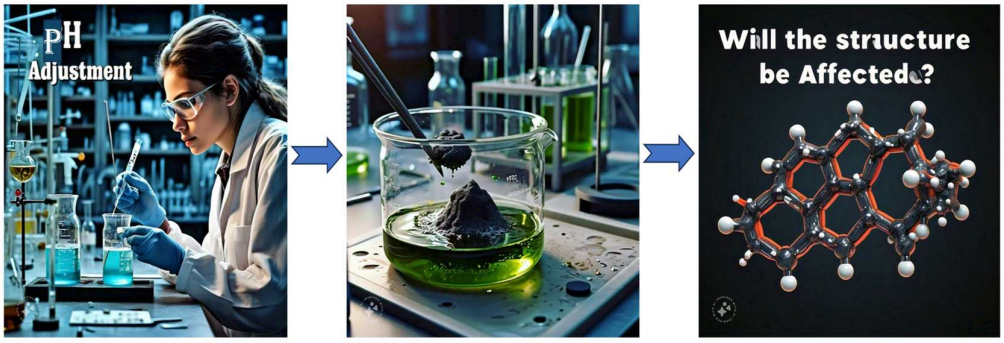

Sodium Hydroxide (NaOH) is commonly used in the synthesis of rGO and its composites for tuning pH. However, the impact of NaOH on the structural integrity and properties of graphene oxide (GO) remains underexplored. If adverse effects occur, they could significantly alter GO's functionality. We aim to investigate these potential effects, ensuring that unnoticed changes are thoroughly understood.

Scope of the chapter

- *Investigate the influence of varying NaOH concentrations on the reduction of graphene oxide (GO) through systematic experimentation.*
- *Determine the minimum NaOH amount required to effectively reduce GO, establishing a threshold value.*
- *Assess the significance of pH in the reduction process of GO.*

Abstract

Prudent knowledge of the factors in the chemical synthesis of reduced graphene oxide (rGO) can provide a considerable impetus for the precise repeatability needed for the technological adoption of graphene nanocomposites. Sodium Hydroxide (NaOH) is a common ingredient in the synthesis of rGO. This chapter presents a systematic study of the effect of NaOH concentration on graphene oxide (GO). The threshold value, where NaOH starts acting as a reducing agent, is proposed in the work. The finding was corroborated based on absorbance maxima obtained from the UV–visible spectrum (π - π^* transitions) and the peak intensity ratio of Raman spectra. The results indicate that NaOH has a remarkable role in tuning the functionality of graphene oxide. Furthermore, it is demonstrated that pH is not a critical factor in GO reduction. All these findings are vital to the NaOH-based pH tuning and industrial scaling of graphene-based nanocomposite synthesis.

3.1 Introduction

Reduced graphene oxide (rGO) is a form of graphene with few oxygen-containing groups. The fewer the oxygen-containing groups, the more similar the rGO to the graphene. rGO serves as a potential candidate for numerous technological applications - such as chemical sensors [1], innovative electrodes [2], supercapacitors [3], photovoltaics [4], biomedical components [5], water remediation [6], etc. At times, rGO is superior to pristine graphene in applications. For example, Sviridova et al. [7] reported that rGO-modified organic molecules could store more energy than their graphene counterpart. Yi et al. found that the NO_2 sensing capabilities of rGO are much better than graphene [8]. Recently, there has been a report that the rGO could also tune the optical properties of perovskites. [9] rGO-based gas sensor achieved a sensitivity of $27\pm2\times10^{-6}$ per part per billion (ppb), which is much higher than that of graphene [10]

The chemical synthesis of rGO, other than being a conventional method within the Top-Down techniques, is a widely explored technique – especially for applications requiring large quantities of cost-effective rGO. Here, graphite is oxidised to produce GO using methods such as Hummer's [11], Brodie's [12], Stauden Maier's [13], and others. There are various routes for the reduction of GO to synthesise rGO and graphene. Within the chemical approach, Hydrazine hydrate [14], borohydride [15] and Sodium hydroxide [16] are the widely used reducing agents for GO. However, the former two reducing agents generate deformations in the carbon backbone of GO [17] and also release toxic gases like borane. As per reports about the chemical synthesis of rGO and rGO-nanocomposites, NaOH is used to tune the pH of the media and make the reaction environment suitable for forming nanocomposites.

The chemical route is promising for industrially scalable synthesis of rGO and graphene. We frequently notice discrepancies in characteristic properties reported on chemically synthesised rGO within the available literature. For example, the XRD 2θ value of rGO prepared using $NaBH_4$ as a reducing agent shows variation from 21 to 25 degrees, and the peak position of UV-visible spectra of these rGO varies from 233 to 268 nm. [18], [19], [20]. The Raman peaks of hydrazine-reduced samples ranged

from 1331 to 1352cm^{-1} for the D-band and 1585 to 1592 cm^{-1} for the G-band. [21], [14]. Therefore, it is essential to understand the effect of all the chemical ingredients for the precise repeatability of the characteristics valid for technological applications. There have been some noteworthy attempts to study the impact of NaOH on rGO synthesis– for example, the theoretical investigations by Chen et al. 2014 [22] need special mention.

In this chapter, we systematically explore the effect of NaOH on the synthesis of rGO from GO. Our findings give an insight into the molecular architecture of GO when treated with NaOH, including the intermediate stages in the journey. We have also formulated a mass threshold ratio of NaOH required to acquire the GO reduction. The obtained results are corroborated with micro-Raman and UV-visible spectroscopic analysis.

3.2 Experimental details

Synthesis

Graphite oxide was prepared using the Hummers method [9], as detailed in section 2.1. The resultant product, graphite oxide, was exfoliated to graphene oxide (GO) using an ultrasonic bath.

8g of NaOH pellets were dissolved in 100 ml of distilled water to prepare a stock solution of 2M sodium hydroxide. The stock solution was introduced to GO in steps of 0.05ml, and the resultant samples were named GNX - where X = 1 to 8 for 0.05 ml to 0.4 ml of NaOH. Samples were kept in an ultrasonic bath for 30 minutes to ensure uniform dispersion.

3.3 Results and Discussion

Figure 3.1 shows the XRD plot of the GO sample coated (drop-casting technique) onto a glass substrate. The prepared GO is a single phase. It's worth noting that a minor peak around 20^{o} can be attributed to the glass substrate. The obtained 2θ value (10.776^{o}) agrees with the reported values [23] [14] [24]. The interlayer spacing calculated using Bragg's law is found to be 8.2Å.

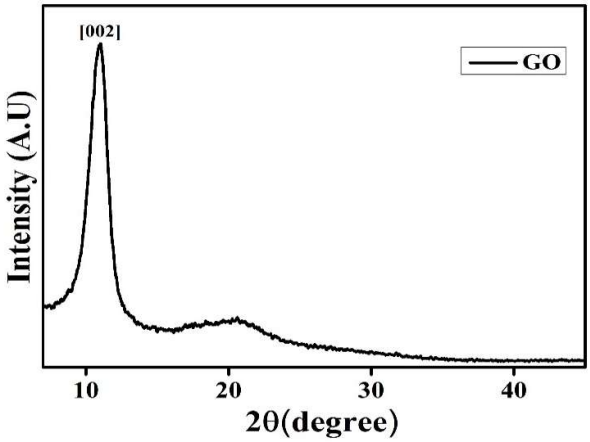

Figure 3.1*: XRD pattern of GO obtained via Hummer's method*

Figure 3.2 shows the UV-visible spectra of all the as-prepared samples. The peaks in the spectra were separated by curve fitting with the Gaussian model (Figure 3.3). The results propose that the UV-visible spectra of all our GO samples contain (i) a major peak located near 230nm (designated as P_{230}), which is assigned to the π - π* transition in the C=C bonding [14] and (ii) a shoulder peak near 300nm (P_{300}), attributed to n - π^* transition of the carbonyl groups (C=O) [25].

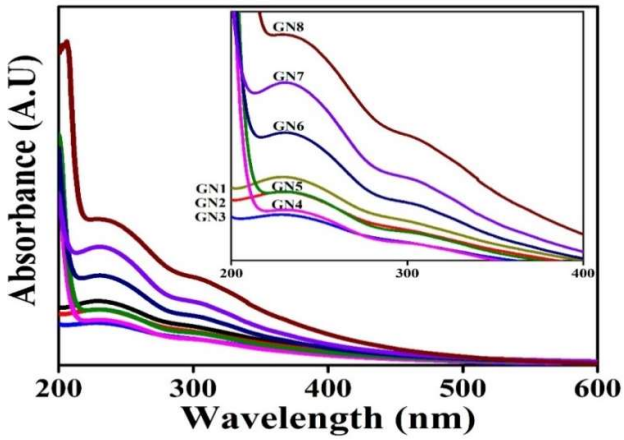

Figure 3.2: *UV plot of NaOH-treated samples. As told in the text, samples were named GNX - where X = 1 to 8 for 0.05 ml to 0.4 ml of NaOH. The observed peak at ~ 200cm^{-1} - for samples beyond GN4 - suggests the presence of NaOH in the samples. The NaOH peak intensity is maximum for GN8. The inset shows the zoomed image of the UV plots in the wavelength range of 200 – 400 cm^{-1}. Peak positions are listed in Table 3.1*

Table 3.1 *Peak shift in UV-visible spectra with respect to NaOH addition*

Amount of NaOH (ml)	Peak Position of P_{230}(nm)
0	226.79
0.05	227.61
0.1	230.00
0.15	232.92
0.2	234.95
0.25	234.95
0.3	236.08
0.35	237.24

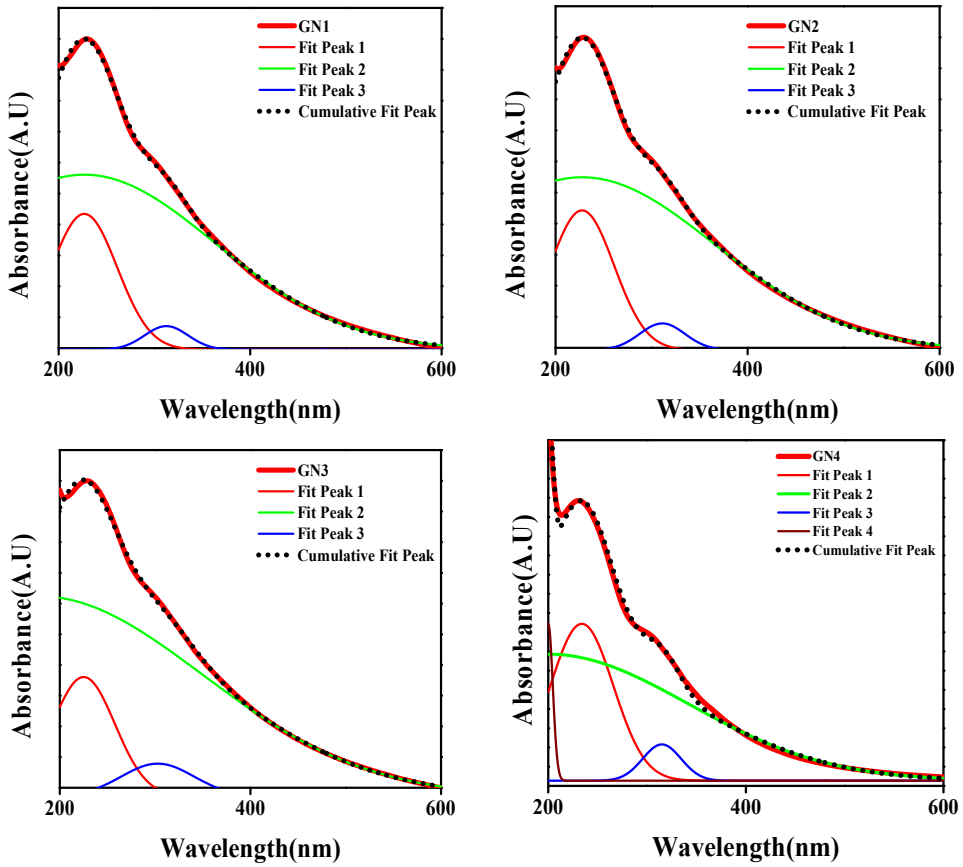

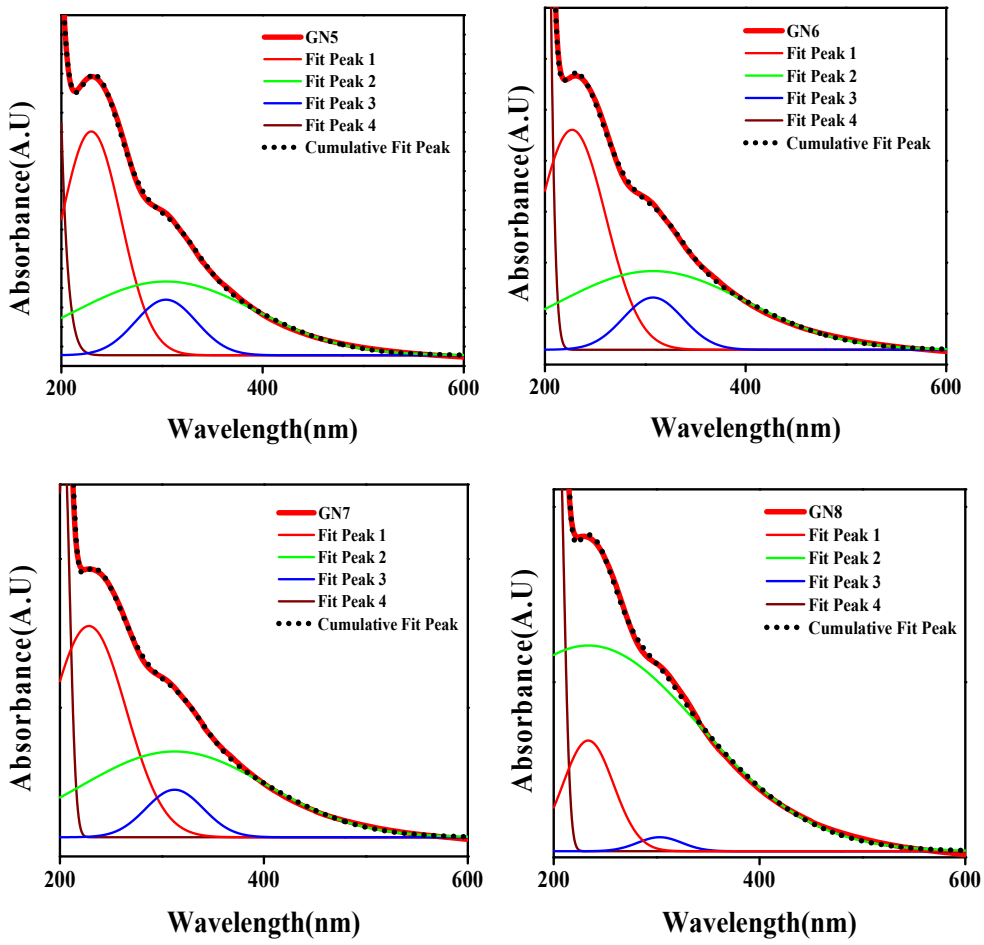

Figure 3.3: *Fitted curves for UV-visible spectra for NaOH-treated GO samples. Peak 1 arises from the π-π* transitions of the C=C bond. The IR region influences peak 2, while peak 3 corresponds to the n-π* transition of carbonyl groups (C=O), and Peak 4 is due to the presence of NaOH in the samples. Our focus is on Peak 1.*

UV-visible spectra show a bathochromic shift for peak position corresponding to π - π* transition (wavelength corresponding to maximum peak intensity is designated as λ_{max}). Its dependence on NaOH concentration is shown in Figure 3.4.

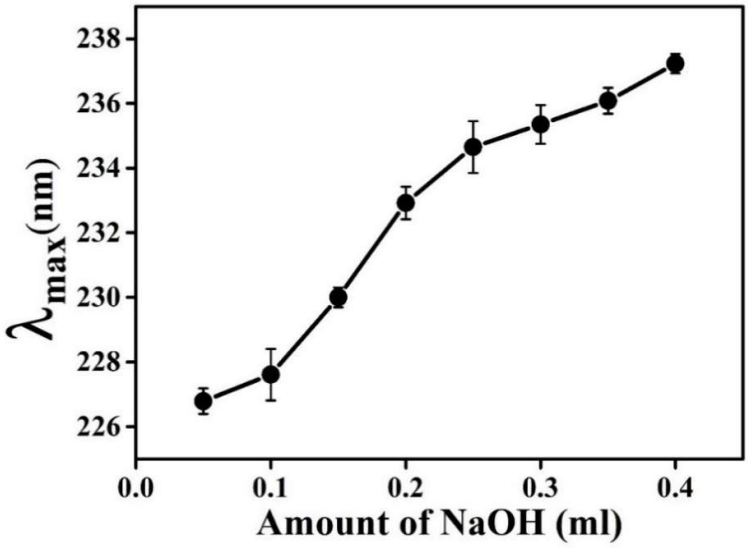

Figure 3.4: *The bathochromic shift in peak position corresponding to maximum absorbance for Peak 1.*

It can be inferred from Figure 3.4 that the λ_{max} shows a regular increase as the NaOH amount increases. Generally, in the literature, the redshift in the peak position of UV-visible spectra is linked to the GO reduction. [14] [26] [27] [28].

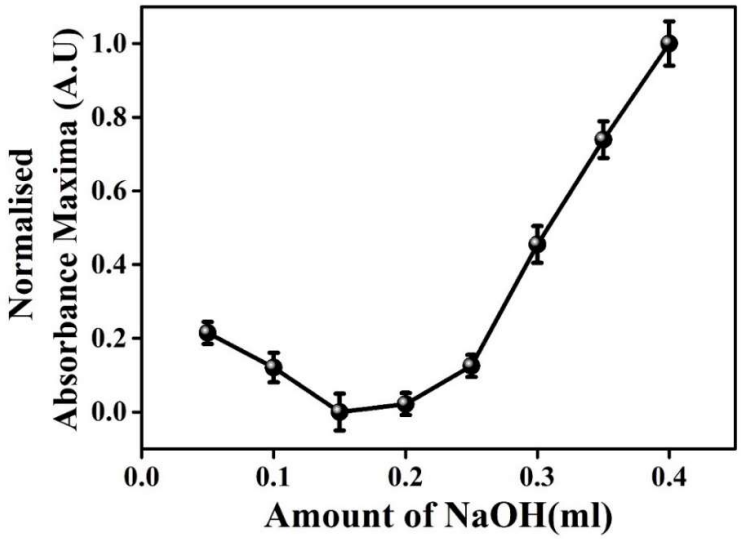

Figure 3.5: *Variation of absorbance maxima of P_{230} with NaOH dose. The lines connecting the points are just drawn as guidance to the eye.*

Absorbance maxima is another reduction parameter (detailed in section 3.2), and it initially decreases up to GN3, and increases thereafter. According to this plot, the effective reduction of graphene oxide happens only with GN6. These two plots are contradictory in the initial few drops of NaOH. Further investigations are done to understand better the reduction of GO samples on addition of NaOH.

3.3.1 Raman Spectra

Figure 3.6 shows the Raman spectra of the samples. The peak near 1580cm^{-1} is commonly known as G Band, and it originates from C-C bond stretching, which is common to all sp^2 carbon systems and can be used to investigate any modifications in graphene structure. [29]. Another essential band in the Raman spectra of GO located at ~1350 cm^{-1}, known as the D band, is ascribed to disorders in GO sheets. The ratio between the D band's intensity and the G band's intensity (ID/IG), as depicted in Table 3.2 and Figure 3.6, indicates the measure of the disorder in the graphene sheets. [30]. The 2D band located near 2700 cm^{-1} originates from a two-phonon double resonance process.

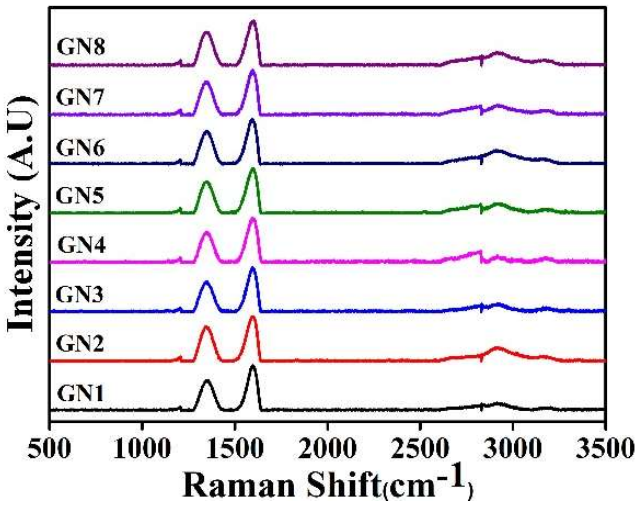

***Figure 3.6**: Raman spectra of GN1 to GN8*

Table 3.2: *Table showing ID/IG ratio of Raman spectra.*

Sl.No	Sample Name	Amount of NaOH (ml)	ID/IG	Error
1	GN1	0.05	0.688	0.002
2	GN2	0.1	0.692	0.016
3	GN3	0.15	0.681	0.006
4	GN4	0.2	0.685	0.012
5	GN5	0.25	0.715	3.3E-4
6	GN6	0.3	0.743	0.010
7	GN7	0.35	0.742	0.020
8	GN8	0.4	0.7560	0.007

It is generally found that vigorous chemical reduction can destroy the hexagonal plane of carbon atoms. Our samples exhibit D, G, and 2D bands, implying that NaOH treatment has not significantly modified the parent material or carbon backbone. [29].

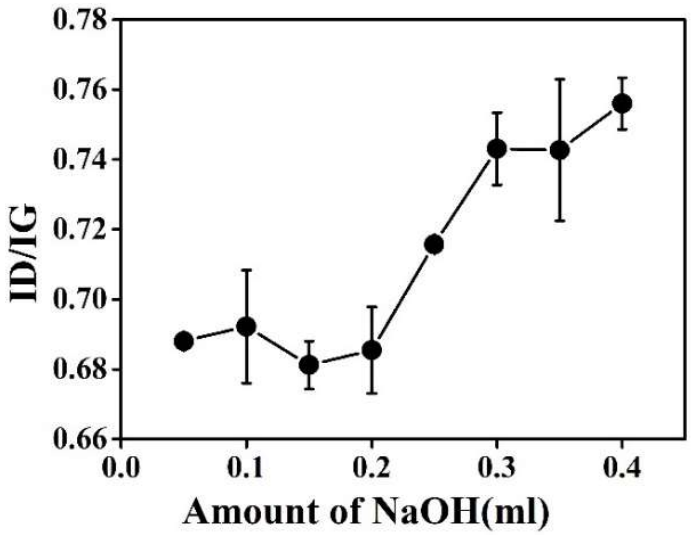

Figure 3.7: *ID/IG ratio with the amount of NaOH*

In conventional systems with carbon in sp^2 hybridisation, such as graphene or graphite, a lower ID/IG, suggests a lower defect concentration. Defects like vacancies, edge effect, development of wrinkles, disruption in the sp^2 bonding caused by heptagon and pentagon rings and the existence of functional groups are the different sources of origin of the D band [31]. In the case of GO, which is not purely an sp^2 system, it also has (i) a significant amount of sp^3 carbon – in proportion to the functional groups and (ii) other structural defects. Thus, the GO can be assumed to have a higher value of ID/IG compared to rGO. However, in situations where 2D peaks are discernible – indicating a low amount of structural defects – the reduction of GO to rGO can increase the ID/IG ratio. The increase derives from the disruption of the system due to the restoration of the pi-conjugated system and deformations created by thermal, chemical or any other means. [30-33] [39-47]. Even though reduction recovers the graphitic backbone, it reduces the lateral size of the graphene sheet, contributing to the measure of defects. [19] [38] Here, in our samples, the ID/IG plot shows an *S*-shaped behaviour with a rising phase from GN4, culminating in saturation beyond the GN6 sample (Figure 3.7, Table 3.2). The saturation beyond GN6 is the outcome of structural defects and the defects due to the removal of functional groups.

3.3.2 Absorbance maxima in UV-visible spectra

Figure 3.4 shows the variation of absorbance maxima of the GO peak, P_{230}, with the amount of NaOH. The absorbance maximum of P_{230} directly depends on i) the intensity of π - π^* transitions in GO and ii) the number of chromophore units such as C=C, C=O, and C–O bonds. [34]. In the initial introduction of NaOH, the mechanism involves forming OH groups that replace the epoxy groups. This substitution reduces the pi-pi* transition, consequently leading to a decrease in absorbance up to GN3. Further addition of NaOH reduces GO by detaching oxygen functional groups from the GO surface. As demonstrated in Figure 3.8, GO reduction leads to the formation of an electron cloud and, hence, an enhancement in the π - π^* transition. The enhancement in π - π^* transition results in the deviation at the GN4 sample.

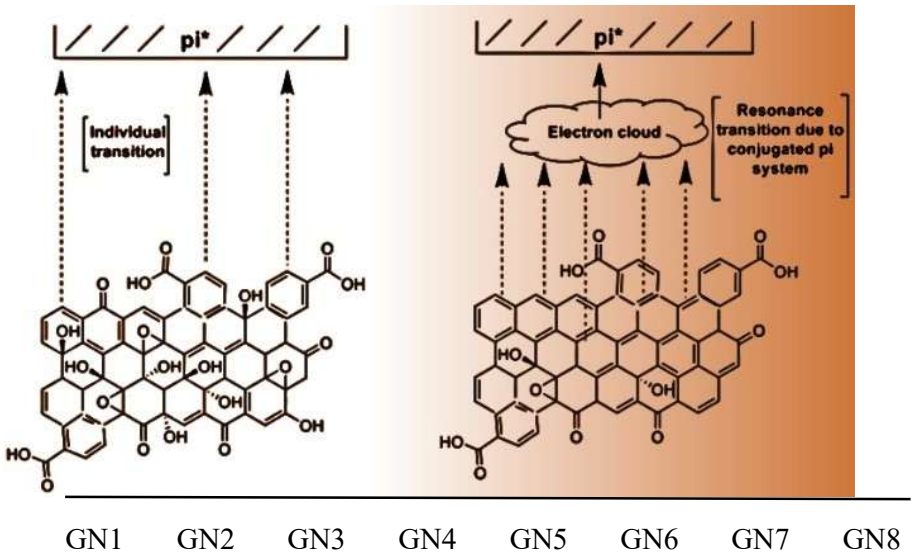

Figure 3.8: *The UV-visible absorbance directly depends on the intensity of π - π* transitions and chromophore units in GO. An electron cloud is formed when GO is slightly reduced, keeping the pi-conjugated system intact. The electron cloud enhances π - π* transitions and thereby increases absorbance (P_{230}).*

3.3.3 Concentration-dependent effect of NaOH

As noted in Figures 3.1 to 3.4, our samples shed insight into the varying role of NaOH at different concentrations.

GO contains many polar oxygen-containing groups, epoxy and hydroxyls being some of them. According to [22], an external field or presence of a strong cation (like the Na^+ generated in NaOH solution – as in our experiment) helps in breaking the C-O bonds by enhancing the polarity and weakening the bond strength, which initially leads to ring-opening of epoxy groups as depicted in reaction ①. According to [35], the binding energy of epoxy and hydroxyl groups is similar. So, epoxy groups are energetically suited to be replaced by hydroxyl groups. The Na^+ breaks an epoxy group in GO, facilitating the -OH groups (from the medium) bonding into the nascent carbon valency arising from the fractured epoxy groups. The new bonding process works until most epoxy moiety is replaced by hydroxyl, creating a graphene hydroxide structure. The formation of Na_2O in reaction ① results in the absence of Na^+ in the solution. The Na^+ could have separated -OH from the basal carbon.

$$GO + 2NaOH \rightarrow GO-2OH + Na_2O$$

Adding more NaOH drops will lead to GO reduction- as depicted in reaction ②. Here, the NaOH can be identified to adorn the role of a catalyst for forming rGO. This idea agrees with the general equation for GO reduction with NaOH proposed by Chen et al. 2014 [22] through their density functional theory-based theoretical simulation.

$$GO-2OH + 2NaOH \rightarrow GO-2O^- + 2Na^+ + 2H_2O$$

$$GO-2O^- + 2Na^+ + H_2O \rightarrow rGO + 2NaOH$$

Further addition of NaOH (beyond that in reaction ②) can initiate further reduction. Simultaneously, the amount of sodium metallic oxides in the solutions will also escalate. This leads to effective basicity in the GO-NaOH solution. The basic solution creates a hindrance to the dispersion of GO into the solution, which results in agglomeration.

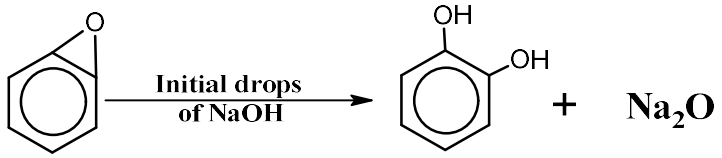

1

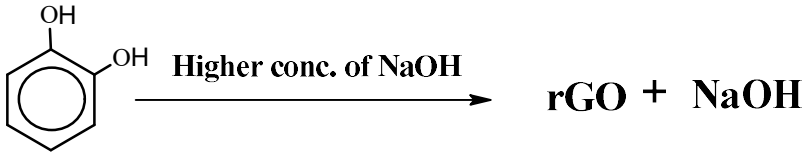

2

(In equations 1 and 2 a single hexagonal ring from graphene oxide is considered for illustration purpose)

Therefore, based on the data in Figures 3.1 to 3.4 and the above-inferred mechanism, one can conclude that an effective reduction of GO happens only at a threshold amount of NaOH – which, in our case, is represented by the sample GN6.

3.3.4 Effect of pH on the reduction of GO

Traditionally, it has been reported that adding NaOH changes the pH and reduces GO [23],[36]. So, it will be remarkable to recognise the effect of pH on GO reduction. For this purpose, we compared the reduction capabilities of NaOH with other well-known reducing agents of GO, sodium borohydride ($NaBH_4$) and sodium carbonate (Na_2CO_3).

0.4 ml of NaOH in GO leads to a solution pH of 11.37. The corresponding GO reduction was evaluated based on UV-visible spectra (Figure 3.9). An equal reduction of GO was achieved using 0.2ml of $NaBH_4$, but the solution pH, in that case, was only 9.60. (Table 3.3). Similar is the case with Na_2CO_3 as a reducing agent. This result demonstrates that solution pH does not have a decisive role in reducing GO.

Table 3.3 *pH variation with respect to addition of reagent to GO*

Amount of reducing agent (ml)	Sample (GO + NaOH)	pH	Sample (GO + $NaBH_4$)	pH	Sample (GO + Na_2CO_3)	pH
0	GN0	7.33	GNB0	7.33	GNC0	7.33
0.05	GN1	9.55	GNB1	7.61	GNC1	8.61
0.1	GN2	10.06	GNB2	7.86	GNC2	9.85
0.15	GN3	10.48	GNB3	8.43	GNC3	10.27
0.2	GN4	10.77	GNB4	9.22	GNC4	10.32
0.25	GN5	10.92	GNB5	9.60	GNC5	10.35
0.3	GN6	11.05	GNB6	10.03	GNC6	10.39
0.35	GN7	11.18	GNB7	10.11	GNC7	10.41
0.4	GN8	11.37	GNB8	10.55	GNC8	10.47

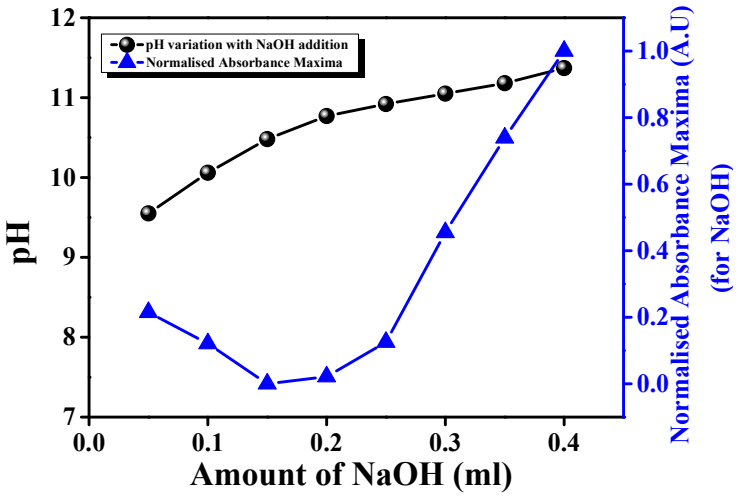

Figure 3.9: *Variation in pH with the addition of NaOH to GO solution (left-axis). Normalised absorbance maxima with respect to NaOH addition(right-axis).*

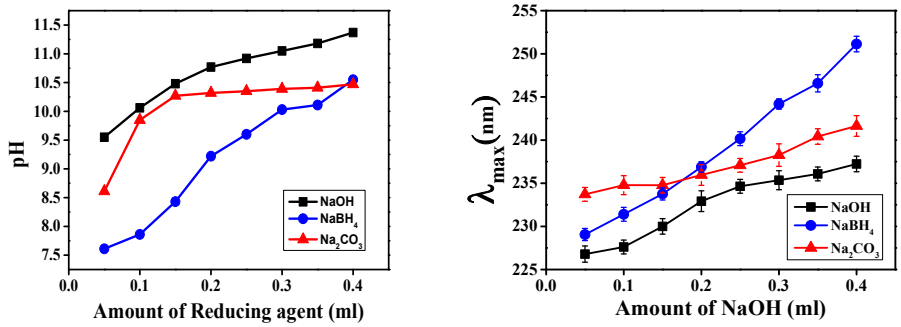

A B

Figure 3.10 A *The study involved assessing pH fluctuations resulting from the introduction of various reducing agents to GO.*

Figure 3.10 B *The alterations in peak positions observed in UV-visible spectra upon the introduction of different reducing agents served as a valuable indicator of the extent of reduction achieved.*

Figure 3.10 represents the pH variation with the addition of NaOH to GO, compared with absorbance maxima for NaOH addition (an indication of reduction). Figure 3.10A compares the pH variation of different reducing agents introduced to GO and Figure 3.10B gives the peak shift in UV-visible spectra of GO by introducing

various reducing agents. Our presented in this chapter rules out the assumption that solution pH decides the extent of GO reduction.

3.3.5 Comparing Peak Shift and Absorbance Maxima: Their Relative Significance

Figure 3.3 suggests a regular increase in λ_{max} or a regular peak shift. Absorption wavelength depends on π - π^* transition and conjugation. [37]. As told earlier, the π - π^* transition results from two factors: i) sp^2 clusters and ii) the number of chromophore units. [33]. In our case, NaOH addition led to the breaking of the chromophore groups – resulting in the shift of P_{230}. However, the breaking out of groups leading to replacement with hydroxyl groups cannot be identified as reduction (or oxidation). On the further increase of NaOH, sodium takes away the hydroxyl groups, resulting in rGO formation. Due to the increased formation of sp^2 clusters, the 230nm peak will continue to show a redshift.

This problem does not arise when the absorbance maxima is considered. An increase in UV-visible absorbance originates from the abundance in the π - π^* transition, which depends on electron cloud formation. Therefore, the absorbance maxima is the significant parameter for analysing GO reduction.

3.3.6 The threshold amount of NaOH for the reduction of GO

Based on the above discussions, it was demonstrated that a minimum amount of NaOH is needed for NaOH to act as a reducing agent for the synthesis of rGO or related composites. Therefore, we propose a mass ratio of NaOH to GO to achieve a minimum level of GO reduction. Based on our experimental investigations on 10ml of GO (0.02939g/ml of GO concentration), we identified that a minimum of 0.3ml of 2M NaOH (6mg of NaOH) is required for attaining reduction in GO (Here designated as GN6 sample). It corresponds to a mass ratio of 5.45 for NaOH to GO to achieve reduction using NaOH. As the ratio increases, the level of reduction will also increase till agglomeration.

3.4 Comparative Analysis with Literature

Numerous studies have explored the use of NaOH in the reduction of graphene oxide (GO). Some reports, with NaOH quantities falling below our recommended threshold ratio of 5.45, have indicated partial reduction or ineffectiveness [23,51-53]. This variability in outcomes is attributed to the NaOH quantity used. Interestingly, successful reduction has been achieved in cases exceeding our suggested threshold (mass ratio of 5.45) [16].

Consistent with our manuscript proposal, it's noteworthy that excessive NaOH usage can have unintended consequences. For instance, as demonstrated by Feng in 2013 [54], excessive NaOH led to sample agglomeration, aligning with our manuscript's findings. Thus, maintaining a delicate balance in NaOH quantity is essential to achieve desired outcomes while preventing adverse effects like agglomeration.

In the report by Lesiak et al. in 2021 [55], they noted a significant increase in the thickness of the reduced graphene oxide (rGO) sheets. This change was attributed to the presence of functional groups in rGO, where NaOH was used as the reducing agent in the GO reduction process. It is reasonable to associate this result with a less efficient reduction of GO, primarily because they employed a mass ratio of 3 - below the threshold value we have proposed, 5.45.

These observations underscore the critical importance of precise control over NaOH dosage in GO reduction processes, significantly influencing final results and reduced graphene oxide material quality.

3.5 Conclusion

In this chapter, we have studied the effect of NaOH on GO samples, recognising the importance of identifying the exact role of common chemical ingredients in the chemical synthesis of graphene and graphene composites. We found a threshold value where NaOH starts acting as a reducing agent. The finding was corroborated based on absorbance maxima of the UV-visible spectrum and ID/IG ratio

of Raman spectra. All these results indicate that NaOH has a remarkable role in tuning the functionality of GO. The obtained results were explained based on the fundamental idea of dependence of π - π^* transitions on the reduction of GO. The enhanced π - π^* transitions can be linked to the electron cloud formation in the reduction path. The threshold concentration of NaOH for the reduction of GO in weight ratio was found to be 5.45:1 (NaOH: GO). We discovered that pH is not the vital factor responsible for GO reduction. All these findings are critical for the NaOH-based pH tuning and synthesis of graphene-based nanocomposites. A clear understanding of the effect of concentrations of various ingredients used to synthesise rGO will open up a new horizon for the industrially scalable chemical synthesis of graphene-based nanocomposites.

References

1. Lu, G., Park, S., Yu, K., Ruoff, R. S., Ocola, L. E., Rosenmann, D., & Chen, J. (2011). Toward practical gas sensing with highly reduced graphene oxide: a new signal processing method to circumvent run-to-run and device-to-device variations. ACS nano, 5(2), 1154-1164. https://doi.org/10.1021/nn102803q

2. Matyba, P., Yamaguchi, H., Eda, G., Chhowalla, M., Edman, L., & Robinson, N. D. (2010). Graphene and mobile ions: the key to all-plastic, solution-processed light-emitting devices. Acs Nano, 4(2), 637-642. https://doi.org/10.1021/nn9018569

3. Rai, S., Bhujel, R., Biswas, J., & Swain, B. P. (2021). Reduced Graphene Oxide for Advanced Energy Applications. In Nanostructured Materials and their Applications (pp. 115-130). Springer, Singapore.

4. Singh, A., Sharma, N., Arif, M., & Katiyar, R. S. (2019). Electrically reduced graphene oxide for photovoltaic application. Journal of Materials Research, 34(4), 652-660. https://doi.org/10.1557/jmr.2019.32

5. Gurunathan, S., Han, J. W., Park, J. H., Kim, E., Choi, Y. J., Kwon, D. N., & Kim, J. H. (2015). Reduced graphene oxide–silver nanoparticle nanocomposite: a potential anticancer nanotherapy. International journal of nanomedicine, 10, 6257. https://doi.org/10.2147/IJN.S92449

6. Ahamed, A. J., & Loganathan, K. (2021). Reduced graphene oxide as effective adsorbent for removal of heavy metals in groundwater of Amaravathi River basin, Tamil Nadu. Geology, Ecology, and Landscapes, 1-10. https://doi.org/10.1080/24749508.2021.1923273

7. Sviridova, E., Li, M., Barras, A., Addad, A., Yusubov, M. S., Zhdankin, V. V., ... & Boukherroub, R. (2021). Aryne cycloaddition reaction as a facile and mild modification method for design of electrode materials for high-performance symmetric supercapacitor. Electrochimica Acta, 369, 137667. 10.1016/j.electacta.2020.137667

8. Yi, N., Cheng, Z., Li, H., Yang, L., Zhu, J., Zheng, X., ... & Cheng, H. (2020). Stretchable, ultrasensitive, and low-temperature NO2 sensors based on MoS2@ rGO nanocomposites. Materials Today Physics, 15, 100265. 10.1016/j.mtphys.2020.100265

9. Vidyarajan, N., & Alexander, L. K. (2018). Strain induced optical properties of perovskite LaFeO3. Materials Research Express, 6(1), 015610. https://doi.org/10.1088/2053-1591/aae857

10. Lee, K., Yoo, Y. K., Chae, M. S., Hwang, K. S., Lee, J., Kim, H., ... & Lee, J. H. (2019). Highly selective reduced graphene oxide (rGO) sensor based on a peptide aptamer receptor for detecting explosives. *Scientific Reports*, *9*(1), 10297. https://doi.org/10.1038/s41598-019-45936-z

11. Hummers Jr, W. S., & Offeman, R. E. (1958). Preparation of graphitic oxide. Journal of the american chemical society, 80(6), 1339-1339. https://doi.org/10.1021/ja01539a017

12. Brodie, B.C.: Sur le poids atomique du graphite. Ann. Chim. Phys. 59, 466–472 (1860)

13. Staudenmaier, L.: Verfahren zur Darstellung der Graphitsa¨ure. Eur. J. Inorg. Chem. 31(2), 1481–1487 (1898). doi:10.1002/cber. 18980310237

14. Venkanna, M., & Chakraborty, A. K. (2014, April). Synthesis and characterisations of graphene oxide and reduced graphene oxide nanosheets. In AIP Conference Proceedings (Vol. 1591, No. 1, pp. 574-576). American Institute of Physics. https://doi.org/10.1063/1.5080846

15. Muda, M. R., Ramli, M. M., Isa, S. S. M., Jamlos, M. F., Murad, S. A. Z., Norhanisah, Z., ... & Khalid, N. (2017, March). Fundamental study of reduction graphene oxide by sodium borohydride for gas sensor application. In AIP Conference Proceedings (Vol. 1808, No. 1, p. 020034). AIP Publishing LLC. https://doi.org/10.1063/1.4975267

16. Luo, D., Zhang, G., Liu, J., & Sun, X. (2011). Evaluation criteria for reduced graphene oxide. The Journal of Physical Chemistry C, 115(23), 11327-11335. https://doi.org/10.1021/jp110001y

17. Larciprete, R., Fabris, S., Sun, T., Lacovig, P., Baraldi, A., & Lizzit, S. (2011). Dual path mechanism in the thermal reduction of graphene oxide. Journal of the American Chemical Society, 133(43), 17315-17321. https://doi.org/10.1021/ja205168x

18. Jiang, X., Wang, J., Guo, J., Liu, M., & Fang, Y. (2022). Reduction in Graphene Oxide by Sodium Borohydride for Enhanced BR13 Dye and Cu2+ Adsorption. Arabian Journal for Science and Engineering, 1-13. https://doi.org/10.1007/s13369-022-06708-6

19. Shin, H. J., Kim, K. K., Benayad, A., Yoon, S. M., Park, H. K., Jung, I. S., ... & Lee, Y. H. (2009). Efficient reduction of graphite oxide by sodium borohydride and its effect on electrical conductance. Advanced Functional Materials, 19(12), 1987-1992. https://doi.org/10.1002/adfm.200900167

20. Rabchinskii, M. K., Dideikin, A. T., Kirilenko, D. A., Baidakova, M. V., Shnitov, V. V., Roth, F., ... & Vul, A. Y. (2018). Facile reduction of graphene oxide suspensions and films using glass wafers. Scientific reports, 8(1), 1-11. https://doi.org/10.1038/s41598-018-32488-x

21. Chen, H., Ding, L., Zhang, K., Chen, Z., Lei, Y., Zhou, Z., & Hou, R. (2020). Preparation of chemically reduced graphene using hydrazine hydrate as the reduction agent and its NO2 sensitivity at room temperature. Int. J. Electrochem. Sci, 15, 10231-10242. doi: 10.20964/2020.10.72

22. Chen, C., Kong, W., Duan, H. M., & Zhang, J. (2014). Theoretical simulation of reduction mechanism of graphene oxide in sodium hydroxide solution. Physical Chemistry Chemical Physics, 16(25), 12858-12864. https://doi.org/10.1039/C4CP01031K

23. Lesiak, B., Trykowski, G., Tóth, J., Biniak, S., Kövér, L., Rangam, N., ... & Malolepszy, A. (2021). Chemical and structural properties of reduced graphene

oxide—dependence on the reducing agent. Journal of Materials Science, 56(5), 3738-3754. https://doi.org/10.1007/s10853-020-05461-1

24. Zhang, H., Yao, J., Zhang, S., & Chen, H. (2021). Carboxylized graphene oxide nanosheet for shale plugging at high temperature. Applied Surface Science, 558, 149901. https://doi.org/10.1016/j.apsusc.2021.149901

25. Kumar, P. V., Bardhan, N. M., Tongay, S., Wu, J., Belcher, A. M., & Grossman, J. C. (2014). Scalable enhancement of graphene oxide properties by thermally driven phase transformation. Nature chemistry, 6(2), 151-158. https://doi.org/10.1038/nchem.1820

26. Rabchinskii, M. K., Shnitov, V. V., Dideikin, A. T., Aleksenskii, A. E., Vul', S. P., Baidakova, M. V., ... & Molodtsov, S. L. (2016). Nanoscale perforation of graphene oxide during photoreduction process in the arGOn atmosphere. The Journal of PHysical Chemistry C, 120(49), 28261-28269. https://doi.org/10.1021/acs.jpcc.6b08758

27. Hessein, A., & El-Moneim, A. A. (2015). Developing Cost Effective Graphene Conductive Coating and its Application as Counter Electrode for CdS Quantum Dot Sensitized Solar Cell. Proc. World Congr. New Technol.(NewTech 2015), 307(1).

28. Sehrawat, P., Islam, S. S., Mishra, P., & Ahmad, S. (2018). Reduced graphene oxide (rGO) based wideband optical sensor and the role of Temperature, Defect States and Quantum Efficiency. Scientific reports, 8(1), 1-13. https://doi.org/10.1038/s41598-018-21686-2

29. Bîru, E. I., & Iovu, H. (2018). Graphene nanocomposites studied by Raman spectroscopy. Raman spectroscopy, 179.

30. Mohan, V. B., Liu, D., Jayaraman, K., Stamm, M., & Bhattacharyya, D. (2016). Improvements in electronic structure and properties of graphene derivatives. Advanced Materials Letters, 7(6), 421-429.

31. Kudin, K. N., Ozbas, B., Schniepp, H. C., Prud'Homme, R. K., Aksay, I. A., & Car, R. (2008). Raman spectra of graphite oxide and functionalised graphene sheets. Nano letters, 8(1), 36-41. https://doi.org/10.1021/nl071822y

32. Pei, S., Zhao, J., Du, J., Ren, W., & Cheng, H. M. (2010). Direct reduction of graphene oxide films into highly conductive and flexible graphene films by hydrohalic acids. Carbon, 48(15), 4466-4474. DOI:10.1016/J.CARBON.2010.08.006

33. Konios, D., Stylianakis, M. M., Stratakis, E., & Kymakis, E. (2014). Dispersion behaviour of graphene oxide and reduced graphene oxide. Journal of colloid and interface science, 430, 108-112. DOI: 10.1016/j.jcis.2014.05.033

34. Lai, Q., Zhu, S., Luo, X., Zou, M., & Huang, S. (2012). Ultraviolet-visible spectroscopy of graphene oxides. Aip Advances, 2(3), 032146. https://doi.org/10.1063/1.4747817

35. Shin, D. S., Kim, H. G., Ahn, H. S., Jeong, H. Y., Kim, Y. J., Odkhuu, D., ... & Kim, B. H. (2017). Distribution of oxygen functional groups of graphene oxide obtained

from low-temperature atomic layer deposition of titanium oxide. RSC advances, 7(23), 13979-13984. https://doi.org/10.1039/C7RA00114B

36. Feng, M., & Feng, H. (2013). Effect of reducing agent on the chemical reduction of graphene oxides. Journal of Nanoscience and Nanotechnology, 13(2), 937-941. DOI: 10.1166/jnn.2013.6005

37. Manoratne, C. H., Rosa, S. R. D., & Kottegoda, I. R. M. (2017). XRD-HTA, UV visible, FTIR and SEM interpretation of reduced graphene oxide synthesised from high purity vein graphite. Material Science Research India, 14(1), 19-30. http://dx.doi.org/10.13005/msri/140104

38. Tan, S. M., Ambrosi, A., Chua, C. K., & Pumera, M. (2014). Electron transfer properties of chemically reduced graphene materials with different oxygen contents. Journal of Materials Chemistry A, 2(27), 10668-10675. https://doi.org/10.1039/C4TA01034E

39. Chua, C. K., & Pumera, M. (2013). Selective removal of hydroxyl groups from graphene oxide. Chemistry–A European Journal, 19(6), 2005-2011. 10.1002/chem.201204002

40. https://doi.org/10.1002/chem.201204002

41. Moon, I. K., Lee, J., Ruoff, R. S., & Lee, H. (2010). Reduced graphene oxide by chemical graphitisation. Nature communications, 1(1), 73. 10.1038/ncomms1067

42. Monika S. Khole, Sanjay K. Tupe, " Synthesis of Reduced Graphene Oxide (RGO) by Using Hydrothermal Method , International Journal of Scientific Research in Science, Engineering and Technology(IJSRSET), Print ISSN : 2395-1990, Online ISSN : 2394-4099, Volume 9, Issue 5, pp.85-88, July-August-2021.

43. Maulana, A., Nugraheni, A. Y., Jayanti, D. N., Mustofa, S., & Baqiya, M. A. (2017, May). Defect and magnetic properties of reduced graphene oxide prepared from old coconut shell. In IOP Conference Series: Materials Science and Engineering (Vol. 196, No. 1, p. 012021). IOP Publishing.

44. Eigler, S., Dotzer, C., & Hirsch, A. (2012). Visualisation of defect densities in reduced graphene oxide. Carbon, 50(10), 3666-3673. https://doi.org/10.1016/j.carbon.2012.03.039

45. Chua, C. K., Ambrosi, A., & Pumera, M. (2012). Graphene oxide reduction by standard industrial reducing agent: thiourea dioxide. Journal of materials chemistry, 22(22), 11054-11061. DOI: 10.1039/C2JM16054D

46. Yap, P. L., Kabiri, S., Auyoong, Y. L., Tran, D. N., & Losic, D. (2019). Tuning the multifunctional surface chemistry of reduced graphene oxide via combined elemental doping and chemical modifications. ACS omega, 4(22), 19787-19798. https://doi.org/10.1021/acsomega.9b02642

47. Sharma, N., Sharma, V., Jain, Y., Kumari, M., Gupta, R., Sharma, S. K., & Sachdev, K. (2017, December). Synthesis and characterisation of graphene oxide (GO) and reduced graphene oxide (rGO) for gas sensing application. In Macromolecular Symposia (Vol. 376, No. 1, p. 1700006).

48. https://doi.org/10.1002/masy.201700006

49. Kumar, G. P., Krishnan, P., Arsha, M. S., Jawahar, I. N., & Biju, V. (2022). Reduced graphene oxide derived from urea-assisted solution combustion route and its electrochemical performance. Bulletin of Materials Science, 45(3), 170. https://doi.org/10.1007/s12034-022-02751-z

50. Chakraborty, S., Ponrasu, T., Chandel, S., Dixit, M., & Muthuvijayan, V. (2018). Reduced graphene oxide-loaded nanocomposite scaffolds for enhancing angiogenesis in tissue engineering applications. Royal Society open science, 5(5), 172017. https://doi.org/10.1098/rsos.172017

51. Soni, M., Kumar, P., Pandey, J., Sharma, S. K., & Soni, A. (2018). Scalable and site specific functionalisation of reduced graphene oxide for circuit elements and flexible electronics. Carbon, 128, 172-178. https://doi.org/10.1016/j.carbon.2017.11.087

52. Prerna Bansal, A. S. Panwar, and D. Bahadur, "Effect of Reaction Temperature on Structural and optical Properties of Reduced Graphene Oxide," International Journal of Materials, Mechanics and Manufacturing vol. 2, no. 1, pp. 18-20, 2014.. DOI 10.7763/IJMMM.2014.V2.90

53. Abulizi, A., Okitsu, K., & Zhu, J. J. (2014). Ultrasound assisted reduction of graphene oxide to graphene in l-ascorbic acid aqueous solutions: Kinetics and effects of various factors on the rate of graphene formation. *Ultrasonics sonochemistry*, *21*(3), 1174-1181.

54. Khan, J., & Jaafar, M. (2021). Reduction efficiencies of natural substances for reduced graphene oxide synthesis. *Journal of Materials Science*, *56*, 18477-18492.

55. Doudrick, K., Nosaka, T., Herckes, P., & Westerhoff, P. (2015). Quantification of graphene and graphene oxide in complex organic matrices. *Environmental Science: Nano*, *2*(1), 60-67.

56. Feng, M., & Feng, H. (2013). Effect of reducing agent on the chemical reduction of graphene oxides. *Journal of nanoscience and nanotechnology*, *13*(2), 937-941.

57. Lesiak, B., Trykowski, G., Tóth, J., Biniak, S., Kövér, L., Rangam, N., ... & Malolepszy, A. (2021). Chemical and structural properties of reduced graphene oxide—dependence on the reducing agent. *Journal of Materials Science*, *56*, 3738-3754.

CHAPTER 4

GRAPHENE OXIDE MODIFICATION USING ACTIVATED CARBON - COMPOSITE FORMATION

Graphene oxide tends to agglomerate in water, limiting its effectiveness. To address this, incorporating materials like activated carbon can prevent agglomeration while enhancing adsorption capabilities. This part of the chapter explores the use of activated carbon to improve GO's performance in aqueous environments.

Scope of the Chapter

- *Investigate the adsorption capabilities of the GOAC composite towards various dyes including methylene blue, rhodamine B, mixture of dyes, and ciprofloxacin antibiotic.*
- *To find the reaction kinetics of the adsorption processes involving the GOAC composite and different dye molecules as well as the antibiotic ciprofloxacin, to understand the underlying mechanisms of the interactions.*

Abstract

This chapter centres on crafting an environmentally sustainable and cost-efficient nanocomposite tailored for chemical adsorption applications. Employing a one-step synthesis approach, we successfully developed a Graphene Oxide-Activated Carbon (GOAC) composite that meets these criteria. Graphene oxide aggregates in water. We strategically introduced activated carbon (AC) unaided by a linker molecule through a facile synthesis route to overcome this issue. In this study, maintaining the structural integrity of constituent materials is a crucial element that guarantees the efficacy of adsorption. The GOAC composite demonstrated exceptional thermal stability, amplifying its prospects for practical applications. In adsorption studies, the composite exhibited notable efficacy in removing dyes like methylene blue, rhodamine B, congo red, their mixtures and ciprofloxacin antibiotic. This removal resulted in remarkable maximum adsorption capacities, achieved in minimum time. The observed adsorption behaviour aligned with the pseudo-second-order kinetic model. This study highlights the successful development of a versatile nanocomposite with promising attributes for environmental remediation. Combining graphene oxide and activated carbon addresses agglomeration challenges and imparts structural stability and high thermal resilience to the composite, making it a compelling candidate for cost-effective and efficient adsorption-driven applications.

4.1 Introduction

Graphene oxide (GO) is the oxidized form of graphene, containing many oxygen-functional groups such as carbonyl, epoxide, hydroxyl, and carboxyl groups is explored as a versatile industrial adsorbent. Due to the abundance of active groups, GO is chemically more reactive and is easier to modify. [1]. GO has attracted attention in wastewater treatment due to its high negative charge density, strong π-π stacking interactions with aromatic compounds and large specific surface area. However, when introduced to water, the GO agglomerates and adsorption efficiency drastically reduced [2]. To address this limitation, coupling another material alongside GO becomes crucial.

Activated Carbon (AC) is a widely employed adsorbent material due to its exceptionally porous structure, large surface area, and adequate adsorption capacity. The pores and surface functional groups in AC are responsible for the adsorption of pollutants. [3]. However, the adsorption kinetics of AC is relatively slow [4,5], and its regeneration involves complex thermal or chemical treatments that may not fully restore the original adsorption capacity [6]. Consequently, combining AC with other adsorbent materials could synergistically enhance the adsorption efficiency.

The GOAC composite exhibits enhanced adsorption capacity, selectivity and kinetics, mechanical and thermal stability, and regeneration capability. [7-14]. The adsorbent material must function effectively at higher temperatures, as industrial effluents often reach temperatures above 300K. The thermal stability of the GOAC composite [15] makes it suitable for the treatment of industrial wastewater. However, most of the current literature on GOAC is concentrated on linker-based GOAC composite. The linker can block the pores of AC and, in turn, lead to reduced adsorption [16]. So, developing GOAC adsorbent unaided by linking agent is necessary.

This chapter aims to synthesize a low-cost adsorbent composite of GO and AC without any linker molecule. The adsorption property of the composite is studied using organic dyes and antibiotics. Reaction kinetics are studied, and the mechanism

behind enhanced adsorption is proposed. A comparison study of GOAC composite with already established GO and AC-based adsorbents is also presented.

4.2 Experimental details

4.2.1 Synthesis of GO and GOAC composite

Graphene oxide was prepared using Hummer's method (section 2.1). The schematic preparation procedure of the GOAC composite is shown in Figure. 4.1.

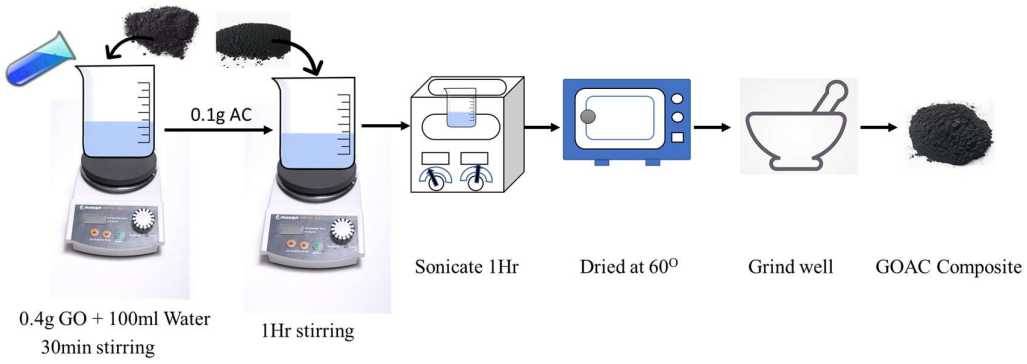

***Figure 4.1**: Synthesis of GOAC composite*

Initially, 0.4 grams of graphene oxide (GO) is introduced into 100 ml of water and stirred for 30 minutes. Then, 0.1 grams of activated carbon (AC) is added to the mixture and stirred for an additional hour. The resulting solution undergoes a series of processes, including sonication, washing, and drying in a vacuum oven at 60 degrees Celsius. Subsequently, the obtained sample is thoroughly ground to achieve the final GOAC composite.

4.3 Results and Discussion

4.3.1 Characterization

The synthesized samples were characterized using a Raman spectrometer. The Raman spectrum shown in Figure. 4.2 depicts two distinct peaks at ~ 1340 cm^{-1} and ~1580 cm^{-1}, corresponding to D (defects) and G (graphitic) bands, respectively. The ID/IG ratio of 0.999 (Table 4.1) indicates that the GOAC composite has the same

structural disorders as GO and AC. This finding highlights the preservation of structural integrity for the individual constituents within the composite material.

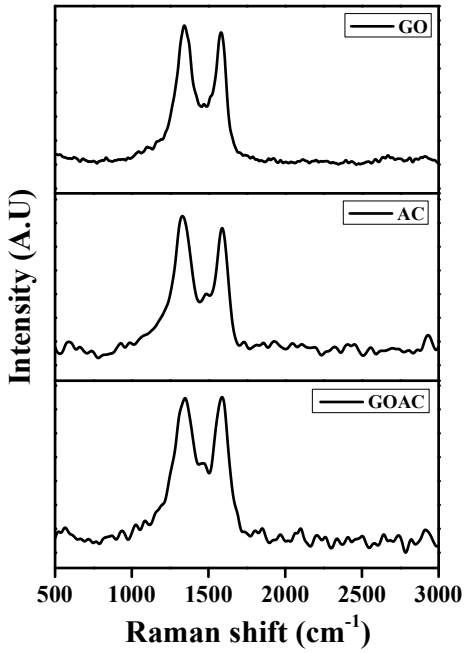

Figure 4.2 *The Raman spectra of graphene oxide (GO), activated carbon (AC), and the GOAC Composite exhibit distinguishable D and G bands. Table 4.1 provides detailed information on the peak positions and intensity ratios (ID/IG) for these bands. The spectra reveal that the structural integrity of both GO and AC is preserved in the composite, as there is minimal variation in the ID/IG ratios across all three samples.*

Table 4.1*: ID/IG ratios of samples*

Sample	Position of D band (cm^{-1})	Position of G band (cm^{-1})	ID/IG
GO	1340	1572	1.007
AC	1335	1582	0.997
GOAC	1342	1581	0.999

The XRD spectra of GO (Figure. 4.3) showed a sharp peak at 10.54° with an interlayer distance of 0.839 nm, broad peaks at 23° and 43° for AC, and GOAC exhibited all these peaks, confirming the structural purity of the composite.

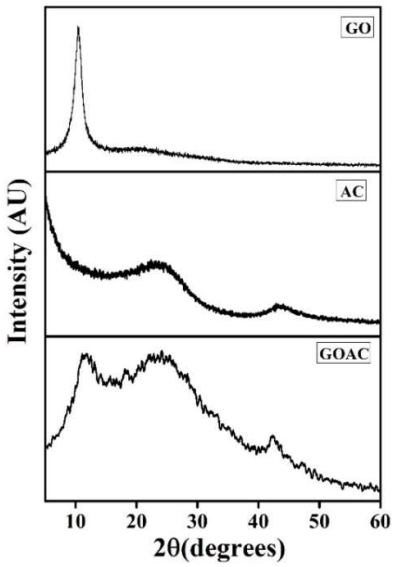

Figure 4.3 *The x-ray diffraction (XRD) spectra of graphene oxide (GO), activated carbon (AC), and the GOAC composite reveal distinct patterns. In GO, a pronounced and sharp peak is observed at 10.54°, corresponding to the [002] plane. Conversely, AC exhibits two broad peaks at 23° and 43°. Remarkably, the composite spectrum integrates all three characteristic peaks, demonstrating the inclusion of structural features from both GO and AC.*

The nitrogen adsorption/desorption isotherms at 77 K and the pore-size distribution of samples derived using the Barrett-Joyner-Halenda (BJH) method were used to measure the specific surface area and porosity of the GOAC composite. (Figure.4. 4, Table 4.2)

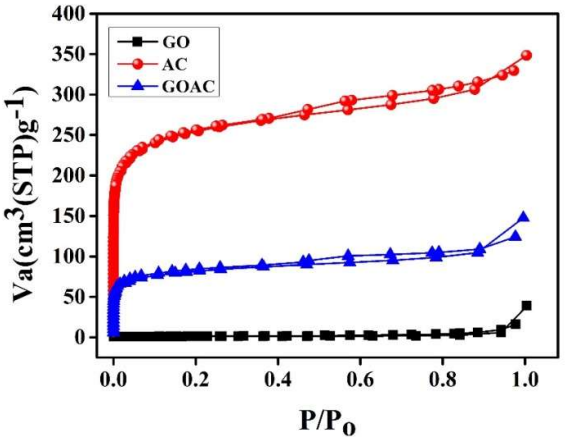

Figure 4.4 *Adsorption - desorption isotherm of the samples.*

***Table 4.2**; BET analysis parameters*

Sample	Specific surface area (m^2/g)	Total Pore volume (cm^3/g)	Mean Pore diameter(nm)
GO	4.16	0.05	46.48
AC	922.31	0.53	2.31
GOAC	289.09	0.22	3.11

The presence and abundance of functional groups in the material were obtained using FTIR spectra. FTIR spectra demonstrate a higher number of oxygen functional groups for GO. AC also possesses similar functional groups. GOAC composite exhibited functional groups from both GO and AC. (Figure. 4.5, Table 4.3)

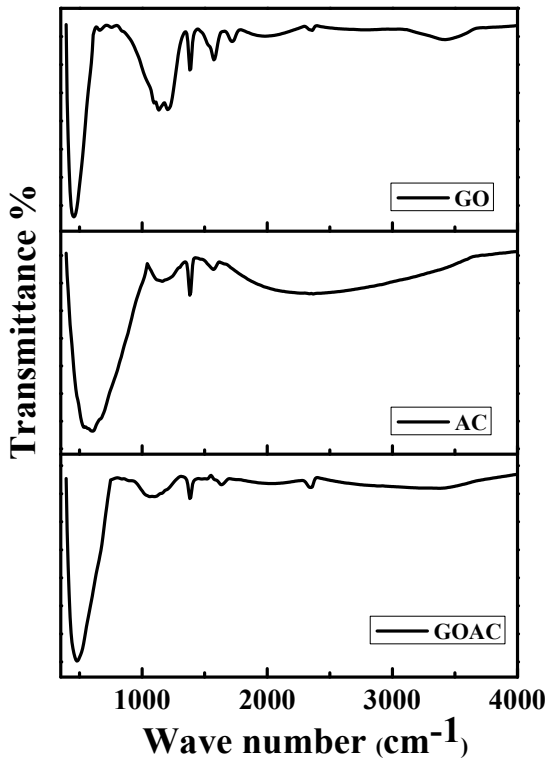

Figure 4.5*: FTIR Spectra of GO, AC and GOAC.*

***Table 4.3**: FTIR Spectra analysis*

GO		AC		GOAC	
Wavenumber (cm^{-1})	**Reason**	**Wavenumber (cm^{-1})**	**Reason**	**Wavenumber (cm^{-1})**	**Reason**
454.96	-	606.72	-	480.69	-
1205.58	C-O stretching	1160.67	C-O stretching alcohol	1097.287	C-O stretching
1384.13	C-H bending alkane	1383.08	O-H bending phenol	1383.58	OH bending phenol
1575.04	C=C stretching	1570.51	C=C stretching	1634.64	C=C stretching
1719.668	C=O stretching carboxylic acid	2367.72	C=O=C stretching	2040.83	
1986.47	C-H bending aromatic compound			2349.665	C=O=C stretching strong
2367.83	C=O=C stretching			3377.914	Strong broad O-H stretching
2763.50	C-H stretching from aldehyde				
3421.59	Strong broad O-H stretching				

The thermal decomposition behaviour of the samples was investigated by TGA and is given in Figure. 4.6. Three distinct degradation stages characterize the thermographic analysis of graphene oxide (GO). The initial stage involves a weight loss occurring within the temperature range of 32°C to 84°C, attributed to the evaporation of water and moisture in the graphite oxide structure. It is followed by the decomposition of COOH in the temperature span of 227°C to 318°C. AC showed higher thermal stability than GO. The thermal stability of GO was greatly improved by the introduction of AC to the GO matrix, resulting in enhanced thermal stability in the range of 100 to 500ºC for GOAC composite.

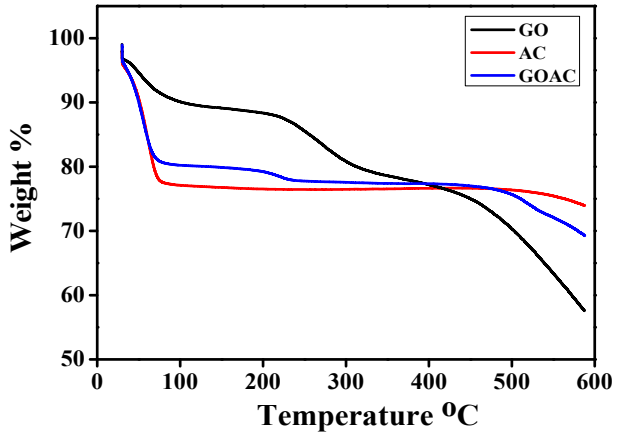

Figure 4.6 *TGA analysis of GO, AC and GOAC*

SEM images indicate the evolution in surface morphology as GO and AC combine to form the composite. Figure 4.7a shows the exfoliated nanosheets of GO, Figures 4.7b and 4.7d the porous, smooth nature of AC, and Figure 4.7c indicates that the GO sheets are distributed between larger activated carbon structures, preventing GO sheets' agglomeration.

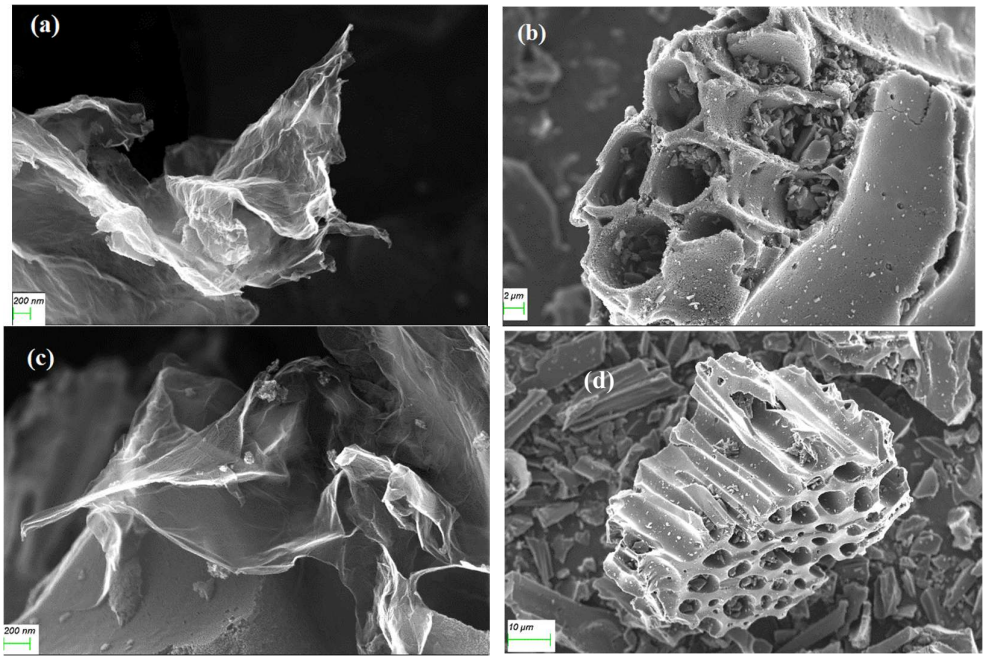

Figure 4.7 *FE-SEM images of (a)GO, (b)AC, (c)GOAC and (d)porous nature of AC in lower magnification.*

4.3.2 Methylene-Blue adsorption experiment

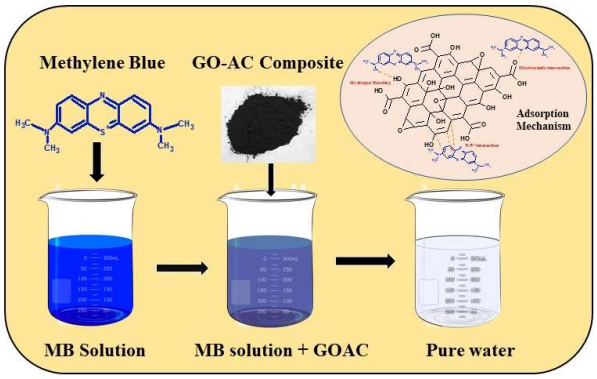

All investigations on dye adsorption were carried out while maintaining ambient conditions. 0.010 g of the adsorbent (GO, AC, and GOAC) was introduced into 100 mL of methylene blue (MB) solution with an initial concentration of 10 ppm. The concentration of the MB solution was regularly assessed at one-minute intervals, employing UV-visible spectrometry within the wavelength range of 400 to 800 nm. The experimental protocol was repeated using 0.005 g of the adsorbent under ambient conditions. Specifically, for 0.01 g of adsorbent, the time intervals ranged from 1 to 14 minutes, while for 0.005 g of adsorbent, they spanned from 5 to 80 minutes. The corresponding UV-visible plots are given in Figure 4.8 and Figure 4.9.

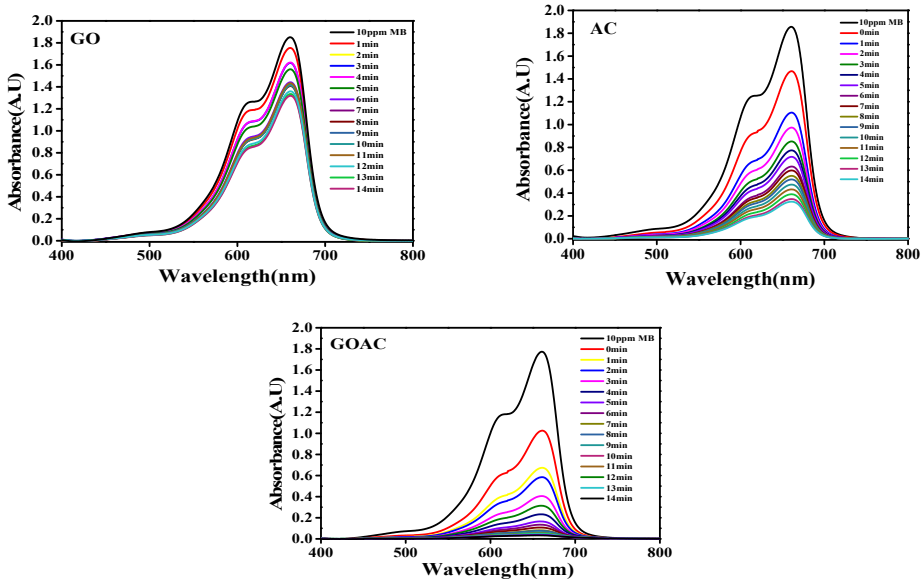

Figure 4.8. *UV-visible spectrum plots of MB dye adsorption by 0.01 g of a) GO, b) AC, and c) GOAC.*

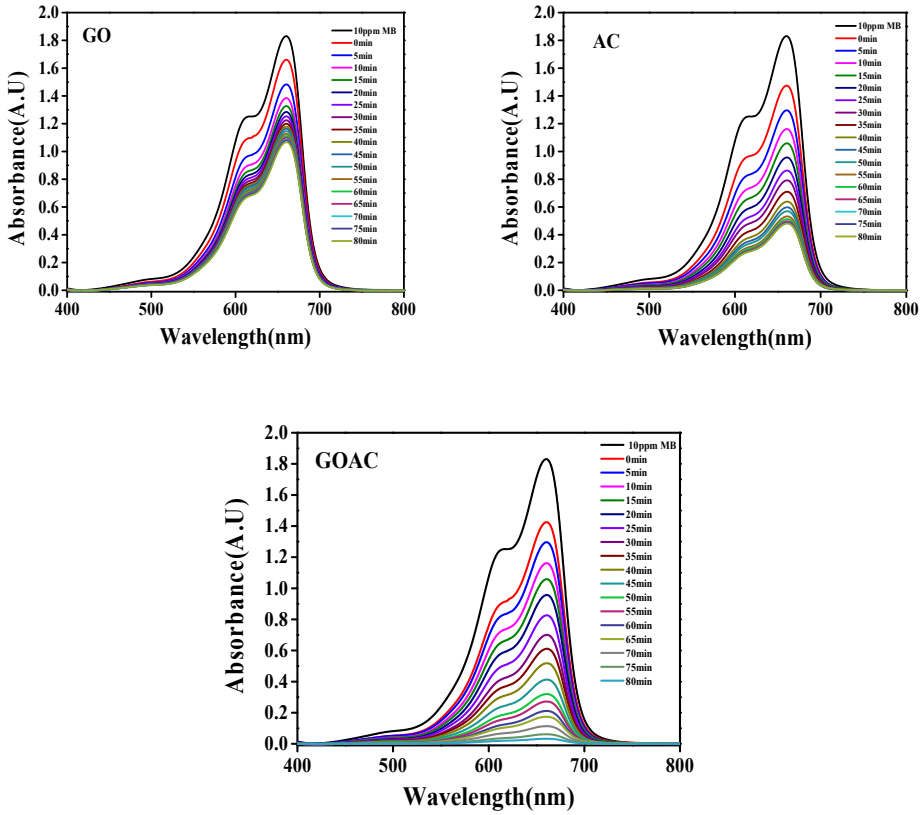

Figure 4.9. *UV-visible spectrum plots of MB dye adsorption by 0.005 g of a) GO, b) AC, and c) GOAC*

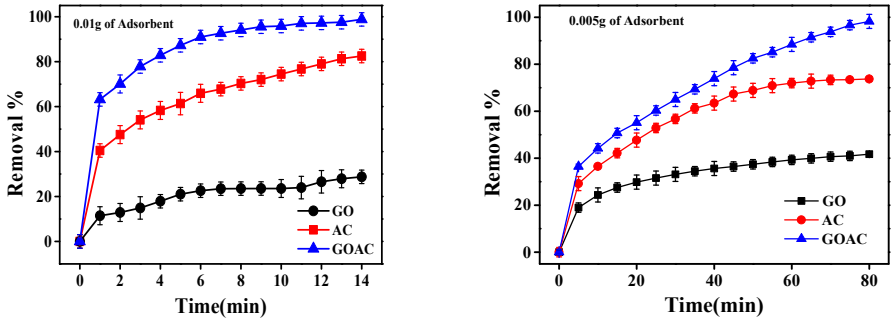

Figure 4.10 *Variation of removal efficiency with contact time for MB using (a) 0.01g of adsorbent, and (b) 0.005g of adsorbent*

The removal efficiency is calculated from eq. 2.4. In identical experimental settings, the GOAC composite exhibits greater removal efficiency than GO and AC separately, as shown in Figure 4.10. This suggests a synergistic enhancement in pollutant adsorption when GO and AC are combined.

4.3.2.1 MB calibration

Calibration of the adsorbate, in this case methylene blue, is the first step towards examining the specifics and kinetics of adsorption. Predefined methylene blue concentrations were prepared to do this calibration, and the absorbance was measured using UV-visible spectroscopy. The data absorbance was fitted and found to follow a straight-line equation. The link between concentration and absorbance that this analysis produces provides vital groundwork for further adsorption research.

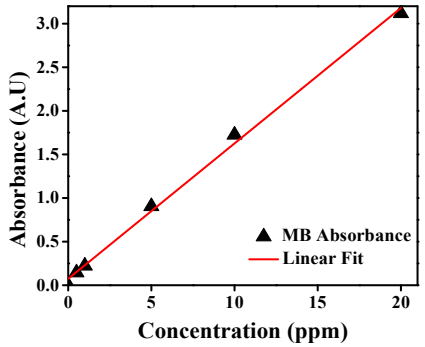

Figure 4.11 *Calibration curve for MB*

Table 4.4 *Calibration for MB*

Concentration (ppm)	**Absorbance (A.U)**
0	0
0.5	0.14
1	0.22
5	0.90
10	1.72
20	3.12

The corresponding straight-line equation is

$$\mathbf{Abs = 0.1552*Conc + 0.0743.}$$

This equation can convert any given absorbance to the corresponding concentration for MB dye.

4.3.2.2 Adsorption kinetics

Understanding adsorption kinetics is crucial as it provides insights into the rate and mechanism of pollutant removal, aiding in designing and optimizing adsorption processes for efficient water treatment.

The experimental adsorption kinetic data were quantitatively modelled and fitted using pseudo-first-order and pseudo-second-order kinetic models **(section 2.5),** detailed in Figures 4.12 and 4.13. The corresponding parameters are given in Table 4.5. $q_{e\ direct}$ indicated the adsorption capacity obtained from eq 2.5 and $q_{e\ kinetic}$, the adsorption capacity obtained after fitting the data.

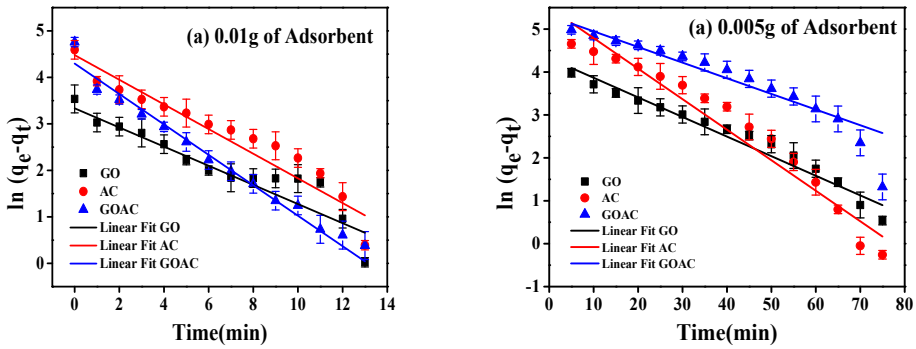

Figure 4.12 *Pseudo first order kinetic model for the adsorption of MB onto (a) 0.01g of adsorbents, (b) 0.005g of adsorbents.*

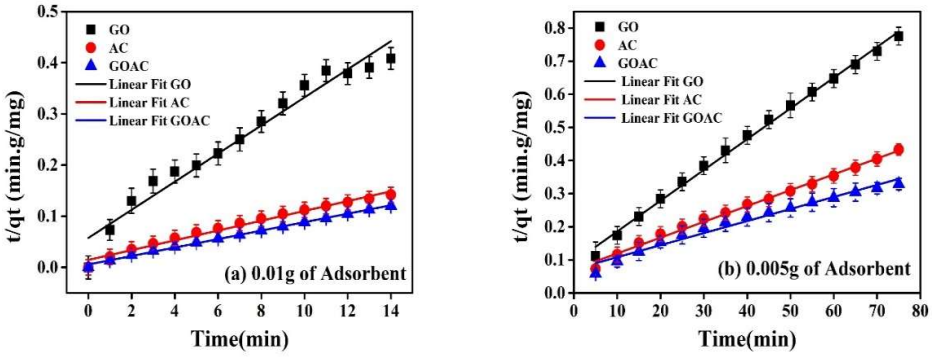

Figure 4.13 *Pseudo second order kinetic model for the adsorption of MB onto (a) 0.01g of adsorbent, (b) 0.005g of adsorbent.*

Table 4.5 *Adsorption kinetic parameters*

Adsorbent amount	Sample name	q_e direct	Pseudo-first-order kinetics			Pseudo-second-order kinetics		
			k_1 (min^{-1})	$q_{e\ kinetic}$ (mg/g)	R^2	k_2 (g/mg min)	$q_{e\ kinetic}$ (mg/g)	R^2
0.01g	GO	34.29	0.20	29.42	0.86	0.013	36.47	0.96
	AC	98.69	0.25	68.71	0.91	0.012	105.26	0.98
	GOAC	116.55	0.31	84.09	0.97	0.006	120.92	0.99
0.005g	GO	98.39	0.04	74.47	0.96	0.001	107.64	0.99
	AC	193.97	0.07	251.56	0.94	0.0003	209.20	0.99
	GOAC	271.71	0.04	255.52	0.88	0.0002	274.70	0.98

The equilibrium adsorption capacity q_e obtained from the fitted data $q_{ekinetic}$ (120.9mg/g for 0.01g composite and 274.7mg/g for 0.005g composite) for the pseudo-second-order model (Figure.4.13) is similar to the q_e obtained from equation (2.2), $q_{e\ direct}$, suggesting that the adsorption process of MB onto GOAC follows pseudo-second-order kinetics and is mainly controlled by chemisorption [17].

4.3.2.3 Regeneration

In sustainable environmental remediation, recyclable materials are crucial. The regenerated adsorbents were dried at 60 °C for eight hours after being washed many times with distilled water. Adsorption studies were carried out again using the regenerated adsorbents for four more adsorption/regeneration cycles, and samples showed efficiency above 50% even in the 5th cycle, as shown in Figure 4.14.

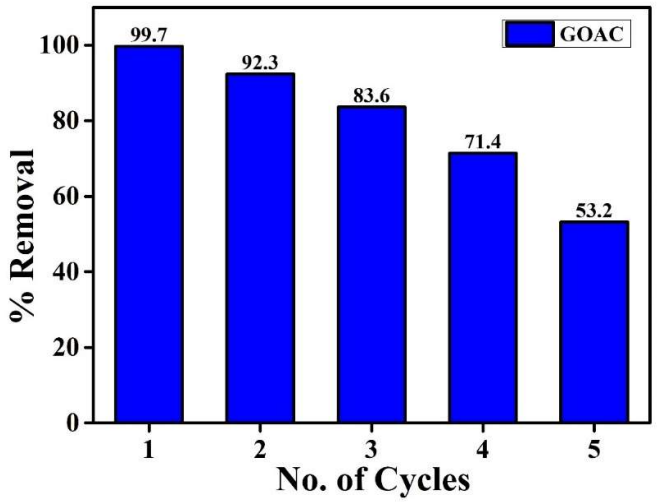

***Figure 4.14**: Percentage removal efficiency of the regenerated GOAC composite in consecutive cycles*

4.3.2.4 Mechanism

GO shows a good affinity towards cationic dye. The deprotonation of surface functional groups present in GO can explain the enhanced affinity. The deprotonation facilitates MB interaction with negatively charged GO surfaces [13]. Literature suggests that GO's abundant oxygen-containing functional groups play a crucial part in the improved adsorption capacity towards MB [14].

The dimension of MB is reported as 1.43, 0.61, and 0.4 nm, respectively, by [15]. These proportions make it possible for this dye to enter into the mesoporous structure of AC quickly.

The interaction of methylene blue with GOAC composite can be attributed to three primary routes: 1) Electrostatic interaction, 2) Hydrogen bond formation and 3) π - π* interactions – as represented in Figure 4.15. The main contributors responsible for MB adsorption are the electrostatic/ionic interactions between the positively charged MB structure and the negatively charged functional groups in GO and AC [14-16]. The oxygen functionalities present at the edges of the composite induce Hydrogen bond formation with MB. When two entities have compatible geometry and extended π systems, they create π - π* interactions between them. [18]. Both GOAC composite and MB have extended π systems, hence the possibility for π - π*

interactions. All three interactions contribute to GOAC composite's superior adsorption of MB or, in general, a cationic dye.

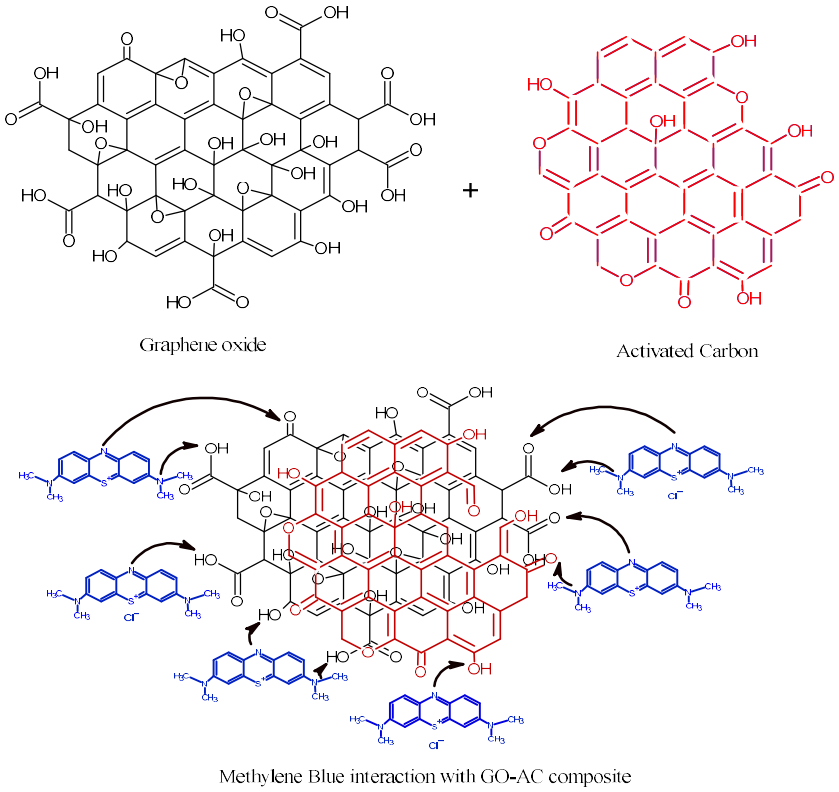

***Figure 4.15**: Interaction of the GOAC composite with methylene blue.*

4.3.2.5 Comparison with other adsorbents

Table 4.6; *Comparison of methylene blue dye adsorption by various adsorbents in literature.*

Sl. No	Adsorbent	Time	Qe (mg g^{-1})	Reference
1	PANI/GO	270 min	14.2	[19]
2	GO–EDTA–CS	180 min	141	[20]
3	G/Fe3O4	-	43.82	[21]
4	GO−Fe3O4 hybrid	150 min	167.2	[22]
5	GO/magnetic cyclodextrin	50 min	228.5	[23]
6	Magnetic chitosan/GO (MCGO)	90 min	95.16	[24]
7	Magnetic cyclodextrin−chitosan/GO(MCCG)	80 min	84.32	[25]
8	Exfoliated graphene oxide	120 min	17.3	[26]
9	Alg/GO	12 hours	12.64	[27]
10	Graphene oxide/gluten	-	214.29	[28]
11	MGO	3500min	64.23	[29]
12	GNS/Fe3O4	60min	35.73	[30]
13	CS/Fe_3O_4/GO	-	30.10	[31]
14	$NiFe_2O_4$-GO	250min	48.15	[32]
15	Fe_3O_4/GO-NH_2	-	236.97	[33]
16	**GOAC**	**14min**	**116.55**	**Present work**
17	**GOAC**	**80min**	**271.72**	**Present work**

4.3.3 Rhodamine-B adsorption experiment

10ppm RhB adsorption by GO, AC and GOAC composite

Adsorption investigations on Rhodamine B dye involving GO, AC, and GOAC were conducted by stirring an aqueous dye solution with the respective adsorbents over defined intervals. Specifically, for 0.01 g of adsorbent, the time intervals ranged from 1 to 60 minutes. (Figure 4.16). The resultant removal percentage is presented graphically in Figure 4.17, emphasizing the rapid adsorption kinetics observed (achieving 95.4% removal within 60 minutes for the composite).

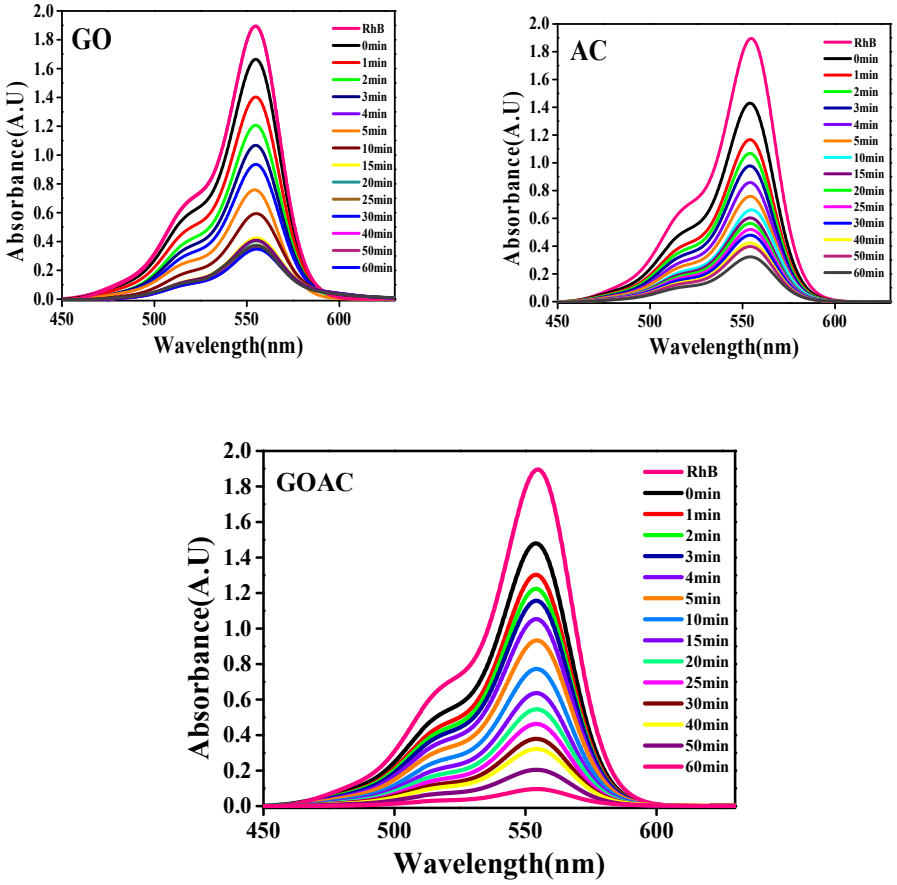

Figure 4.16 *UV-visible plots of RhB dye adsorption by 0.01 g of a) GO, b) AC, and c) GOAC*

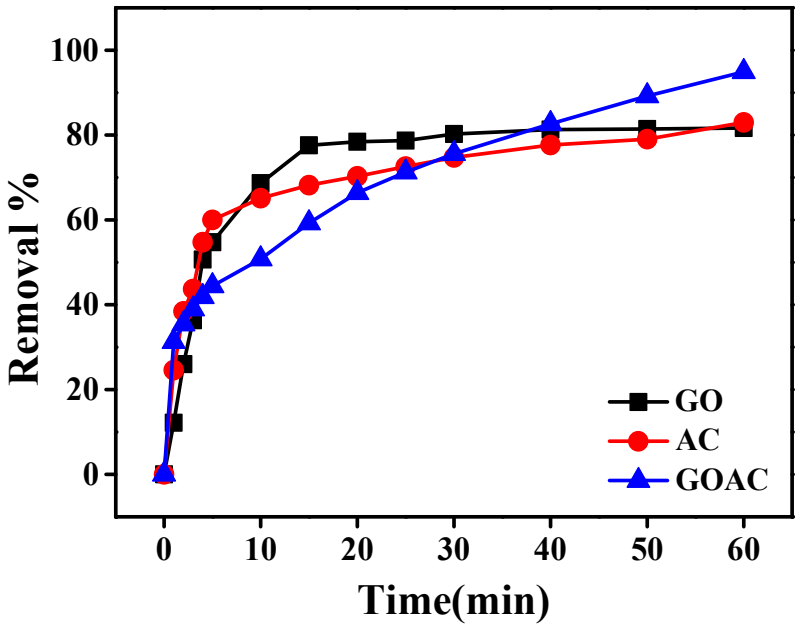

Figure 4.17 *Removal percentage of RhB dye adsorption by 0.01 g of a) GO, AC, and GOAC*

4.3.3.1 RhB Calibration

The calibration curve for RhB, fitted to a straight line, is given in Figure 18.

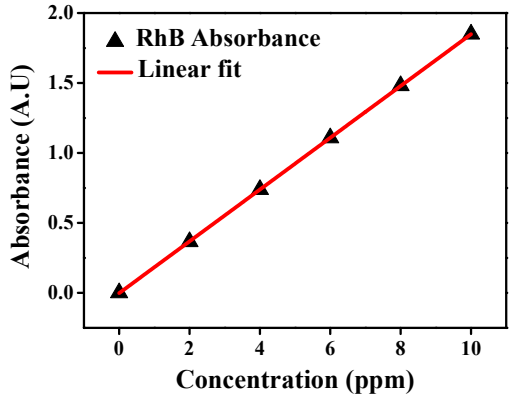

Figure 4.18 Calibration curve for RhB.

Table 4.7 Calibration for RhB

Concentration (ppm)	Absorbance (AU)
0	0
2	0.36
4	0.74
6	1.11
8	1.48
10	1.85

From this plot the equation connecting absorbance and concentration is obtained as

Abs = 0.1850*Conc

This equation can be used to convert any given absorbance to the corresponding concentration for RhB dye.

4.3.3.2 Adsorption Kinetics

The pseudo-first-order and pseudo-second-order kinetic models, along with the Elovich model **(section 2.5)** have been employed to elucidate the adsorption behaviour of RhB on GOAC.

a) Pseudo-first order kinetic model

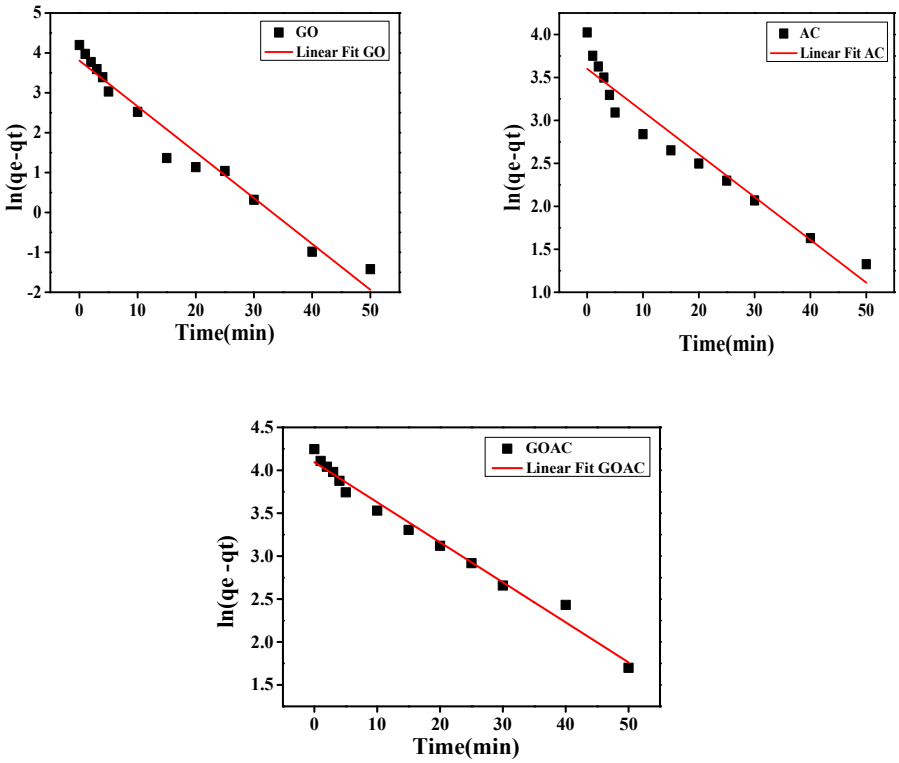

Figure 4.19 *Pseudo-first-order kinetic fit*

Table 4.8 *Pseudo-first-order kinetic variables of RhB adsorption onto GOAC composite*

Adsorbent amount	Sample name	$q_{e\ direct}$	Pseudo-first-order kinetics		
			k_1 (min^{-1})	q_e kinetic (mg/g)	R^2
0.01g	GO	78.09	0.11	45.15	0.97
	AC	79.36	0.05	36.64	0.94
	GOAC	90.77	0.05	57.17	0.98

b) Pseudo Second Order Kinetic Model

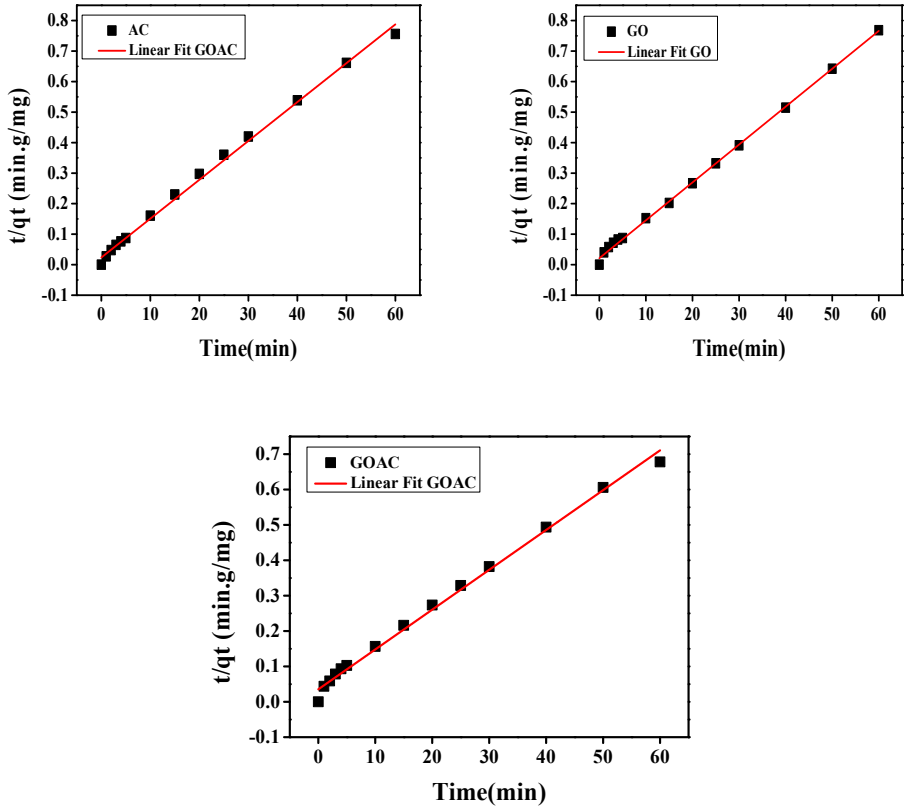

Figure 4.20 *Pseudo second-order kinetic fit*

Table 4.9 *Pseudo-second-order kinetic variables of RhB adsorption onto GOAC composite*

Adsorbent amount	**Sample name**	$q_{e\ direct}$	**Pseudo-second-order kinetics**		
			k_2 (min^{-1})	$q_{e\ kinetic}$ (mg/g)	R^2
0.01g	GO	78.09	0.20	80.64	0.998
	AC	79.36	0.25	78.74	0.997
	GOAC	90.77	0.31	90.91	0.997

Tables 4.8 and 4.9 provide a concise overview of the variables characterizing the adsorption kinetics of Rhodamine B on GOAC. Notably, the calculated $q_{ekinetic}$ values derived from the pseudo-second-order model closely align with the experimental data, suggesting that the adsorption process of rhodamine B onto GOAC may be primarily governed by chemisorption, as indicated by Arias et al. (2017)[17].

c) **Elovich kinetic model**

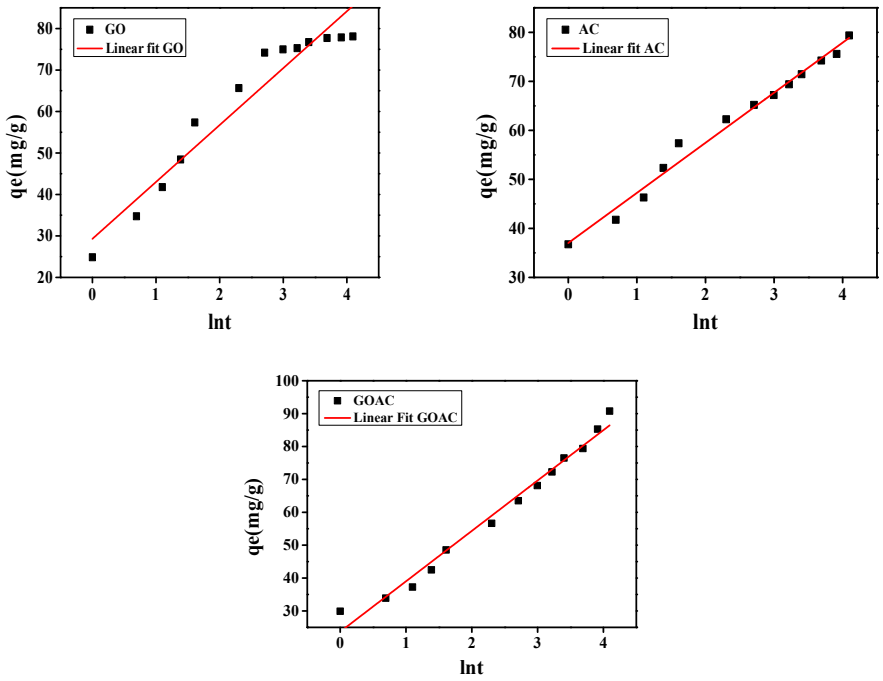

Figure 4.21 *Elovich kinetic model fit*

Table 4.10 *Elovich kinetic variables of RhB adsorption onto GOAC composite*

Adsorbent amount	**Sample name**	$q_{edirect}$	**Elovich kinetics Model**		
			β **(min^{-1})**	**α (mg/g)**	R^2
0.01g	GO	78.09	0.07	116.07	0.93
	AC	79.36	0.09	382.21	0.98
	GOAC	90.77	0.06	71.81	0.98

The significantly better fit of the pseudo-second-order model for GOAC suggests a chemisorption mechanism and strong interaction between RhB molecules and the GOAC composite surface. This can be attributed to the presence of functional groups on both graphene oxide (GO) and activated carbon (AC), enhancing adsorption sites and chemical interactions.

The Elovich model, characterized by parameters α and β, describes adsorption as a multilayered, chemisorptive process evaluated and plotted in Figure 4.21. The α values for GO, AC, and GOAC are determined to be 116.075, 382.214, and 71.8115, respectively. These values reflect the initial adsorption rate and suggest that AC exhibits the highest initial adsorption rate, possibly due to its extensive porous structure. The Elovich model provides insight into the kinetics of surface reactions during adsorption and complements the information gained from the pseudo-first and pseudo-second-order models.

4.3.3.3 Mechanism

The enhanced dye absorption on graphene oxide (GO) can be attributed to its higher specific surface area. This absorption process can be broken down into three distinct consecutive steps.

Firstly, the dye molecules migrate towards the outer surface of the adsorbent nanomaterial. Secondly, these dye molecules penetrate the tiny pores within the particles of the adsorbent nanomaterial. Lastly, the actual adsorption of the dye molecules onto the surface of the nanomaterial takes place.

During this chemisorption process, electrostatic interactions and hydrogen bonding are at play. These interactions occur between the π electrons of the graphene oxide and the cationic dyes.

Rhodamine B (RhB), a planar molecule, readily adheres to the GO surface due to π-π interactions. These interactions result from the aromatic backbones of the dyes aligning and binding to the hexagonal structure of GO.

The presence of oxygen functional groups within graphene oxide (GO) positively impacts the GOAC composite's capacity to eliminate organic molecules in the form of contaminants.

4.3.3.4 Comparison with other adsorbents

Table 4.11: *Comparison of rhodamine B dye adsorption by various adsorbents in the literature.*

Sl No	Adsorbent	Maximum adsorption capacity (mg/g)	Time (min)	Reference
1.	Activated sugar-based carbon (ASC)	123.46	12	[34]
2.	Zeolite (Ze)	6.964	15	[35]
3.	Three-dimensional layered double hydroxide	49.6	30	[36]
4.	Banana peel	211.9	30	[37]
5.	L-Serine capped magnetite nanoparticles	6.82	60	[38]
6.	RGO–Ni nanocomposite	47.62	60	[39]
7.	Graphene oxide/Beta zeolite	64.67	60	[40]
8.	Paper waste	75	60	[41]
9.	Iron oxide/carbon nanocomposites	93.35	60	[42]
10.	ABL@$ZnCl_2$	190.63	120	[43]
11.	Zinc oxide-loaded activated carbon(ZnO-AC)	128.2	140	[44]
12.	Uranyl coordination polymer	10	270	[45]
13.	Natural Moroccan Clay	83.95	270	[46]
14.	Grass-Waste	54	400	[47]
15.	$ZnFe_2O_4$ nanocomposite	9.83	1440	[48]
16.	Zeolitic imidazolate frameworks (ZIF)	85	1440	[49]
17.	**GOAC**	**90.77**	**60**	**Present work**

4.3.4 Congo-Red adsorption

Adsorption investigations on Congo Red (CR) dye, involving GO, AC, and GOAC were conducted by stirring an aqueous solution of 100ml, 10ppm dye with 0.01g of the respective adsorbents over defined time intervals. (Figure. 4.22). The resultant removal percentage is presented graphically in Figure. 4.23, and it emphasizes the slow adsorption kinetics observed (achieving only 51.77% removal within 60 minutes for the composite).

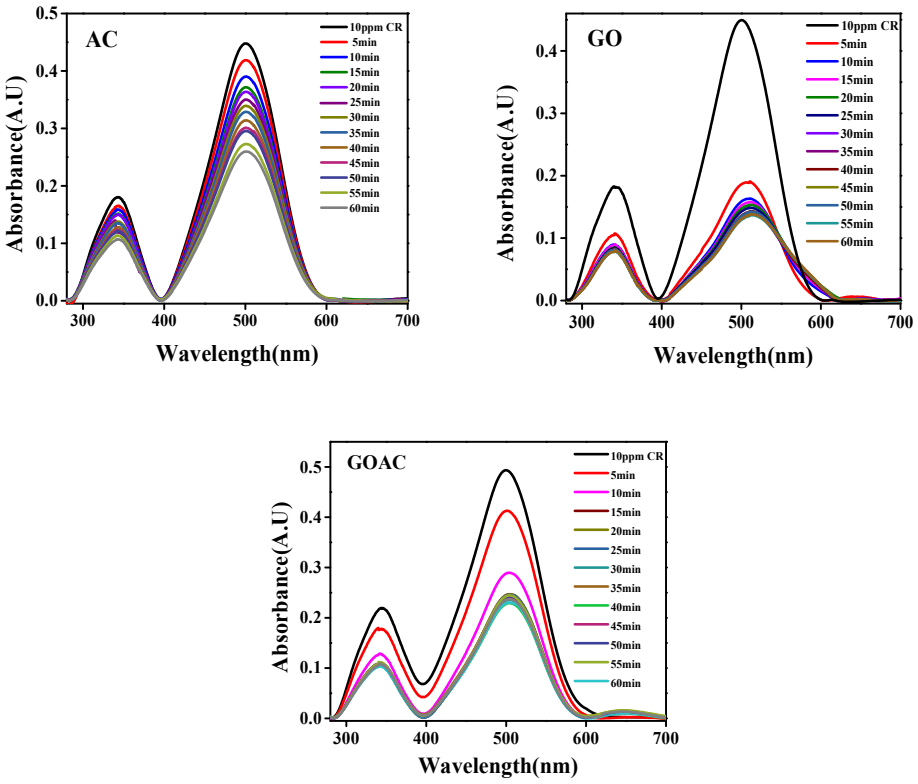

Figure 4.22 *UV-visible plots of CR dye adsorption by 0.01 g of a) GO, b) AC, and c) GOAC*

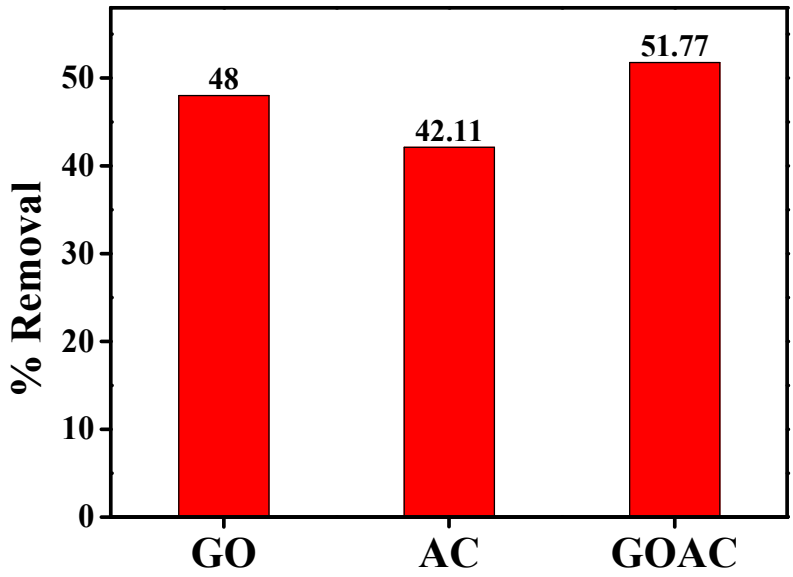

Figure 4.23 *Removal percentage of CR dye adsorption by 0.01 g of GO, AC, and GOAC*

GO, AC, and GOAC are ineffective adsorbents for congo red dye. This can be attributed to the fact that these adsorbents carry a negative charge, while congo red is also an anionic dye. As a result, there is a lower affinity for adsorption due to electrostatic repulsion between the negatively charged adsorbents and the dye molecules.

4.3.5 The mixture of dyes

Adsorption Experiment

The experimental procedure involves utilizing a solution comprising 100ml of 10ppm concentration for each dye (Methylene Blue, Rhodamine B, and Congo Red). To this solution, 0.01g of the adsorbent (GOAC) is introduced and stirred. Note that the concentrations are just the same as their single pollutant counterparts. The UV-visible absorbance of the solution is consistently monitored during the experiment. This process is replicated with a mixture containing all three dyes to investigate the adsorption impact within the dye mixture.

The assessment of individual dye and tertiary system percentage removal (from the equation) has been depicted graphically in Figure 4.24. Moreover, Table 4.12 provides a tabulated representation of the experimental data's removal percentage (equation 2.1). and equilibrium adsorption coefficient (qe, equation 2.2).

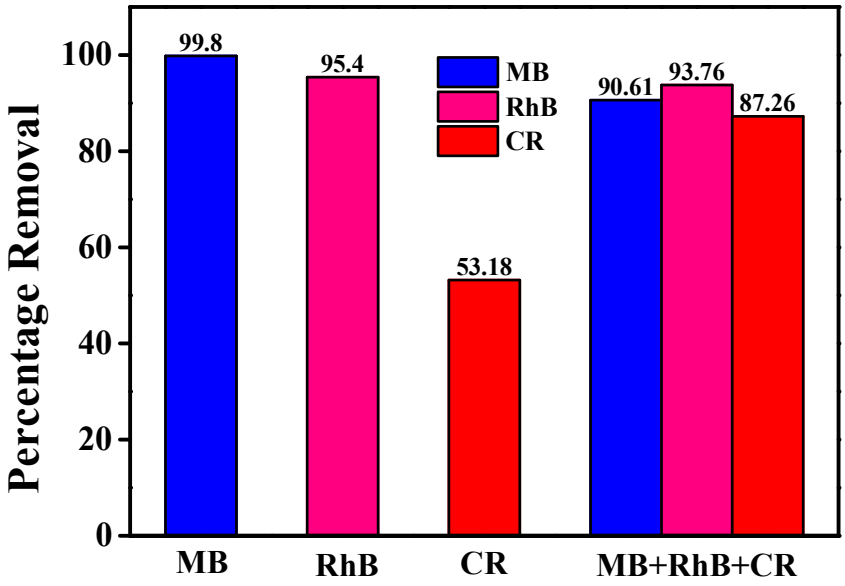

Figure 4.24 *Removal percentage of methylene blue, rhodamine B and congo red dye and the mixture of these three dyes with 0.01g of GOAC composite. Compared to individual dyes, the GOAC shows excellent adsorption towards the tertiary dye system.*

Table 4.12 *Removal percentage and adsorption capacity of methylene blue, rhodamine B and congo red dye and the mixture of these three dyes with 0.01g of GOAC composite*

Dye	Single system		Tertiary System	
	Removal percentage R_1	Adsorption Capacity Q_1 (mg/g)	Removal percentage R_3	Adsorption Capacity Q_3 (mg/g)
MB	99.81	120.90	90.61	17.28
RhB	95.42	90.77	93.76	38.80
CR	69.65	58.47	87.26	36.76

The adsorption experiment on three different dyes, namely MB, RhB, and CR, both individually and in combination, during activity with a GOAC composite, yielded intriguing results. Individually, MB exhibited an impressive removal percentage of 99.8%, showcasing the high affinity of the GOAC composite for this dye. RhB followed closely behind with a removal percentage of 95.4%, indicating its strong interaction with the composite material. However, CR displayed a comparatively lower removal percentage of 69.65%, suggesting a lesser affinity for adsorption onto the GOAC composite. A notable trend emerged when these dyes were combined in a tertiary system. The removal percentages for MB and RhB experienced a decrease to 90.61% and 93.76%, respectively, whereas CR showed an increase in removal in the tertiary system compared to individual systems. This phenomenon can be attributed to competitive adsorption, where the presence of multiple dye molecules hinders the adsorption capacity of the GOAC composite for each dye individually. The differences in the molecular structures and properties of the dyes may contribute to variations in their adsorption behaviour within the composite material. Overall, these results underscore the complex interplay between dye molecules and the adsorbent surface, offering insights crucial for optimizing the efficiency of wastewater treatment processes.

4.3.5.1 Regeneration

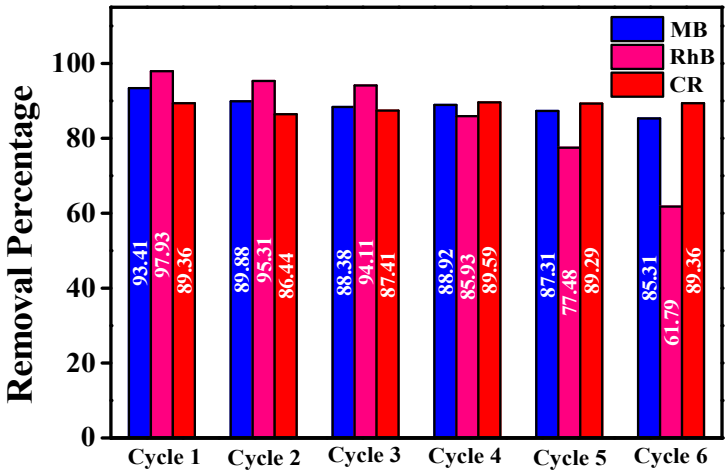

Figure 4.25 *Consecutive cycles of dye mixture removal*

Following each cycle, the GOAC composite underwent a regeneration procedure involving washing with distilled water and drying in a vacuum oven at 60 degrees Celsius for 12 hours. Across five cycles, the removal percentages of each dye within the tertiary system were tracked, revealing a notable trend depicted in Figure 4.25. MB and CR exhibited consistent removal percentages throughout the cycles, suggesting a stable interaction between these dyes and the composite material. Conversely, RhB displayed a distinct pattern of gradual decrease in removal percentage after each cycle. This divergence in behaviour may stem from differences in the dye molecules' affinity for the composite surface and their susceptibility to changes induced by the regeneration process. While MB and CR likely form strong and stable bonds with the composite, RhB's decreasing removal percentage hints at potential alterations in the composite's surface properties or the dye's interaction mechanisms over successive cycles.

4.3.6 Ciprofloxacin antibiotic adsorption

Following the methodology employed in previous dye adsorption experiments, graphene oxide (GO), activated carbon (AC), and the GOAC composite were evaluated for their effectiveness in removing the antibiotic ciprofloxacin from wastewater. Similar to the previous tests, 0.01g of each adsorbent was introduced into a solution containing 100 ml of 10 ppm ciprofloxacin (CF), and absorbance measurements were taken at regular 5-minute intervals. The corresponding UV-visible absorbance plots can be found in Figure 4.26.

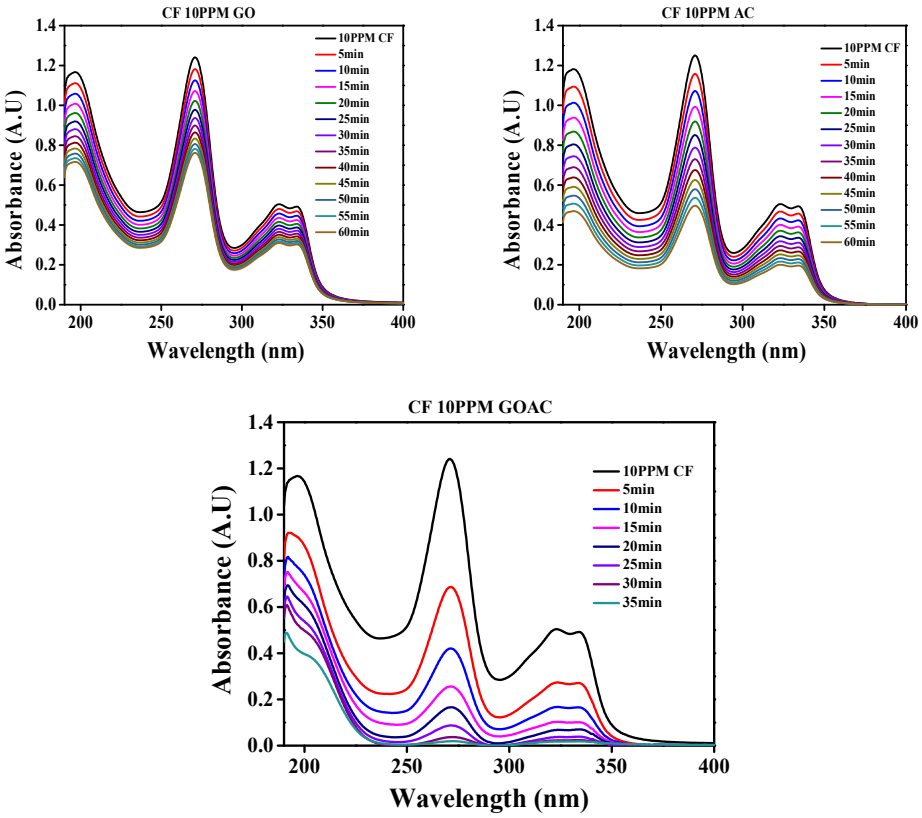

Figure 4.26 *UV-visible absorbance spectra of CF adsorption onto a) GO, b) AC and c) GOAC composite*

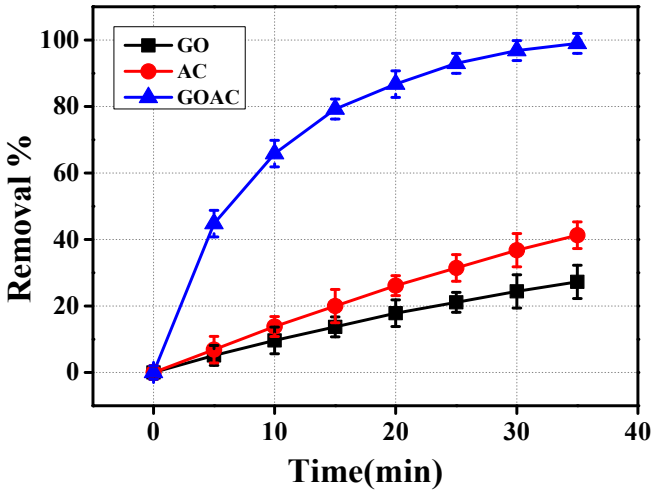

Figure 4.27 *Percentage of removal of CF with time for GO, AC and GOAC composite*

The percentage of CF removal within a 35-minute duration is illustrated and provided in Figure 4.27. This plot demonstrates the remarkable efficacy of CF

removal by the GOAC composite. Notably, the GOAC composite achieved a removal rate of 99% for 10ppm CF within 35 minutes, whereas GO and AC individually removed only less than 40% of CF within the same timeframe.

4.3.6.1 Ciprofloxacin calibration

The calibration curve for CF, fitted to a straight line, is given in Figure 4.28.

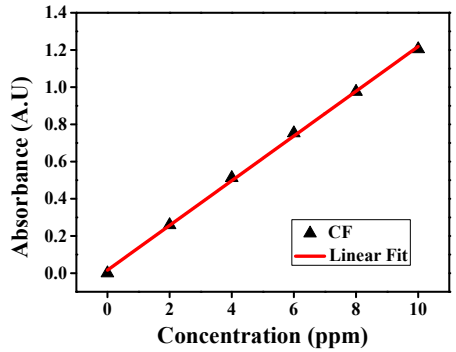

Figure 4.28 *Calibration curve for CF*

Table 4.13 *Calibration for CF*

Concentration (ppm)	Absorbance (AU)
0	0
2	0.258
4	0.512
6	0.753
8	0.976
10	1.205

From this plot, the equation connecting absorbance and concentration is obtained as

$$\mathbf{Abs = 0.120*Conc + 0.016}$$

This equation can convert any given absorbance to the corresponding concentration for CF.

4.3.6.2 Adsorption kinetics

The adsorption behaviour of CF on GOAC has been investigated using the pseudo-first-order and pseudo-second-order kinetic models to understand the kinetics involved in the process.

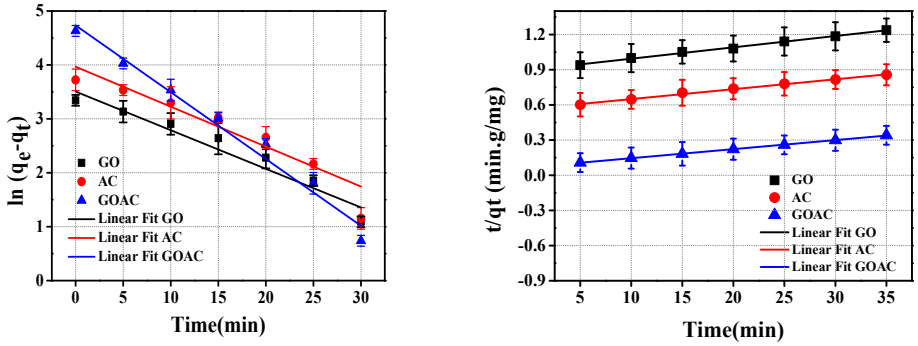

Figure 4.29 *[A] Pseudo First order kinetic model for adsorption of 10ppm CF onto GO, AC and GOAC composite. [B] Pseudo Second-order kinetic model for adsorption of 10ppm CF onto GO, AC and GOAC composite.*

Table 4.14 Adsorption kinetic parameters for pseudo-first and pseudo-second order kinetics for the adsorption of CF onto GO, AC and GOAC composite.

Sample name	$q_{e\ direct}$ **(mg/g)**	**Pseudo-first-order kinetics**		**Pseudo-second-order kinetics**	
		$q_{e\ kinetic}$ **(mg/g)**	R^2	$q_{e\ kinetic}$ **(mg/g)**	R^2
GO	28.29	33.31	0.93	30.09	0.994
AC	42.84	52.77	0.91	46.48	0.995
GOAC	122.73	113.75	0.97	129.53	0.999

The pseudo-first-order and pseudo-second-order models were fitted to the data and are shown in **Figure4.29**, and the corresponding kinetic parameters obtained are tabulated in **Table 4.14**. The best fit is observed with the pseudo-second-order kinetics model, indicating the chemical interaction between the composite and CF. This provides valuable insight into the mechanism of adsorption. The pseudo-first-order fit also matches well, suggesting physical interactions between CF and the adsorbents. Pore filling, a key mechanism in physical adsorption, plays a significant role in adsorption.

Furthermore, the maximum adsorption efficiency was determined to be 123 mg/g for GOAC in CF adsorption, which aligns with the pseudo-second-order fit.

These data indicate that the adsorption capacity of the GOAC composite surpasses that of its individual components, namely GO and AC, highlighting its exceptional adsorption capabilities as a composite.

4.3.6.3 Mechanism

The adsorption removal mechanism of ciprofloxacin by GOAC primarily involves four concurrent pathways: (a) π-π interaction, (b) hydrogen bonding, (c) electrostatic interaction, and (d) pore filling **[50][51].**

Numerous studies have highlighted π-π electron donor-acceptor interaction as a significant driving force for the sorption of organic compounds containing benzene rings onto carbon surfaces. The presence of residual -OH groups on the graphene surface renders the benzene ring π-electron-rich, facilitating π-π electron donor-acceptor interaction [50].

Previous research has revealed that ciprofloxacin molecules, featuring two -C=O and one -OH groups, can establish hydrogen bonds with the surface oxygen of carbon materials and functional groups on the surface. Functional groups found in organic chemicals, like -NH and -OH, act as donors for hydrogen bonding, enabling the formation of hydrogen bonds with graphene oxide sheets and AC, with benzene rings serving as acceptors for hydrogen bonding. Similarly, polar functional groups within ciprofloxacin can also function as acceptors for hydrogen bonding, facilitating the formation of hydrogen bonds with -OH groups on graphene. The cumulative effect of multiple hydrogen bonds between ciprofloxacin and adsorbents further enhances adsorption affinity [50].

The charged groups in ciprofloxacin molecules, such as the quinolone ring, can interact with oppositely charged functional groups on the surface of the graphene oxide-activated carbon composite through electrostatic interactions, facilitating adsorption.

The porous structure of the graphene oxide-activated carbon composite allows ciprofloxacin molecules to diffuse into the pores and get trapped through physical and chemical interactions with the internal surface of the composite material.

Overall, the adsorption of ciprofloxacin antibiotic using a graphene oxide-activated carbon composite is a complex process involving a combination of physical and chemical interactions between the composite material's surface functional groups and ciprofloxacin's molecular structure.

4.3.6.4 Comparison with other adsorbents

Table 4.15 *Comparison table showing the adsorption parameters of various adsorbents towards ciprofloxacin antibiotic.*

Sl. No,	Adsorbent	Q_{max} (mg/g)	Removal percentage (%)	Adsorbent Dosage/time	Ref
1	MGO@PANI	106.4	97	20 mg, time 30 min	[52]
2	Diatomaceous earth	105.1	97	2mg	[53]
3	Fe-based MIL-88B MOF	102.5		240 min	[54]
4	sodium alginate/graphene oxide hydrogel beads (GSA)	100		480 mg 72h	[55]
5	nickel oxide nanoparticles	99.81	99.8	120min, 0.04–0.14 g/L	[56]
6	Metal organic frameworks	98.20	-	0.05 g to 0.1 g, 540 min	[57]
7	$CoFe_2O_4$/activated carbon@chitosan	93.50	93.5	12–100 mg/L, 30 min	[58]
8	banyan aerial roots	86.58	96.93	120 mg, 48 h	[59]
9	AC from hazelnut	73.64	-	0.3–3.0 g/L,60min	[60]
10	Aluminum-Pillared Kaolin Sodium Alginate Beads	68.36	-	0.1 g/50 mL, 1440 min	[61]
11	metal organic framework MIL-101	63.28	-	1 and 15 mg,90 min	[62]
12	Biochar	42.90		12 h, 50 mg	[63]
13	bamboo char-coal	36.02	9-0	0.1g, 48 h	[64]
14	carbon nanofibers	10.36	-	300 mg, 4 h	[65]
15	schorl	8.49	75	120min	[66]
16	**GOAC**	**123**	**99**	**0.01g. 60min**	**Present work**

4.4 Conclusion

In this study, we successfully synthesized a graphene oxide-activated carbon (GOAC) composite employing a single-step mixing approach. The composite effectively adsorbed different dyes and antibiotics, with considerably high adsorption capacities, from contaminated water. Incorporating activated carbon (AC) into the graphene oxide (GO) matrix notably bolstered the composite's thermal stability. Furthermore, the propensity of GO to agglomerate upon water exposure was effectively mitigated through the strategic inclusion of AC. Of paramount importance for adsorption applications, the structural integrity of both GO and AC remained unaltered following composite formation. This aspect underpins the composite's suitability for practical implementation.

Adsorption studies using Methylene Blue (MB) dye demonstrated the exceptional performance of the GOAC composite, with adsorption capacities of 120.9 mg/g and 274.7 mg/g achieved at adsorption durations of 14 and 80 minutes for 0.01g and 0.005g of adsorbent respectively, resulting in 100% dye removal. Similarly, experiments with Rhodamine B under comparable conditions showed a removal efficiency of 95.4% within 60 minutes, corresponding to an adsorption capacity of 90.9 mg/g. Congo Red, an anionic dye, exhibited relatively lower adsorption on the GOAC composite. However, in mixed-dye systems, the adsorption of all dyes, including congo red, significantly improved, indicating potential synergistic interactions. For the pharmaceutical pollutant ciprofloxacin, the composite achieved an impressive 99% removal within 35 minutes, with an adsorption capacity of 123 mg/g. All adsorption processes were found to conform to pseudo-second-order kinetics, suggesting that chemisorption is the dominant mechanism involving electron sharing or exchange between the adsorbent and adsorbate.

Even after multiple regeneration cycles, the GOAC composite maintained high adsorption efficiency, highlighting its durability and sustained performance. Additionally, our analysis of contaminant interactions with the GOAC composite offered valuable insights into the complex adsorption mechanisms.

4.5 References

1. Arabpour, A., Dan, S. & Hashemipour, H. Preparation and optimization of novel graphene oxide and adsorption isotherm study of methylene blue. Arab. J. Chem. 14, 103003 (2021).

2. Ying, T. Y., Raman, A. A. A., Bello, M. M., & Buthiyappan, A. (2020). Magnetic graphene oxide-biomass activated carbon composite for dye removal. Korean Journal of Chemical Engineering, 37, 2179-2191.

3. Vargas, A. M., Cazetta, A. L., Kunita, M. H., Silva, T. L., & Almeida, V. C. (2011). Adsorption of methylene blue on activated carbon produced from flamboyant pods (Delonix regia): Study of adsorption isotherms and kinetic models. Chemical Engineering Journal, 168(2), 722-730.

4. Wilczak, A., & Keinath, T. M. (1993). Kinetics of sorption and desorption of copper (II) and lead (II) on activated carbon. Water Environment Research, 65(3), 238-244.

5. Machida, M., Kikuchi, Y., Aikawa, M., & Tatsumoto, H. (2004). Kinetics of adsorption and desorption of Pb (II) in aqueous solution on activated carbon by two-site adsorption model. Colloids and Surfaces A: Physicochemical and Engineering Aspects, 240(1-3), 179-186.

6. Dai, K., Peng, X., Yang, P., Li, M., Tang, C., Zhuang, W., ... & Wu, J. (2020). Highly selective and efficient lignin-magnesium for removing cationic dyes from wastewater. Journal of Environmental Chemical Engineering, 8(5), 104283.

7. Li, H., Pan, L., Nie, C., Liu, Y., & Sun, Z. (2012). Reduced graphene oxide and activated carbon composites for capacitive deionization. Journal of Materials Chemistry, 22(31), 15556-15561.

8. Abd-Elhamid, A. I., Elgoud, E. M., Emam, S., & Aly, H. F. (2022). Superior adsorption performance of citrate modified graphene oxide as nano material for removal organic and inorganic pollutants from aqueous solution. Scientific Reports, 12(1), 1-14.

9. Yang, Z., Ju, X., Liao, H., Meng, Z., Ning, H., Li, Y., ... & Long, J. (2021). Preparation of activated carbon doped with graphene oxide porous materials and their high gas adsorption performance. ACS omega, 6(30), 19799-19810.

10. Liu, X., & Wang, J. (2020). Electro-assisted adsorption of Cs (I) and Co (II) from aqueous solution by capacitive deionization with activated carbon cloth/graphene oxide composite electrode. Science of the Total Environment, 749, 141524.

11. Saeidi, N., Parvini, M., & Niavarani, Z. (2015). High surface area and mesoporous graphene/activated carbon composite for adsorption of Pb (II) from wastewater. Journal of Environmental Chemical Engineering, 3(4), 2697-2706.

12. Qiu, X., Xiao, Z., Wang, L., & Fan, L. Z. (2018). High rate integrated quasi-solid state supercapacitors based on nitrogen-enriched active carbon fiber/reduced graphene oxide nanocomposite. Carbon, 130, 196-205.

13. Baishya, P., & Maji, T. K. (2018). A comparative study on the properties of graphene oxide and activated carbon based sustainable wood starch composites. International journal of biological macromolecules, 115, 970-977.

14. Bhattacharyya, A., Ghorai, S., Rana, D., Roy, I., Sarkar, G., Saha, N. R., ... & Chattopadhyay, D. (2021). Design of an efficient and selective adsorbent of cationic dye through activated carbon-graphene oxide nanocomposite: Study on mechanism and synergy. Materials Chemistry and Physics, 260, 124090.

15. Pal, A., Uddin, K., Rocky, K. A., Thu, K., & Saha, B. B. (2019). CO2 adsorption onto activated carbon–graphene composite for cooling applications. International Journal of Refrigeration, 106, 558-569

16. Ndagijimana, P., Rong, H., Ndokoye, P., Mwizerwa, J. P., Nkinahamira, F., Luo, S., ... & Cui, B. (2023). A review on activated carbon/graphene composite-based materials: Synthesis and applications. Journal of Cleaner Production, 138006.

17. Arias F.E.A., Beneduci A., Chidichimo F., Furia E., Straface S. Study of the adsorption of mercury (II) on lignocellulosic materials under static and dynamic conditions. Chemosphere. 2017;180:11–23. doi: 10.1016/j.chemosphere.2017.03.137

18. Nasiri, A., Heidari, M. R., Javid, N., & Yazdanpanah, G. (2022). New efficient and recyclable magnetic nanohybrid adsorbent for the metronidazole removal from simulated wastewater. *Journal of Materials Science Materials in Electronics*, *33*(33), 25103–25126. https://doi.org/10.1007/s10854-022-09216-3

19. El-Sharkaway, E. A., Kamel, R. M., El-Sherbiny, I. M. & Gharib, S. S. Removal of methylene blue from aqueous solutions using polyaniline/graphene oxide or polyaniline/reduced graphene oxide composites. Environ. Technol. 41(22), 2854–2862. https://doi. org/10.1080/09593330.2019.1585481 (2020).

20. Verma, M., Lee, I., Oh, J., Kumar, V. & Kim, H. Synthesis of EDTA-functionalized graphene oxide-chitosan nanocomposite for simultaneous removal of inorganic and organic pollutants from complex wastewater. Chemosphere 287(4), 132385 (2022)

21. Ai, L., Zhang, C., & Chen, Z. (2011). Removal of methylene blue from aqueous solution by a solvothermal-synthesized graphene/magnetite composite. Journal of hazardous materials, 192(3), 1515-1524.

22. Xie, G.; Xi, P.; Liu, H.; Chen, F.; Huang, L.; Shi, Y.; Hou, F.; Zeng, Z.; Shao, C.; Wang, J. A Facile Chemical Method to Produce Superparamagnetic Graphene Oxide-Fe3O4 Hybrid Composite and Its Application in the Removal of Dyes from Aqueous Solution. J. Mater. Chem. 2012, 22, 1033−1039.

23. Li, L.; Fan, L.; Duan, H.; Wang, X.; Luo, C. Magnetically Separable Functionalized Graphene Oxide Decorated with Magnetic Cyclodextrin as an Excellent Adsorbent for Dye Removal. RSC Adv. 2014, 4, 37114

24. Fan, L.; Luo, C.; Li, X.; Lu, F.; Qiu, H.; Sun, M. Fabrication of Novel Magnetic Chitosan Grafted with Graphene Oxide to Enhance Adsorption Properties for Methyl Blue. J. Hazard. Mater. 2012, 215− 216, 272−279.

25. Fan, L.; Luo, C.; Sun, M.; Qiu, H.; Li, X. Synthesis of Magnetic β-Cyclodextrin−chitosan/Graphene Oxide as Nanoadsorbent and Its Application in Dye Adsorption and Removal. Colloids Surf., B 2013, 103, 601−607.

26. Ramesha, G. K., Kumara, A. V., Muralidhara, H. B., & Sampath, S. (2011). Graphene and graphene oxide as effective adsorbents toward anionic and cationic dyes. Journal of colloid and interface science, 361(1), 270-277.

27. Ajeel, S. J., Beddai, A. A., & Almohaisen, A. M. N. (2022). Preparation of alginate/graphene oxide composite for methylene blue removal. Materials Today: Proceedings, 51, 289-297.

28. Zhang, X., Li, Y., Li, M., Du, Q., Li, H., Wang, Y., ... & Yu, Y. (2020). Removal behavior of methylene blue from graphene oxide/gluten composite material: kinetics, isotherms and thermodynamics. International Journal of Clothing Science and Technology.

29. Deng, J. H., Zhang, X. R., Zeng, G. M., Gong, J. L., Niu, Q. Y., & Liang, J. (2013). Simultaneous removal of Cd (II) and ionic dyes from aqueous solution using magnetic graphene oxide nanocomposite as an adsorbent. Chemical Engineering Journal, 226, 189–200.

30. Ai, L., Zhang, C., & Chen, Z. (2011). Removal of methylene blue from aqueous solution by a solvothermal-synthesized graphene/magnetite composite. Journal of hazardous materials, 192(3), 1515-1524.

31. Tran, H. V., Bui, L. T., Dinh, T. T., Le, D. H., Huynh, C. D., & Trinh, A. X. (2017). Graphene oxide/Fe3O4/chitosan nanocomposite: a recoverable and recyclable adsorbent for organic dyes removal. Application to methylene blue. Materials Research Express, 4(3), 035701.

32. Ahmed, T., & Gupta, S. S. (2021). Adsorptive Accumulation of Methylene Blue Dye from Aqueous Effluent by NiFe2O4-GO Nano-adsorbent. World, 9(1), 28-41.

33. Shao, W., Ma, Y., Jin, P., & Yang, H. (2020). Removal of Hg (II) and methylene blue from single aqueous solution by ethylenediamine modified magnetic graphene oxide nanocomposites. International Journal of Environmental Technology and Management, 23(5-6), 386-396.

34. Xiao, W., Garba, Z.N., Sun, S., Lawan, I., Wang, L.,Lin, M., and Yuan, Z., 2020, Preparation andevaluation of an effective activated carbon fromwhite sugar for the adsorption of Rhodamine B dye,J. Cleaner Prod., 253, 119989

35. Kuśmierek, K., Fronczyk, J., & Świątkowski, A. (2023). Adsorptive removal of rhodamine B dye from aqueous solutions using mineral materials as low-cost adsorbents. *Water, Air, & Soil Pollution*, *234*(8), 531.

36. Zhu, Z., Xiang, M., Li, P., Shan, L., and Zhang, P.,2020, Surfactant-modified three-dimensionallayered double hydroxide for the removal of methylorange and

Rhodamine B: Extended investigations inbinary dye systems, J. Solid State Chem., 288, 121448

37. Stavrinou, A., Aggelopoulos, C.A., and Tsakiroglou,C.D., 2018, Exploring the adsorption mechanismsof cationic and anionic dyes onto agricultural wastepeels of banana, cucumber and potato: Adsorptionkinetics and equilibrium isotherms as a tool, J.Environ. Chem. Eng., 6 (6), 6958–6970.

38. Belachew, N., Rama Devi, D., and Basavaiah, K.,2017, Green synthesis and characterization of L-Serine capped magnetite nanoparticles for removalof Rhodamine B from contaminated water, J. Exp.Nanosci., 12 (1), 114–128

39. Jinendra, U., Bilehal, D., Nagabhushana, B., & Kumar, A. P. (2021, April). Adsorptive removal of Rhodamine B dye from aqueous solution by using graphene–based nickel nanocomposite. *Heliyon*, *7*(4), e06851. https://doi.org/10.1016/j.heliyon.2021.e06851

40. Cheng, Z.L., Li, Y.X., and Liu, Z., 2017, Noveladsorption materials based on graphene oxide/Betazeolite composite materials and their adsorptionperformance for rhodamine B , J. Alloys Compd.,708, 255–263

41. Thakur, A., and Kaur, H., 2017, Response surfaceoptimization of Rhodamine B dye removal using paper industry waste as adsorbent, Int. J. Ind. Chem.,8 (2), 175–186

42. Ianoş, R., Păcurariu, C., Muntean, S.G., Muntean, E.,Nistor, M.A., and Nižňanský, D., 2018, Combustionsynthesis of iron oxide/carbon nanocomposites,efficient adsorbents for anionic and cationic dyesremoval from wastewaters, J. Alloys Compd., 741,1235–1246

43. Li, P., Zhao, T., Zhao, Z., Tang, H., Feng, W., & Zhang, Z. (2023). Biochar derived from Chinese herb medicine residues for rhodamine B dye adsorption. *ACS omega*, *8*(5), 4813-4825.

44. Li, Y., Yan, X., Hu, X., Feng, R., and Zhou, M., 2019,Trace pyrolyzed ZIF-67 loaded activated carbonpellets for enhanced adsorption and catalyticdegradation of Rhodamine B in water, Chem. Eng.J., 375, 122003

45. Ren, Y.N., Xu, W., Zhou, L.X., and Zheng, Y.Q., 2017,Efficient tetracycline adsorption and photocatalyticdegradation of rhodamine B by uranyl coordinationpolymer, J. Solid State Chem., 251, 105–112.

46. Damiyine, B., Guenbour, A., and Boussen, R., 2017,Rhodamine B adsorption on natural and modifiedMoroccan clay with cetyltrimethylammoniumbromide: Kinetics, equilibrium and thermodynamics,J. Mater. Environ. Sci., 8 (3), 860–871.

47. Zahir, A., Aslam, Z., Aslam, U., Abdullah, A., Ali, R.,and Bello, M.M., 2020, Paspalum notatum grass-waste-based adsorbent for Rhodamine B removalfrom polluted water, Chem. Biochem. Eng. Q., 34 (2),93–104

48. Konicki, W., Siber, D., and Narkiewicz, U., 2017,Removal of Rhodamine B from aqueous solution byZnFe2O4 nanocomposite with magnetic separationperformance, Pol. J. Chem. Technol., 19 (4), 65–74

49. Zhang, J., Hu, X., Yan, X., Feng, R., Zhou, M., andXue, J., 2019, Enhanced adsorption of RhodamineB by magnetic nitrogen-doped porous carbon prepared from bimetallic ZIFs, Colloids Surf., A, 575,10–17

50. Ma, J., Yang, M., Yu, F., & Zheng, J. (2015, September 4). Water-enhanced Removal of Ciprofloxacin from Water by Porous Graphene Hydrogel. *Scientific Reports*, *5*(1). https://doi.org/10.1038/srep13578

51. Priyanka, Pal, B., Singh, S., & Bansal, M. (2024, March). Superior adsorptive removal of ciprofloxacin by graphene oxide modified Ni-Al layered double hydroxide composites. *Journal of Alloys and Compounds*, *976*, 173220. https://doi.org/10.1016/j.jallcom.2023.173220

52. Balarak, D., Mostafapour, F., & Azarpira, H. (2016). Adsorption Kinetics and Equilibrium of Ciprofloxacin from Aqueous Solutions Using Corylus avellana (Hazelnut) Activated Carbon. *British Journal of Pharmaceutical Research*, *13*(3), 1–14. https://doi.org/10.9734/bjpr/2016/29357

53. Bayazit, Ş. S., Danalıoğlu, S. T., Salam, M. A., & Kuyumcu, Ö. K. (2017). Preparation of magnetic MIL-101 (Cr) for efficient removal of ciprofloxacin. *Environmental Science and Pollution Research*, *24*(32), 25452–25461. https://doi.org/10.1007/s11356-017-0121-0

54. Fan, H., Ma, Y., Wan, J., Wang, Y., Li, Z., & Chen, Y. (2020). Adsorption properties and mechanisms of novel biomaterials from banyan aerial roots via simple modification for ciprofloxacin removal. *The Science of the Total Environment*, *708*, 134630. https://doi.org/10.1016/j.scitotenv.2019.134630

55. Gadipelly, C. R., Marathe, K. V., & Rathod, V. K. (2018). Effective adsorption of ciprofloxacin hydrochloride from aqueous solutions using metal-organic framework. *Separation Science and Technology*, *53*(17), 2826–2832. https://doi.org/10.1080/01496395.2018.1474225

56. García-Alonso, J. A., Sulbarán-Rangel, B. C., Bandala, E. R., & Del Real-Olvera, J. (2019). Adsorption and kinetic studies of the removal of ciprofloxacin from aqueous solutions by diatomaceous earth. *DESALINATION AND WATER TREATMENT*, *162*, 331–340. https://doi.org/10.5004/dwt.2019.24313

57. Hu, Y., Pan, C., Zheng, X., Liu, S., Hu, F., Xu, L., Xu, G., & Peng, X. (2020). Removal of Ciprofloxacin with Aluminum-Pillared Kaolin Sodium Alginate Beads (CA-Al-KABs): Kinetics, Isotherms, and BBD Model. *Water*, *12*(3), 905. https://doi.org/10.3390/w12030905

58. Li, X., Wang, W., Dou, J., Gao, J., Chen, S., Quan, X., & Zhao, H. (2016). Dynamic adsorption of ciprofloxacin on carbon nanofibers: Quantitative measurement by in situ fluorescence. *Journal of Water Process Engineering*, *9*, e14–e20. https://doi.org/10.1016/j.jwpe.2014.12.006

59. Malakootian, M., Nasiri, A., & Mahdizadeh, H. (2018). Preparation of CoFe2O4/activated carbon@chitosan as a new magnetic nanobiocomposite for adsorption of ciprofloxacin in aqueous solutions. *Water Science & Technology*, *78*(10), 2158–2170. https://doi.org/10.2166/wst.2018.494

60. Nodeh, M. K. M., Soltani, S., Shahabuddin, S., Nodeh, H. R., & Sereshti, H. (2018). Equilibrium, Kinetic and Thermodynamic Study of Magnetic Polyaniline/Graphene Oxide Based Nanocomposites for Ciprofloxacin Removal from Water. *Journal of Inorganic and Organometallic Polymers and Materials*, *28*(3), 1226–1234. https://doi.org/10.1007/s10904-018-0782-2

61. Rahdar, S., Rahdar, A., Igwegbe, C. A., Moghaddam, F., & Ahmadia, S. (2019). Synthesis and physical characterization of nickel oxide nanoparticles and its application study in the removal of ciprofloxacin from contaminated water by adsorption: Equilibrium and kinetic studies. *Desalination and Water Treatment*, *141*, 386–393. https://doi.org/10.5004/dwt.2019.23473

62. Shang, J. G., Kong, X. R., He, L. L., Li, W. H., & Liao, Q. J. H. (2016). Low-cost biochar derived from herbal residue: characterization and application for ciprofloxacin adsorption. *International Journal of Environmental Science and Technology*, *13*(10), 2449–2458. https://doi.org/10.1007/s13762-016-1075-3

63. Van Tran, T., Nguyen, D. T. C., Le, H. T. N., Vo, D. N., Doan, V., Dinh, V., Nguyen, H. T., Nguyen, T. D., & Bach, L. G. (2019). Amino-functionalized MIL-88B(Fe)-based porous carbon for enhanced adsorption toward ciprofloxacin pharmaceutical from aquatic solutions. *Comptes Rendus Chimie*, *22*(11–12), 804–812. https://doi.org/10.1016/j.crci.2019.09.003

64. Wang, L., Chen, G., Ling, C., Zhang, J., & Szerlag, K. (2017). Adsorption of ciprofloxacin on to bamboo charcoal: Effects of pH, salinity, cations, and phosphate. *Environmental Progress & Sustainable Energy*, *36*(4), 1108–1115. https://doi.org/10.1002/ep.12579

65. Yin, D., Xu, Z., Shi, J., Shen, L., & He, Z. (2017). Adsorption characteristics of ciprofloxacin on the schorl: kinetics, thermodynamics, effect of metal ion and mechanisms. *Journal of Water Reuse and Desalination*, *8*(3), 350–359. https://doi.org/10.2166/wrd.2017.143

66. Zhao, P., Yu, F., Wang, R., Ma, Y., & Wu, Y. (2018). Sodium alginate/graphene oxide hydrogel beads as permeable reactive barrier material for the remediation of ciprofloxacin-contaminated groundwater. *Chemosphere*, *200*, 612–620. https://doi.org/10.1016/j .chemosphere.2018.02.157

CHAPTER 5

GRAPHENE OXIDE MODIFICATION USING GOLD NANOPARTICLES - COMPOSITE FORMATION

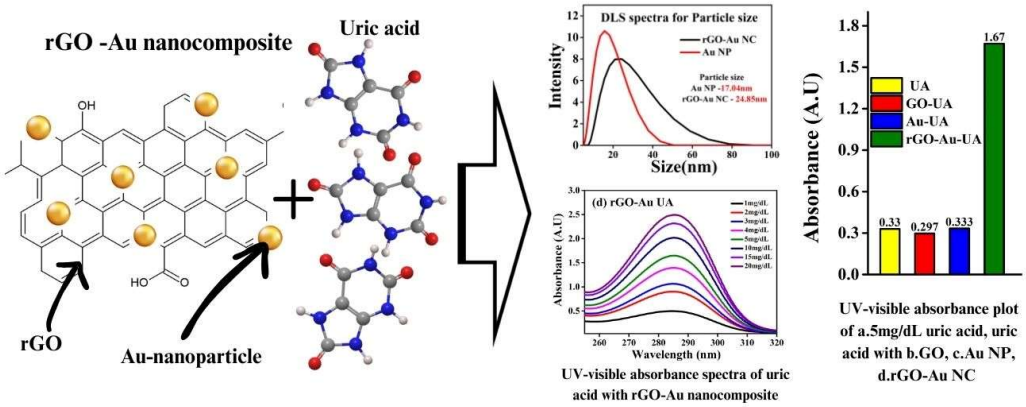

Scope of the Chapter

- *rGO-Au nanocomposite boosts uric acid detection sensitivity significantly*
- *Detection sensitivity aligns with uric acid levels in bodily fluids.*
- *Composite's enhanced sensitivity aids reliable biosensing applications*

Abstract

This chapter presents a facile method for biosensing uric acid using reduced graphene oxide-gold (rGO-Au) nanocomposite. Uric acid serves as a crucial biomarker for various pathological conditions, including gout, metabolic syndrome, type-2 diabetes, kidney malfunctions and cardiovascular diseases. Therefore, facile techniques for monitoring uric acid in the blood serum levels (2 – 10 mg/dL) are in demand. Here, we demonstrate uric acid sensing with a 2 mg/dL detection limit and 1mg/dL sensitivity. The synthesized graphene oxide (GO), gold nanoparticles (AuNPs), and the rGO-Au nanocomposite were studied based on UV-visible spectroscopy- varying the levels of uric acid (1 to 20 mg/dL). Our findings reveal that the uric acid exhibits significantly higher UV-visible absorbance (five times) when combined with rGO-Au nanocomposite. The enhancement is attributed to the synergistic effect of surface plasmon resonance (SPR) and the unique properties of the nanocomposite. This work provides valuable insights into designing highly sensitive and cost-effective uric acid biosensors with potential applications in clinical diagnostics and health monitoring.

5.1 Introduction

Uric acid (UA) is a metabolic end-product of human purine nucleotides. It serves as a crucial biomarker for various pathological conditions, including gout, metabolic syndrome, type-2 diabetes, kidney malfunctions and cardiovascular diseases [1]. The upper concentration limits for uric acid are 7 mg/dL in men and 6 mg/dL in women [2]. Accurate and timely detection of uric acid levels is critical for effective clinical management and early intervention in various health issues.

The phosphotungstic method is one of the earliest techniques for uric acid (UA) detection [3]. However, this method has several drawbacks, including the toxicity and instability of cyanide solutions, the tendency for final reaction mixtures to become cloudy, and poor reproducibility and operability [4]. Conventional methods for detecting uric acid (UA) include chemiluminescence, fluorescence, spectrophotometry, high-performance liquid chromatography (HPLC) paired with mass spectrometry, ion chromatography, and capillary electrophoresis combined with either amperometry or chemiluminescence detection. Colorimetric methods and enzymatic assays are also commonly employed for UA detection [5]. To enhance detection performance, researchers often combine two or more detection techniques. The traditional methods for uric acid detection usually suffer from limitations such as complexity, high cost, and lack of portability - underscoring the urgent need for innovative and efficient sensing platforms.

In recent years, nanotechnology has emerged as a promising avenue for developing sensitive and selective biosensors due to its inherent properties, such as high surface area, excellent conductivity, and tunable surface chemistry [6]. Gold nanoparticles (AuNPs) have garnered significant attention for their electronic and surface properties among various nanomaterials. The surface plasmon resonance (SPR) makes AuNPs highly sensitive to changes in their local environment, enabling the detection of biomolecular interactions at very low concentrations. [7]. Reduced graphene oxide (rGO), a two-dimensional carbon nanomaterial, has demonstrated exceptional potential in enhancing the performance of biosensors through its large surface area, excellent mechanical strength, and facile functionalization capabilities [8].

Lee et al. developed a gas sensor based on rGO that demonstrated high selectivity for detecting dinitrotoluene (DNT), a compound commonly associated with explosives [9]. Sharma et al. observed that incorporating rGO significantly enhanced gas sensing performance [10]. Du et al. reported improved sensitivity in NO_2 detection when using rGO-based composites [11].

rGO enhances the electron transfer rate at the sensor surface, improving sensitivity [12][13]. rGO-based composites have been reported to be attractive for detecting DNA, RNA, and proteins [14].

This study explores the utility of a novel nanocomposite comprising gold nanoparticles and reduced graphene oxide (rGO-Au) to detect uric acid. The synergistic combination of AuNPs and GO is expected to exploit the advantages of both materials, leading to improved sensitivity, selectivity, and stability of the sensing platform. Investigating UV-visible spectra absorbance intensity as a readout mechanism attempts a simple and cost-effective means for quantifying uric acid concentrations with high precision and accuracy. [15]

Herein, we elucidate the synthesis process of the rGO-Au nanocomposite and investigate its physicochemical properties using various analytical techniques. Subsequently, the performance of the developed biosensing element is evaluated through systematic characterization of its sensing capabilities, including sensitivity, selectivity, response time, and stability. Finally, we discuss the potential applications of the rGO-Au nanocomposite in clinical diagnostics, point-of-care testing, and biomedical research, highlighting its significance in advancing the field of uric acid sensing and beyond.

5.2 Experimental Section

5.2.1 Gold nanoparticle synthesis

Gold nanoparticles were prepared using the modified Turkevich chemical reduction technique using gold (III) chloride dihydrate solution and trisodium citrate dihydrate [16].

5.2.2 Graphene Oxide Synthesis

GO was synthesized using the Hummers method [17] and is detailed in section 2.1

5.2.3 rGO-Au nanocomposite synthesis

The GO aqueous dispersion was diluted to achieve a final concentration of 0.4 mg/mL and then subjected to ultrasonication until achieving a homogeneous dispersion. For synthesizing the rGO-Au nanocomposite, 20 mL of gold (III) chloride dihydrate solution (1 mM) in double distilled water was heated to its boiling point under vigorous stirring on a magnetic hot plate.

Subsequently, 2 mL of GO dispersion (0.3 mg/mL) in a solution of trisodium citrate dihydrate (1% w/v) was added to the gold solution to obtain wine-red coloured rGO-Au nanocomposite [18].

5.3 Results and Discussion

5.3.1 Characterization

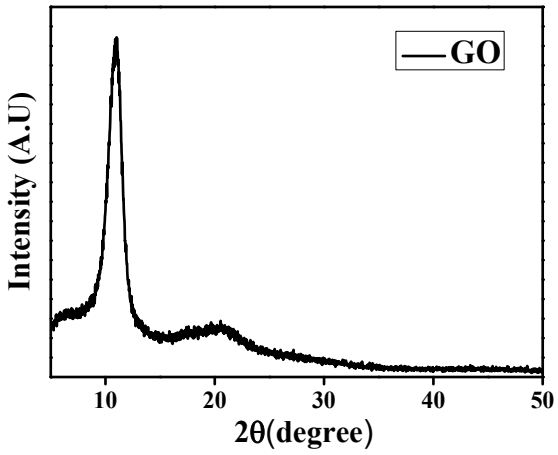

Figure 5.1: *X-ray diffraction pattern of GO with a single intense peak at 11.04° indicating [001] plane of GO. The slight hump near 20° corresponds to the peak of the glass substrate.*

Figure 5.1 shows the synthesized graphene oxide (GO) X-ray diffraction pattern, featuring a peak at $2\theta = 11.04°$. This peak corresponds to an interlayer spacing (d) of approximately 8.01 Å, consistent with previously reported values for GO [19]. This interlayer spacing suggests a well-oxidized sample.

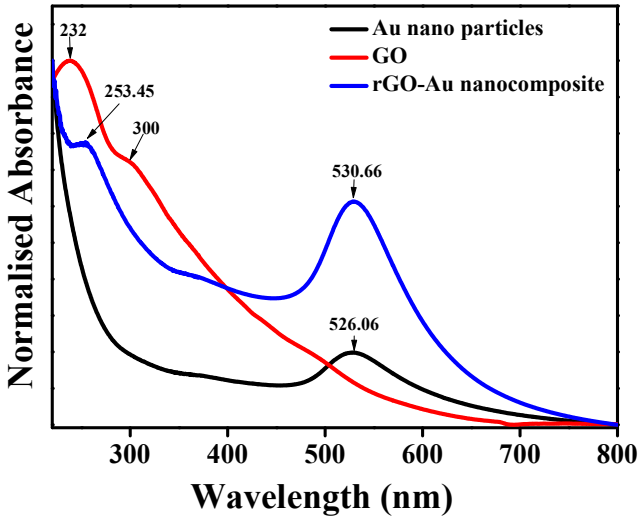

Figure 5.2: *UV-visible absorbance spectra of gold nanoparticles (Au-nanoparticle), graphene oxide (GO), and the reduced graphene oxide-gold (rGO-Au) nanocomposite.*

Figure 5.2 shows the UV-visible absorbance spectra for gold nanoparticles, GO, and the reduced graphene oxide-gold (rGO-Au) nanocomposite. Localized surface plasma resonance (LSPR) of gold nanoparticles results in a strong absorbance band in the visible region at 526.06 nm. GO has an absorbance peak at 232 nm with a shoulder peak at 300 nm. In the rGO-Au composite, instead of the peak of GO at 232 nm, a new peak appears at 253.45 nm, indicating the formation of rGO in the composite. The heating process during the synthesis of Au is responsible for the formation of rGO in the composite. The peak of gold nanoparticles at 526.06 nm shifts to 530.66 nm in the rGO-Au nanocomposite, further confirming the integration of rGO with gold nanoparticles - which can also indicate a change in particle size of gold nanoparticles in those two samples.

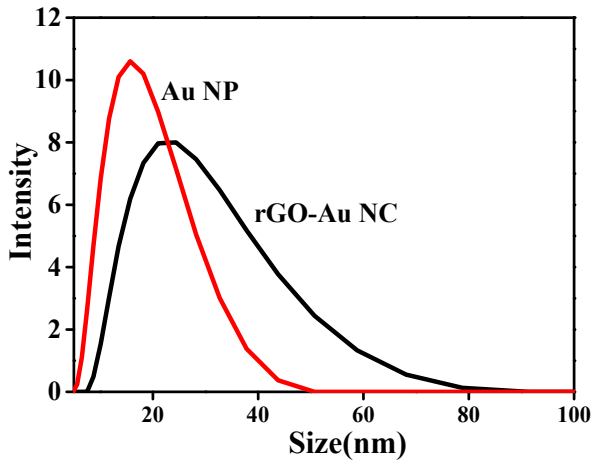

Figure 5.3: *DLS spectra for Au nanoparticles and rGO-Au nanocomposite. DLS spectra give the average particle size of the materials.*

Dynamic Light Scattering (DLS) (Figure 5.3) analysis reveals that the average particle size is 17.04 ± 0.8 nm for gold (Au) nanoparticles and 24.85 ± 0.5 nm for the reduced graphene oxide-gold (rGO-Au) nanocomposite. The increase in particle size for the rGO-Au nanocomposite can be attributed to several factors. Firstly, integrating rGO sheets with gold nanoparticles leads to composite structure formation, which inherently increases the overall particle size. Secondly, rGO can provide a platform for the gold nanoparticles to anchor, potentially causing slight aggregation and contributing to a larger hydrodynamic diameter, as observed in DLS measurements. Additionally, the functionalization and reduction processes involved in forming the rGO-Au composite may induce slight changes in morphology and size distribution, resulting in a larger average particle size than gold nanoparticles alone. These observations suggest that the composite formation with rGO effectively modifies the physical characteristics of the gold nanoparticles, as observed in an increase in the measured particle size.

5.3.2 Uric acid sensing

Different concentrations of uric acid, ranging from 1 mg/dL to 20 mg/dL (considering the healthy uric acid level in the human body fluid [2]), were mixed with graphene oxide (GO) solution, and the UV-visible absorbance spectra were recorded. This experiment was repeated by replacing the GO solution with a gold nanoparticle

(Au) solution and subsequently with a reduced graphene oxide-gold (rGO-Au) nanocomposite solution. The resulting UV-visible spectra are presented in Figure 5.4.

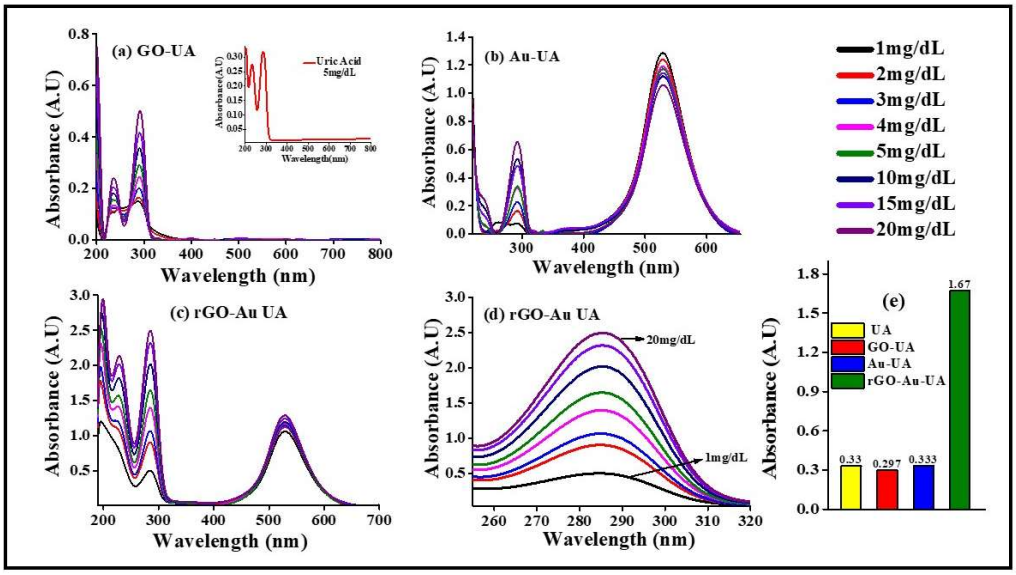

Figure 5.4: *UV-visible absorbance spectra when varied concentrations of uric acid (1 mg/dL to 20 mg/dL) interact with a solution of (a) GO - the inset of the figure shows the UV vis spectra of uric acid solution at 5 mg/dL concentration resulting in absorption maxima at 0.33 A.U, (b) Au nanoparticles (c) rGO-Au nanocomposite and (d) magnified image of the peak ~ 285 nm with rGO-Au nanocomposite (e) absorbance maxima of UV vis spectra peak at ~285 nm for the sensing elements in contact with 5mg/dL solution of uric acid. It can be observed that the uric acid absorbance peak at ~ 285 nm showed a five-fold increase when combined with rGOAu nanocomposite. The peak at ~ 285 nm originates from $\pi \rightarrow \pi^*$ transitions in its conjugated double bonds and aromatic ring structure, and at ~530 nm corresponds to the SPR effect of the gold nanoparticles.*

Uric acid exhibits a strong absorbance peak around 285 nm and a less intense peak near 234 nm. When combined with graphene oxide (GO), the absorbance of uric acid at a concentration of 20 mg/dL is 0.5, with no additional peaks observed beyond those of uric acid. It indicates that GO does not significantly alter the absorbance characteristics of uric acid. In contrast, when uric acid is combined with gold nanoparticles, the intensity of its peaks remains unchanged, but a new peak appears near 530 nm, corresponding to the SPR effect of the gold nanoparticles. However, when uric acid is combined with the rGO-Au nanocomposite, there is a significant increase in the absorbance intensity, as seen in Figure 5.4 and Figure 5.5. At a concentration of 20 mg/dL, the intensity rises dramatically to 2.49, nearly a fivefold increase compared to the other cases. This substantial enhancement highlights the synergistic effect of the rGO-Au nanocomposite, which is not observed with GO or

gold nanoparticles alone when combined with uric acid. This remarkable increase in intensity underscores the importance of the rGO-Au composite in enhancing the absorbance properties of uric acid.

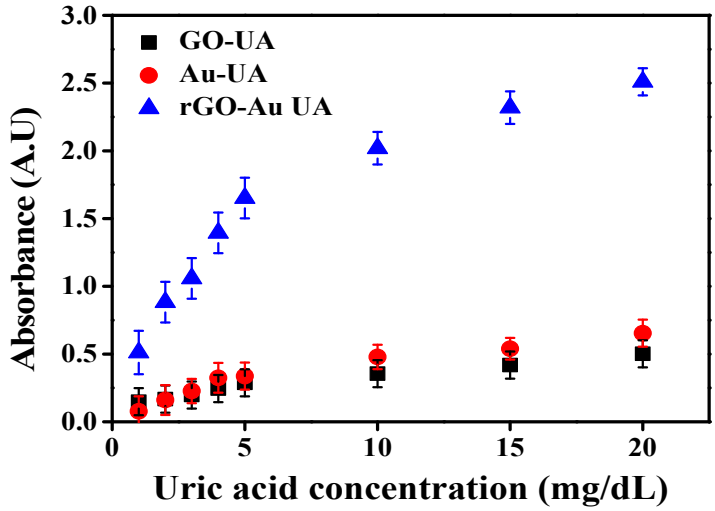

Figure 5.5: *Variation of absorbance maxima with analyte concentration, corresponding to the 285 nm peak of uric acid, with graphene oxide, gold nanoparticles, and rGO-Au nanocomposite as the biosensing element. The points are drawn based on the data shown in Figure5.4, and the error bar is based on the data from the repeated set of experiments. The detection range of 59.48 to 1189.6 µM with a LOD of (2 mg/dL) and sensitivity of 1 mg/dL, as demonstrated in the figure, is particularly noteworthy as it aligns with the human serum levels.*

The increase in UV-visible absorbance of uric acid when combined with rGO-Au nanoparticles (Figures 4 & 5) can be attributed to the synergistic interaction between uric acid and the composite material. The rGO-Au nanoparticles provide a large surface area and functional groups for strong interactions with uric acid molecules. These interactions, including π-π stacking and hydrogen bonding, bringing uric acid molecules closer to the nanoparticles, enhancing their absorbance properties. Additionally, the unique electronic properties of rGO, such as its high electrical conductivity, large surface area, and defect-rich structure, facilitate better charge transfer between the nanoparticles and uric acid, further boosting the absorbance signal.

Surface plasmon resonance (SPR) plays a significant role in this increased absorbance. Gold nanoparticles exhibit SPR, where conduction electrons oscillate in resonance with incident light, enhancing the local electromagnetic field. When uric acid molecules are in proximity to Au nanoparticles, the amplified field increases their absorbance by enhancing electronic transitions. However, in our case, no significant increase in absorbance is observed when only gold nanoparticles interact with the uric acid solution. It highlights the importance of rGO in the rGO-Au composite. The rGO in the nanocomposite provides a high surface area to ensure a stable dispersion of gold nanoparticles, preventing reasons that can quench the SPR effect, such as the aggregation of gold nanoparticles, contributing to maximizing the SPR effect, leading to a more substantial increase in the absorbance peak in the case of rGO-Au sensing element.

Compared to other nanocomposite-based uric acid detection methods, using gold-reduced graphene oxide (rGO-Au) nanocomposites in UV-visible spectroscopy offers several advantages. Unlike electrochemical or fluorescence-based techniques, UV-visible spectroscopy allows for a non-destructive, rapid, and cost-effective analysis without the need for complex equipment or calibration. The detection range aligns well with physiological uric acid levels, making this approach highly relevant for clinical diagnostics.

5.4 Comparison of uric acid sensing with reports from the literature

Compared to existing electrochemical methods for uric acid detection, this work involving an rGO-Au nanocomposite stands out due to its novel use of UV-visible-based sensing. Unlike traditional approaches that employ cyclic voltammetry [20–22], differential pulse voltammetry, or amperometry [23, 24], this study provides a straightforward alternative for detecting uric acid. The detection range of 59.48 to 1189.6 μM with an LOD of 2 mg/dL in the present work is particularly noteworthy, aligning with physiological levels in body fluids (Male: 4.0–8.5 mg/dL, Female: 2.7–7.3 mg/dL, Child: 2.5–5.5 mg/dL, Newborn: 2.0–6.2 mg/dL [2][25])—making it highly relevant for medical diagnostics.

Although specific electrochemical sensors demonstrate ultralow LODs, such as 33.3 nM reported by Hu et al. (2021) [26] and 48 nM by Hadi & Ghanbari (2022) [22], these methods face significant challenges. For example, the single-atom cobalt-based electrochemical method reported by Hu requires specific conditions, such as a high-pH environment (NaOH at pH 13), which limits its versatility for broader applications. Additionally, the synthesis of single-atom catalysts like A-Co-NG involves labour-intensive steps, including ball milling, freeze-drying, and high-temperature pyrolysis, making it both complex and costly. Similarly, enzyme-based sensors, such as the uricase/CNT-CMC-based system discussed by Fukuda et al. (2020) [27], exhibit a linear range of 0.02–2.7 mM with an LOD of 2.8 μM. However, enzymatic approaches often suffer from stability issues due to enzyme degradation, making them less robust for practical, long-term applications. Another example is the CuO-based electrochemical sensor reported by Buledi et al. (2021) [28], which demonstrates a wide detection range of 0.001–351 mM with an LOD of 0.6 μM. However, its performance is highly influenced by environmental and operational conditions, such as sensitivity to interfering agents like urea, and requires a specific pH (phosphate buffer at pH 7.4) for optimal functioning. Furthermore, its fabrication involves high-temperature annealing at 500°C, adding complexity and cost to the production process.

In contrast, the UV-visible approach presented in this study provides significant advantages in simplicity, accessibility, and cost-effectiveness. Unlike enzymatic or high-complexity electrochemical methods, this method eliminates the need for stringent conditions, such as controlled pH, temperature, or intricate synthesis processes. Additionally, the innovative use of rGO-Au in this context, to the best of our knowledge, is being reported for the first time, distinguishing it from enzymatic and non-enzymatic electrochemical sensors. This development points out the potential of UV-visible spectroscopy as a practical diagnostic tool for uric acid sensing, particularly in resource-limited settings.

5.5 Conclusion

The study reported in this chapter demonstrated a novel approach to uric acid detection in body fluids using reduced graphene oxide-gold (rGO-Au) nanocomposite, resulting in a potential sensing element with 2 mg/dL detection limit and 1mg/dL sensitivity. The synthesized graphene oxide (GO), gold nanoparticles (AuNPs), and the rGO-Au nanocomposite were characterized using X-ray diffraction, UV-vis spectroscopy and dynamic light scattering techniques. Our findings based on varying uric acid levels (1 to 20 mg/dL) reveal that the analyte exhibited significantly higher UV-visible absorbance (five times) when combined with rGO-Au nanocomposite. The enhancement is attributed to the synergistic effect of surface plasmon resonance (SPR) and the unique properties of the nanocomposite aided by rGO. rGO provided a platform for the gold nanoparticles to anchor, potentially causing reduced aggregation and a larger hydrodynamic diameter, as observed in DLS measurements. Unlike traditional approaches that employ cyclic voltammetry, differential pulse voltammetry, or amperometry, this study provides a straightforward alternative for detecting uric acid. The detection range in the present work is particularly noteworthy, as it aligns with physiological levels in human body fluids. The insights gained from this work pave the way for developing susceptible and cost-effective uric acid sensors, offering significant promise for use in clinical diagnostics and routine health monitoring.

5.6 References

1. Ding, Y., Xu, Z., Zhou, X., Luo, Y., Xie, R., & Li, Y. (2023). Association between weight-adjusted-waist index and the risk of hyperuricemia in adults: a population-based investigation. Frontiers in Endocrinology, 14. https://doi.org/10.3389/fendo.2023.1236401

2. George C, Leslie SW, Minter DA. Hyperuricemia. 2023 Oct 14. In: StatPearls [Internet]. Treasure Island (FL): StatPearls Publishing; 2024 Jan–. PMID: 29083565.

3. Pileggi, V. J., Di Giorgio, J., & Wybenga, D. K. (1972). A one-tube serum uric acid method using phosphotungstic acid as protein precipitant and color reagent. Clinica Chimica Acta, 37, 141–149. https://doi.org/10.1016/0009-8981(72)90425-1

4. Caraway, W. T. (1955). Determination of Uric Acid in Serum by a Carbonate Method. American Journal of Clinical Pathology, 25(7_ts), 840–845. https://doi.org/10.1093/ajcp/25.7_ts.0840

5. Erden, P. E., & Kılıç, E. (2013). A review of enzymatic uric acid biosensors based on amperometric detection. Talanta, 107, 312–323. https://doi.org/10.1016/j.talanta.2013.01.043

6. Zhang, X., Guo, Q., & Cui, D. (2009). Recent Advances in Nanotechnology Applied to Biosensors. Sensors, 9(2), 1033–1053. https://doi.org/10.3390/s90201033

7. Peng, H., Tang, H., & Jiang, J. (2016). Recent progress in gold nanoparticle-based biosensing and cellular imaging. Science China Chemistry, 59(7), 783–793. https://doi.org/10.1007/s11426-016-5570-7

8. Chung, C., Kim, Y. K., Shin, D., Ryoo, S. R., Hong, B. H., & Min, D. H. (2013). Biomedical Applications of Graphene and Graphene Oxide. Accounts of Chemical Research, 46(10), 2211–2224. https://doi.org/10.1021/ar300159f

9. Lee, K., Yoo, Y. K., Chae, M. S., Hwang, K. S., Lee, J., Kim, H., Hur, D., & Lee, J. H. (2019). Highly selective reduced graphene oxide (rGO) sensor based on a peptide aptamer receptor for detecting explosives. Scientific Reports, 9(1). https://doi.org/10.1038/s41598-019-45936-z

10. Sharma, N., Vyas, R., Sharma, V., Rahman, H., Sharma, S. K., & Sachdev, K. (2019). A comparative study on gas-sensing behavior of reduced graphene oxide (rGO) synthesized by chemical and environment-friendly green method. Applied Nanoscience, 10(2), 517–528. https://doi.org/10.1007/s13204-019-01138-7

11. Du, H., Xie, G., & Zhang, Q. (2019). Enhanced Room Temperature NO2 Sensing Performance of RGO Nanosheets by Building RGO/SnO2 Nanocomposite System. Sensors, 19(21), 4650. https://doi.org/10.3390/s19214650

12. Kumar, V., Gupta, R. K., Gundampati, R. K., Singh, D. K., Mohan, S., Hasan, S. H., & Malviya, M. (2018). Enhanced electron transfer mediated detection of hydrogen peroxide using a silver nanoparticle–reduced graphene oxide–polyaniline fabricated electrochemical sensor. RSC Advances, 8(2), 619–631. https://doi.org/10.1039/c7ra11466d

13. Laghrib, F., Azriouil, M., Aghris, S., Farahi, A., Saqrane, S., Bakasse, M., Lahrich, S., & Mhammedi, M. a. E. (2024). Green Synthesis of Clay/rGO Composite for Sensitive Detection of Para Nitrophenol in the Environment. ChemistrySelect, 9(35). https://doi.org/10.1002/slct.202402540

14. Unnikrishnan, A., Megha, V., & Alexander, L. K. (2024). Ascorbic acid sensing utilizing graphene oxide based on UV–Visible bathochromic shift. Journal of Materials Science Materials in Electronics, 35(13). https://doi.org/10.1007/s10854-024-12672-8

15. Chiticaru, E. A., Pilan, L., & Ioniță, M. (2022). Electrochemical Detection Platform Based on RGO Functionalized with Diazonium Salt for DNA Hybridization. Biosensors, 12(1), 39. https://doi.org/10.3390/bios12010039

16. Turkevich, J., Stevenson, P. C., & Hillier, J. (1951). A study of the nucleation and growth processes in the synthesis of colloidal gold. Discussions of the Faraday Society, 11, 55. https://doi.org/10.1039/df9511100055

17. Hummers, W. S., & Offeman, R. E. (1958). Preparation of Graphitic Oxide. Journal of the American Chemical Society, 80(6), 1339. https://doi.org/10.1021/ja01539a017

18. Cucci, L. M., Naletova, I., Consiglio, G., & Satriano, C. (2019). A Hybrid Nanoplatform of Graphene Oxide/Nanogold for Plasmonic Sensing and Cellular Applications at the Nanobiointerface. Applied Sciences, 9(4), 676. https://doi.org/10.3390/app9040676

19. Unnikrishnan, A., & Alexander, L. K. (2024). The concentration-dependent effect of NaOH on graphene oxide: Revisited as a reducing agent. Journal of Physics and Chemistry of Solids, 190, 111978. https://doi.org/10.1016/j.jpcs.2024.111978

20. Piedras, J. J., Dominguez, R. B., & Gutierrez, J. M. (2021). Electrochemical Biosensor Development for Uric Acid Detection. ECS Transactions, 101(1), 19–24. https://doi.org/10.1149/10101.0019ecst

21. Rajendrachari, S., Arslanoglu, H., Yaras, A., & Golabhanvi, S. M. (2023). Electrochemical Detection of Uric Acid Based on a Carbon Paste Electrode Modified with Ta2O5 Recovered from Ore by a Novel Method. ACS omega, 8(49), 46946-46954.

22. Hadi, Z., & Ghanbari, K. (2022). A novel electrochemical sensor for determination of uric acid in the presence of ascorbic acid and dopamine based on a carbon paste electrode modified with an electrochemically reduced para-nitrobenzoic acid/graphene oxide nanocomposite. New Journal of Chemistry, 46(27), 12941–12951. https://doi.org/10.1039/d2nj01358d

23. Masrat, S., Nagal, V., Khan, M., Ahmad, A., Alshammari, M. B., Alam, S., Nakate, U. T., Lee, B., Mishra, P., Bhat, K. S., & Ahmad, R. (2023). Electrochemical Sensing of Uric Acid with Zinc Oxide Nanorods Decorated with Copper Oxide Nanoseeds. ACS Applied Nano Materials, 6(18), 16615–16624. https://doi.org/10.1021/acsanm.3c02794

24. Ahmed, J., Faisal, M., Alsareii, S. A., & Harraz, F. A. (2022). Highly sensitive and selective non-enzymatic uric acid electrochemical sensor based on novel polypyrrole-

carbon black-Co3O4 nanocomposite. Advanced Composites and Hybrid Materials, 5(2), 920–933. https://doi.org/10.1007/s42114-021-00391-1

25. Pagana KD, Pagana TJ, Pagana TN. Mosby's Diagnostic & Laboratory Test Reference. 14th ed. St. Louis, Mo: Elsevier; 2019.

26. Hu, F. X., Hu, T., Chen, S., Wang, D., Rao, Q., Liu, Y., Dai, F., Guo, C., Yang, H. B., & Li, C. M. (2020). Single-Atom Cobalt-Based Electrochemical Biomimetic Uric Acid Sensor with Wide Linear Range and Ultralow Detection Limit. Nano-Micro Letters, 13(1). https://doi.org/10.1007/s40820-020-00536-9

27. Fukuda, T., Muguruma, H., Iwasa, H., Tanaka, T., Hiratsuka, A., Shimizu, T., Tsuji, K., & Kishimoto, T. (2019). Electrochemical determination of uric acid in urine and serum with uricase/carbon nanotube /carboxymethylcellulose electrode. Analytical Biochemistry, 590, 113533. https://doi.org/10.1016/j.ab.2019.113533

28. Buledi, J. A., Ameen, S., Memon, S. A., Fatima, A., Solangi, A. R., Mallah, A., Karimi, F., Malakmohammadi, S., Agarwal, S., & Gupta, V. K. (2021). An improved non-enzymatic electrochemical sensor amplified with CuO nanostructures for sensitive determination of uric acid. Open Chemistry, 19(1), 481–491. https://doi.org/10.1515/chem-2021-0029

CHAPTER 6

GRAPHENE OXIDE MODIFICATION BY TIME-VARYING REACTION

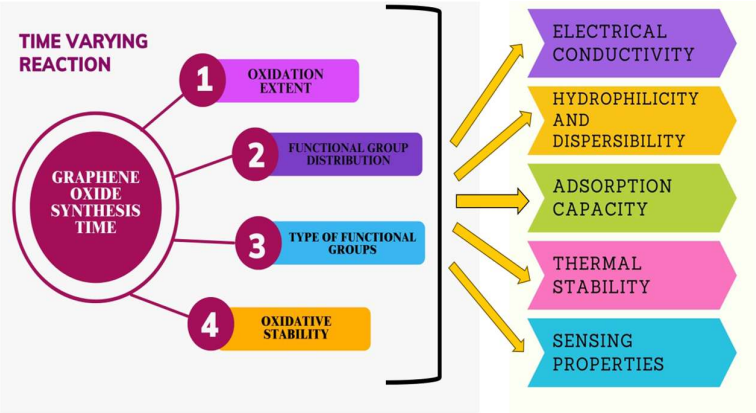

Scope of the Chapter

- *Investigate the impact of modification time variation on graphene oxide oxidation, functional groups, and subsequent adsorption properties.*
- *Optimise the system to achieve the highest adsorption capacity within experimental constraints.*
- *Analyse the kinetics and mechanism of the reaction for deeper understanding.*
- *Exploit the adsorption capacity for ascorbic acid sensing.*

Abstract

A critical aspect of GO synthesis is the time, which governs the degree of oxidation and the concentration of functional groups. Despite its importance, the synthesis of GO predominantly focuses on highly oxidised states or fixed synthesis durations, often neglecting the intermediate stages. Exploring these intermediate modification times can provide a comprehensive understanding of how they impact GO's structural and chemical attributes, paving the way for better control over its properties. The stirring time could directly influence the oxidation level and the distribution of oxygen-containing functional groups, determining GO's chemical reactivity and adsorption capabilities. In our study, we synthesised four GO samples with varying stirring durations: GO2Hr (2 hours), GO4Hr (4 hours), GO8Hr (8 hours), and GO18Hr (18 hours). These GO samples were well-characterised using advanced techniques to thoroughly understand the effects of varying stirring times on their structural and chemical properties. We then evaluated their adsorption performance using methylene blue dye and naphthalene as test adsorbates. GO2Hr sample showed exceptional adsorption; within ***4 minutes****, 100% MB dye was adsorbed, and we achieved the highest adsorption capacity of* ***1285mg/g*** *for any GO samples in the literature. High adsorption capacity was observed for naphthalene pollutant as well. We conducted additional evaluations of the GO samples for ascorbic acid sensing using UV-visible spectroscopy and confirmed their suitability for sensing applications*

6.1 Introduction

Graphene oxide (GO), a chemically modified form of graphene, is characterised by oxygen-containing functional groups, including hydroxyl (-OH), epoxy (-O-), carboxyl (-COOH), and carbonyl (C=O) groups. These groups are primarily located on its basal plane and edges, imparting hydrophilicity and enhancing dispersion in water and other solvents. The presence and distribution of these functional groups significantly influence GO's electronic, mechanical, and chemical properties, making it a versatile material for advanced applications [1].

A critical aspect of GO synthesis is the time, which governs the degree of oxidation and the concentration of functional groups [2]. Despite its importance, the synthesis of GO predominantly focuses on highly oxidised states or fixed synthesis durations, often neglecting the intermediate stages. Despite its importance, research predominantly focuses on either highly oxidised states or fixed synthesis durations, often neglecting the intermediate stages. Exploring these intermediate modification times can provide a comprehensive understanding of how they impact GO's structural and chemical attributes, paving the way for better control over its properties.

The functional groups in GO, such as hydroxyl and carboxyl, enhance its adsorption capabilities [3,4], while epoxy groups contribute to catalytic performance [5]. Understanding the influence of modification time on the distribution and composition of these groups allows precise tuning of GO properties, enabling its effective use in fields such as sensing, environmental remediation, and biomedicine. Therefore, systematic studies on modification time variations can unlock new possibilities for optimising GO's functionality in targeted applications.

Rapid adsorption of pollutants from water bodies is critical for minimising environmental and health hazards caused by contaminants such as dyes and other organic compounds. High adsorption capacities are essential for ensuring efficient pollutant removal, even at low adsorbent dosages, reducing the overall cost and environmental footprint of water treatment processes. Developing a single adsorbent capable of removing multiple pollutants is particularly noteworthy, as it simplifies

treatment systems, enhances operational efficiency, and offers a versatile solution for addressing complex pollution scenarios sustainably and economically.

In this chapter, we explore the adsorption properties of GO samples synthesised with varying modification times, ranging from 2 hours to 18 hours. The adsorption capability is studied using methylene blue and naphthalene as model pollutants. The impact of the adsorption capability driven by variation in modification time is explored with the chemical sensing potential of the GO samples.

6.2 Experimental details

6.2.1 Synthesis of GO

In this study, graphene oxide (GO) was synthesised via Hummer's method [section 2.1], utilising different stirring times to yield four distinct GO samples: GO2Hr, GO4Hr, GO8Hr, and GO18Hr. Each sample was produced under specific stirring conditions, with GO2Hr corresponding to a 2-hour stirring time, GO4Hr with a 4-hour stirring time, GO8Hr with an 8-hour stirring time, and GO18Hr with an 18-hour stirring time after the addition of $KMnO_4$ which now onwards we call as the GO **modification time**. The variation in stirring time was implemented to investigate the impact of synthesis duration on the structural and chemical properties of the resulting GO and, subsequently, to discern how these alterations influence the adsorption capability of the synthesised GO materials.

6.3 Results and Discussion

6.3.1 Characterisation techniques

The X-ray diffraction (XRD) pattern of the (GO) samples, as depicted in Figure 6.1, reveals distinct 2θ value shifts, correlating with variations in interlayer spacing, as shown in Figure 6.2. The variation in interlayer distance can be linked to the oxidation levels of the samples. Thus, it can be indirectly concluded that the modification time of GO influences the oxidation levels of the samples.

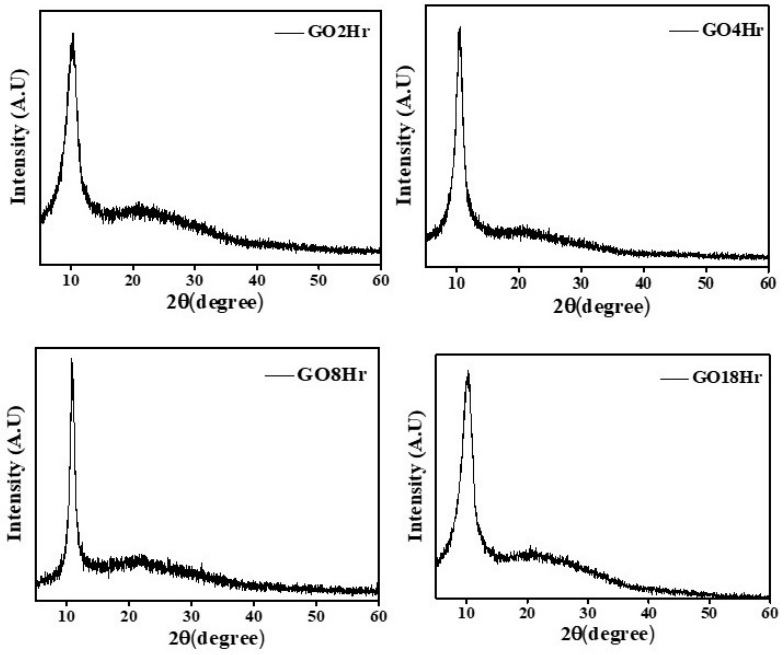

Figure 6.1 *XRD patterns of graphene oxide samples synthesised under different modification times [GO2Hr, GO4Hr, GO8Hr, and GO18Hr]. The sample variety is related to the stirring time after adding $KMnO_4$, termed* ***modification time****. GO2Hr corresponds to a 2-hour stirring time, GO4Hr with a 4-hour stirring time, GO8Hr with an 8-hour stirring time, and GO18Hr with an 18-hour stirring time after adding $KMnO_4$.*

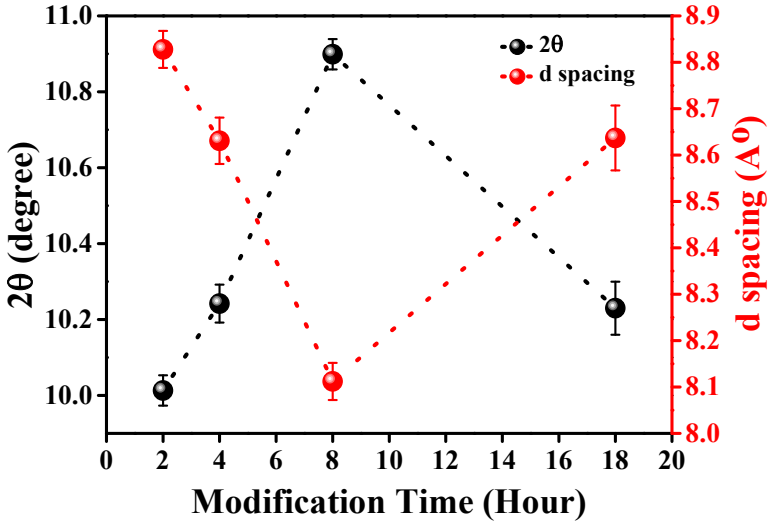

Figure 6.2 *Effect of modification time on the variation of 2θ and d-spacing.*

Figure 6.3 illustrates the Raman spectra obtained from all the samples, providing crucial insights into the material properties. Notably, the plot correlating the ratio of the D band to the G band (ID/IG) against the modification time (Figure 6.4) reveals a distinctive trend. The sample synthesised with the minimum modification time exhibits the highest ID/IG ratio, indicating a greater abundance of oxygen functional groups, particularly in sample GO2Hr. Conversely, samples GO4Hr and GO18Hr exhibit similar ID/IG ratios, suggesting a comparable level of oxygen functional groups within these samples. These findings stress the intricate relationship between the reaction duration and the resulting oxygen functionalities, thereby emphasising the critical role of modification time in tailoring the structural and chemical characteristics of the produced graphene-based materials.

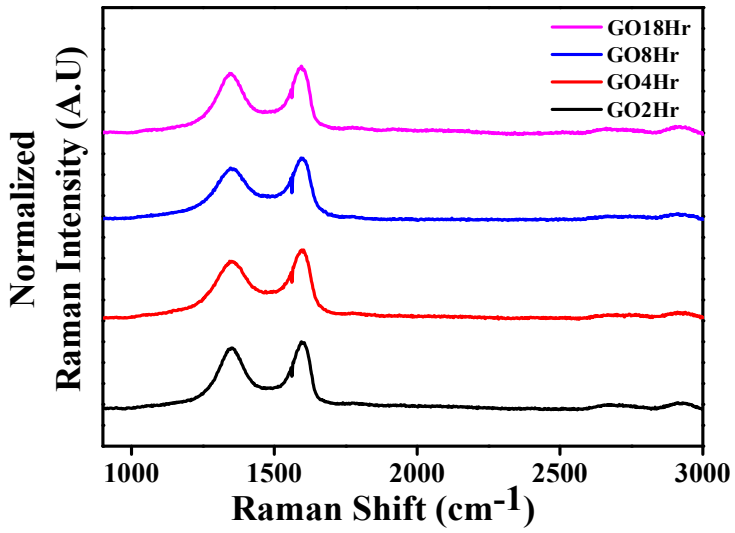

Figure 6.3 *Raman spectra of graphene oxide samples [GO2Hr, GO4Hr, GO8Hr, and GO18Hr].*

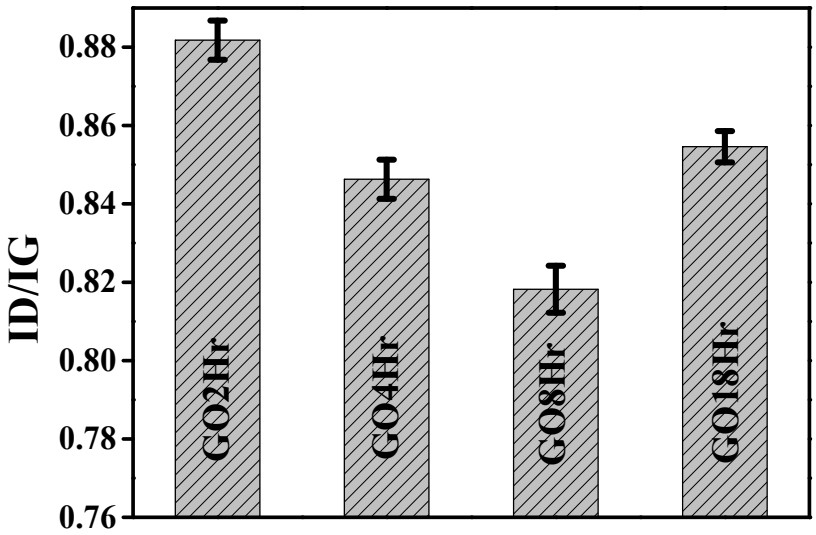

Figure 6.4 *Variation of ID/IG ratio of Raman spectra for each set of GO samples.*

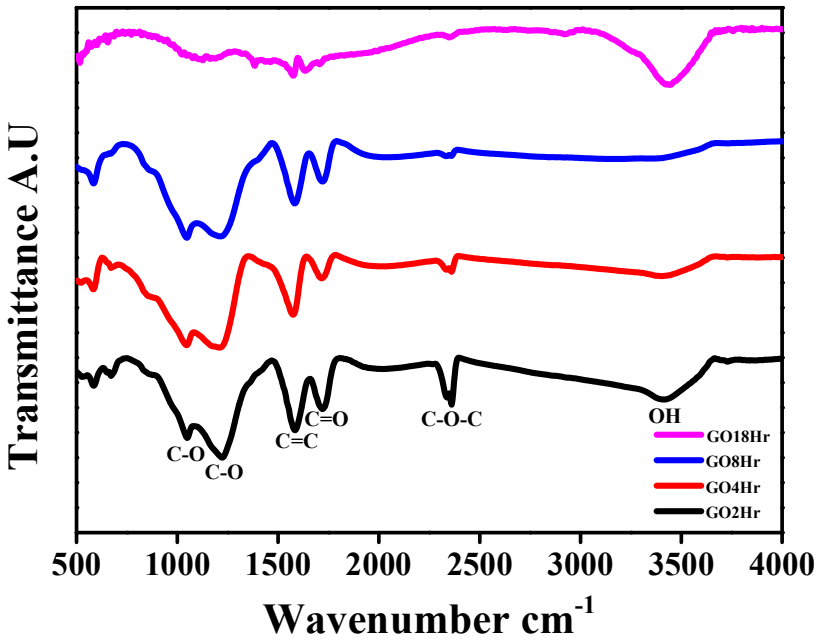

Figure 6.5 *FTIR spectra of different GO samples [GO2Hr, GO4Hr, GO8Hr, and GO18Hr].*

The characteristic peaks identified in the Fourier transform infrared (FTIR) spectra analysis of GO samples (Figure 6.5) provide valuable insights into their molecular structure and functional groups. The peak at around 3400 cm^{-1} corresponds to the stretching vibration of hydroxyl (-OH) groups, indicating the presence of hydroxyl functionalities on the GO surface. The peak near 2354 cm^{-1} is that of CO_2. The peak at approximately 1720 cm^{-1} and 1590 cm^{-1} is attributed to the stretching vibrations of carbonyl (C=O) groups, which are typically associated with carboxyl, epoxy, and ketone functionalities. Additionally, the peak observed at 1050 cm^{-1} and 1220 cm^{-1} signifies the C-O stretching vibration, suggesting the presence of oxygen-containing functional groups such as epoxy and alkoxy [6,7]. The appearance of these characteristic peaks validates the successful oxidation of graphene, leading to the formation of graphene oxide. Moreover, the relative intensities and positions of these peaks provide valuable information regarding the degree of oxidation, the abundance of functional groups, and the structural integrity of the GO sheets.

The Fourier transform infrared (FTIR) spectra of GO2Hr, GO4Hr, and GO8Hr exhibit noticeable similarities, suggesting comparable molecular structures and functional groups. However, a distinct observation emerges in GO2Hr, where certain peaks appear more intense and well-defined than the other samples. This heightened intensity in GO2Hr implies a higher abundance of specific oxygen functional groups within its structure. Conversely, GO18Hr displays a markedly different FTIR spectrum, characterised by the highest intensity observed for the OH peak, consequently suppressing the visibility of other functional groups. This finding suggests a pronounced prevalence of hydroxyl groups in GO18Hr, indicating variations in the degree and nature of oxidation across the different samples.

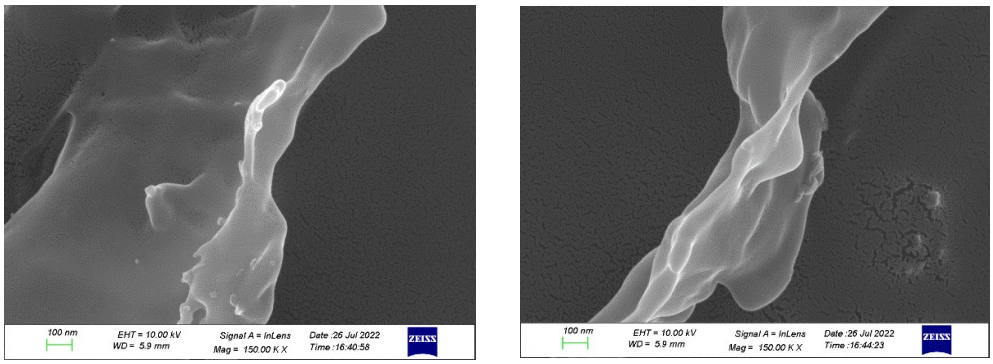

Figure 6.6 *FESEM images of sample GO2Hr*

The SEM images presented in Figure 6.6 offer a comprehensive visual depiction of the GO samples. These images distinctly reveal the presence of sheet-like layers of GO, providing valuable insights into the morphological attributes of the material. Notably, the individual, single sheets of GO are conspicuously discernible within the micrograph, confirming the successful exfoliation and isolation of these ultra-thin GO layers. The visual evidence of individual GO sheets within the samples emphasises the remarkable exfoliation achieved during the synthesis process, highlighting the unique two-dimensional nature of GO, which is paramount for its diverse applications in the realm of adsorption-based applications.

6.3.2.1 Adsorption Experiment

In this study, we conducted adsorption experiments using GO samples of varied modification time - labelled GO2Hr, GO4Hr, GO8Hr, and GO18Hr. The adsorption tests were performed with a 10ppm methylene blue dye solution in 100 mL volumes, utilising 0.01 g of the respective adsorbent. UV-visible absorbance was continuously monitored at 30-second intervals throughout the adsorption process. The resulting adsorption curves, depicting the changes in absorbance over time, are presented in Figure 6.7.

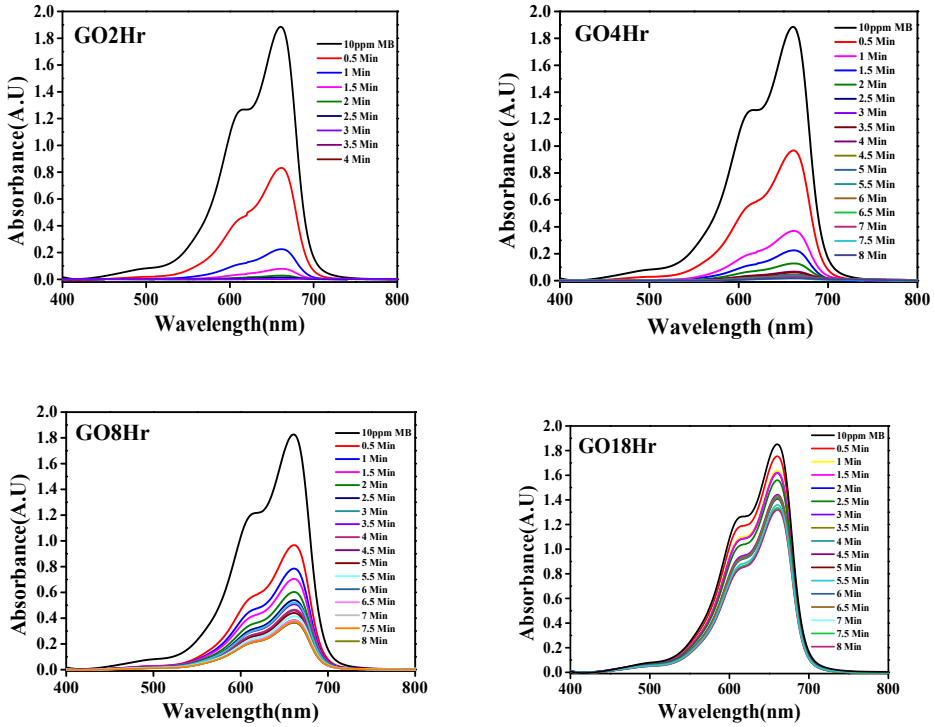

Figure 6.7: *UV-visible absorbance plots of MB dye adsorption by 0.01 g of GO2Hr, GO4Hr, GO8Hr and GO18Hr. The absorbance of 10ppm MB is 1.8914, and after adsorption, the absorbance became 0.0038, 0.0075, 0.3506 and 1.3108 for GO2Hr, GO4Hr, GO8Hr and GO18Hr samples respectively.*

The adsorption reactions were characterised by exceptionally rapid adsorption kinetics exhibited by the GO materials. The remarkable adsorption performance of sample GO2Hr is of particular significance, wherein a notable 100% adsorption of the 10 ppm MB dye was achieved within an unprecedented time frame of merely 4 minutes. To the best of our knowledge, this notably brief duration represents the shortest reported time for the efficient adsorption of dyes by GO-based materials. These findings highlight the exceptional adsorption efficiency and rapid kinetics of the synthesised GO samples, showcasing their potential for addressing pressing environmental challenges through efficient wastewater treatment and pollutant removal applications.

6.3.2.2 Adsorption kinetics

In-depth investigations were conducted to analyse the adsorption kinetics of MB on GO samples. The kinetics study involved an examination of both the pseudo-first-order and pseudo-second-order kinetics. Remarkably, the adsorption process of MB onto the GO samples was observed to conform to the pseudo-second-order kinetics model. Notably characterised by rapid reactions, the adsorption capacity and associated parameters have been comprehensively documented and are presented in detail in Table 6.1 and figure 6.8.

This analysis offers valuable insights into the intricate adsorption dynamics governing the interaction between MB and GO, further elucidating the underlying mechanisms that dictate the adsorption behaviour and capacity of these materials.

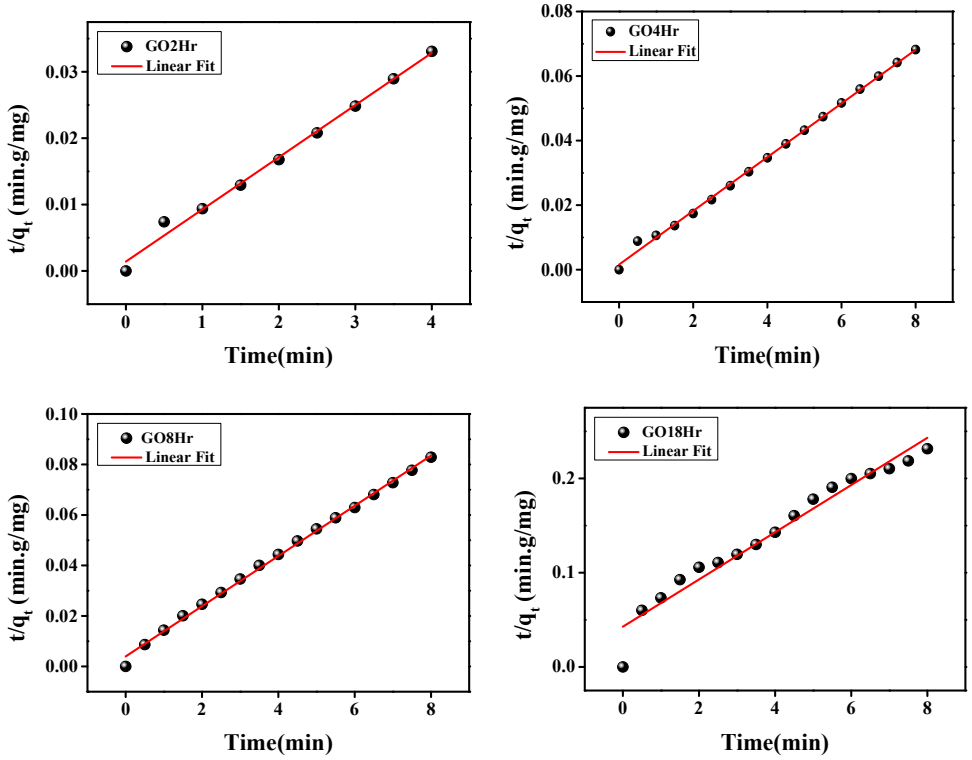

Figure 6.8 *Pseudo-second-order kinetic model fit*

Table 6.1 *Summary of the kinetics variables for MB adsorption onto GO samples*

Sample name	$q_{e\ direct}$ (mg/g)	Pseudo-first-order kinetics			Pseudo-second-order kinetics		
		k_1 (min^{-1})	$q_{ekinetic}$ (mg/g)	R^2	k_2 (g/mg min)	$q_{e\ kinetic}$ (mg/g)	R^2
GO2Hr	120.9	2.61	205.05	0.95	0.04	127.23	0.99
GO4Hr	117.6	0.55	28.29	0.77	0.04	120.19	0.99
GO8Hr	96.5	0.85	113.68	0.85	0.02	100.60	0.99
GO18Hr	34.5	0.46	42.03	0.79	0.01	39.92	0.95

Aimed at higher adsorption capacities, the experimental procedures were meticulously replicated, using 20 ppm, 30 ppm, and 35 ppm MB solutions. Notably, this set of analyses observed a remarkable surge in adsorption capacity. To maximise the adsorption potential, adjustments were made by tuning the pH to the basic end and reducing the amount of the adsorbent. Intriguingly, when employing 0.0025 g of GO2Hr sample for the 35 ppm MB solution in basic pH, an unprecedentedly high adsorption capacity of **1285 mg/g** was achieved. This staggering value represents an unparalleled milestone in the field of graphene oxide adsorption and, to the best of our knowledge, stands as the highest adsorption capacity for graphene oxide with dye reported to date in the existing literature for any GO. These ground-breaking findings highlight the immense potential of graphene oxide in revolutionising the landscape of high-capacity adsorption materials, fostering new avenues for environmental remediation and water purification technologies.

Table 6.2 *Comparison of adsorption capacities of GO for different dyes in the literature*

Sl.No	Sample	Specification	Adsorption capacity (mg/g)	References
1	GO	30ppm MB 180min 30mg	300	[8]
2	GO	30mg GO MB	354.84	[8]
3	GO	0.02g GO Malanchite green 25ml 300g/L	384.62	[9]
4	Modified GO	0.015 g of GO 600 mg dm^{-3} 100cm^3 MB	570.4	[10]
5	Agar Graphene Oxide. AGO	200 mg/L MB 20 mg AGO aerogel into 50 mL solution	578	[11]
6	GO	60 mg/L 50 ml MB 50mg GO	686.6	[12]
7	GO	300mg/L 100ml MB 0.1g GO	700	[13]
8	GO	GO (400 lL, 1.500 g/L) 800 lL0.188–1.000 g/L MB	714	[14]
9	GO	250MG/L MB 15mg GO	833.11	[15]
10	GO	-	963	[16]
11	**GO**	**35ppm MB 100ml 0.0025g GO2Hr**	**1285**	**Present work**

6.3.2.3 Regeneration

Recyclable materials play a pivotal role in sustainable environmental remediation and sensing applications. Following multiple washes with distilled water, the regenerated adsorbents underwent a twelve-hour drying process at 60°C. Subsequently, adsorption studies were systematically conducted using the regenerated adsorbents across four additional adsorption/regeneration cycles. Remarkably, the samples exhibited a consistently impressive 100% efficiency throughout each cycle (figure 6.9), underscoring the heightened effectiveness of the material in these applications.

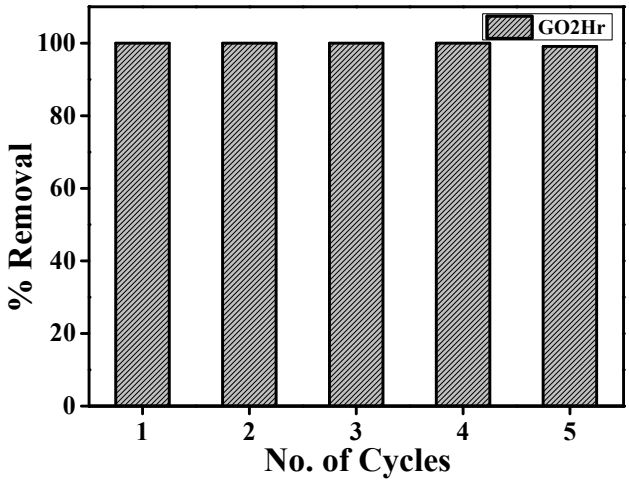

Figure 6.9 *The GO2Hr sample was regenerated after each adsorption cycle, and the adsorption experiment was repeated for four additional consecutive cycles. 100% dye removal was obtained even after five cycles.*

6.3.2.4 Mechanism

The interaction mechanism between methylene blue dye and graphene oxide can be described as follows. Methylene blue, as a cationic dye, exhibits a benzene ring structure that engages in pi-pi stacking interactions with the aromatic rings of graphene oxide, facilitating the initial adsorption onto the graphene oxide surface. Concurrently, electrostatic attraction comes into play as negatively charged functional groups on the graphene oxide surface, including oxygen-containing groups like hydroxyl and carboxyl groups, interact with the positively charged methylene blue molecules, enhancing the overall adsorption capacity. The porous nature of graphene oxide further contributes to the adsorption process, with methylene blue molecules penetrating and filling the pores, resulting in physical adsorption within the porous network. Additionally, under specific conditions, chemical interactions, such as hydrogen bonding, may occur between certain functional groups on the graphene oxide surface and those on methylene blue molecules, thereby contributing to a more robust adsorption mechanism (figure6.10). This comprehensive interplay of pi-pi stacking, electrostatic attraction, pore filling, and potential chemical bonding

underscores the multifaceted nature of methylene blue adsorption onto graphene oxide.

In our study, the characterisation techniques reveal an elevation in oxygen functional groups within graphene oxide (GO) samples subjected to a 2-hour modification time. This observation suggests the initial formation of hydroxyl (OH) functional groups [17]. As the reaction progresses, additional functional groups emerge, gradually replacing the initially formed OH groups. This dynamic process is reflected in the enhanced adsorption behaviour observed in the GO samples with a 2-hour modification time, denoted as GO2Hr.

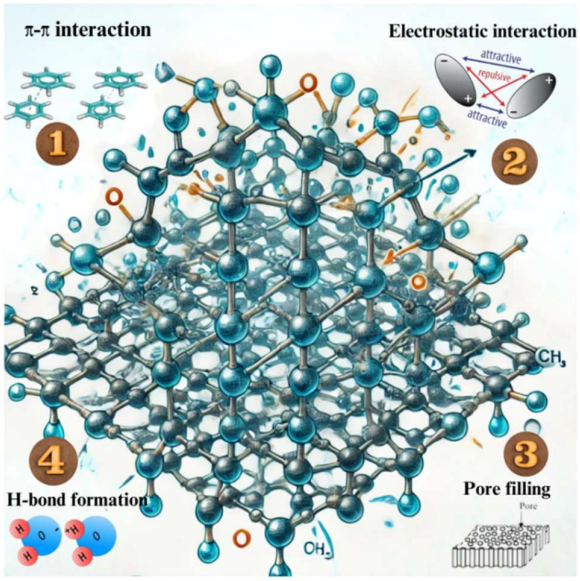

Figure 6.10: *Depiction of the four different interaction mechanisms of MB adsorption by GO sample.*

6.3.3Naphthalene Adsorption Experiment

Time-varied synthesised GO samples demonstrated excellent results in dye removal, prompting further exploration of their adsorption capabilities with another class of pollutants: naphthalene, a polycyclic aromatic hydrocarbon (PAH). Naphthalene is highly toxic and significantly threatens aquatic ecosystems by harming fish, invertebrates, and microorganisms, even at low concentrations. Its persistence in water bodies is attributed to its chemical stability and low biodegradability, resulting

in long-term sediment accumulation and water quality degradation. Furthermore, Naphthalene (NP) has been labelled a harmful pollutant by the US Environmental Protection Agency (USEPA) due to its carcinogenic and mutagenic impact on humans. U.S. Environmental Protection Agency 1986 also poses serious health risks to humans, including skin irritation and liver damage, making its removal from water bodies a critical environmental and public health priority.[18,19]

In this research, we carried out adsorption trials employing graphene oxide samples denoted as GO2Hr, GO4Hr, GO8Hr, and GO18Hr. The adsorption experiments involved a 10ppm naphthalene solution in 100 mL quantities, using 0.005g of the specific adsorbent for each trial. UV-visible absorbance was consistently tracked at 2-minute intervals during the adsorption procedure. The resultant adsorption graphs, illustrating variations in absorbance over time, are depicted in Figure 6.11, and the removal percentage is determined utilising equation 2.4 and shown in Figure 6.12.

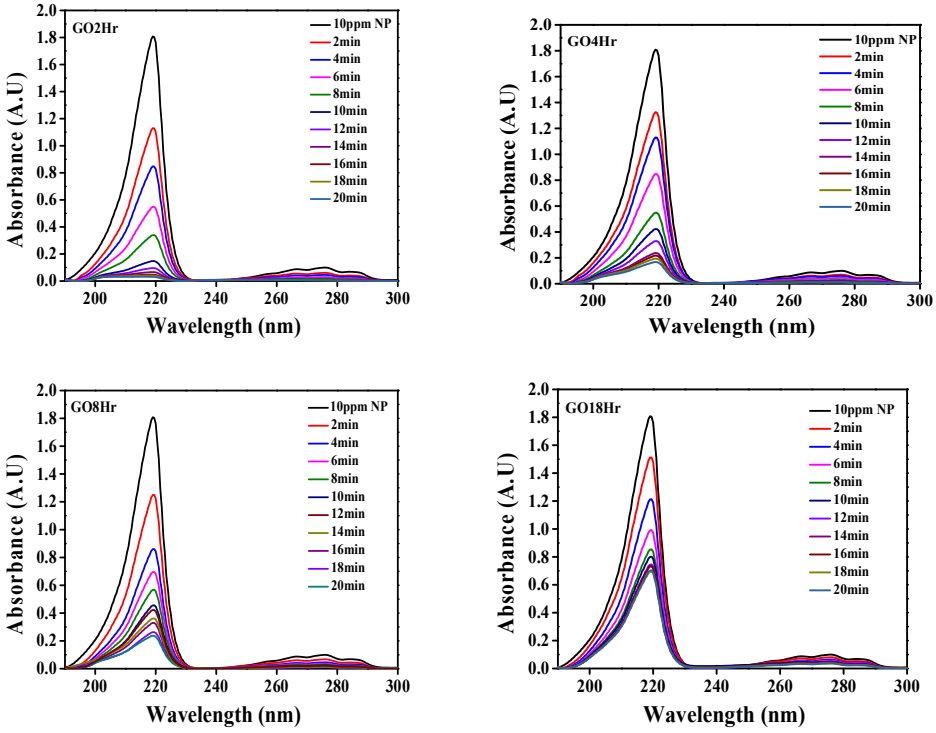

Figure 6.11 *UV-visible absorbance for naphthalene adsorption on GO samples.*

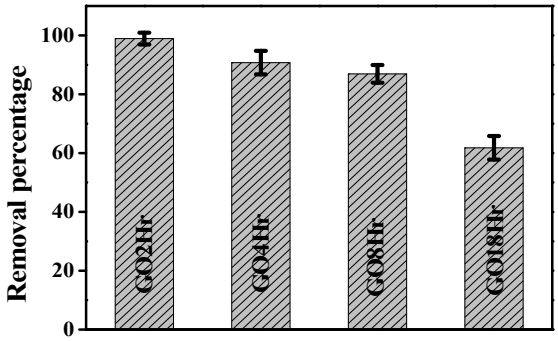

Figure 6.12 *Naphthalene removal percentage for GO samples*

6.3.3.1 Adsorption Kinetics

The adsorption of naphthalene onto various GO samples was studied using pseudo-first-order and pseudo-second-order kinetic models. Figure 6.13 presents the pseudo-first-order kinetic fit, while Figure 6.14 illustrates the pseudo-second-order kinetic fit. The adsorption kinetic parameters are summarised in Table 3.

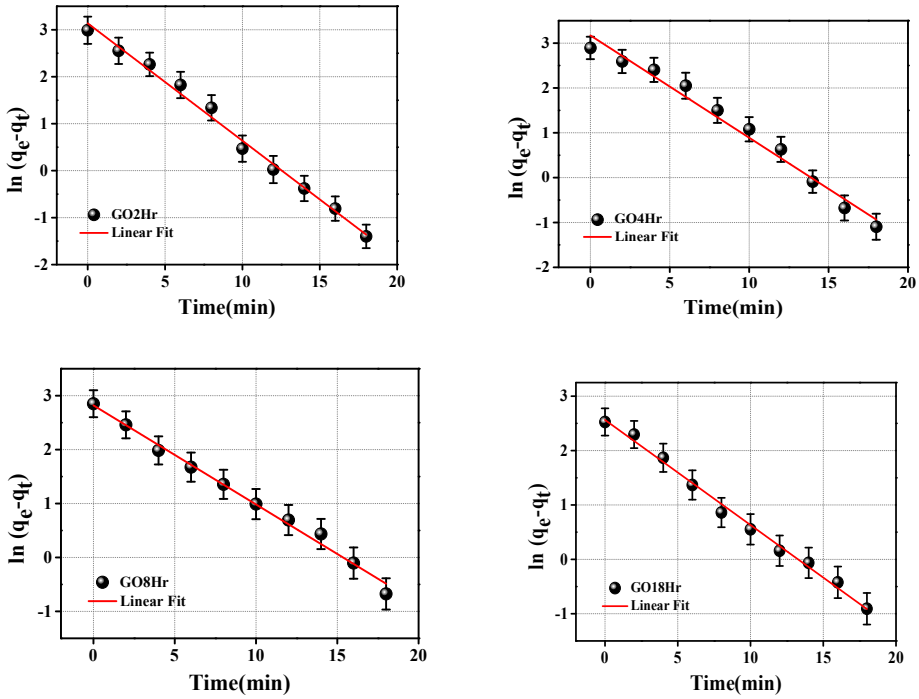

Figure 6.13 *Pseudo-first-order kinetic fit for naphthalene adsorption for GO samples*

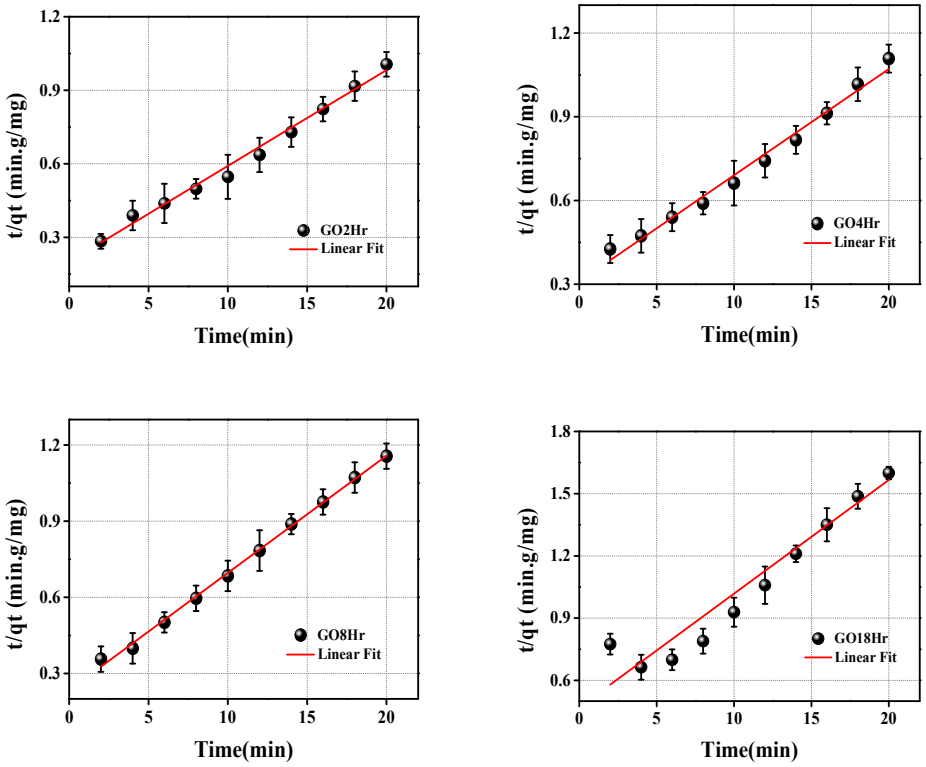

Figure 6.14 *Pseudo-second-order kinetic fit for naphthalene adsorption for GO samples*

Table 6.3 *Adsorption kinetic parameters for naphthalene adsorption for GO samples*

Sample name	q_{e_direct}	Pseudo-first-order kinetics			Pseudo-second-order kinetics		
		k_1 (min^{-1})	$q_{e\_kinetic}$ (mg/g)	R^2	k_2 (g/mg min)	$q_{e\_kinetic}$ (mg/g)	R^2
GO2Hr	23.88	0.25	23.04	0.99	0.007	25.64	0.99
GO4Hr	20.04	0.23	22.84	0.98	0.004	26.31	0.98
GO8Hr	17.30	0.18	16.79	0.99	0.009	21.66	0.99
GO18Hr	12.50	0.19	12.97	0.99	0.006	18.52	0.94

For the GO2Hr sample, corresponding to 2 hours of stirring time, the adsorption capacity (q_e) determined from direct measurement is 23.88 mg/g. This value indicates the amount of naphthalene adsorbed per gram of GO under the given

experimental conditions, highlighting the high adsorption potential of the GO sample stirred for 2 hours.

The pseudo-first-order kinetic model assumes that the adsorption rate is proportional to the number of available adsorption sites. For the GO2Hr sample, the rate constant (k_1) is 0.25 min^{-1}, and the adsorption capacity from the fit is $q_{e\_kinetic}$ = 23.04 mg/g, close to q_{e_direct} of 23.88 mg/g. The high correlation coefficient (R^2 = 0.99) suggests that the pseudo-first-order model provides a good fit for describing the adsorption process for this sample. However, the slight difference between q_{e_direct} and $q_{e\_kinetic}$ shows that this model doesn't fully capture the adsorption mechanism.

The pseudo-second-order model assumes that adsorption occurs due to chemisorption, involving electron sharing or exchange between adsorbate and adsorbent. For the GO2Hr sample, the rate constant (k_2) is 0.007 g/mg·min, and the adsorption capacity is $q_{e\_kinetic}$ =25.64mg/g. The even higher correlation coefficient (R^2 = 0.99) indicates that the pseudo-second-order model fits the data more accurately than the first-order model.

The adsorption of naphthalene onto the GO samples is primarily governed by pseudo-second-order kinetics, indicating that the process is dominated by chemisorption, where naphthalene molecules form strong chemical bonds with the graphene oxide surface, possibly involving electron sharing or exchange. This is reflected in the higher R^2 values obtained for the pseudo-second-order model, which suggests that the adsorption rate is more dependent on the chemical interaction between naphthalene and GO than on the availability of adsorption sites. However, the pseudo-first-order model, typically associated with physical adsorption through weaker forces such as van der Waals interactions, also reasonably fits the experimental data. This suggests that while chemisorption is the dominant mechanism, some degree of physisorption occurs, particularly in the initial stages of the process. The agreement with both models implies that the adsorption process may begin with faster, weaker physical interactions, followed by slower, stronger chemical bonding, resulting in the observed adsorption behaviour.

6.3.3.2 Mechanism

The adsorption mechanism of naphthalene onto graphene oxide (GO) involves a combination of physical and chemical interactions, primarily driven by π-π stacking and the presence of oxygen-containing functional groups on the GO surface. Naphthalene, as a polycyclic aromatic hydrocarbon, possesses π-electrons that interact with the delocalised π-electrons in the graphitic structure of GO. These π-π interactions allow naphthalene molecules to adhere to the basal planes of GO through non-covalent bonding, which is a key factor in the adsorption process. Additionally, the GO surface may contain various oxygen-containing functional groups such as hydroxyl (-OH), carboxyl (-COOH), and epoxy (-C-O-C) groups. These groups potentially enhance adsorption by facilitating hydrogen bonding and dipole-dipole interactions between naphthalene and the GO surface.

Among the samples tested, GO2Hr, which was subjected to the shortest oxidation time, exhibited the highest adsorption capacity. This suggests that the GO2Hr sample retains an optimal balance between functional groups and the integrity of its graphitic structure. While the oxidation process introduces oxygen-containing groups that can enhance adsorption through chemical interactions, the relatively intact graphitic domains in GO2Hr likely contribute to stronger π-π interactions with naphthalene, making this sample more effective at adsorption. A sufficient number of functional groups, without excessive oxidation, enables physical adsorption via π-π stacking and chemical adsorption through hydrogen bonding and electrostatic interactions.

In contrast, the GO4Hr, GO8Hr, and GO18Hr samples, which underwent longer oxidation times, may have a higher concentration of oxygen-containing functional groups. While this increases the potential for chemical interactions with naphthalene, the prolonged oxidation could disrupt the graphitic structure, diminishing the extent of π-π interactions. This disruption likely reduces the adsorption efficiency in these samples compared to GO2Hr. The combined effect of the increased functional groups and the decreased π-π stacking ability in the more

oxidised samples illustrates the delicate balance between physical and chemical interactions that govern adsorption.

In conclusion, the superior adsorption performance of the GO2Hr sample can be attributed to its preserved graphitic regions, which support strong π-π interactions with naphthalene alongside a sufficient but not excessive presence of functional groups. The gradual increase in oxidation time for GO4Hr, GO8Hr, and GO18Hr leads to a higher degree of functionalisation but at the cost of disrupting the π-conjugation, resulting in reduced adsorption capacity. This balance between π-π interactions and functional group contributions plays a crucial role in the overall adsorption mechanism of naphthalene onto graphene oxide.

6.3.3.3 Comparison Table

Table 6.4 *Comparison table showing the adsorption parameters of various adsorbents towards naphthalene*

Sl No	**Adsorbent**	**Maximum adsorption capacity (mg/g)**	**Parameters**	**Reference**
1.	Graphene oxide	0.167 μg/g	0.025 g/100 mL, 0.03–10 ppm, 0–24 h	**[20]**
2.	Steel slag	0.041	0.1 g/100 mL, 3–10 ppm, 0.5–5 g, 0–48 h	**[21]**
3.	Synthetic zeolite (Na-X)	0.067	5–20 ppm	**[22]**
4.	Clinoptilolite	1.63	5–30 ppm, 0–1 h	**[23]**
5.	Kaolin/Fe3O4 composite	1.70	0.05 g/10 mL, 2–10 ppm, 0–100 min	**[24]**
6.	Amino-modifed clinoptilolite	1.88	5–30 ppm, 0–1 h	**[23]**
7.	Surfactant-modified mesoporous silica	2.60	100 mg/ 20 mL, 2–60 ppm, 0–48 h	**[25]**
8.	AC from petroleum coke	3.2	0.25–6.5 ppm, 25 °C	**[26]**
9.	Graphene oxide from rice straw	3.33	0.05–2 g, 25–, 0–1 h	**[27]**

10.	Rice straw	3.58	0.5 g/25 mL, 50–150 ppm, 0–720 min	**[28]**
11.	Sugarcane bagasse	3.73	0.5 g/25 mL, 50–150 ppm, 0–720 min	**[28]**
12.	Graphene from rice straw	5.99	0.05–2 g, 0–1 h	**[27]**
13.	Graphene oxide	7.44	2 -25 ppm,	**[29]**
14.	Red clay	9.23	25 mg/50 mL 6.4 to 25.6 ppm, 0–3 h	**[30]**
15.	Hydroxyapatite	12.9	0.2 g/100 mL 5 to 100 ppm, 0–240 min	**[31]**
16.	Metal azolate framework	14	4 mg/50 mL, 0.04– 0.14 g, 5–20 ppm, 0–8 h	**[32]**
17.	AC from coal tar pitch/furfural	18.75	0.1 g/50 mL, 5–20 ppm, 0–120 min	**[33]**
18.	AC from wood waste	22.33	2–10 ppm, 0.025– 0.1 g, 0–120 min	**[34]**
19.	Hexadecyltrimethylammonium -modified bentonite	22.45	0.05 g/ 50 mL, 7.5– 20 ppm, 0–2 h	**[35]**
20.	Graphene oxide	22.93	1 -30 ppm,	**[36]**
21.	**Modified Graphene oxide**	**23.88**	**0.005g/100ml 10ppm**	**Present work**

6.3.4 Biosensing with ascorbic acid

With a sense of accomplishment in developing a material boasting an exceptionally high adsorption capacity, our focus has shifted toward applying biosensing using these advanced materials. This study aims to detect ascorbic acid by employing a complex formation involving ferric chloride, potassium ferricyanide, and the target analyte – ascorbic acid. Specifically, a 50 mL solution containing 5 mM potassium ferricyanide and another 50 mL solution containing 1 mM ferric chloride are combined, and then 50 mL of 1 mM ascorbic acid is added. The desired outcome of this reaction is the formation of Prussian blue, resulting in a distinct colour change.

A novel approach is employed before introducing ascorbic acid to enhance the sensitivity of our biosensing system. Before its addition, the ascorbic acid is treated with graphene oxide samples that have been meticulously prepared. Subsequently, the treated ascorbic acid is introduced into the reaction mixture containing ferric chloride and potassium ferricyanide, leading to intriguing and noteworthy results.

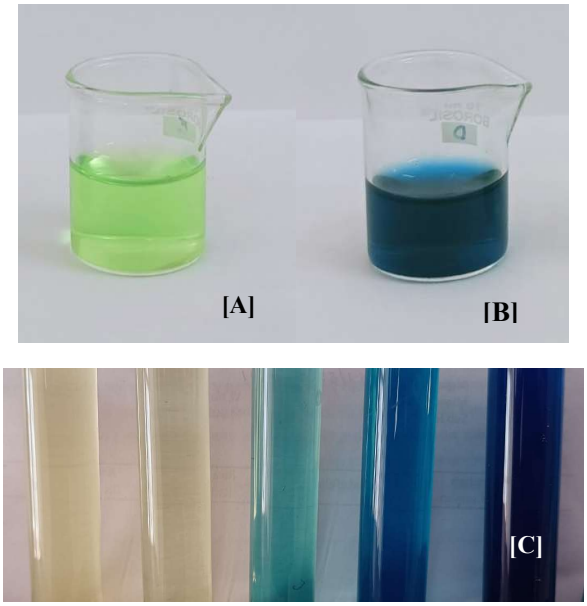

Figure 6.15 *[A] $FeCl_3$ and $K_3[Fe(CN)_6]$ are mixed in desired concentrations and we have a light green hue coloured solution. [B] When Ascorbic acid is added to the mixture of $FeCl_3$ and K_3 $[Fe(CN)_6]$ Prussian blue colour is formed. [C] The figure illustrates the colour variation depending on the concentration of ascorbic acid. At lower concentrations of ascorbic acid, a light green hue is observed, whereas with increasing amounts of ascorbic acid in the solution, while keeping other reagent concentrations constant, the formation of Prussian blue intensifies. (Note that the experiments in the above figure does not have GO as a reactant).*

At the highest concentration of ascorbic acid, we have prussian blue same as that in figure 6.15[A]. As ascorbic acid concentration reduces, the colour changes from Prussian blue to light green hue as in figure 6.15[C]. When ascorbic acid is initially treated with graphene oxide (GO), prussian blue colour is not formed upon introducing the mixture with $FeCl_3$ and $K_3[Fe(CN)_6]$. The colour inhibition can be attributed to ascorbic acid adsorption onto GO and subsequent utilisation for GO

reduction. This experiment helps us to standardise the colourimetric evaluation of ascorbic acid concentration in our further adsorption experiment involving GO.

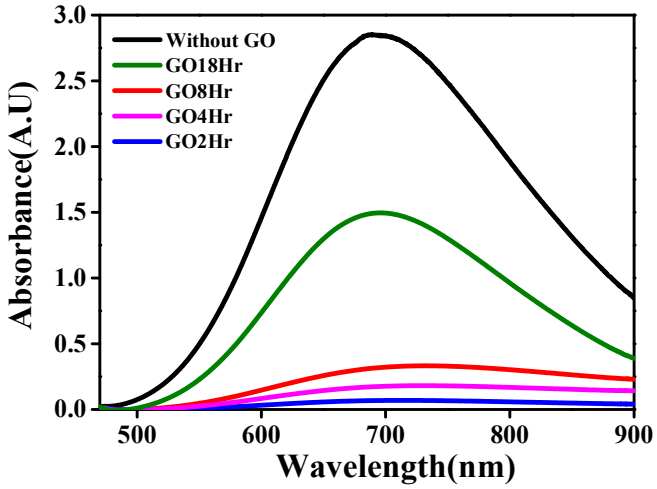

Figure 6.16: *UV visible spectra of solution with ascorbic acid, GO, $FeCl_3$ and $K_3[Fe(CN)_6]$, to compare the effect of GO2Hr, GO4Hr, GO8Hr, GO18Hr.*

To examine the impact of modified GO based on varying modification times, ascorbic acid (AA) was treated with each of the graphene oxide samples (GO2Hr, GO4Hr, GO8Hr, GO18Hr.) before their reaction with $FeCl_3$ and $K_3[Fe(CN)_6]$. The GO2Hr sample exhibits high adsorption of ascorbic acid, resulting in the lowest intensity of the UV-visible spectra among the samples treated with GO, as in Figure 6.16.

The interaction among ascorbic acid (AA), $FeCl_3$, and $K_3[Fe(CN)_6$ results in the formation of prussian blue dye, as illustrated in Figure 15A. The colour variation observed in Figure 15C is attributed to fluctuations in the concentration of prussian blue, directly influenced by changes in ascorbic acid levels within the reaction mixture. The fundamental detection principle hinges on the capacity of vitamin C ($C_6H_8O_6$) to reduce Fe_{III}, creating a Prussian blue colloid.

In the initial step, vitamin C ($C_6H_8O_6$) actively reduces Fe^{III} to generate Fe^{II} [a]. Subsequently, the second step involves the synthesis of Prussian blue ($KFe^{III}[Fe^{II}(CN)_6]$) as Fe^{II} reacts with potassium ferricyanide ($K_3[Fe^{III}(CN)_6]$) [b].

This method forms the basis for detecting ascorbic acid, exploiting its role in the reduction process and subsequent Prussian blue formation.[37]

$$2\mathrm{Fe^{III}} + C_6H_8O_6 \rightarrow 2\mathrm{Fe^{II}} + C_6H_8O_6 + 2\mathrm{H^+} \quad [a]$$

$$Fe^{II} + K_3[Fe^{III}(\mathrm{CN})^6] \rightarrow \mathrm{K}Fe^{III}[Fe^{II}(\mathrm{CN})^6] + 2K^+ \quad [b]$$

A unique approach has been adopted to enhance the sensitivity of the biosensing system. Before the complex reaction, ascorbic acid undergoes treatment with graphene oxide (GO) samples. This pre-treatment leads to the adsorption of AA onto GO, resulting in reduced AA availability for the subsequent reaction with $FeCl_3$ and ferricyanide.

The impact of these interactions is discerned through the intensity of the produced Prussian blue, as reflected in the UV-visible spectra of the solutions. Notably, among the graphene oxide samples, GO2Hr exhibits the highest reactivity with ascorbic acid. This observation underscores the significance of GO samples in influencing the reaction dynamics and product outcomes, providing valuable insights for the advancement of biosensing technologies.

6.3 Conclusion

In this chapter, we investigated the synthesis of graphene oxide (GO) synthesis by varying modification times and systematically analysed its impact on its functional properties. Our primary aim was to explore how modification time influences the functional groups in GO and its performance in adsorption and sensing applications. Through our studies, we were successful in achieving this goal and have made a valuable contribution to the growing body of research on graphene oxide.

The adsorption experiments with methylene blue and naphthalene as model pollutants demonstrated the superior performance of GO synthesised with a 2-hour modification time (GO2Hr) compared to the other samples. GO2Hr exhibited excellent adsorption capacity in just 4 minutes, which we attribute to the optimal concentration of functional groups, such as hydroxyl and carboxyl groups, that facilitate efficient pollutant interactions. We could also achieve the highest adsorption capacity of 1285mg/g for any GO sample in the literature by tuning the experimental

conditions. This highlights the importance of modification time in controlling GO's functional group composition, directly affecting its adsorption efficiency.

Time-varied synthesised GO samples demonstrated excellent results in dye removal, prompting further exploration of their adsorption capabilities with another class of pollutants: naphthalene, a polycyclic aromatic hydrocarbon (PAH). Naphthalene adsorption with GO samples was evaluated, and nearly 100% removal was observed within 20 minutes. The reaction kinetics was assessed, and found that it contributed from both pseudo-first and pseudo-second-order kinetics, as physical adsorption from pore filling and chemical adsorption by various interactions contributed to the adsorption.

In the ascorbic acid sensing experiment, we utilised a unique approach by coupling ascorbic acid with ferric chloride and potassium ferricyanide in a specified ratio, forming Prussian blue dye. This method allowed us to sense ascorbic acid indirectly using GO as a sensing platform. Once again, GO2Hr outperformed the other samples, demonstrating the best sensing capabilities. This success further validates GO2Hr's effectiveness, suggesting that the functional groups formed during the 2-hour modification time are ideally suited for such applications.

It was observed that when the modification time was too short—specifically less than 1 hour—graphene oxide (GO) was not formed, which was experimentally verified. This indicates that a minimum modification time is necessary to induce sufficient oxidation and the formation of oxygen-containing functional groups. Conversely, when the modification time was too long, as in the case of 18 hours, the excessive oxidation led to a reduction in the number of functional groups, which in turn negatively impacted the adsorption and sensing capabilities of the GO. It further emphasised the critical impact of modification time to optimise GO's performance.

This chapter represents a significant milestone in graphene oxide research, especially in understanding how varying synthesis times can tailor GO for specific applications. By fine-tuning the modification time, we have demonstrated that GO2Hr is a highly effective material for adsorption and sensing, paving the way for further advancements in GO-based technologies.

6.5 References

1. Paredes, J. I., Villar-Rodil, S., Martínez-Alonso, A., & Tascón, J. M. D. (2008). Graphene Oxide Dispersions in Organic Solvents. *Langmuir*, *24*(19), 10560–10564. https://doi.org/10.1021/la801744a

2. Zhao, X., Zhang, Q., Chen, D., & Lu, P. (2010). Enhanced Mechanical Properties of Graphene-Based Poly(vinyl alcohol) Composites. *Macromolecules*, *43*(5), 2357–2363. https://doi.org/10.1021/ma902862u

3. Zhao, L., Chen, J., Xiong, N., Bai, Y., Yilihamu, A., Ma, Q., Yang, S., Wu, D., & Yang, S. (2019). Carboxylation as an effective approach to improve the adsorption performance of graphene materials for Cu2+ removal. *The Science of the Total Environment*, *682*, 591–600. https://doi.org/10.1016/j.scitotenv.2019.05.190

4. Wang, X., Gui, W., Duan, F., & Mu, X. (2021). Effect of functional groups on the adsorption of graphene oxide on iron oxide surface. *Surface Science*, *716*, 121982. https://doi.org/10.1016/j.susc.2021.121982

5. An, X., & Yu, J. C. (2011). Graphene-based photocatalytic composites. *RSC Advances*, *1*(8), 1426. https://doi.org/10.1039/c1ra00382h

6. Zhu C, Guo S, Fang Y, Dong S (2010) Reducing sugar: new functional molecules for the green synthesis of graphene nanosheets. ACS Nano 4:2429–2437. https://doi.org/10.1021/nn1002387

7. Wang Y, Shi Z, Yin J (2011) Facile synthesis of soluble graphene via a green reduction of graphene oxide in tea solution and its biocomposites. J ACS Appl Mater Interfaces 3(4):1127–1133

8. Paton-Carrero, A., Sanchez, P., Sánchez-Silva, L., & Romero, A. (2022). Graphene-based materials behaviour for dyes adsorption. *Materials Today Communications*, *30*, 103033.

9. Nuengmatcha, P., Mahachai, R., & Chanthai, S. (2014). Thermodynamic and kinetic study of the intrinsic adsorption capacity of graphene oxide for malachite green removal from aqueous solution. *Oriental journal of chemistry*, *30*(4), 1463.

10. Yan, H., Tao, X., Yang, Z., Li, K., Yang, H., Li, A., & Cheng, R. (2014). Effects of the oxidation degree of graphene oxide on the adsorption of methylene blue. *Journal of hazardous materials*, *268*, 191-198.

11. Chen, L., Li, Y., Du, Q., Wang, Z., Xia, Y., Yedinak, E., ... & Ci, L. (2017). High-performance agar/graphene oxide composite aerogel for methylene blue removal. *Carbohydrate polymers*, *155*, 345-353.

12. Mao, B., Sidhureddy, B., Thiruppathi, A. R., Wood, P. C., & Chen, A. (2020). Efficient dye removal and separation based on graphene oxide nanomaterials. *New Journal of Chemistry*, *44*(11), 4519-4528.

13. Chia, C., Nur, F. R., Mohd, S. S., Sarani, Z., Huang, N., & Lim, H. (2013). 7Methylene blue adsorption on graphene oxide. *Sains Malaysiana*, *42*(6), 819-826.

14. Yang, S. T., Chen, S., Chang, Y., Cao, A., Liu, Y., & Wang, H. (2011). Removal of methylene blue from aqueous solution by graphene oxide. *Journal of colloid and interface science*, *359*(1), 24-29.

15. Qiao, Y., Zhao, H., Rao, Z., & Lei, Y. (2022). High Adsorption Graphene Oxide Prepared by Graphite Anode from Spent Lithium-Ion Batteries for Methylene Blue Removal. *Batteries*, *8*(11), 249.

16. Tao X, Wang S, Li Z. Ultrasound-assisted bottom-up synthesis of Ni-graphene hybrid composites and their excellent rhodamine B removal properties. Journal of Environmental Management. 2020;255:109834. DOI: 10.1016/j.jenvman.2019.109834

17. Yan, J. A., & Chou, M. Y. (2010). Oxidation functional groups on graphene: Structural and electronic properties. *Physical Review B—Condensed Matter and Materials Physics*, *82*(12), 125403.

18. Xiufang, H., Wu, Z., Sun, Z., Wei, X., Wu, Z., Ge, X., & Cravotto, G. (2018). A novel hybrid of β-cyclodextrin grafted onto activated carbon for rapid adsorption of naphthalene from aqueous solution.

19. Ghasemi, S., & Nematollahzadeh, A. (2018). Molecularly imprinted polymer membrane for the removal of naphthalene from petrochemical wastewater streams. Advances in Polymer Technology, 37(6), 2288-2293.

20. Li X, Li F, Fang L (2015) Effect of Microbes on the Adsorption of Naphthalene by Graphene Oxide. J Nanoparticles 2015:1–7. https://doi.org/10.1155/2015/816982

21. Yang L, Qian X, Wang Z et al (2018b) Steel slag as a low-cost adsorbent for the removal of phenanthrene and naphthalene. Adsorpt Sci Technol 36:1160–1177. https://doi.org/10.1177/0263617418 756407

22. Wołowiec M, Muir B, Zieba K et al (2017) Experimental Study on the Removal of VOCs and PAHs by Zeolites and SurfactantModifed Zeolites. Energy Fuels 31:8803–8812. https://doi.org/ 10.1021/acs.energyfuels.7b01124

23. Wang C, Leng S, Xu Y et al (2018) Preparation of amino functionalised hydrophobic zeolite and its adsorption properties for chromate and naphthalene. Minerals. https://doi.org/10.3390/ min8040145

24. Arizavi A, Mirbagheri NS, Hosseini Z et al (2020) Efficient removal of naphthalene from aqueous solutions using a nanoporous kaolin/Fe3O4 composite. Int J Environ Sci Technol 17:1991–2002. https://doi.org/10.1007/s13762-019-02521-1

25. Vidal CB, Barros AL, Moura CP et al (2011) Adsorption of polycyclic aromatic hydrocarbons from aqueous solutions by modifed periodic mesoporous organosilica. J Colloid Interface Sci 357:466–473. https://doi.org/10.1016/j.jcis.2011.02.013

26. Yuan M, Tong S, Zhao S, Jia CQ (2010) Adsorption of polycyclic aromatic hydrocarbons from water using petroleum coke-derived porous carbon. J Hazard Mater 181:1115–1120. https://doi.org/ 10.1016/j.jhazmat.2010.05.130

27. Das P, Goswami S, Maiti S (2016) Removal of naphthalene present in synthetic waste water using novel Graphene /Graphene Oxide nano sheet synthesised from rice straw: comparative analysis, isotherm and kinetics. Front Nanosci Nanotechnol. https://doi. org/10.15761/fnn.1000107

28. Younis SA, El-Gendy NS, El-Azab WI, Moustafa YM (2015) Kinetic, isotherm, and thermodynamic studies of polycyclic aromatic hydrocarbons biosorption from petroleum refnery wastewater using spent waste biomass. Desalin Water Treat 56:3013–3023. https://doi.org/10.1080/19443994.2014.964331

29. Pei Z, Li L, Sun L et al (2013) Adsorption characteristics of 1,2,4-trichlorobenzene, 2,4,6- trichlorophenol, 2-naphthol and naphthalene on graphene and graphene oxide. Carbon N Y 51:156–163. https://doi.org/10.1016/j.carbon.2012.08.024

30. Gładysz-Płaska A, Lipke A, Tarasiuk B et al (2017) Naphthalene sorption on red clay and halloysite modifed by quaternary ammonium salts. Adsorpt Sci Technol 35:464–472. https://doi.org/10. 1177/0263617417696090

31. Bouiahya K, Oulguidoum A, Laghzizil A et al (2020) Hydrophobic chemical surface functionalisation of hydroxyapatite nanoparticles for naphthalene removal. Colloids Surf A Physicochem Eng Asp 595:124706. https://doi.org/10.1016/j.colsurfa.2020.124706

32. Bhadra BN, Song JY, Lee SK et al (2018) Adsorptive removal of aromatic hydrocarbons from water over metal azolate framework6-derived carbons. J Hazard Mater 344:1069–1077. https://doi. org/10.1016/j.jhazmat.2017.11.057

33. Tsyntsarski B, Petrova B, Budinova T et al (2011) Characterisation and application of activated carbon from biomass and coal wastes for naphthalene removal. Bulg Chem Commun 43:552–557

34. Barman SR, Banerjee P, Das P, Mukhopadhayay A (2018) Urban wood waste as precursor of activated carbon and its subsequent application for adsorption of polyaromatic hydrocarbons. Int J Energy Water Resour 2:1–13. https://doi.org/10.1007/ s42108-018-0001-4

35. Kaya EMÖ, Özcan AS, Gök Ö, Özcan A (2013) Adsorption kinetics and isotherm parameters of naphthalene onto natural- and chemically modifed bentonite from aqueous solutions. In: Adsorption. pp 879–888

36. Balati A, Shahbazi A, Amini MM, Hashemi SH (2015) Adsorption of polycyclic aromatic hydrocarbons from wastewater by using silica-based organic–inorganic nanohybrid material. J Water Reuse Desalin 5:50–63. https://doi.org/10.2166/wrd.2014.013

37. Teepoo, S., Chumsaeng, P., Jongjinakool, S., Chantu, K., & Nolykad, W. (2012). A new simple and rapid colorimetric screening test for semi-qualitative analysis of vitamin C in fruit juices based on Prussian blue. *Journal of Applied Sciences*, *12*(6), 568-574.

CHAPTER 7

GRAPHENE OXIDE MODIFICATION USING MELAMINE SPONGE

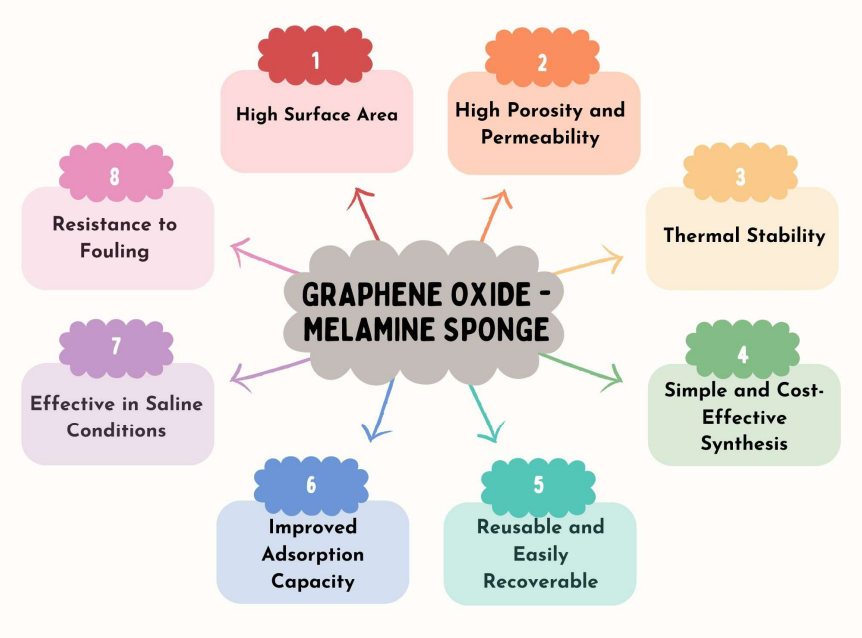

Scope of the Chapter

- *Low-cost synthesis with minimal experimental setup.*
- *Material demonstrated simultaneous oil-water separation and dye removal*
- *Achieved excellent performance for oil-water separation and dye adsorption, even in saline conditions.*

Abstract

This chapter focuses on developing and characterizing melamine sponge-graphene oxide (MSGO) composites for environmental remediation applications. By incorporating graphene oxide synthesized over varying durations (GO2Hr, GO4Hr, GO8Hr, and GO18Hr) into a melamine sponge, we aimed to enhance its adsorption properties. The primary objective is to evaluate the adsorption efficiency of MSGO composites using methylene blue dye alongside their oil-water separation capabilities. The composite exhibited remarkable performance, achieving over 95% dye removal even in various oil-water mixtures, including almond oil, coconut oil, diesel, kerosene, olive oil, palm oil, sesame oil, and sunflower oil. The adsorption kinetics were also analyzed through pseudo-first and pseudo-second-order models to understand the underlying mechanisms. The results highlight the potential of MSGO, particularly in saline conditions, for tackling water pollution and oil spills.

7.1 Introduction

Graphene oxide (GO) possesses abundant surface oxygen-containing functional groups, a large surface area, and hydrophilicity, making it an effective adsorbent [1]. It can be easily fabricated from inexpensive graphite through chemical oxidation routes. While GO sheets can be directly used as adsorbents by dispersing them in solution, challenges arise in separating and recollecting them after adsorption due to their high dispersibility, ultra-light nature, and superhydrophilic properties in aqueous solutions. Additionally, random aggregation or stacking of GO sheets is inevitable, reducing adsorption capacity and making consistent adsorbent performance challenging to maintain [2,3].

Recent research has focused on constructing GO-based composites as adsorbents to address these issues. By incorporating targeted materials to the GO sheets, the tendency for aggregation in GO-based composite powder adsorbents can be minimized, simplifying their recollection. However, these nanoparticles block the adsorption sites of GO, thereby limiting the adsorption capacity [4,5,6].

In comparison, a 3D loading offers distinct advantages as a practical adsorbent. When produced as a sponge-like adsorbent, it fully exposes the adsorption sites, prevents agglomeration, and enhances recoverability. Melamine sponge (MS) is an ideal carrier due to its low density, high porosity, flexibility, and low cost [6,7,8]. With its unique structure, MS can exhibit excellent adsorption capacity when loaded with a specific adsorbent, making it a promising material for practical applications. The superb adsorption properties of GO, combined with the 3D porous nature of melamine sponge, overcome the limitations of each material individually, resulting in an outstanding adsorbent material.

Several studies have demonstrated the successful incorporation of GO sheets into melamine sponge (MS), resulting in composite materials with excellent adsorption performance and oil-water separation [9,10]. However, achieving specific adsorption often requires species-specific modifications of GO or MS, which can reduce the available functional groups and decrease GO's adsorption efficiency.

A recent study [11] employed a direct immersion method to load GO sheets onto MS for dye adsorption in aqueous solutions. Although this technique is straightforward, the GO sheets adsorbed onto the MS surface can block the pore channels, leading to accumulation primarily on the surface and hindering penetration into the interior. This blockage limits the effective utilization of the MS's porous structure and, consequently, the composite's overall adsorption capacity [12].

Therefore, further research is necessary to optimize the loading of pure GO sheets into MS and evaluate the resulting adsorbent's performance for dye removal in aqueous solutions.

In the present work, we employ a straightforward loading technique to incorporate GO into MS, achieving uniformly dispersed GO without altering the pores of the MS. The MSGO samples will be first evaluated for their adsorption efficiency using methylene blue as a model pollutant. This optimal MSGO sample will then be subjected to oil-water separation experiments, leveraging the hydrophobic and oleophilic properties of the composite to assess its effectiveness in environmental remediation applications.

7.2 Experimental Details

7.2.1 Loading Graphene oxide to Melamine sponge

Graphene oxide samples (GO2Hr, GO4Hr, GO8Hr, GO18Hr) are synthesized as detailed in section 6.1.1. Melamine sponges are cut into 1x1x1 cm^3 cubes, washed with distilled water, and dried in a vacuum oven at 60°C. A 100 ml solution of 0.5 g/L graphene oxide (GO) is prepared, and 20 melamine sponge cubes are added. The mixture is sonicated for two hours. After sonication, the GO-loaded sponges are removed from the solution and subjected to mechanical compressions to remove excess GO solution, ensuring that the GO does not block the pores of the sponges. These cubes are then dried in a vacuum oven at 60°C for 24 hours.

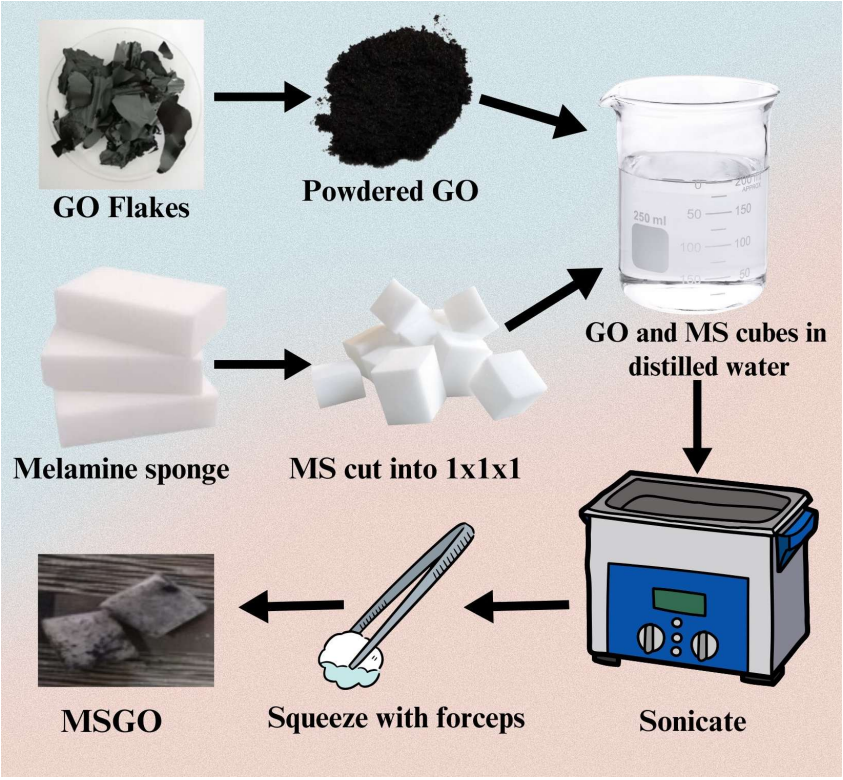

Figure 7.1 *Synthesis of MSGO samples*

7.2.2 Adsorption experiment

A 100 mL solution of methylene blue (10 ppm) was stirred in the dark. An MSGO cube was then added to the solution, and adsorption was monitored by measuring the absorbance at 5-minute intervals for 35 minutes. The adsorption experiment was repeated using four MSGO samples, each loaded with GO synthesized at different durations: 2 hours (MSGO2), 4 hours (MSGO4), 8 hours (MSGO8), and 18 hours (MSGO18). The UV-vis absorbance results are given in Figure 7.2.

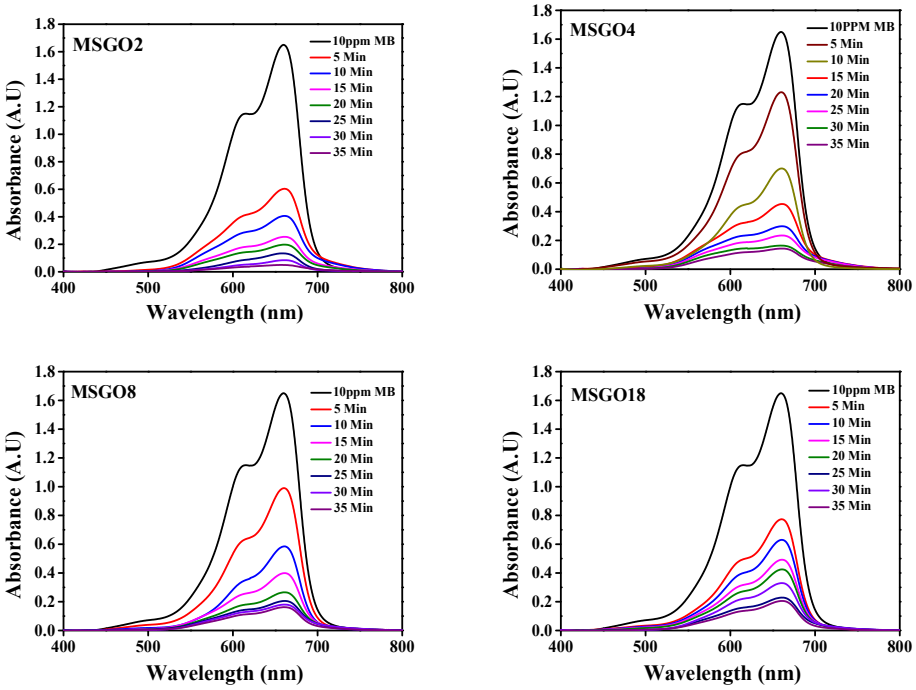

Figure 7.2 *UV-visible absorbance plots of MB dye adsorption using MSGO2, MSGO4, MSGO8 and MSGO18. Initial absorbance of 10ppm MB is 1.665 and it reduced to 0.035, 0.139, 0.154 and 0.201 for MSGO2, MSGO4, MSGO8 and MSGO18respectively*

The dye removal percentage has been evaluated and presented in a figure7.3.

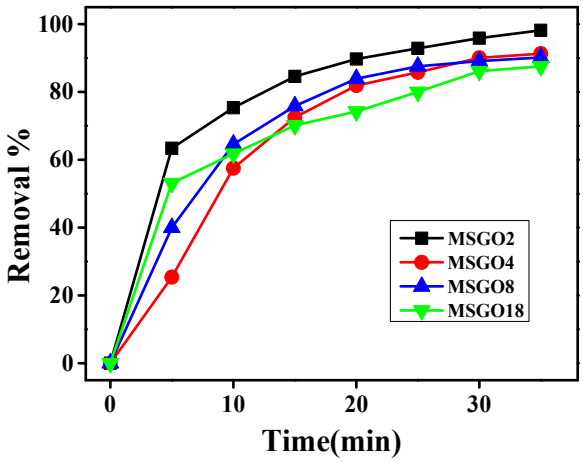

Figure 7.3 *Dye removal percentage for each MSGO sample. The error bars are contained within the symbol size.*

When evaluating the dye removal percentage for each MSGO sample, it was found that MSGO2 exhibited a slightly higher removal percentage than the others, which showed similar removal percentages within the experimental limits.

7.2.3 Adsorption kinetics

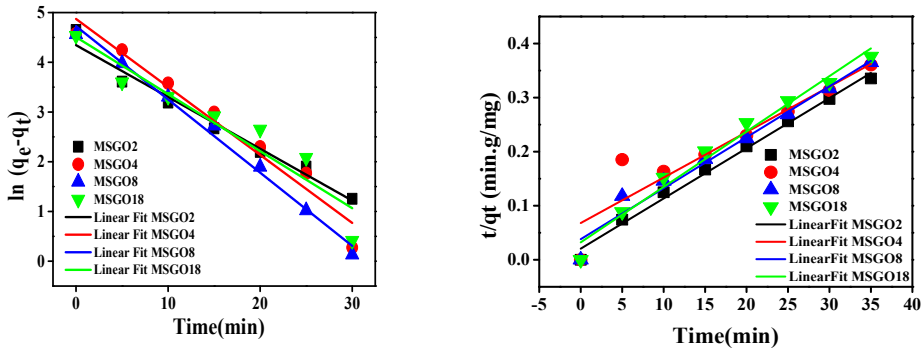

Figure 7.4(a) *Pseudo first-order kinetic model and* ***(b)*** *pseudo-second-order kinetic model fit for dye adsorption using MSGO samples.*

The adsorption kinetics were evaluated using both pseudo-first-order and pseudo-second-order kinetic models, and the results are presented in the figure 7.4(a) and 7.4(b) and tabulated in table7.1

Table7.1 *Adsorption kinetic parameters*

Sample name	$q_{e\ direct}$	Pseudo-first-order kinetics			Pseudo-second-order kinetics		
		k_1 (min^{-1})	$q_{ekinetic}$ (mg/g)	R^2	k_2 (g/mg min)	$q_{ekinetic}$ (mg/g)	R^2
GO2Hr	104.36	0.104	77.09	96.9	8.630×10^{-5}	107.64	99.6
GO4Hr	97.03	0.136	130.582	95.6	7.072×10^{-5}	118.91	90.6
GO8Hr	95.84	0.147	112.843	99.1	8.893×10^{-5}	106.04	98.5
GO18Hr	93.06	0.115	90.695	95.2	10.50×10^{-5}	97.561	98.9

The adsorption kinetics of methylene blue dye onto MSGO align more closely with pseudo-second-order kinetics, but the contribution of pseudo-first-order kinetics cannot be ignored. Pseudo-first-order kinetics indicate physical adsorption, where the dye molecules enter the pores of MSGO. In contrast, pseudo-second-order kinetics represent chemical adsorption involving electrostatic interactions, hydrogen bonding, and π-π interactions between the dye molecules and MSGO. The porous structure of MSGO was intentionally designed to enhance dye adsorption.

Now that MSGO has been identified as an excellent adsorbent, we can expand our discussion and results to include its broader application in two different scenarios: oil-water separation and dye removal. From all the MSGO variants, we selected the sample with the best adsorption efficiency, MSGO2, for the application.

7.1.4 Oil-water separation experiment

Methodology

In order to carry out a facile methodology to illustrate oil water separation experiment we have given different colours to water and oil. Water was coloured with methylene blue dye and oil with sudan red dye. The oil-water mixture is prepared by mixing 10ml of 5ppm methylene blue coloured water with 10 ml of sudan red coloured oil, here in this case its almond oil. The mixture is dropped into a funnel with MSGO inserted to the small opening. The filtrate is collected into a measuring cylinder and UV-visible absorbance analysis is done. This experiment is repeated with the almond oil being tested sequentially with coconut oil, diesel, kerosene, olive oil, palm oil, sesame oil, and sunflower oil.

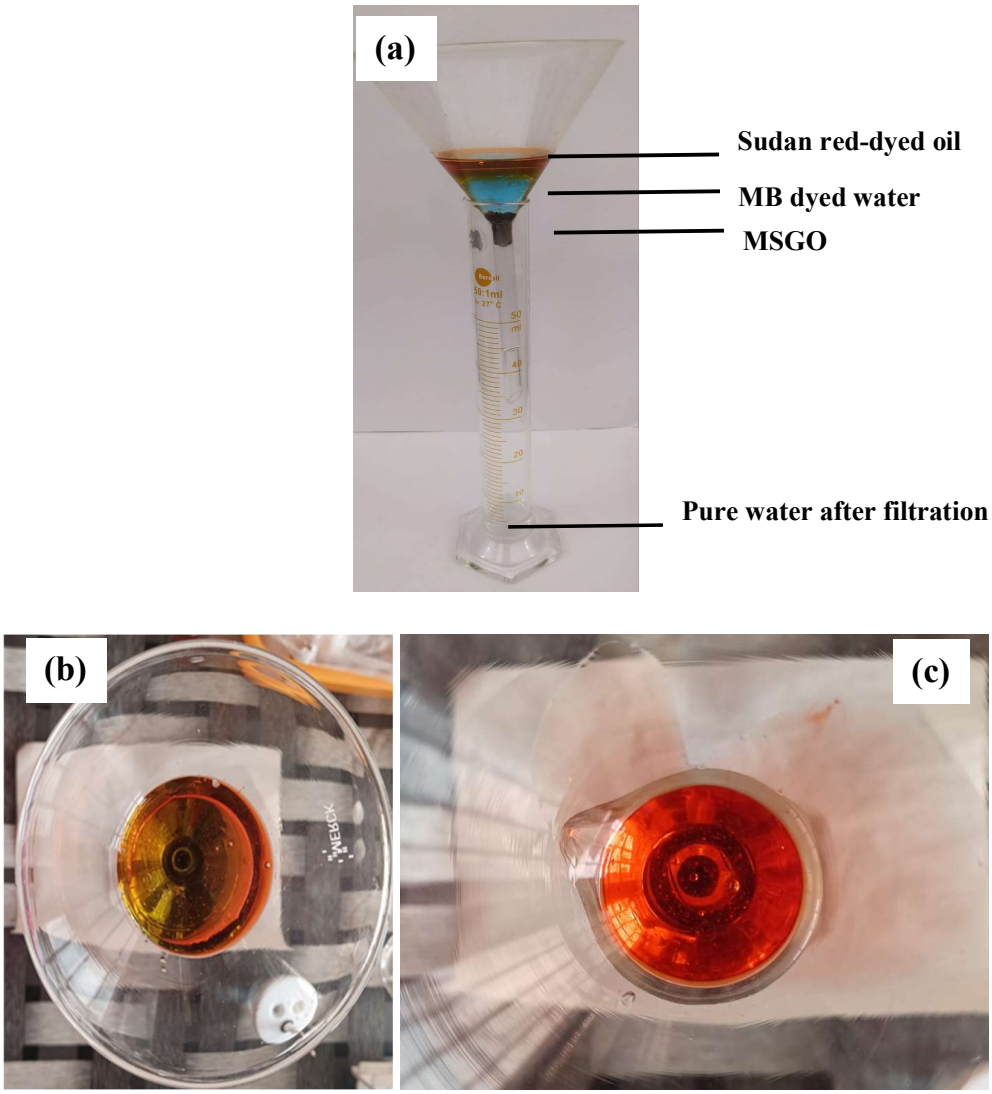

Figure 7.5: (a) *Schematic of the experimental setup for oil-water separation. A funnel loaded with MSGO is connected to a measuring cylinder, allowing a mixture of oil and water to pass through the material.* ***(b)*** *Oil water mixture top view* ***(c)*** *oil remaining in the funnel, after the water has been filtered out.*

7.3 Results and Discussions

The UV-visible absorbance spectrum of the 5ppm methylene blue (MB) solution is measured. The absorbance spectra of the oil-water mixtures (for all types of oils) after passing through the MSGO2 (via the funnel) are also recorded. These results are then compared with the spectrum of the 5 ppm MB solution and are given in the figure7.6.

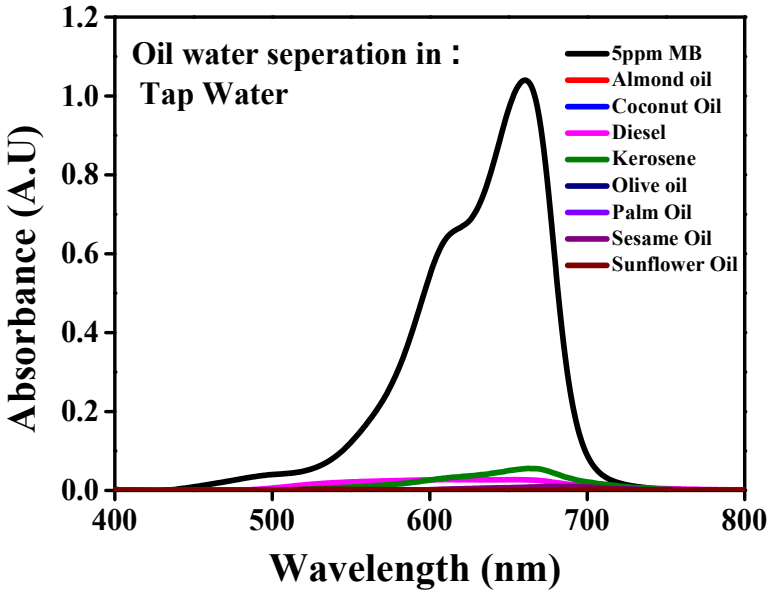

Figure 7.6: *UV-visible absorbance spectra of various oil-water mixtures prepared in tap water. Initially, a 5 ppm Methylene Blue (MB) solution is prepared in tap water, and its spectrum is recorded. The oil-water mixtures prepared, are passed through MSGO2, and the UV-visible spectra of the filtrates are also recorded.*

When introduced to MSGO, the oil-water mixture wets the sponge at first due to the presence of hydrophilic GO in them, thereby preventing the flow of oil through it. Consequently, the resultant suspension contains no trace of oil, as evidenced by the absence of Sudan Red in the filtrate. Additionally, because the melamine sponge is coated with graphene oxide (GO), the methylene blue (MB) is completely adsorbed by the GO, leaving the suspension free of MB as well. The dye removal percentage of MB from each set of oil-water mixture by MSGO2 is listed in Table7.2. The table shows that the dye removal percentage is greater than 99% for most of the oil mixtures tested. This experiment demonstrates the high efficiency of the prepared GO as an adsorbent and the effective oil-water separation capability of the melamine sponge. Thus, the combination of MSGO proves to be an excellent solution for dye adsorption and oil-water separation.

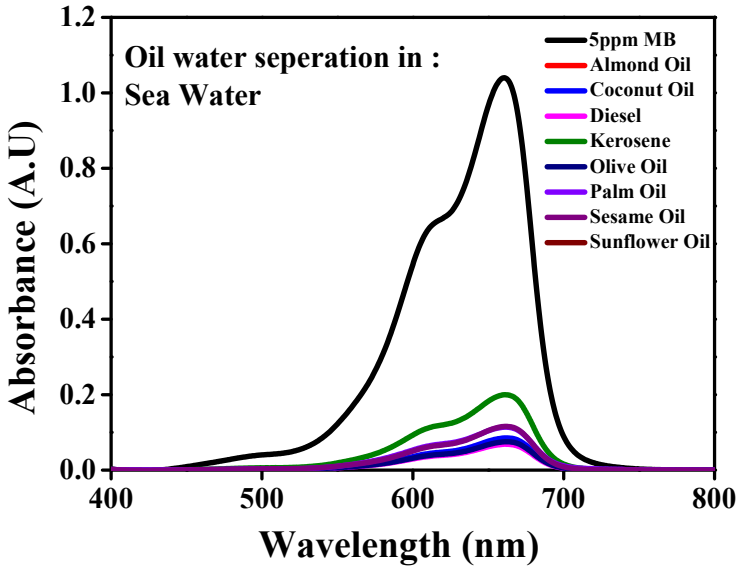

Figure 7.7: *UV-visible absorbance spectra of various oil-water mixtures prepared in sea water. Initially, a 5 ppm Methylene Blue (MB) solution is prepared in sea water, and its spectrum is recorded. The oil-water mixtures prepared, are passed through MSGO2, and the UV-visible spectra of the filtrates are also recorded.*

The purification of water from oil-water mixtures is crucial to addressing spills in seas and oceans. Therefore, testing this experiment with seawater is essential. To this end, we collected seawater, measured its salinity, and repeated the experiment under these conditions.

The salinity of the collected seawater was measured using a salinity refractometer and was found to be 33g/L, which aligns with the standard salinity range for seawater [13].

Figure 7.7 shows the UV-visible absorbance spectra of 5ppm MB compared with MB solution in seawater mixed with different oils after passing through MSGO. The dye removal percentage of MB from each set of oil-water mixture in seawater by MSGO is listed in Table 7.2. Comparison between the removal percentage of a dye-oil mixture from tap water and seawater is graphically represented in figure 7.8.

Table7.2: *Absorbance values after adsorption and removal percentage of methylene blue (MB) for different sets of oil-water mixture in tap water and sea water*

Sl. No	Oil	Absorbance after Adsorption in tap water	Dye removal percentage (%) $R = \frac{A_0 - A_T}{A_0} \times 100$	Absorbance after Adsorption in sea water	Dye removal percentage (%) $R = \frac{A_0 - A_T}{A_0} \times 100$
1.	Almond oil	0.004	99.6	0.073	92.9
2.	Coconut oil	0.003	99.6	0.093	91.0
3.	Diesel	0.027	97.4	0.063	94.0
4.	Kerosene	0.056	94.6	0.202	80.8
5.	Olive oil	0.006	99.4	0.080	92.3
6.	Palm oil	0.007	99.3	0.070	93.2
7.	Sesame oil	0.010	99.0	0.124	88.1
8.	Sunflower oil	0.003	99.7	0.076	92.7

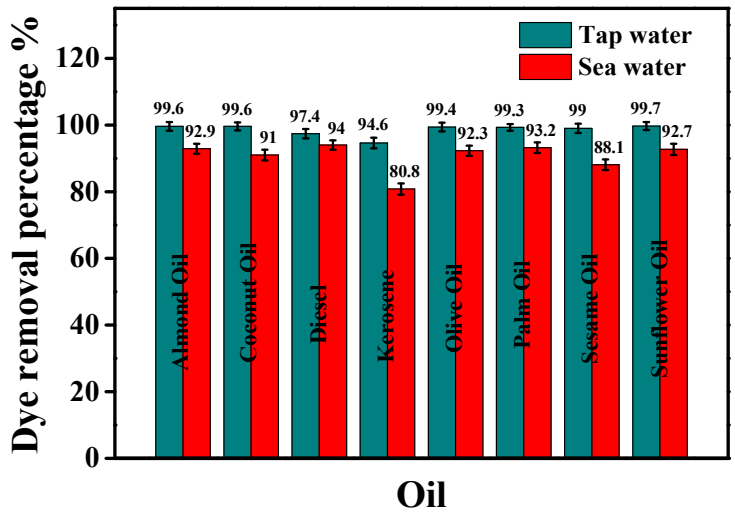

Figure 7.8: *Dye removal percentage of methylene blue (MB) for different sets of oil-water mixture in tap water and sea water.*

When the experiment was repeated using seawater, the removal percentages were somewhat lower compared to that of tap water, reflecting the more challenging conditions presented by the saline environment. However, even under these harsh conditions, the removal efficiencies remained high. Specifically, the removal percentages for diesel and palm oil are as high as 94 and 93.2%. These results indicate the robustness of the method even in the presence of salinity.

The slight decrease in the removal percentage observed in sea water compared to tap water can be attributed to the competitive interactions between salt ions and the dye molecules. In a saline environment, the presence of dissolved salts increases the ionic strength of the solution, which can lead to a reduction in the electrostatic attraction between the adsorbent surface and the dye molecules. This competition between salt ions and dye molecules can interfere with the adsorption process, causing a decrease in the overall removal efficiency. Additionally, the high salinity can affect the surface properties and stability of the adsorbent material, further influencing the adsorption capacity. Despite these challenges, the method remains highly effective for oil-water separation, demonstrating its effectiveness even in saline conditions.

7.4 Conclusion

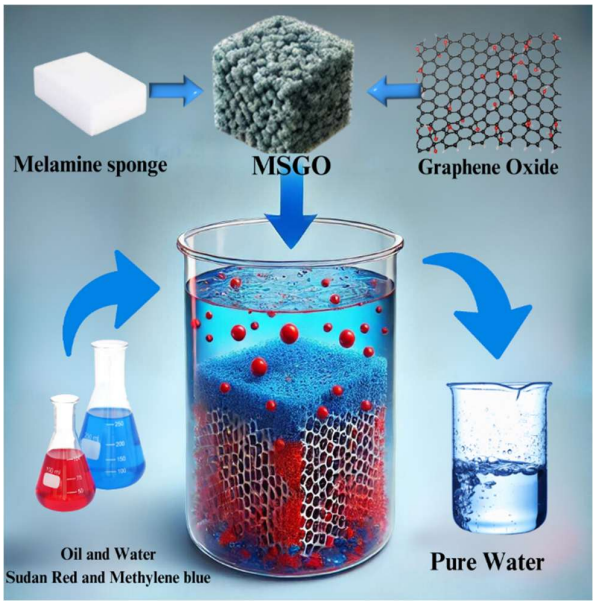

In this chapter, we successfully synthesized melamine sponge-graphene oxide (MSGO) composites using four different graphene oxide samples, designated as GO2Hr, GO4Hr, GO8Hr, and GO18Hr, based on their varying synthesis durations. Each MSGO composite was prepared by incorporating graphene oxide into a melamine sponge through a simple yet effective loading technique, ensuring uniform dispersion of GO within the sponge while maintaining the porous structure essential for adsorption applications.

The adsorption capabilities of the MSGO composites were evaluated using methylene blue dye as a model pollutant. Among the samples, MSGO2 exhibited the most efficient dye adsorption, demonstrating significant removal rates in a short duration. The adsorption kinetics of these composites were systematically analyzed using pseudo-first and pseudo-second-order kinetic models. The results suggest that the pseudo-second-order model better describes the adsorption process, indicating chemisorption as the dominant mechanism.

Moreover, the MSGO composite's performance in oil-water separation was thoroughly investigated. The composite demonstrated remarkable efficiency, achieving over 95% dye removal in various oil-water mixtures, including almond oil, coconut oil, diesel, kerosene, olive oil, palm oil, sesame oil, and sunflower oil. Significantly, we demonstrated that the MSGO composite's effectiveness is extended to both tap and sea water environments, which is particularly relevant for real-world applications where oil spills commonly occur in marine ecosystems.

7.5 References

1. T. Ma, P.R. Chang, P. Zheng, F. Zhao, X. Ma, Fabrication of ultra-light graphene-based gels and their adsorption of methylene blue, Chem. Eng. J. 240 (2014) 595–600, https://doi.org/10.1016/j.cej.2013.10.077

2. Zhao, Y., Ran, W., He, J., Huang, Y., Liu, Z., Liu, W., Tang, Y., Zhang, L., Gao, D., & Gao, F. (2014). High-Performance Asymmetric Supercapacitors Based on Multilayer MnO2/Graphene Oxide Nanoflakes and Hierarchical Porous Carbon with Enhanced Cycling Stability. *Small*, *11*(11), 1310–1319. https://doi.org/10.1002/smll.201401922

3. Zhu, X., Zhou, G., He, G., Ma, L., Xu, B., & Sun, F. (2023). Directly loading graphene oxide into melamine sponge for fast and high-efficiency adsorption of methylene blue. *Surfaces and Interfaces*, *36*, 102575. https://doi.org/10.1016/j.surfin.2022.102575

4. L. Chen, D. Zhao, S. Chen, X. Wang, C. Chen, One-step fabrication of amino functionalized magnetic graphene oxide composite for uranium(VI) removal, J. colloid interface sci 472 (2016) 99–107, https://doi.org/10.1016/j. jcis.2016.03.044.

5. S. Wang, X. Li, Y. Liu, C. Zhang, X. Tan, G. Zeng, B. Song, L. Jiang, Nitrogen-containing amino compounds functionalized graphene oxide: synthesis, characterization and application for the removal of pollutants from wastewater: a review, J. Hazard. Mater. 342 (2018) 177–191, https://doi.org/10.1016/j. jhazmat.2017.06.071

6. Xia, J., Zhu, Y., He, Z., Wang, F., & Wu, H. (2019). Superstrong noncovalent interface between melamine and graphene oxide. *ACS applied materials & interfaces*, *11*(18), 17068-17078.

7. Y. Yao, S. Miao, S. Yu, L.P. Ma, H. Sun, S. Wang, Fabrication of Fe 3 O 4 /SiO 2 shell nanoparticles attached to graphene oxide and its use as an adsorbent, J. Colloid Interface Sci. 379 (2012) 20–26, https://doi.org/10.1016/j. jcis.2012.04.030

8. F. Wang, L. Zhang, Y. Wang, X. Liu, S. Rohani, J. Lu, Fe 3 O 4 @SiO 2 core/ @CS-TETA functionalized graphene oxide for the adsorption of methylene blue (MB) and Cu (II), Appl. Surf. Sci. 420 (2017) 970–981, https://doi.org/10.1016/j. apsusc.2017.05.179

9. C. Wu, X.Y. Huang, X.F. Wu, R. Qian, P.K. Jiang, Mechanically flexible and multifunctional polymer-based graphene foams for elastic conductors and oil- water separators, Adv. Mater. 25 (2013) 5658–5662, https://doi.org/10.1002/ adma.201302406

10. Zhu, X., Zhou, G., He, G., Ma, L., Xu, B., & Sun, F. (2023). Directly loading graphene oxide into melamine sponge for fast and high-efficiency adsorption of methylene blue. *Surfaces and Interfaces*, *36*, 102575.

11. J. Ge, L.A. Shi, Y.C. Wang, H.Y. Zhao, H.B. Yao, Y.B. Zhu, Y. Zhang, H.W. Zhu, H. A. Wu, S.H. Yu, Joule-heated graphene-wrapped sponge enables fast clean-up of viscous crude-oil spill, Nat. Nano. 12 (2017) 434–440, https://doi.org/10.1038/ nnano.2017.33

12. M. Peng, G. Chen, G. Zeng, A. Chen, K. He, Z. Huang, L. Hu, J. Shi, H. Li, L. Yuan, T. Huang, Superhydrophobic kaolinite modified graphene oxide-melamine sponge with excellent properties for oil-water separation, Appl. Clay Sci. 163 (2018) 63–71, https://doi.org/10.1016/j.clay.2018.07.008.

13. National Oceanic and atmospheric administration US, Department of Commerce. https://www.noaa.gov/jetstream/ocean/sea-water

CHAPTER 8

SUMMARY AND CONCLUSION

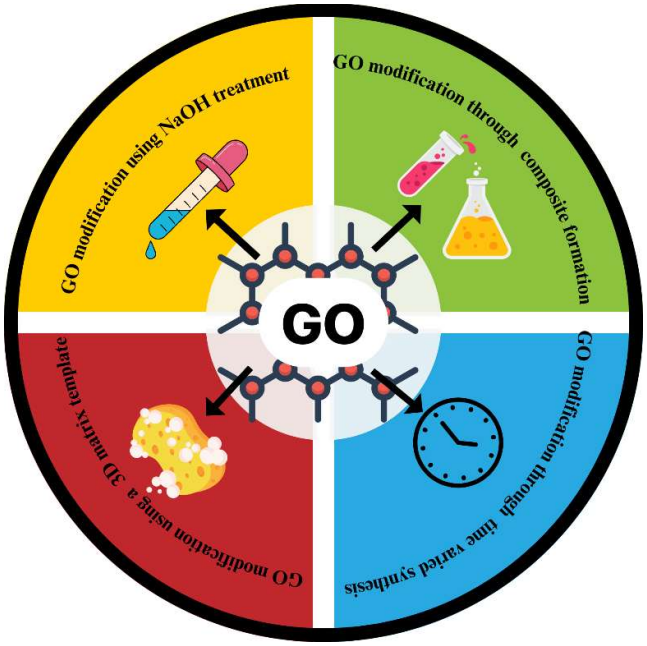

The thesis, titled ***Tuning the Functionality of Graphene Oxide for Adsorption and Sensing Applications*****,** focuses on modifying graphene oxide to optimise its functional properties through various approaches and subsequent use in adsorption and sensing applications. Nearly 100% adsorption of diverse pollutants, including dyes, antibiotics, and polycyclic aromatic hydrocarbons, was achieved in all cases. The reaction kinetics were thoroughly evaluated, and mechanisms were proposed for each set of reactions. Furthermore, this exceptional adsorption capacity was leveraged for successfully sensing bodily fluids such as ascorbic acid (Vitamin C) and uric acid.

The thesis is organised into five working chapters, each aligned with the objectives outlined in Section 1.6. The following paragraphs provide an overview of each chapter along with its key outcomes.

In the first working chapter [chapter 3], we explored the critical role of sodium hydroxide (NaOH) in tuning the functionality of graphene oxide (GO). Our systematic study revealed a threshold NaOH concentration of 5.45:1 (NaOH: GO by weight), at which it acts as a reducing agent. This finding was supported by UV-visible spectroscopy and Raman spectral analysis, where the enhanced π-π* transitions and the ID/IG ratio highlighted the reduction pathway facilitated by NaOH. We proposed that UV-visible absorbance maxima, rather than peak shift, is the critical parameter in analysing GO reduction. Our results also demonstrated that pH does not play a decisive role in GO reduction. This conclusion was experimentally validated using $NaBH_4$ as a reducing agent, where both pH and absorbance maxima exhibited a similar trend, potentially leading to the misinterpretation that pH is a decisive parameter for GO reduction. However, in the case of NaOH as the reducing agent, the pH and absorbance maxima trends differed. Absorbance maxima were found to be more indicative of reduction, as confirmed by Raman ID/IG analysis.

Additionally, our study identified the threshold value for GO reduction using NaOH, which is strongly supported by a random literature assessment. We found that in works where GO was reported to be not fully reduced by NaOH, the NaOH: GO mass ratio was below the proposed threshold in this thesis. Conversely, reduction occurred when the weight ratio exceeded the threshold, confirming the critical importance of this ratio. Interestingly, our results demonstrated that pH does not have a decisive role in GO reduction. These findings have significant implications for the scalable synthesis of graphene-based nanocomposites, where precise control of chemical ingredient concentrations can lead to enhanced functionality and industrial applicability.

The second working chapter [chapter 4] focused on synthesising a graphene oxide-activated carbon (GOAC) composite using a single-step mixing technique without any linker molecules. This composite demonstrated exceptional adsorption capacities for various dyes and pharmaceutical contaminants, including methylene blue, rhodamine B, and ciprofloxacin antibiotic, achieving up to 100% removal efficiency under optimised conditions. Including activated carbon not only improved

the thermal stability of the composite but also mitigated GO's natural tendency to agglomerate in water. Moreover, the durability of the GOAC composite was evidenced by its sustained adsorption performance over five consecutive regeneration cycles, making it a highly promising material for water purification applications. We also evaluated the adsorption kinetics and proposed possible adsorption mechanisms for the reaction of GOAC with given pollutants. The adsorption followed a pseudo-second-order kinetic model indicating chemical interaction between adsorbent and adsorbate molecules.

In the third working chapter [chapter 5], we synthesised and introduced a novel reduced graphene oxide-gold (rGO-Au) nanocomposite for uric acid sensing in body fluids. Dynamic Light Scattering (DLS) analysis revealed the average particle size is 17.04 ± 0.04 nm for gold (Au) nanoparticles, and 24.85 ± 0.02 nm for the rGO-Au nanocomposite. The rGO-Au composite exhibited a remarkable fivefold enhancement in UV-visible absorbance for uric acid compared to GO or gold nanoparticles alone. This synergistic effect, attributed to the surface plasmon resonance of gold nanoparticles and the unique anchoring properties of rGO, enabled detection limits and sensitivity aligned with physiological uric acid levels (experiment done in the range 1 to 20 mg/dL of uric acid, physiological uric acid levels - male: 4.0–8.5 mg/dL, female: 2.7–7.3 mg/dL, child: 2.5–5.5 mg/dL, newborn: 2.0–6.2 mg/dL). Unlike conventional sensing methods, our approach offered a simpler and cost-effective alternative, paving the way for advanced clinical diagnostics and routine health monitoring solutions.

The fourth working chapter [chapter 6] detailed the impact of varying synthesis durations on the functional properties of GO. We prepared four samples by varying the stirring duration, referred to as the modification time, after adding $KMnO_4$. The modification times were set to 2 hours, 4 hours, 8 hours, and 18 hours, and the resulting GO samples were designated as GO2Hr, GO4Hr, GO8Hr, and GO18Hr, respectively. We tested the sample interactions with (a) methylene blue dye, (b) naphthalene and (c) ascorbic acid. GO2Hr stood out among the samples for its superior adsorption and sensing performance. Its optimal functional group

composition enabled the highest adsorption capacities for methylene blue and naphthalene among reported GO materials. For MB adsorption, we achieved the highest adsorption capacity of 1285mg/g at the best time of 4 minutes. The sample was regenerated and reused for five additional cycles, consistently achieving 100% dye adsorption, underscoring the effectiveness of the material. GO2Hr also showed excellent results in ascorbic acid sensing, validating its utility in both environmental and biochemical applications. This chapter highlighted the importance of carefully tuning synthesis time to optimise GO's performance, as excessive or insufficient oxidation can adversely affect its functionality.

Finally, the fifth working chapter [chapter 7] showcased the successful integration of GO into a melamine sponge to form MSGO composites by mechanical compression method without blocking the pores of the sponge to tune the functional properties of GO. MSGO samples demonstrated exceptional performance in both dye adsorption and oil-water separation. Among the samples, MSGO2, derived from the GO2Hr sample, exhibited the highest efficiency in removing pollutants, with adsorption kinetics favouring chemisorption mechanisms. The performance of MSGO in oil-water separation was evaluated in both tap water and seawater, using a diverse range of oils, including almond oil, coconut oil, diesel, kerosene, olive oil, palm oil, sesame oil, and sunflower oil. The MSGO composites achieved remarkable oil-water separation efficiencies exceeding 95%, even in saline environments, highlighting their practical relevance for marine ecosystem applications. This chapter emphasised the versatility and robustness of MSGO composites, offering concurrent sustainable solutions for environmental remediation and oil water separation applications.

In summary, we successfully optimised the functionality of GO for targeted applications in adsorption and sensing through various modification strategies, specifically (a) NaOH treatment, (b) composite formation, (c) time-varied synthesis and (d) using a 3D matrix template. Fine-tuning the functionality of GO is crucial for gaining deeper insights into its structure and composition, which directly influence its performance in specific applications. Understanding the relationship between synthesis conditions, functional group distribution, and structural modifications

enabled precise tailoring of GO for adsorption and sensing. Moreover, this knowledge is vital when synthesising GO-based composites, as it helps optimise their properties for enhanced functionality and broader applicability. Notably, in all adsorption experiments conducted, our material demonstrated superior adsorption performance compared to those reported in the literature, further highlighting the effectiveness of our optimisation strategies. These findings offer valuable insights into graphene and graphene oxide-based synthesis and applications, paving the way for further research and advancements in these fields.

CHAPTER 9
RECOMMENDATIONS

The thesis has been focused on tuning the functionality of graphene oxide (GO) through systematic modifications to enhance its application potential in adsorption and sensing. Significant milestones have been achieved, including the successful synthesis and characterization of GO and its composites with varying synthesis times, functionalization techniques, and material integrations. The adsorption capabilities of GO and its composites, such as melamine sponge-GO (MSGO) and GO-activated carbon composites (GOAC), have been demonstrated in removing pollutants like dyes, oil, and organic contaminants. The sensing capabilities of reduced graphene oxide-gold (rGO-Au) nanocomposites for uric acid and ascorbic acid detection using UV-visible spectroscopy have also been explored. The performance of GO-based materials in specific environmental scenarios, such as oil-water separation in saline conditions, has also been investigated.

While the present work has contributed significantly to understanding and advancing the functionality of GO, it has also opened up several avenues for further research. Addressing these unexplored areas will be crucial for developing GO and its composites as versatile materials for environmental and biological applications.

Future Work

Future research is recommended to focus on further **chemical functionalization** of graphene oxide (GO) using a variety of metals, polymers, and other materials **to enhance its adsorption capacity and selectivity**. These functionalized materials should be tailored for specific contaminants, including heavy metals, pharmaceuticals, and organic pollutants. Efforts to strengthen the interaction between GO and target molecules are expected to improve efficiency and expand the material's application scope in environmental remediation.

To enable industrial applications, it is essential to prioritize the scalability of GO and its composite synthesis processes. While laboratory-scale synthesis has

demonstrated effectiveness, **scaling up** the production of GO and its composites, such as GOAC and MSGO, is recommended. This will require optimizing reaction parameters, reducing production costs, and **ensuring reproducibility** to facilitate large-scale deployment of GO-based materials in real-world environmental settings.

Simultaneous **removal of multiple pollutants** should also be a key area of exploration. GO and its composites should be evaluated for their ability to remove diverse pollutants under real-world conditions, including organic dyes, heavy metals, and pharmaceuticals. It is recommended that their performance in complex matrices like wastewater and industrial effluents be investigated to develop GO-based materials with broader environmental applications.

Special attention should be given to the use of **GO-based composites in marine environments**. Research is recommended to focus on their application in separating oil-water mixtures under saline conditions. Evaluating their durability, reusability, and environmental impact in challenging marine settings will be critical for practical implementation and could significantly contribute to addressing marine oil spills and related pollution challenges.

Additionally, in-depth studies on the **biocompatibility and potential environmental toxicity of GO and its composites** are essential. Emphasis should be placed on their use in biological and environmental applications, such as water purification. Understanding the long-term effects of these materials on living organisms and ecosystems is crucial to ensure their safe and sustainable utilization.

These recommendations aim to guide future research toward developing advanced GO-based materials for environmental and biological applications. The anticipated outcomes include enhancing the practical applicability of GO in water treatment, pollution management, and sensing technologies while contributing to global efforts to mitigate environmental pollution and ensure access to clean water. By addressing these research directions, the potential of graphene oxide as a versatile and impactful material can be fully realized, paving the way for sustainable technological advancements and solutions to pressing environmental challenges.